



UNIVERSITÀ
DEGLI STUDI
FIRENZE

INTERNATIONAL DOCTORATE IN CIVIL AND
ENVIRONMENTAL ENGINEERING

XXXII CYCLE

*Rockfall detection, localization and early warning
with micro-seismic monitoring network*

PhD student

Dr. Feng Liang

Supervisor

Prof. Tucci Grazia

Supervisor

Prof. Gigli Giovanni

Coordinator

Prof. Borri Claudio

Years 2016-2019

Table of Contents

- Abstract III**
- Acknowledgements V**
- 1. Introduction 1**
- 2. Study area and instrumentations 7**
 - 2.1 Geographical, Geomorphological and Geological Setting.....7
 - 2.2 Rockslide characteristics and seismic monitoring11
 - 2.2.1 The characteristics of monitoring rockslide11
 - 2.2.2 Instruments and deployment of seismic monitoring13
- 3. Methodology..... 19**
 - 3.1 Fast Fourier transform (FFT) in MATLAB19
 - 3.2 Seismic event detection methods22
 - 3.2.1 STA/LTA22
 - 3.2.2 Cross-Correlation23
 - 3.2.3 Methods comparison.....24
 - 3.3 Rockfall localization methods.....26
 - 3.3.1 Polarization-bearing26
 - 3.3.2 Time-bearing.....35
 - 3.3.3 Methods comparison.....36
- 4. Seismic features analysis of rockfall 39**
 - 4.1 Artificial released rockfall test.....39
 - 4.2 Frequency content.....41
 - 4.2.1 Frequency with impacted material41
 - 4.2.2 Frequency with distance45
 - 4.2.3 Maximum frequency46
 - 4.3 Amplitude47
 - 4.3.1 Amplitude ratio.....47
 - 4.3.2 Waveform-peaks49
 - 4.4 Duration.....52
 - 4.5 Conclusions.....53
- 5. DESTRO: joint detection and classification of rockfall in seismic monitoring 55**
 - 5.1 Seismic event detection flowchart56

5.2 Seismic features definition	57
5.2.1 Definition of the types of seismic events	57
5.2.2 Spectral attributes	59
5.2.3 Event-power attributes.....	63
5.2.4 Network geometry attributes (<i>Ra</i> and <i>Rf</i>)	68
5.2.5 Waveform-peaks (<i>Np</i>).....	69
5.2.6 Duration (<i>D</i>).....	70
5.3 Classifier design	72
5.3.1 Classifier design in a single component (classifier S).....	72
5.3.2 Classification in multi-component (classifier C)	75
5.3.3 Classification in multi-station (classifier M).....	77
5.4 DESTRO performances.....	78
5.4.1 DESTRO detection accuracy.....	78
5.4.2 DESTRO classification accuracy.....	80
5.5 Conclusions and discussions	83
6. Slope susceptible area mapping and risk early warning studies	85
6.1 Risk early warning methodology	85
6.1.1 Temporal forecasting.....	92
6.1.2 Spatial estimation	94
6.2 Susceptible area mapping.....	96
6.3 Discussions.....	102
7. Conclusions and outlook	104
References	107

Abstract

Landslides are ubiquitous in any terrestrial environment area with slopes, driven by tectonic, climate and/or human activities. Related to other natural disasters, the International Disaster Database (EM-DAT) suggests that landslides account for 4.9% of all-natural disaster events and 1.3% of all nature hazard fatalities between 1990 and 2015, and the fatalities caused by landslides might be underestimated in EM-DAT demonstrated by scholars. Every year, there are amount of human loss and economic cost, and safe estimated the average number of fatalities as 4300 per year worldwide. The United Nations International Strategy for Disaster Reduce addressed early warning systems as a powerful tool to reduce risk in a vast range of fields, including landslides.

There are many established instruments applied in slope hazard early warning monitoring system, such as borehole-based measures (inclinometer, extensometer, etc.), image-based mapping, airborne and terrestrial laser scanning (TLS) and ground based interferometric synthetic aperture radar (GB-InSAR). Each technique has its own drawbacks. Borehole-based measurements provide a precise point sample useful for deep-seated continuous monitoring but not appropriate for wide area monitoring and for landslides that do not show ductile failure; on the other hand, image-based techniques, like TSL and GB-InSAR, provide constraints on the surface changes but have limitations concerning the subsurface changes, time lapse between surveys, and slope failure process mechanism. Seismic monitoring offers a unique measurement for brittle rock slope hazard study, the seismic signals emitted by slope dynamic activities from surface to subsurface, such as debris, rockfall, cracks, etc. are continuously reflecting the dynamic state of monitoring objective, that provides a complementary solution to these shortcomings from estimated instruments.

For the purpose of this research motivation, a long-period seismic monitoring case was carried in a limestone quarry in Umbria Region (Italy) to verifying the performance of a small-scale seismic network as a part of an early-warning system dedicated to an unstable rock mass monitoring, and in that monitoring period, an artificial released rockfall in-situ test was performed to study the seismic features of rockfall. Accordingly, in this thesis: a) the seismic features of artificial rockfall are studied, and show a qualitative relationship between seismic features (frequency content, amplitude, waveform, and duration) and local characteristics (geological material, geomorphology, topography). b) In order to achieve seismic event automatic detection and classification, a program DESTRO (DEtection and SStorage of Rockfall Occurrence) is specially designed for rockfall hazard monitoring and also combined with earthquake detection. The performance of DESTRO are evaluated within the monitoring data in Torgiovanetto quarry. A program for seismic event automatic detection and classification is a kind of foundational and useful way for rock masses dynamic monitoring, even for slope instability forecasting and risk evaluation in earthquake prone areas. c) At last, an improved polarization-bearing method is proposed for rockfall localization in seismic monitoring and a seismic monitoring early warning method in rock slope is proposed, that provides an interesting way to track rockfall trajectory and slope susceptible area mapping.

This thesis, aims to provide a state-of-the-art review about micro-seismic monitoring, and improve an algorithm for seismic event automatic detection and classification, finally, provide a novel solution for slope susceptible area mapping and risk early warning in rockfall occurrence with micro-seismic monitoring. The proposed methodology could be helpful for slope hazard early warning and instant mitigation and evacuation, especially applied in inaccessible mountainous area and earthquake prone area where transportation lines are at risk.

“地球不需要被拯救，需要被拯救的是人类自己。

(The Earth always be there and naturally, doesn't need to be saved.

What need to be saved is human beings themselves.)”

丁仲礼 (Ding Zhongli)

Acknowledgements

This thesis is the result of a three-year Ph.D. program, in the fantastic and historic city, Firenze. In the abroad study period, I'm honored to work and interact with many people, all of them are the most important profound memories and wealth of my life. It's difficult to describe in a few words as each one of them deserves, so may I be forgiven if the following acknowledgments do not live up to someone's expectations.

First of all, I would like to express my great gratitude to Prof. Nicola Casagli, Prof. Giovanni Gigli and Prof. Grazia Tucci for giving me the opportunity, research financial support, and tools to undertake and complete my Ph.D. program. Particular gratitude to Dr. Veronica Pazzi and Dr. Emanuele Intrieri for their continuous technique and research support, with great patience, motivation and immense knowledge. Sometimes, I am more anxious and rough expression about thesis writing, conference presentation and publish, but their guidance always stays with me. Moreover, I would like to show my sincere thanks to Dr. Luca Tanteri and Dr. Giulia Dotta for their warm help and dealing with a lot of life troubles or concerns that I may have had. Thanks also go to Dr. Teresa Gracchi, Dr. Elena Benetteda Masi, Dr. Mattia Ceccatelli, Dr. Monan Shan, Dr. Genming Du, Dr. Carlo Tacconi, Dr. Ascanio Rosi, Dr. Fedrico Raspini, Dr. Fedrico Marini, Miss Melania Scacciati and all the people of engineering geology research group at University of Florence.

Apart from my tutors and colleagues, I won't forget to thank all the Chinese friends who studying in Florence, for all the tours and dinners we were together. Special thank Dr. Lin Gao for research methods and MATLAB discussion, that made my research fast involved.

I am also great gratitude to China Scholarship Council for the financial support, and my M.sc supervisor Prof. Xiyong Wu at Southwest Jiaotong University.

All the love cannot closely compare to the gratitude to my parents and my sister. Parents' son is profound. Thanks to your love and inspirit always stay live with me, whenever I am happy, discourage or weepy. Thank you for always keeping me in your prayers and letting me chase my dreams with no doubt. I love you beyond words.

Last but not least, warm thanks to beloved Ma Xingyu. I have finally tracked you down. Thank everything that let me met you in stars. As we said: "I love you very much at this moment, with this love, I desiring this feeling would continue forever." Ti amo e Eres mi media naranja.

1. Introduction

Rockfalls, or rock fall according to Hungr et al. (2014), are instability processes consisting of the intermittent and rapid mobilization of various sizes, types, and volumes of rock, that consists of the free fall, rebounding, rolling and sliding of a block that can fragmentate or impact with each other, which are difficult to observe directly and pose significant risk for human habitation, security and transportation. That’s a ubiquitous geomorphic process that shapes steep slopes and landforms constituting significant portions of mountainous areas (Dietze et al. 2017a). The economic and population development, increasing access and construction in mountainous area bring people and infrastructures to a greater exposure to slope hazards (Dammeier et al. 2011; Fiorucci et al. 2015; Fan et al. 2018; Fuchs et al. 2018). Many Italian valley slopes are affected by unstable rock masses as a consequence of bedrock and soil properties, steep slopes, and high seismic activity (Atkinson and Massari 1998; Romeo et al. 2017). There are many already established image-based methods for geohazard monitoring (McCarroll et al. 1998; Gigli et al. 2014a; Dietze et al. 2017a), while the temporal information on the occurrence of events delivered by these methods is very limited as it is bound to the survey lapse times, and which are typically on the order of days to months. Moreover, these techniques are also subjected to constraints such as vegetative cover and instrument resolution (Dietze et al. 2017a).

On the other hand, recently, geo-hazard characterization and monitoring have been carried out by passive seismic techniques thanks to the abovementioned advantages of the technique (La Rocca et al. 2004; Roux et al. 2008; Lin et al. 2010; Hibert et al. 2011; Feng et al. 2011; Yamada et al. 2013; Hibert et al. 2014a; Van Herwijnen et al. 2016; Dammeier et al. 2016; Coviello et al. 2019; Guinau et al. 2019; Li et al. 2019; Matsuoka 2019; Zhang et al. 2019). Seismic monitoring networks provide a complementary solution to these shortcomings bring by image-based methods (Lotti et al. 2015; Dietze et al. 2017a). Seismic signals generated by geomorphic processes (i.e., tectonic, climatic and anthropogenic activities) propagate from source through earth (Burtin et al. 2014). The seismic signal emitted carries abundant information of the event that generated it and allows researchers to reconstruct the event process (e.g. Manconi et al. 2016; Hibert et al. 2017; Arosio et al. 2018; Gracchi et al. 2017). According to the application cases of seismic monitoring performed (e.g. Ohnaka et al. 1982; Mykkeltveit et al. 1984; Norris et al. 1994; Tang et al. 1998; Guéguen et al. 2007; Moran et al. 2008; Mendecki et al. 2010; Hibert et al. 2011; 2014b; 2017a; Lacroix, et al. 2011, 2012; Curilem et al. 2014; Yamada et al. 2016; Manconi et al. 2016; Dietze et al. 2017a; Hammer et al. 2017; Del Gaudio et al. 2018; Glasgow et al. 2018; Bai et al. 2019), the analysis of seismic signals can provide useful information about the movement onset time within a few milliseconds, the location, the volume, the kinetic energy, and the kinematic mechanics of the detached rock mass. Some researchers applied seismic monitoring network to predict rock collapses through analyzing and identifying the features of seismic signals created by cracks developing processes, or study the evolution of recording seismic events (Amitrano et al. 2005; Arosio et al. 2009, 2018; Senfaute et al. 2009; Lenti et al. 2012; Walter et al. 2012a, 2012b; Zobin et al. 2016, 2018); Some scholars analyzed the correlation between physical characteristics of rockfalls and the features of seismic signal traces, generated by rockfalls, performing an events classification through measures as Hidden Markov Model, Artificial Neural Network, Random Forest algorithm (Sasaki et al. 1998; Suriñach et al. 2005; Beyreuther et al. 2008a, 2008b, 2011, 2012; Diersen et al. 2011; Hibert et al. 2011; Farin et al. 2015; Levy et al. 2015; Wyss et al. 2016; Hibert et al. 2017c; Provost et al. 2017; Weber et al. 2018; Bagheri et al. 2019). Hibert et al. (2011) studied rockfall characteristics from seismic signals, and made automatic identification, location and volume estimation of rockfalls, and performed a long period monitoring of

spatiotemporal evolution of rockfall activity from 2007 to 2011 at the Piton de la Fournaise volcano inferred from seismic data and organized an experiment consisting of the controlled release of 28 rock blocks (Hibert et al. 2011, 2014a, 2014b, 2017a, 2017b, 2017c). Arosio et al. performed a long-period seismic monitoring in Italian Prealps, and tried to make rock collapse forecasting through observing slope deformations with remote sensing techniques and combining seismic signals classification and correlation with methodology (Arosio et al. 2009, 2018); Dietze et al. validated the precision and limitation of seismic monitoring by terrestrial laser scanner measurements analyzing the spatiotemporal patterns and triggers of rockfalls through seismic signal analysis (Dietze et al. 2017a, 2017b). Burtin et al. and Coviello et al. studied the seismic features of debris fluvial processes and analyzed the correlation between geomorphic process with debris flow and meteorological condition (Burtin et al. 2009, 2013, 2014, 2016; Coviello et al. 2019). Farin et al. insight from the laboratory experiment to set the link between the dynamics of granular flow and seismic signals (Farin et al. 2015, 2016, 2018); Pazzi et al. studied the seismic noise to characterize the landslide in terms of volumes and physical properties of the involved materials and to assess the site seismic response (Pazzi et al. 2017a; Lotti et al. 2015, 2018). Moreover, there are many researchers who payed attention to the technics of seismic data analytic, like seismic events classification, try to automatically classify volcanoes, earthquakes, explosions or rockfalls from raw signals using neural networks or fuzzy expert system method giving different weights to several parameters of seismic signal (Joswig 1995; Kim et al. 1998; Langer et al. 2006; Benitez et al. 2007; Allmann et al. 2008; Carniel et al. 2013; Chouet et al. 2013; Laasri et al. 2015; Lara-Cueva et al. 2016; Beccar-Varela et al. 2016; Bhatti et al. 2016; Schimmel et al. 2018; Schöpa et al. 2018; Soto et al. 2018; Kleibrod et al. 2019).

Concerning the advantages and innovation of seismic monitoring in geohazard, the project of seismic monitoring was performed in Torgiovannetto Quarry on December 2012. This thesis is performed based on the seven-month long-period monitoring data, and one in-situ artificial rockfall released test and some other image-based monitoring technics in Torgiovannetto Quarry, the thesis would like to reach four targets that faced in seismic monitoring applied in rockfall:

- Understanding the seismic features of rockfall activity;
- Recognizing and classifying the correct signals of rockfall, earthquake, cracks or noise from huge seismic events detected automatically and extracting their seismic features;
- Localizing rockfall events, and try to track the moving trajectory;
- Try to map the rock slope susceptible area and to comply with risk early warning.

Two basic algorithms are generally used in seismic event detection: (1) the most popular and widely used was proposed by Allen (1978, 1982) and Trnkoczy (1998), which computes the ratio of short time energy average over long time energy average (STA/LTA); and that's used to adapt from previous raw seismic data or experience. This algorithm is applied in Kinematic K2 firmware and Geopsy software (Trnkoczy 1998; Picotti et al. 2017). (2) The second algorithm is cross-correlation as widely used in similarity analysis in a dataset between two signals, images, sounds and so on to recognize specific patterns. It calculates the covariance between two traces to detect events (since it is a measurement of similarity as a function of the lag of one relative to the other). The final value of cross-correlation falls between -1 and +1. Within real-world data, the values = ± 1 can never be achieved, and the absolute value will fall somewhere in between, with a high value indicating a high degree of signal similarity and a low value indicating low similarity (Bendat and Piersol 2000; Akhouayri et al. 2014; Kortstrom et al. 2016).

In addition, some algorithms are used with combined denoise filters (Panagiotakis et al. 2008; Küperkoch et al. 2010; Rodriguez 2011; Gibbons et al. 2012; Akram and Eaton 2016), such as wavelet transforms (Hafez et al. 2009,

2010, 2013; Rodriguez, 2011a, 2011b, 2012a, 2012b; Wu et al. 2016), that can remove useless noise from the original signal to obtain a stationary and clean signal for subsequent research; While notably, we should pay attention to apply denoise filters to avoid removed important information, before seismic features be fully understood.

Concerning seismic event classification, there are now wealth of new approaches (HMM, neural network, SVM, classification trees, fuzzy logic, clustering, etc.) that have been tested and work well on seismic data for multiple purposes. For example, Hidden Markov Model (HMM) was initially introduced and studied since the late 1960s and early 1970s for speech recognition (Rabiner 1989). HMM recognition is based on the spectral properties of signals and a transformation of the raw data into a parametric representation as other methods. Benítez et al. (2007) applied HMM in seismic-event classification for a volcano. For the HMM architecture, they designed 39 features relative to the energies in given frequency bands of the seismic signal, and they also performed a training in a standard database of each event category. Heck et al. (2018) applied HMM for snow avalanche precursors detection and classification, they defined 6 features (central frequency, dominate frequency, instantaneous bandwidth, instantaneous frequency, cepstral coefficients, and half-octave bands), and then trained one model for detection. HMM is an efficient method for seismic event classification in real-time with a high accuracy, but that’s significantly depends on training data set and seismic features defined, and in this case, there is only one seismic component applied in HMM training. The HMM accuracy could be improved with more station-combined features, such as the ratio of frequency and/or amplitude between two different seismic stations, the energy variation between different frequency bands, etc., that proposed before in context. Neural network through defining many key seismic features, creates a neural network model and trains it in a standard database to obtain a weight for each feature or an empirical function to describe these features (Romeo et al. 1994; Curilem et al. 2009; Scarpetta et al. 2005; Akhouayri et al. 2015; Provost et al. 2017). Provost et al. (2017) constituted a random tree defined by 71 features that include seismic signal waveform, spectrum, spectrogram, network geometry, and polarity. They also analyzed the importance of each feature. Vallejos et al. (2013) defined 29 features for event classification, such as seismic energy, frequency, magnitude and some mechanical parameters estimated in the event motion process.

For successful detection and classification, the most important issues are how to build a good training database and how to define several suitable seismic features and training without any confusion and confliction generated. This not only includes the characteristics of signal time-series but also the combination of signal features recorded by multiple stations, and efficiently takes full advantage of monitoring array.

Seismic localization is commonly used in earthquake localization as a dispensable part of a seismic monitoring system and has also been developed for volcanic, bombing and geohazard non-tectonic events (Bataille et al. 1991; Kao et al. 2004; Gibbons et al. 2007; Vilajosana et al. 2008; Guinau et al. 2019). Studying from literatures, two main methods are utilized for seismic localization. One method uses arrival times (time-bearing, T-B in the following) based on the shortest-path method that minimizes the differences among seismic signal first-arrival times recorded by multiple stations and gridded topographic map searching (Moser et al. 1992; Rodi et al. 2000; Jolly et al. 2002; Kao et al. 2004; Dammeier et al. 2011; Lacroix and Helmstetter 2011; Xu et al. 2011; Lacroix et al. 2012; Grigoli et al. 2013; Gracchi et al. 2017. The second method utilizes seismic polarization (polarization-bearing, P-B in the following), commonly used in earthquake localization, that deals with seismic source back-azimuth calculations by means of the analysis of the seismic polarization of the signals recorded by three-axis geophones (Flinn 1965; Samson and Olson 1980; Magotra et al. 1987; Jurkevics 1988). At present, Vilajosana et

al. (2008) extended the P-B technique to an artificially triggered rockfall by using two three-component seismic stations located at the foot of the Montserrat massif approximately 200 m from the rockfall explosion point. They calculated the seismic polarization of the trace of the first block that fell onto the terrace, and the propagation velocity estimated was in a good agreement with the measured P-wave velocity. There are also many other methods that result from T-B optimization, such as those discussed by Almendros et al. (1999) or by Myers et al. (2007). One approach uses the ZL-CC (zero-lag cross-correlation) technique with a circular sensor array for nearby seismic source localization, while another method formulates a Bayesian hierarchical statistical model to describe the seismic localization problem of multiple events; to determine the hypocenter of the multiple events, three distinct components of the model are estimated, including i) arrival-time measurements, ii) travel-time predictions, and iii) an a priori statistical model.

Each method has advantages and drawbacks. In T-B, the method is easily understood and widely applied, but the localization precision is heavily dependent on the accuracy of picking the first-arrival times, especially for near-field microseismic monitoring, such as geohazard monitoring. Moreover, the seismic wave attenuation and propagation velocities are influenced by topography, lithology, and geological formations that strongly influence high-accuracy picking of the first-arrival times (Kao et al. 2004). In fact, in the T-B method, because of the seismic propagation attenuation a) it is easy to obtain the first-arrival time from a powerful signal from a nearby station, but it is difficult to determine the correct first-arrival time from a distant station, and b) the first ground motion can be similar to seismic noise at the far station, and it is difficult to distinguish the two after a heavy attenuation, c) in near-field monitoring, given the small network scale and the small source-station distances, small differences in the first-arrival times result in a large errors if the ground has a high seismic wave velocity (i.e., an arrival time error of 0.1 s causes a 200 m location error if the wave velocity is 2,000 m/s); and d) the strict high accuracy requirement for arrival time picking would be a barrier to automatic processing. In P-B, as previously stated, the localization is carried by using the seismic signal polarization, so the accuracy requirement for picking arrival times is not as strict as it is for the T-B method. The main problem of the P-B method is determining the P-wave phases and the correct frequency bands for polarization and back-azimuth calculations from the recorded time series.

Starting with the P-B method drawbacks mentioned above (e.g., frequency band selection and multi-station joint localization), we decided to use these data to attempt to define marker parameters that would indicate the most appropriate frequency bands for calculations of seismic polarization and back azimuths. Moreover, to use the signals recorded by all geophones deployed in the network, an overdetermined matrix was proposed for joint localization based on signal record quality and energy. This methodology would be helpful for slope susceptible area mapping and risk early warning.

In rock slope hazard early warning, a reliable prediction is still a difficult task, due to the lack of noticeable forerunners preceding abrupt failures as well as to complex mechanisms not fully understood yet (Intrieri et al. 2019; Carlà et al., 2017). There are several ways to perform landslide monitoring and early warning.

One way is to monitor displacements (Iovine et al., 2006; Blikra, 2012; Kristensen et al., 2013; Lombardi et al., 2017; Intrieri et al., 2019), which are a direct indicator of slope instability. Although future developments in the exploitation of interferometric satellites might lead to a bloom of regional-scale early warning systems (Raspini et al., 2018), displacement is normally exploited at slope-scale. The reasons why displacement monitoring is not suitable for rockfalls is that rockfall usually lack long-term pre-failure deformations compatible with the acquisition frequency of even the most modern displacement monitoring systems; furthermore, the typically

small dimensions of detaching blocks are often beyond the spatial resolution capabilities of imaging instruments or even single points networks, which would require to be installed at every single block that is potentially unstable.

Another, more common, approach to perform landslide early warning is based on rainfall monitoring. Through defining a duration-intensity threshold of rainfall, and considering the susceptible map and catalogues of landslide, a spatiotemporal forecasting of landslides can be achieved. Rainfall is mostly used for regional-scale systems (Rosi et al. 2012; Segoni et al. 2015, 2018); furthermore, the relation between rockfall occurrence and rainfall is not very clear, since many other factors are involved, such as rock temperature, rock moisture, wind intensity and air temperature (Matsuoka 2019). For these reasons, rainfall is not optimal for a rockfall early warning system.

On the other hand, rockfalls generate ground vibrations during crack nucleation, crack propagation and eventually with the collapse and subsequent movement along the slope and to the ground. These can be recorded by a geophone network, and important information on the characteristics of the seismic source could be derived from a three-axis seismogram (e.g. the event type, energy, duration, location, back-azimuth and developing process) that not only occurred on the surface but also in the subsurface (Deparis et al., 2007; Vilajosana et al., 2008; Helmstetter and Garambois, 2010; Hibert et al., 2011 and Coviello et al., 2019). Therefore, an early warning system can be set up by monitoring the seismic signals emitted by surface and subsurface slope dynamics (Amitrano et al. 2005; Lacroix et al. 2011; Lenti et al. 2012; Walter et al. 2012b; Van Herwijnen et al. 2016; Schöpa et al. 2018). Seismic monitoring offers a unique measurement for rockfall study and provides a complementary solution to displacement-based early warning systems since they can give information also about sub-surficial processes. The micro-seismic monitoring can be applied:

- in a short time inversion analysis for an individual landslide: the seismograms and spectrograms are consistent with the dynamic processes (location, trajectory, volume, energy and mechanism evolution) of the landslide, i.e. different waveform peaks recorded in the seismogram correspond to the collapsed material impacting and rebounding on the ground; the onset time, duration and speed of a landslide can also be interpreted from the seismogram and the spectrogram (Hibert et al. 2017a; Yamada et al. 2013; Burtin et al. 2014; Fan et al. 2017; Hibert et al. 2017a; Li et al. 2019; Hu et al. 2018; Zhang et al. 2019);
- in a long-period unmanned slope dynamics monitoring: micro-seismic monitoring could help to develop an early warning by observing the parameters variation in both waveform and seismic events detected; in addition, by estimating the hypocenters of the seismic sources, it could help to identify the most dangerous zones in the monitored area and analyze the correlation with tectonics, climate, etc., to design effective mitigation measures accordingly (Satriano et al. 2011; Kao et al. 2012; Coviello et al. 2015; Manconi et al. 2018; Hibert et al. 2017b; Hibert et al. 2017c; Arosio et al. 2018; Ma et al. 2019).

Based on the observation that the number of rockfalls increases before a larger rockslide (Suwa 1991; Suwa et al. 1991; Amitrano et al. 2005; Huggel et al. 2005; Rosser et al. 2007; Szwedzicki 2003; Hibert et al. 2017a) and the fundamental law for failure material proposed by Voight (1988) after Fukuzono (1985), here we propose a framework for a rockfall spatiotemporal early warning using micro-seismic monitoring. This framework is complemented with two algorithms for rockfall detection and classification and for seismic event localization as discussed above. However, the algorithms used here can also be replaced in the proposed methodology with any suitable alternative.

According to the four targets, there are seven chapters performed in this thesis.

In Section 1, state of the art on seismic monitoring in geohazard is studied, and scheduled four interest study points in seismic monitoring applied in rockfall; In the Section 2, we introduced the geology setting of study area and monitoring instruments deployed in Torgiovannetto Quarry, and also made detail geological surveys in Torgiovannetto Quarry and a potential landslide developed in that slope.

In Section 3, we introduced the basic theory of frequency transform and compared the difference of signal amplitude between pre-transformed and transformed in MATLAB; and compared the seismic detection methods: STA/LTA method and cross-correlation method, to find the fittest one that could apply in this case; we also compared two localization methods: time-bearing and polarization-bearing, and made an improvement in the method of polarization analysis.

Section 4 deals with the basic part of this study that focus on seismic features analysis of rockfall, such as frequency, energy, seismic waveform and duration. Although many researchers use frequency as the main parameter for seismic events classification, the frequency content and other seismic features of rockfall (like duration or amplitude) are still not completely understood (Boore et al. 2014; Colombero et al. 2018). Understanding the rockfall features is of great importance and that's a fundamental step for the subsequent rockfall seismic detection and the physic-mechanical characterization in seismic monitoring. Therefore, this Section analyzed six typical artificial released rockfall cases that selected from the whole dataset, and presented statistics on the signals recorded by four seismometers in a quarry site during an artificial rockfall test, and the correlation of rockfall seismic feature with geomorphological and geological setting (Gracchi et al. 2017; Feng et al. 2019; Lotti et al. 2015, 2018).

In Section 5, an ad hoc classification model, DESTRO (DEtection and STorage of ROckfall), is proposed for rockfall and earthquake detection and classification, that takes full use of the monitoring array and specially designed a three-step classifier that consists of three classifiers. The algorithm of DESTRO could be segmented in three phases: 1) define seismic features; 2) then manually sets weight from a training set; 3) finally input the features in a three-step classifier. The presented application of DESTRO is based on a small-scale station network that monitored an unstable rock slope in a former limestone quarry at Torgiovannetto (near Assisi town, Central Italy) for seven months (Gracchi et al. 2017; Lotti et al. 2015, 2018). To calibrate the system, 95 rock blocks were manually released from the benches of the former cave to simulate the occurrence of rockfalls, of which 90 were used for validation (Gracchi et al. 2017; Feng et al. 2019). The occurrence of earthquakes was cross-checked on the Italian National Institute of Geophysics and Volcanology (INGV) earthquake database (<http://cnt.rm.ingv.it/>). At the end of this section, the performance of seismic event detection and classification are discussed.

In Section 6, a methodology of slope risk early warning is introduced, and applied in Torgiovannetto quarry. Finally, the susceptible areas in monitoring slope of Torgiovannetto quarry are mapped, and validated with LiDAR scanning image, according to the localization.

In the final section, Section 7, we made a conclusion about this thesis and explored the possible research points in the future.

2. Study area and instrumentations

2.1 Geographical, Geomorphological and Geological Setting

The study area, Torgiovanetto Quarry, is a former quarry located in the northward facing slope of Mount Subasio, 2 km NE from the city of Assisi (Perugia, Umbria Region, Central Italy, Figure 1). The landscape of investigated area is hilly or mountainous that covers 8456 km² in Central Italy, with open valleys and intra-mountain basins, and the elevation range from 50 m to 2436 m a.s.l., the drainage in the area is led by the Tiber River, a tributary of the Tyrrhenian Sea. The rain season mainly occurs from October to February, with cumulative values ranging from 700 mm to 2000 mm.

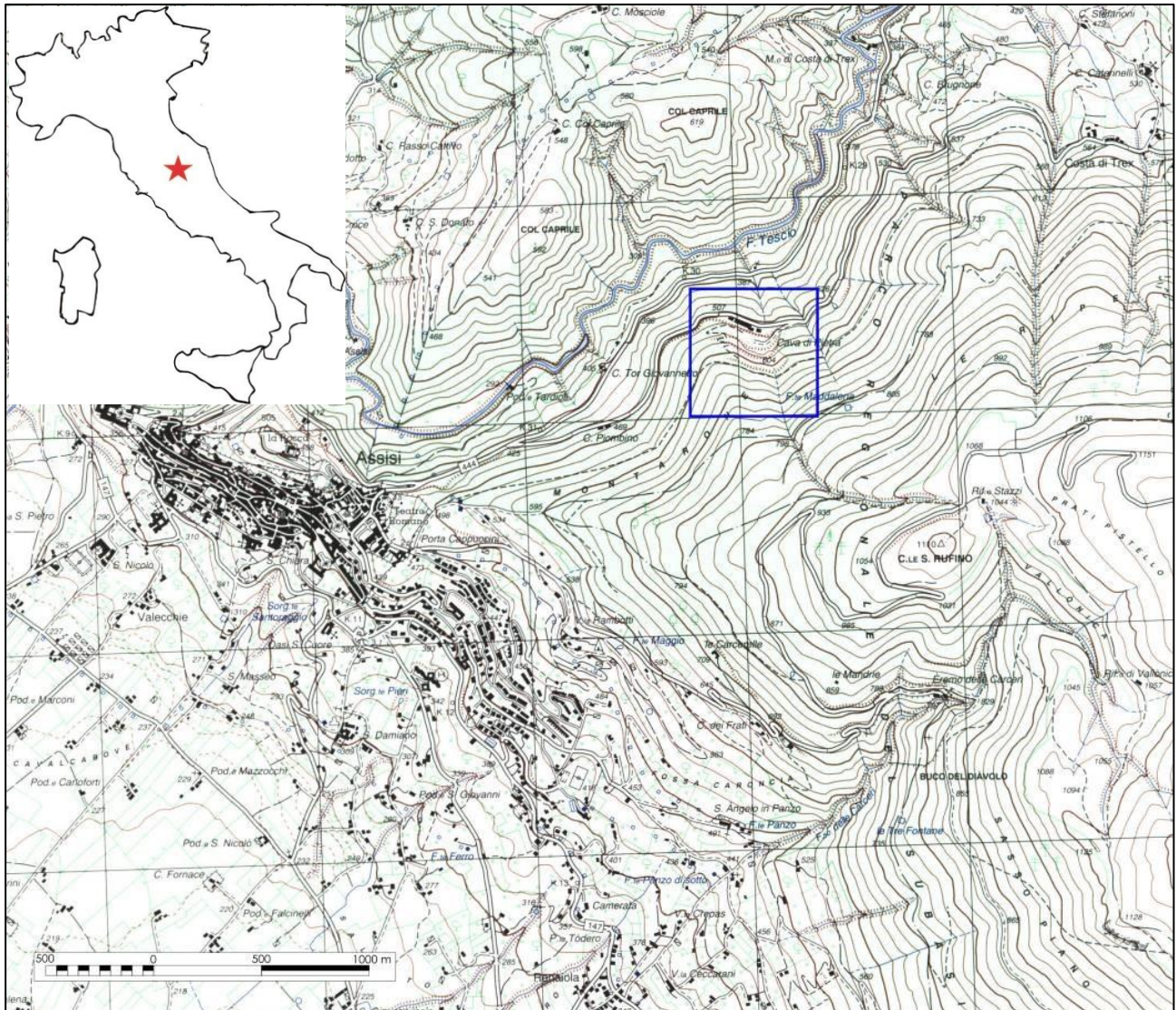


Figure 1. The outline of study area, about 2km northeast of Assisi (Balducci 2011).

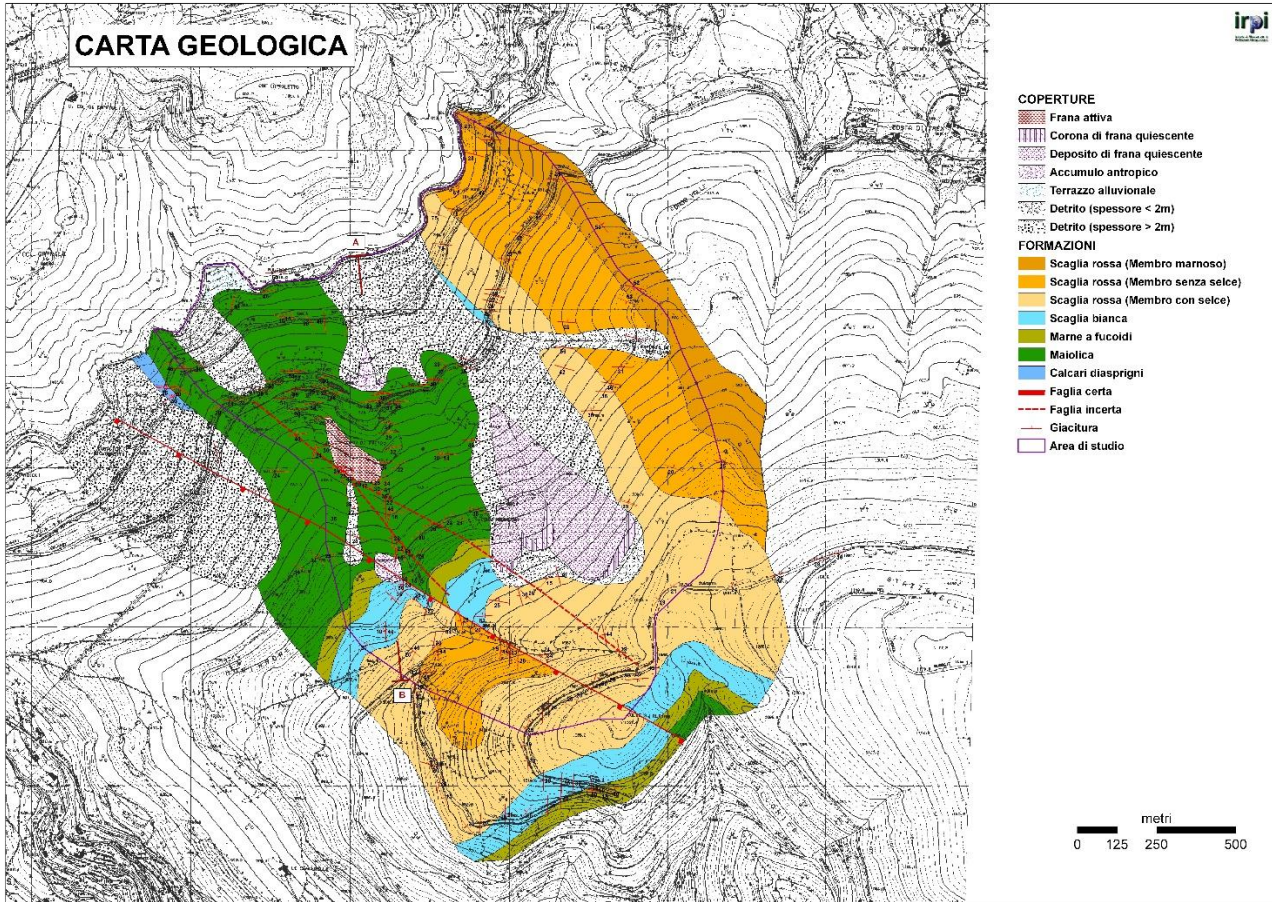


Figure 2. The geological setting in study area (from IRPI, 2006).

Mount Subasio (1109 m a.s.l.) is a part of the Umbria-Marche Apennines, a complex fold and thrust arcuate belt which occupies the outer zones of the Northern Apennines of Italy. The belt developed during the Neogene as a result of the closure of the Ligurian Ocean followed by the continental collision between the European Corsica-Sardinia Margin and the African Adria Promontory (Boccaletti et al. 1971): a northeast-directed compressional tectonic phase started during the middle Miocene and is still active near the Adriatic coast (Barchi et al. 1998). During the upper Pliocene started an extensional phase with a principal stress oriented about NE-SW which resulted in the dissection of the Umbria-Marche Apennines and the opening of a NW-SE-trending set of continental basins (Figure 2 and Figure 3).

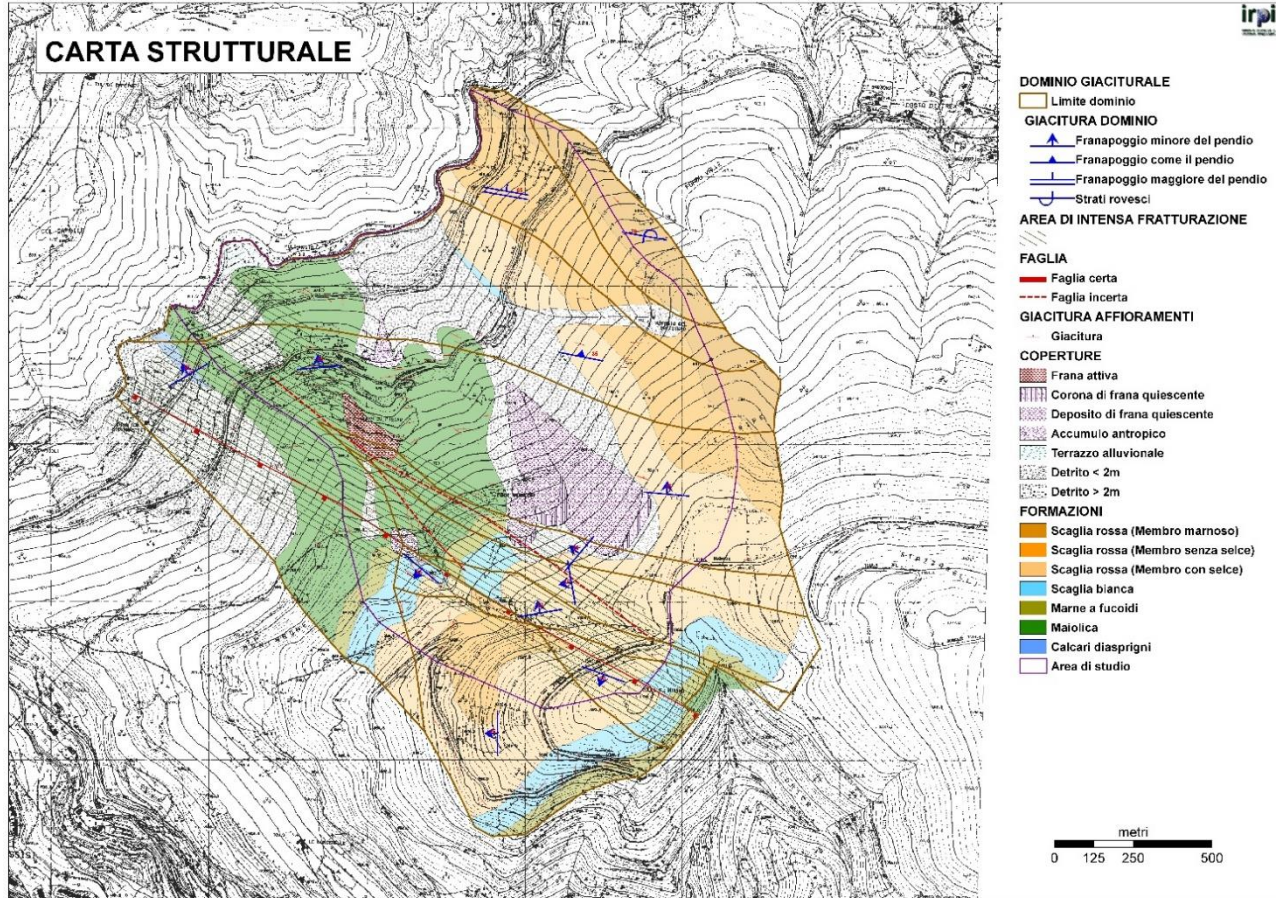


Figure 3. Structure distribution in study area (from IRPI, 2006).

Mount Subasio area consists in an SSE-NNW trending anticline (Intrieri et al. 2012) with layers dipping almost vertically in the NE side of the mountain with several NW-SE striking normal faults on the eastern and western flanks. The local geological formations, belonging to Serie Umbro-Marchigiana (from Calcare Massiccio to Marnoso Arenacea), represent the progressive sinking of a marine environment (Figure 4).

The test site is located in a micritic limestone former quarry (dismissed in the late '90s), 2 km NE from Assisi

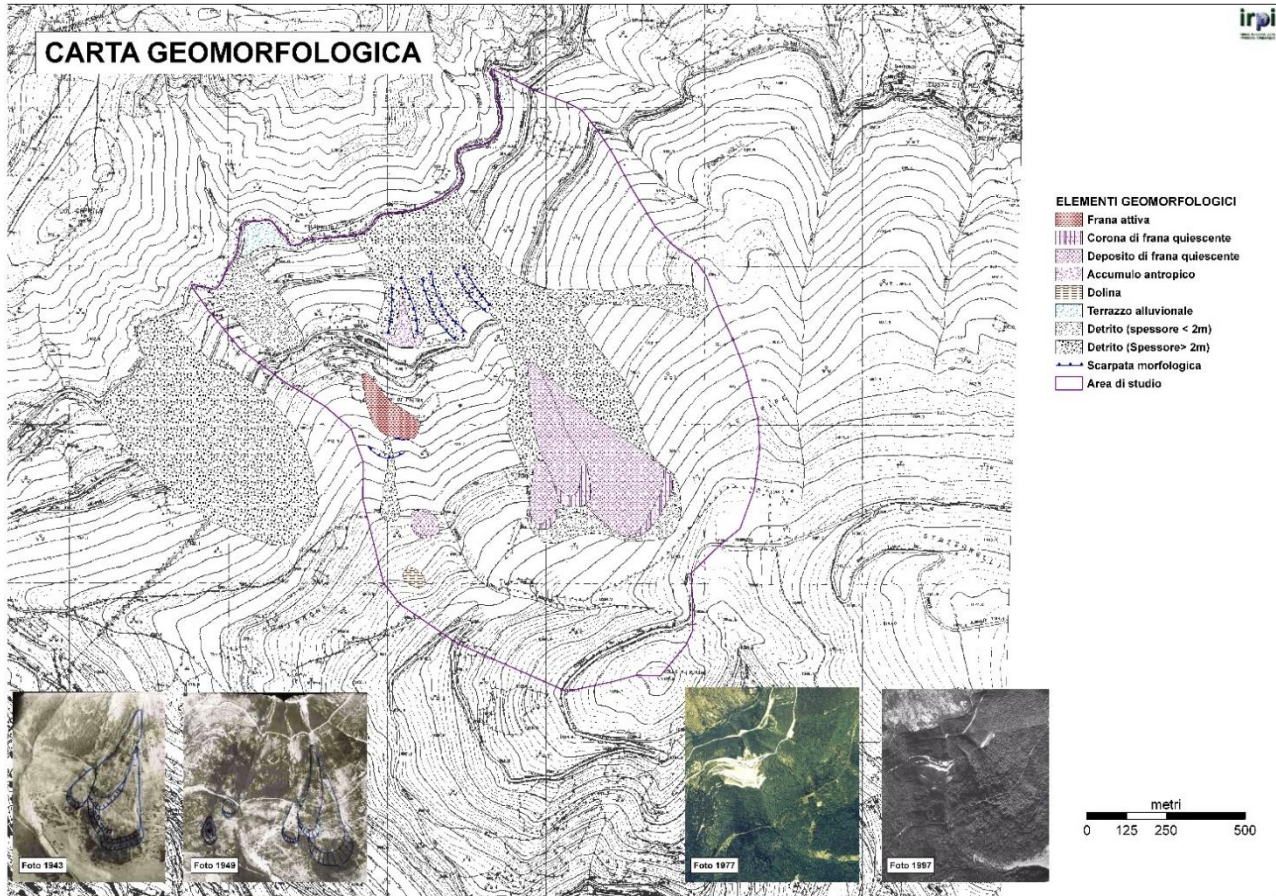


Figure 4. Geomorphology in study area (from IRPI, 2006).

2.2 Rockslide characteristics and seismic monitoring

2.2.1 The characteristics of monitoring rockslide

There is a potential landslide (classified as a rockslide), covering a 200 x 100 m area between elevations of 550 and 680 m, with a volume of 182,000 m³ developed in the top part of Torgiovanetto Quarry (Lotti et al. 2014; Antolini et al. 2016; Gracchi et al. 2017; Lotti et al. 2018), and where seismic monitoring was deployed. The upper boundary is defined by a big open fracture; this sub-vertical back fracture is a tension crack with an EW strike, which in some places displays a width up to 2 m and depth of about 20 meters (Balducci et al., 2011). The fault can be seen in Figure 5. The area located in a seismically active part of the Apennine chain (seismic zone 2; OPCM n.3274/2003 updated BUR n.47 3/10/2012) which in past generated earthquakes of magnitude up to 6.3 Mw. It was first observed on May 2003 and it is assured that the main predisposing factor of the instability was the quarrying activity that heavily altered the original front, actually structured in four main terraces with an overall height of about 140 m, but also the process of earthquakes-induced landslides cannot be neglected (Intrieri et al. 2012). In fact, the interconnection between those events is well-documented especially in the cases of high-magnitude seismic event (Wilson and Keefer 1983; Jibson and Keefer 1992, 1993; Khazai and Sitar 2004). Given this it clearly appears that another triggering factor has to be sought in the seismic sequence that affected the area southeast of the quarry (Colfiorito basin) in the 1997-98, that reached macro-seismic intensity (MCS) Io of 8-9 (Locati et al. 2011) in the Assisi area.

Now the extracting activities are stopped, and the potential collapse is dealt with some mitigation measurements (Gigli et al. 2014b). The quarry area covers 67,800 m² and is almost completely free of vegetation.

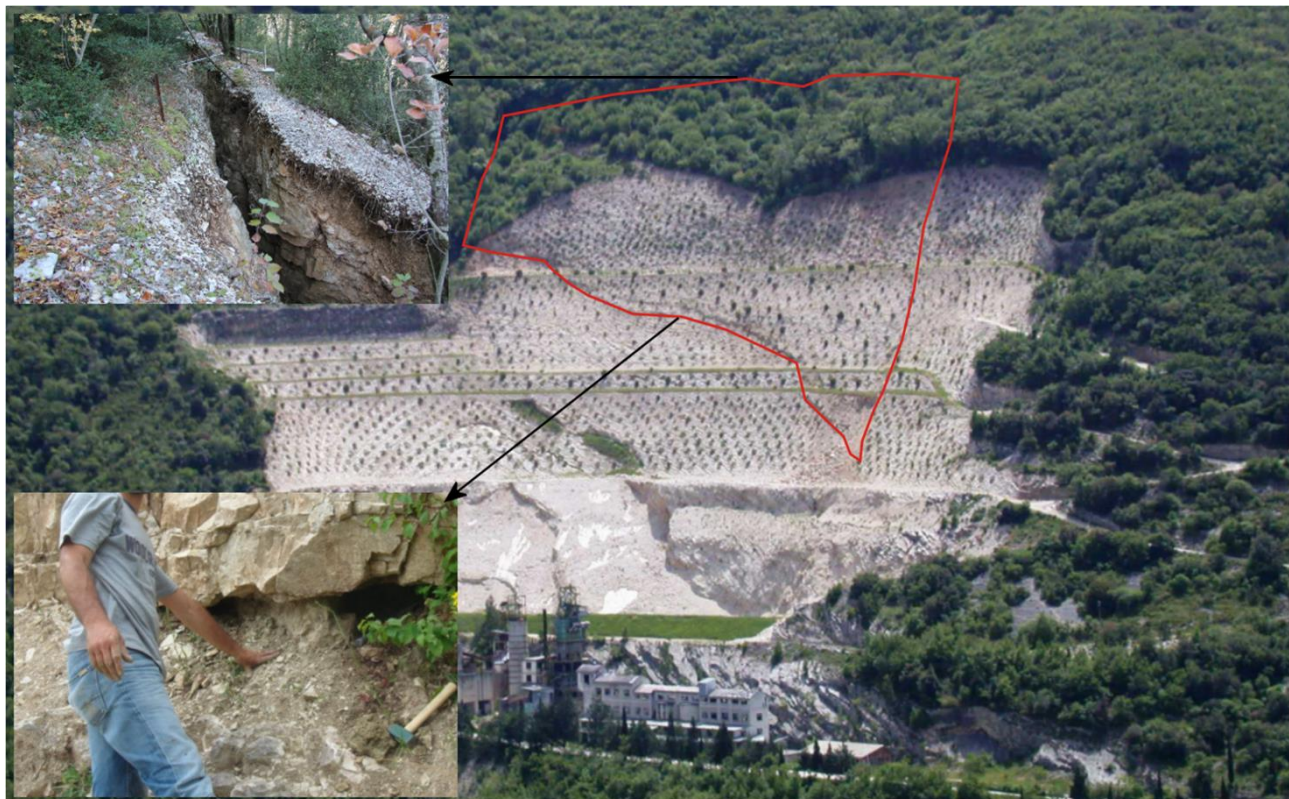


Figure 5. The outline of study slope and the upper boundary as a big open fracture.

The slope consists mainly of micritic limestone belonging to the Maiolica Formation (Upper Jurassic-Lower Cretaceous) that widely outcrops in the area (Figure 6 and Figure 7). The thickness of the Formation is about 100 m and is composed by white or light grey well stratified micritic limestone layers, whose thickness ranges between 10 cm and 1 m, and, sporadically, thin clay interlayers may occur.

The geometry and other soil parameters (such as densities, body waves velocities etc.) are well known thanks to the geotechnical and geophysical investigations carried on the site by Alta Scuola di Perugia (2005a; 2005b; 2006a; 2006b) and Università degli Studi di Firenze (Casagli et al. 2006a, 2006b, 2007a, 2007b; Intrieri et al. 2012) since the first activity was detected.

From the geomorphology of this rockslide, in general, the dip direction and the dip of bedrock bedding planes may vary from 350° to 5° and from 25° to 35° respectively, e.g. the rock base layers have the same dip direction as the slope surface but with a gentler dip angle, and that's the reason of a potential landslide developing. The rockslide outcrop is shown in Figure 6.

The site is also partially covered by very heterometric debris (from pebble- to cobble-sized angular clasts, with scattered boulders, in a silty or coarse-grained sandy matrix), some of which are anthropic in nature. The covered debris is shown in Figure 7, and more detail rockslide characteristics and geomorphology of artificial released test site is shown in Section 4.1.



Figure 6. The rockslide characteristics. Picture a is the eastern part of the slope, and picture b is western part of the slope.



Figure 7. The distribution of cover debris in study slope.

The downhill boundary, associated to a major clay interbed, is represented by a stratigraphic layer (355°/24°) that acts as sliding surface and cuts obliquely the quarry front which is associated to a major clay interbed. The eastern side of the landslide is un-continuously delimited by persistent fractures belonging to a sub-vertical set having an N-S strike. The poles of discontinuities are represented in stereographic projection and 3D representation of the sliding block in Figure 10: the main delimiting planes that more affect the kinematic of the rock block (basal (1) and western (2) plan) belong respectively to the BG (stratification) and JN1 families.

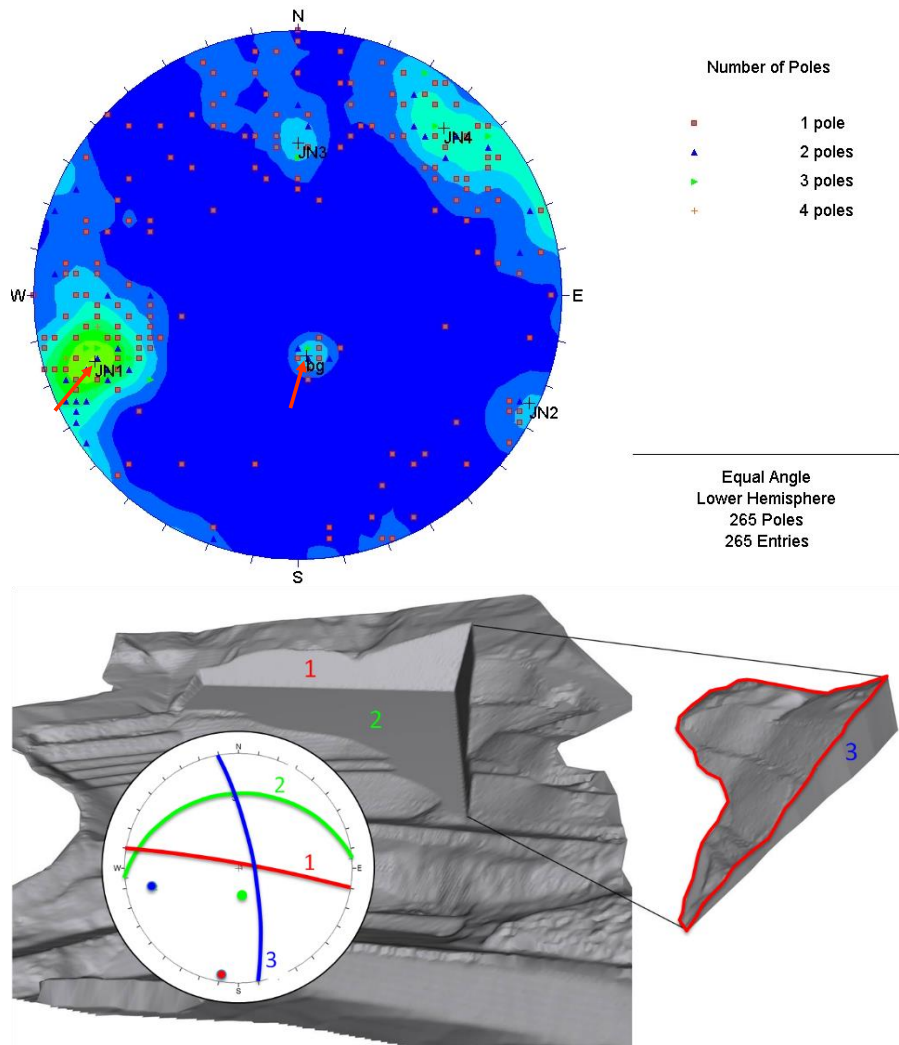


Figure 8. Stereographic projection of the poles of discontinuous grouped into families (bg, JN1, JN2, JN3 and JN4) and 3D representation of the sliding block. Red arrows in picture a show the basal and western plan belonging family.

2.2.2 Instruments and deployment of seismic monitoring

Starting with the first observation of some tension cracks in the vegetated area above and within the quarry front by the State Forestry Corps, several monitoring campaigns were carried out by means of different instrumentations (topographic total station, inclinometers, extensometers, ground-based interferometric radar, laser scanner and infrared thermal camera). The monitoring system distribution and some instruments are shown in Figure 9 and Figure 10.

The site for seismic monitoring was chosen based on the consideration that background noise level is relatively low so that even events characterized by low maximum amplitude can be easily detected. Among these investigations a passive seismic network, in continuous recording, was installed on this rockslide from December 2012 to July 2013 to support the “traditional” monitoring network composed by 13 wire extensometers, 1 accelerometer, 1 meteorological station (composed of 1 thermometer and 1 rain gauge), 3 cameras and 3 inclinometers. The monitoring network, progressively enhanced and improved through the years, was completed by means of hydrological (Ponziani et al. 2010), modeling computation analysis (Casagli et al. 2006a.; Balducci et al. 2011) and in the end by our seismological stations.

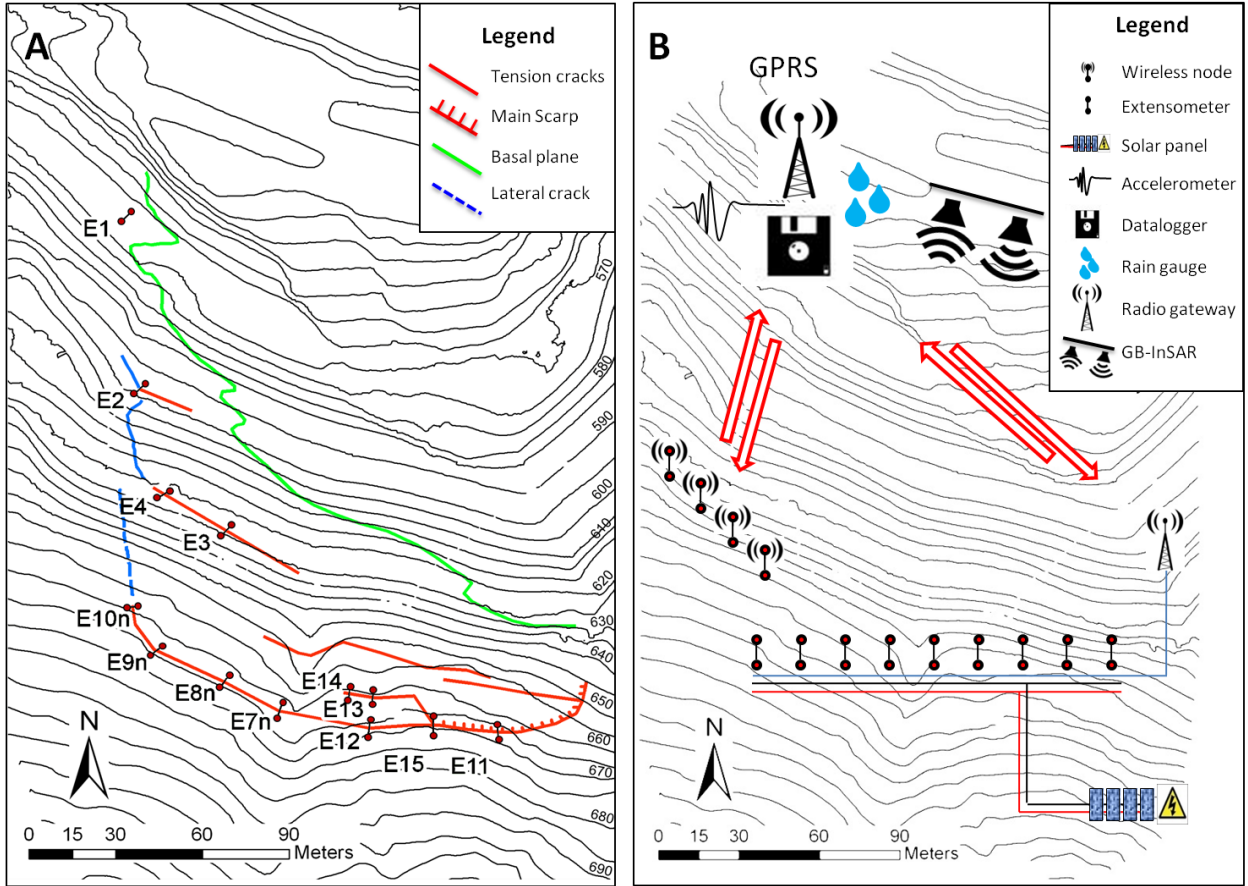


Figure 9. Torgiovannetto rockslide monitoring system.



Figure 10. Some examples of instruments employed in Torgiovannetto. Picture a is seismic station (velocimeter sensor) employed in seismic monitoring; picture b is extensometer; picture c is Ground Based Interferometric Synthetic Aperture Radar (GB-InSAR); and picture d is Light Detection and Ranging (LiDAR)

Seismic measurements were performed using a small-scale network composed of four seismic stations whose locations are shown in Figure 11 and Figure 12: station TOR4 was located over the sliding mass while the other three stations (TOR1, TOR2 and TOR3) were located at the edge of the quarry arranged in pairs with diametrically opposite position with respect to the barycenter of the landslide, and there is a small collapse developed near TOR2 that highlight with red dash line in Figure 11 and Figure 12. Installation at the site was not an easy challenge. Some aspects have to be considered to obtain reliable data: locations of the seismometer, access to the site, type of seismometer and electric power source. This configuration allows us to retrieve punctual information both inside and outside the landslide; furthermore, working on pairs of sensors, one can retrieve information on the state of the propagation medium in between the two sensors.

Each station is equipped with a SARA 24bit A/D converters (SL06) coupled with a S45 triaxial velocimeter sensor with a natural frequency of 4.5 Hz and transduction factor of 78 V/m/s. Every sensor was placed on a concrete base with supporting plinth, isolated from the exterior in order to attain protection from severe weather. Battery supply and digitizer, connected to the sensors through a connector cable, were housed in a separate case. A covering sheet coated all the equipment (Figure 10)

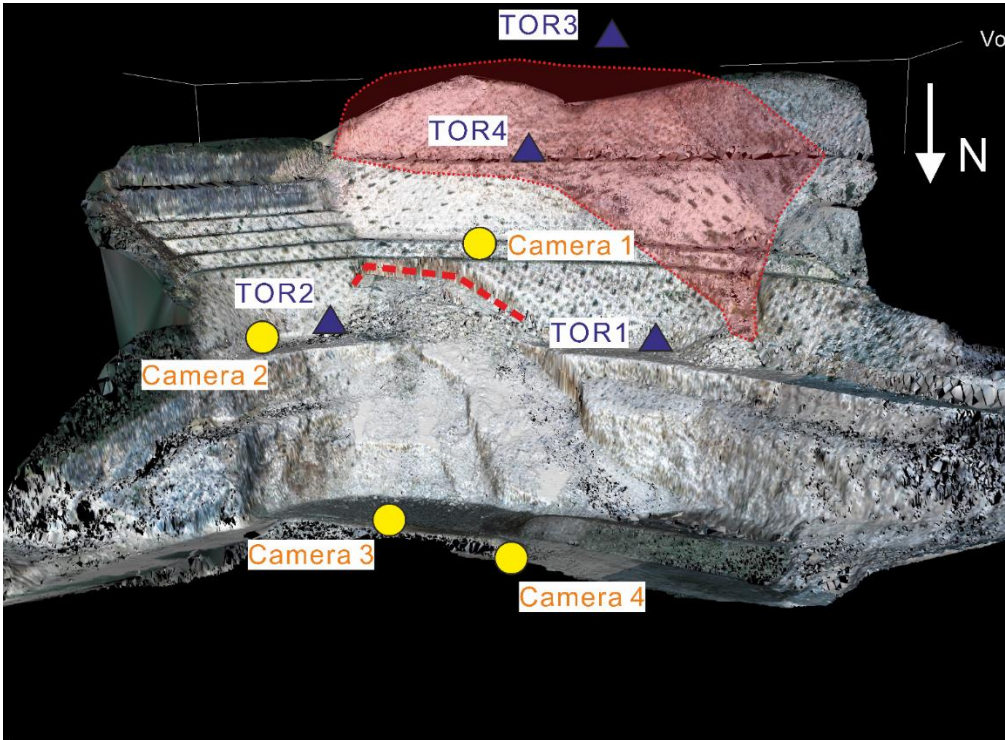


Figure 11. The DEM of rockslide with resolution of 0.25 m and the distribution of seismic stations (TOR1, TOR2, TOR3 and TOR4) and video cameras (Camera 1, Camera 2, Camera 3 and Camera 4). In picture, the red transparent covered area is the potential rockslide, and the red dash line is a small collapse.

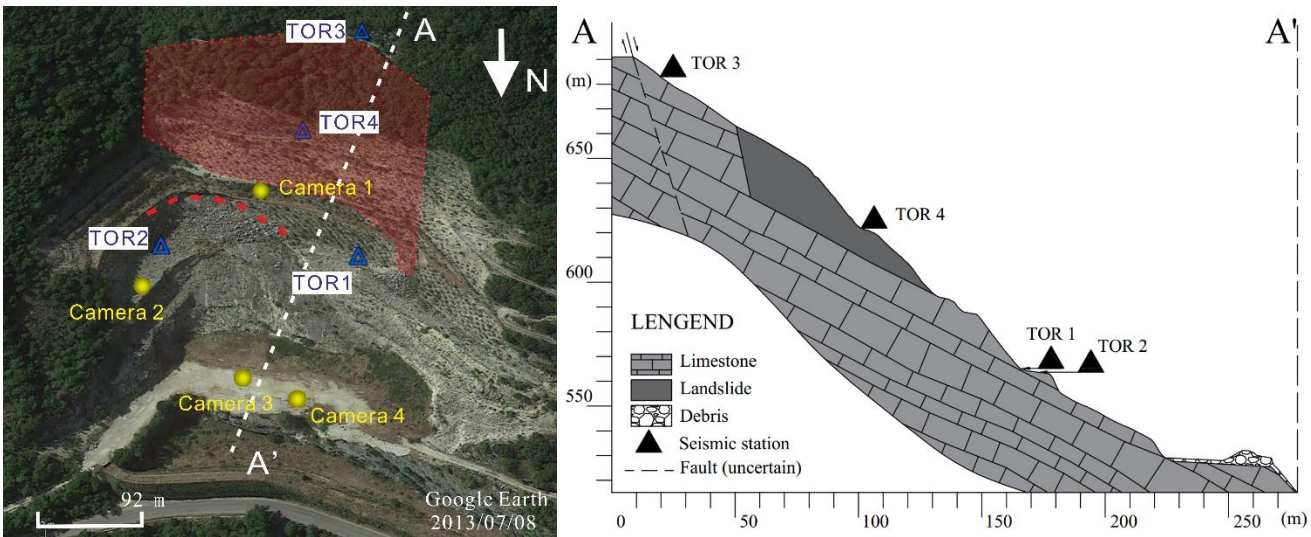


Figure 12. The distribution of seismic monitoring in latitude.

Instruments response is flat down to 2 Hz, with an upper-corner frequency of 100 Hz. All of them used Global Positioning System (GPS) receivers for time synchronization; data were recorded in continuous mode at 200 Hz sampling frequency, as the best compromise between signal resolution and data storage. The Nyquist sampling theorem says we should sample with a frequency that is more than twice the highest frequency of interest so the choice of this sampling rate derived from the compromise between maintain limited the amount of data acquiring in continuous mode and obtain information concerning high frequencies (characteristic of microcrack) at least up to 100 Hz.

The electric power supply for the sensors came from a set of four 12V-60A batteries for each station that needed to be substituted every 40 days to recharge them and download the data stored in the digitizer. Unfortunately, given the orientation towards NW of the slope, it was not possible to use solar panels to recharge batteries; moreover, the panels were likely to be destroyed due to falling blocks. Data acquisition was continuous for 210 days from 07 December 2012 to 03 July 2013 except for some short intervals due to the batteries change. Table 1 and Table 2 show a summary statement of each station.

Table 1. Technical characteristics and location of seismic stations.

Station Code	Digitizer	sensor	Power supply	Lat (°N)	Lon (°E)	Sampling frequency (Hz)
TOR1	SL06 24 bit	SS45 4.5 Hz	4 batteries 12V-60A	43.077305	12.641280	200
TOR2	SL06 24 bit	SS45 4.5 Hz	4 batteries 12V-60A	43.076983	12.642637	200
TOR3	SL06 24 bit	SS45 4.5 Hz	4 batteries 12V-60A	43.075848	12.641042	200
TOR4	SL06 24 bit	SS45 4.5 Hz	4 batteries 12V-60A	43.076567	12.641422	200

Table 2. Working period and data quality of the four seismic stations

Station code	Start recording	Stop recording	Interruption (missing data)	Data quality
TOR1	06.12.2012 18:00:01	04.07.2013 18:00:00	20.12.2012 12:00:01-21.12.2012 00:00:00 15.01.2013 00:00:01- 15.01.2013 06:00:00 01.04.2013 00:00:01- 04.04.2013 00:00:00 04.06.2013 00:00:01- 06.06.2013 12:00:00	97%
TOR2	06.12.2012 18:00:01	04.07.2013 18:00:00	20.12.2012 12:00:01-21.12.2012 12:00:00 15.01.2013 00:00:01- 15.01.2013 06:00:00 01.04.2013 00:00:01- 04.04.2013 00:00:00	98%
TOR3	06.12.2012 18:00:01	04.07.2013 18:00:00	20.12.2012 18:00:01-21.12.2012 00:00:00 15.01.2013 00:00:01- 15.01.2013 06:00:00 01.04.2013 00:00:01- 04.04.2013 00:00:00 03.06.2013 00:00:01- 04.06.2013 00:00:00	98%
TOR4	06.12.2012 18:00:01	04.07.2013 18:00:00	20.12.2012 18:00:01-21.12.2012 00:00:00 01.04.2013 00:00:01- 04.04.2013 00:00:00 01.06.2013 00:00:01- 06.06.2013 18:00:00	96%

Data format of the seismic records retrieved from SL06 is miniSEED (‘Data-only’ volume); nevertheless, this format was mainly designed for the exchange of geophysical data and not for analysis so they had to be converted into SAC (Seismological Analysis Code; Goldstein et al. 2003; Goldstein and Snoke 2005) format, more suitable for elaborations. The conversion was performed in Matlab with mseed2sac code and the codes wrote by Peng (2018). Data set, for each station, is split in 6-hr sections files (4 files/day) with tstart = t0 =00:00:01; 06:00:01; 12:00:01; 18:00:01 to synchronize the file start at all the stations. The size of each file is equal to 16.876 Kb. For each station, three separate files are generated, which correspond to the north-south (SHN), east-west (SHE) and vertical or up-down (SHZ) components of ground velocity. The amplitude (y-axis) is expressed in counts, x-axis express time. Traces are displayed by using any software package for interactive visualization of earthquake seismograms such as SeisGram2K Seismogram Viewer (Lomax and Michelini 2009, <http://www.alomax.net/software>) or Geopsy (Geophysical Signal Database for Noise Array Processing; <http://www.geopsy.org>). For further information about SAC format consult the IRIS website (https://ds.iris.edu/files/sac-manual/manual/file_format.html)

One period of recorded signal that occurred at time 12:00 to 18:00, 11st, December 2012, is shown in Figure 13a, that from three components of seismic station TOR1, and in that period, four seismic events are amplified in Figure 13b.

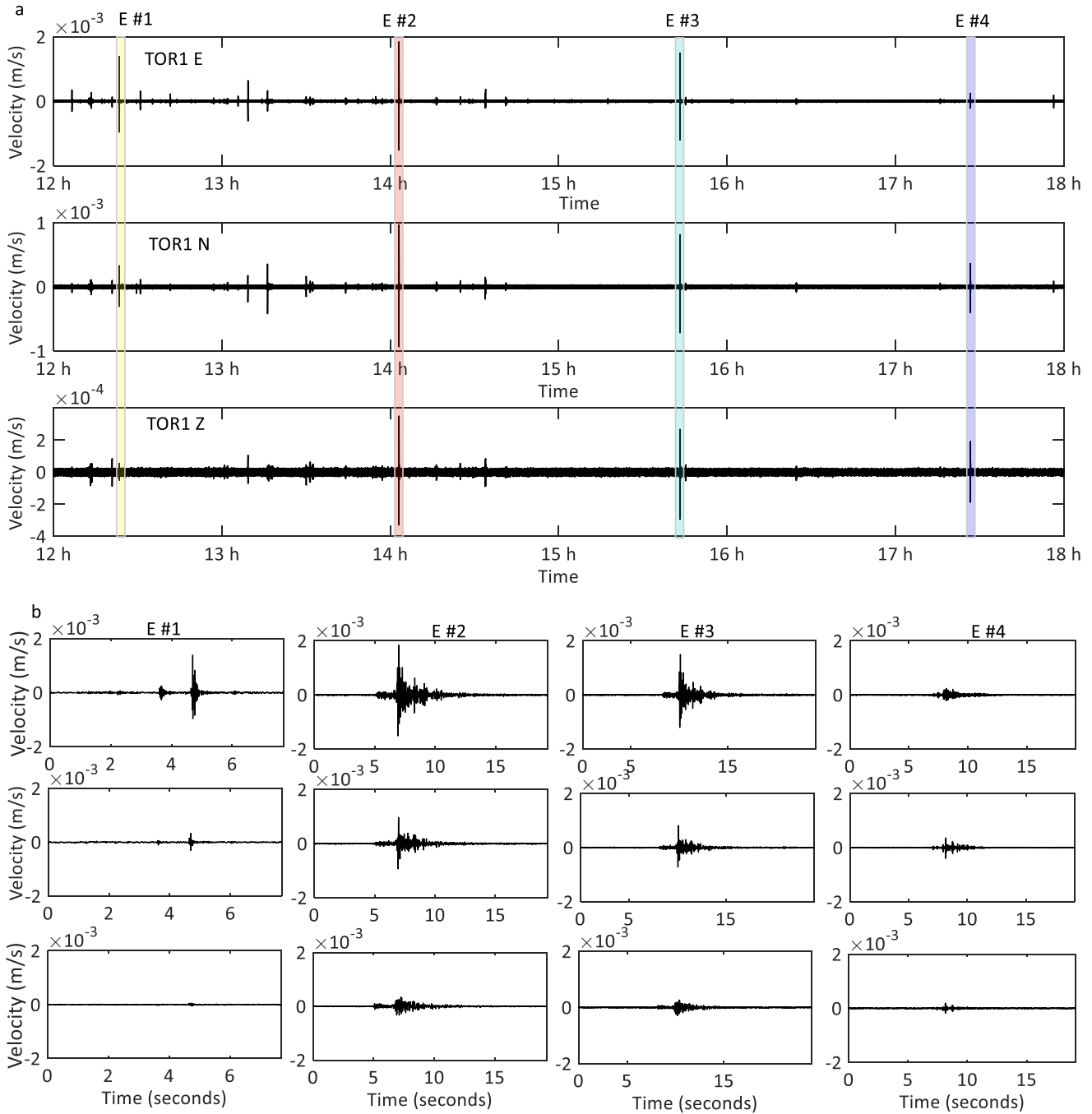


Figure 13. Example of recording data and four seismic events amplified.

3. Methodology

3.1 Fast Fourier transform (FFT) in MATLAB

Standard Fourier Transform and Wavelet Transform are two well-known functions employed in signal analysis to move from time domain to frequency domain. These two transforms give a representation of the frequency content of a signal with only few differences (see Daubechies 1992 for a complete dissertation on this subject). In the following we shortly introduce the FFT coefficients (FFTA in the text), since they are strictly related with the original signal amplitude. For a more detailed discussion on FFT, please refer to the widely literature.

In frequency analysis, we wrote a small script to convert signals from time domain to frequency domain based on the discrete fast Fourier transform (FFT) function (Equation 2) in MATLAB R2017b. Supposed a seismic signal trace \mathbf{X} :

$$\mathbf{X} = [x_1, x_2, \dots, x_i, \dots, x_L], \quad (1)$$

And FFT coefficients \mathbf{Y} :

$$\mathbf{Y} = \text{fft}(\mathbf{X}, L), \quad (2)$$

Where L is the length of input signal, and \mathbf{Y} in complex number. In terms of the FFT theory, the absolute values of \mathbf{Y} equal to $\frac{L}{2}$ multiple the absolute values of \mathbf{X} (except for the first sample in input signal), while for the first sample of \mathbf{Y} , the absolute value equal to L multiple the absolute value of the first sample value of \mathbf{X} . Therefore, in order to obtain the real amplitude value of the signal \mathbf{X} in frequency domain, we need to convert them into absolute number by absolute value function (*abs*) in MATLAB and only select half coefficients of \mathbf{Y} since the symmetry of FFT:

$$\text{FFTA}(i) = \begin{cases} \frac{\text{abs}(\mathbf{Y}(i))}{L}, i = 1 \\ \frac{2 \times \text{abs}(\mathbf{Y}(i))}{L}, i = 2, 3, \dots, \frac{L}{2} \\ \frac{\text{abs}(\mathbf{Y}(i))}{L}, i = \frac{L}{2} + 1 \end{cases} \quad (3)$$

In this moment, the locations of \mathbf{Y} are still distributed in time domain, therefore, transformed them into frequency domain by Equation (4).

$$f(i) = \frac{F_s \times i}{L}, i = 1, 2, \dots, L, \quad (4)$$

Where $f(i)$ is the frequency of each sample in trace \mathbf{Y} . The sampling frequency (F_s) of the seismic instrument used in Torgiovannetto is 200 Hz, and the sampling in 0.005 seconds. The resolution of frequency equal to $\frac{F_s}{L}$, and it's depended on the number of samples (length) of input signal.

In order to evaluate the FFT values coefficients (FFTA) performance after analyzed in MATLAB and to try to estimate the relationship between the real amplitude of original signal (ground velocity) and FFTA, we constructed three synthesized signals ($\mathbf{S}_1, \mathbf{S}_2, \mathbf{S}_3$) starting from four basic signals ($\mathbf{B}_1, \mathbf{B}_2, \mathbf{B}_3, \mathbf{B}_4$) that consist of different amplitudes and frequencies defined as follows:

$$\text{Basic signals: } \begin{cases} \mathbf{B}_1 = 5 \cdot \sin(20 \cdot \pi \cdot i) \\ \mathbf{B}_2 = 1 \cdot \sin(20 \cdot \pi \cdot i) \\ \mathbf{B}_3 = 4 \cdot \sin(80 \cdot \pi \cdot i) \\ \mathbf{B}_4 = 4 \cdot \sin(10 \cdot \pi \cdot i) \end{cases} \quad (5)$$

Where the basic signals \mathbf{B}_1 and \mathbf{B}_2 have the same frequency (10 Hz), and \mathbf{B}_3 and \mathbf{B}_4 have the same amplitude (4 m/s). The synthesized signals were defined as follows:

Synthesized signals:

$$\begin{cases} \mathbf{S}_1 = 5 \cdot \sin(20 \cdot \pi \cdot i) + 4 \cdot \sin(10 \cdot \pi \cdot i), i = 0.005 \text{ s}, 0.01 \text{ s}, \dots, 2 \text{ s}; \\ \mathbf{S}_2 = 1 \cdot \sin(20 \cdot \pi \cdot i) + 4 \cdot \sin(80 \cdot \pi \cdot i), i = 0.005 \text{ s}, 0.01 \text{ s}, \dots, 1 \text{ s}; \\ \mathbf{S}_3 = \begin{cases} 5 \cdot \sin(20 \cdot \pi \cdot i) + 4 \cdot \sin(10 \cdot \pi \cdot i), i < 2 \text{ s}, i = 0.005 \text{ s}, 0.01 \text{ s}, \dots, 2 \text{ s}; \\ 1 \cdot \sin(20 \cdot \pi \cdot i) + 4 \cdot \sin(80 \cdot \pi \cdot i), 2 \text{ s} < i < 3 \text{ s}, i = 2.005 \text{ s}, 2.01 \text{ s}, \dots, 3 \text{ s}; \end{cases} \end{cases} \quad (6)$$

where signal \mathbf{S}_1 is composed by \mathbf{S}_1 and \mathbf{S}_2 . These signals have been constructed in five conditions (Figure 14) to a) simulate the situations that corresponded to natural signals and b) to compare the difference of amplitude between original and transformed signals.

The five conditions are defined as follows: i) condition 1 and ii) condition 2 are synthesized signals \mathbf{S}_1 and \mathbf{S}_2 , respectively, in their real length; iii) conditions 3 and iv) condition 4 are synthesized signals \mathbf{S}_1 and \mathbf{S}_2 , respectively, in a unified length (i.e., 3 s) with the residual parts of signals corresponding to zero (i.e., the amplitude of the last 1 second of condition 3 is zero, and the amplitude of the first 2 seconds of condition 4 is zero, more visible please refer to Figure 14); v) condition 5 is the synthesized signal \mathbf{S}_3 in its real length (i.e., 3 seconds).

Figure 14 shows the shape of three synthesized signals in the five conditions.

From the FFT analysis results of comparison tests, condition 1 vs condition 3 and condition 2 vs condition 4, we found the FFTA value is equal to the ratio of input signal real length over unified length (l/L) times the real amplitude in each frequency value. All the FFT analysis results of amplitude comparison are shown in Figure 15 and Table 3.

Moreover, for the FFTA analysis in condition 5, the values of FFTA of \mathbf{S}_3 are calculated as below:

$$\text{FFTA}(f = 5 \text{ Hz}) = \frac{l(\mathbf{B}_4) \times A(\mathbf{B}_4)}{L} \quad (7)$$

$$\text{FFTA}(f = 10 \text{ Hz}) = \frac{l(\mathbf{B}_1) \times A(\mathbf{B}_1) + l(\mathbf{B}_2) \times A(\mathbf{B}_2)}{L} \quad (8)$$

$$\text{FFTA}(f = 40 \text{ Hz}) = \frac{l(\mathbf{B}_3) \times A(\mathbf{B}_3)}{L} \quad (9)$$

Finally, a universal equation between the original amplitude of basic signal and FFTA is shown in Equation 10. However, the spectral estimation could also be affected by the bias and variability in the periodogram, and that can be reduced with utilizing window and window with averaging.

$$\text{FFTA}(f(i)) = \sum_{k=1}^N \frac{l(\mathbf{B}_k) \times A(\mathbf{B}_k)}{L} \quad (10)$$

Where $\text{FFTA}(f(i))$ is the value of FFT coefficients after the FFT analysis in the frequency content $f(i)$; \mathbf{B}_k ($k = 1, 2, \dots, N$) is all the basic signals, whose frequency content is $f(i)$; $l(\mathbf{B}_k)$ is the real length of basic signal; $A(\mathbf{B}_k)$ is the real amplitude of basic signal; L is the length of input signal.

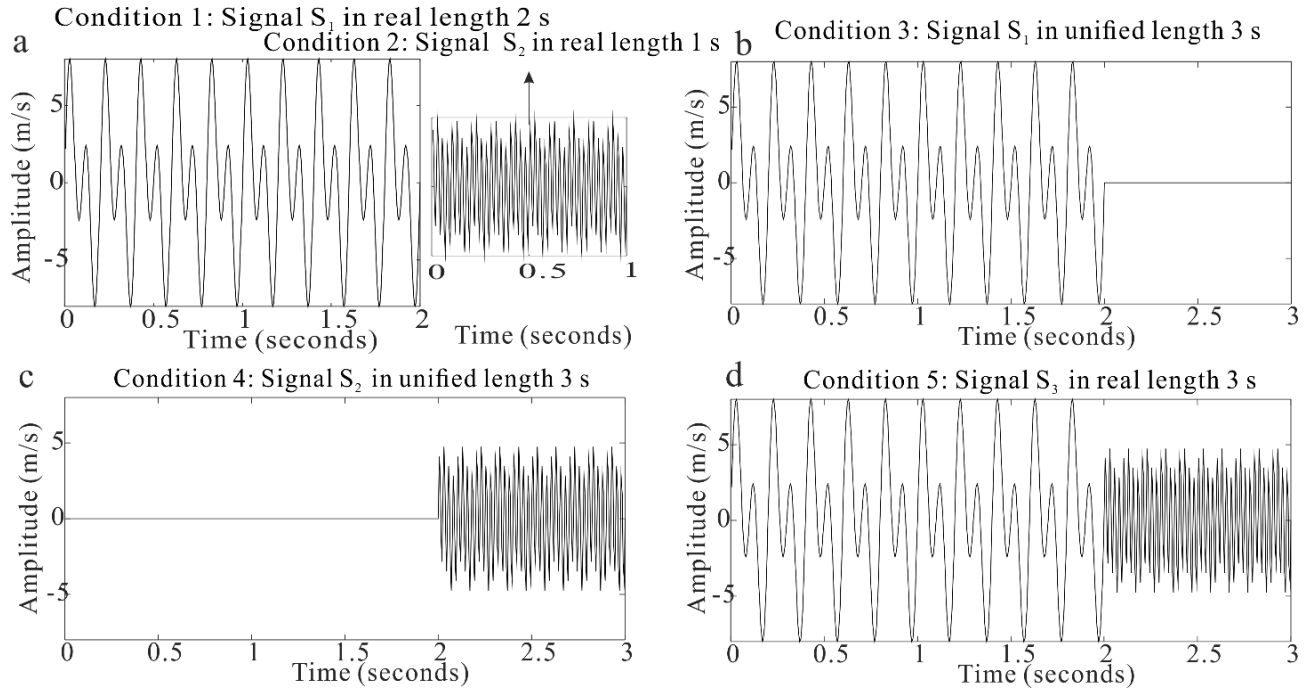


Figure 14. The traces of three synthesized signals S_1 , S_2 , and S_3 in five conditions; a: condition 1 and condition 2; b: conditions 3; c: condition 4; d: condition 5. See the text for the description of the five conditions.

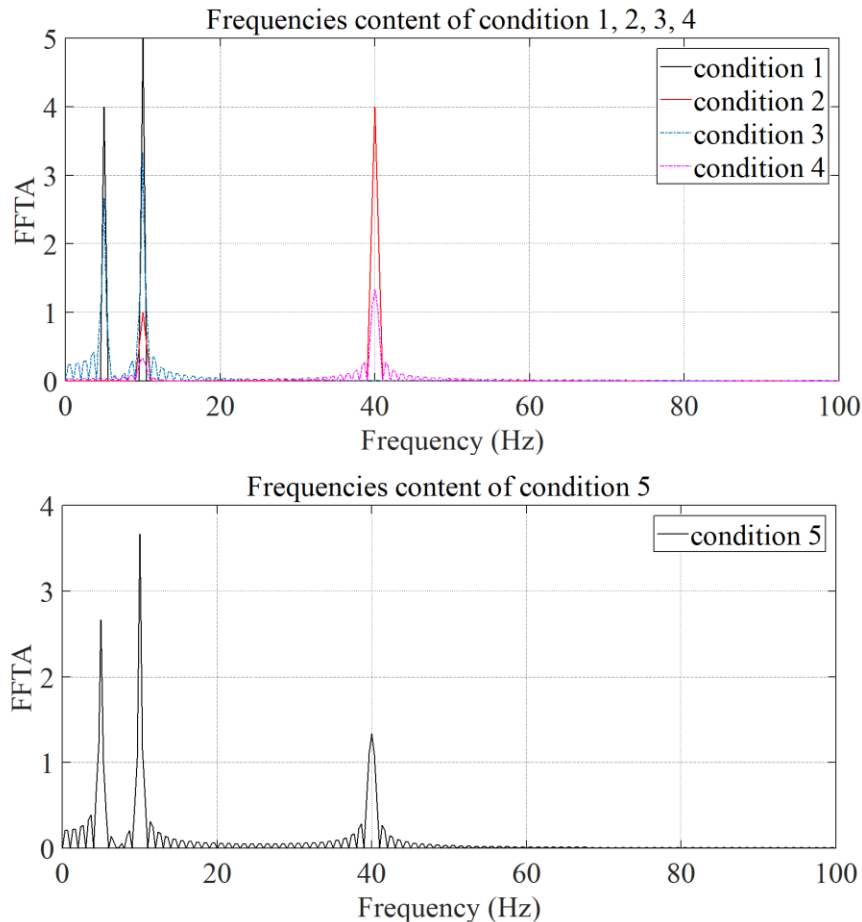


Figure 15. The frequency content of the five conditions transformed by FFT.

Table 3. The amplitude contents of synthesized signals (S_1, S_2, S_3) in five conditions after the FFT analysis.

Frequency (Hz)	Amplitude (m/s)		FFT coefficients (FFTA)				
	Basic signals		Condition 1: $l(\mathbf{B}_1 + \mathbf{B}_4) = 2 s$	Condition 2: $l(\mathbf{B}_2 + \mathbf{B}_3) = 1 s$	Condition 3: $l(\mathbf{B}_1 + \mathbf{B}_4 + \text{Zeros}) = 3 s$	Condition 4: $l(\mathbf{B}_2 + \mathbf{B}_3 + \text{Zeros}) = 3 s$	Condition 5: $l(\mathbf{B}_1 + \mathbf{B}_2 + \mathbf{B}_3 + \mathbf{B}_4) = 3 s$
5	\mathbf{B}_4	4	4	\	2.667	\	2.667
10	\mathbf{B}_1	5	5	1	3.333	0.333	3.667
	\mathbf{B}_2	1					
40	\mathbf{B}_3	4	\	4	\	1.333	1.333

3.2 Seismic event detection methods

3.2.1 STA/LTA

STA/LTA method is the ratio of short-time average through long-time average (Allen 1978; Trnkoczy 1998) that is broadly used for seismic events detection. It continuously calibrates the average absolute amplitude of a seismic signal in two consecutive moving windows. It is important to note that in this work, in this thesis, to enhance amplitude changes, STA/LTA takes into account the average values of squared amplitudes, as suggested by Allen (1982), instead of the average values of the absolute amplitudes, as proposed by Trnkoczy (1998). The short-time window (V_i in Figure 16) is sensitive to seismic events while the long-time window (W_i in Figure 16) provides the level of the temporal background noise at the site. When the ratio of STA/LTA exceeds a threshold, an event is 'declared'. The STA/LTA is usually adopted in weak motion applications that try to record as many seismic events as possible when not only the strongest events are of importance. However, it is also useful in many strong motion applications.

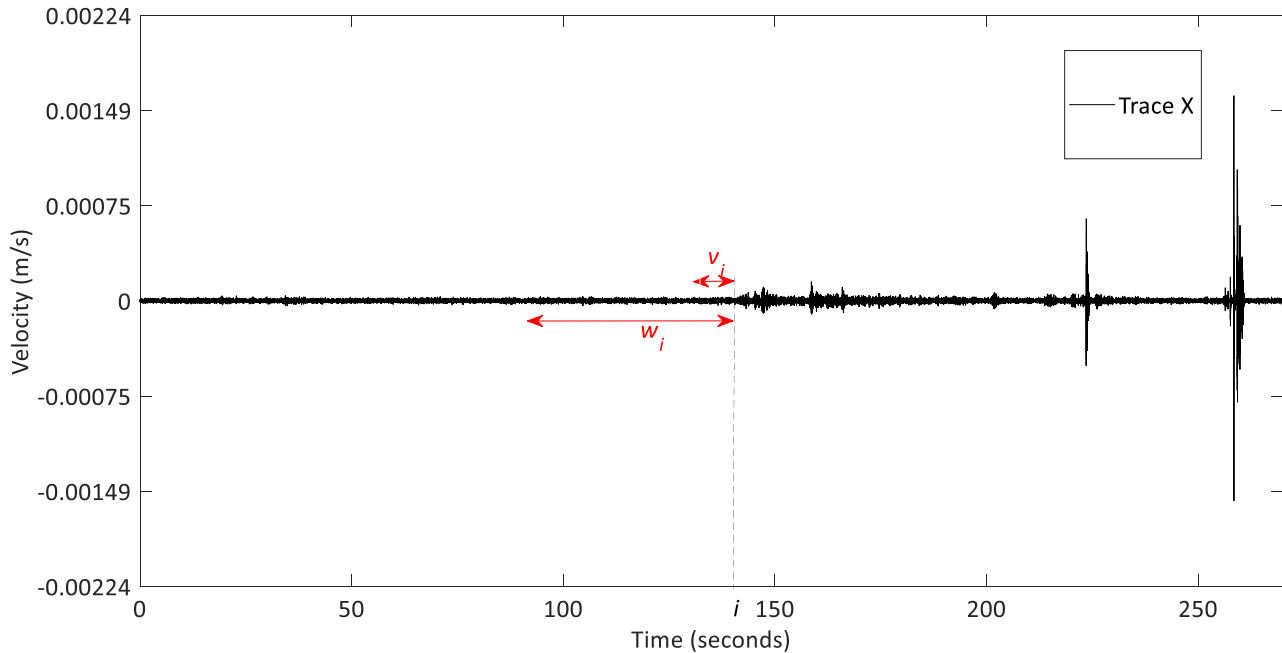


Figure 16. Graphical representation of a long-window (W_i) and a short-time window (V_i); both will move at same time in one sample, anyway, the moving pitch can also be changed to speed the calculation.

In each original seismic trace $\mathbf{X} = [x_1, x_2, x_3, \dots, x_n]$, the length of short-time window is M , and the length of long-time window is N , with $N > M$. At the time sample i , the matrix of each window can be obtained:

The short-time window trace: $v_i = [x_{i-M+1}, x_{i-M+2}, \dots, x_i]$;

The long-time window trace: $w_i = [x_{i-N+1}, x_{i-N+2}, \dots, x_i]$;

$$STA(i) = \frac{1}{M} \sum_{i-M+1}^i v_i^2, \quad (11)$$

$$LTA(i) = \frac{1}{N} \sum_{i-N+1}^i w_i^2, \quad (12)$$

$$R_i = \frac{STA(i)}{LTA(i)}, \quad (13)$$

Where the length of the two windows N , M and the ratio R_i are usually defined based on previous experiments at the site, user experience and literature review, with respect to the kind of events to be detected and to the background noise.

3.2.2 Cross-Correlation

In signal processing, the cross-correlation method is a measure of similarity of two series as a function of the lag of one relative to the other. It is commonly applied for recognizing specific patterns in a dataset.

For two continuous signals f and k , the cross-correlation is defined as:

$$(f * k)(\tau) = \int_{-\infty}^{+\infty} f'(t)k(t + \tau), \quad (14)$$

Where $f'(t)$ is the conjugate of $f(t)$, and τ is the lag time (samples).

In literatures, there are many methods modified from cross-correlation. In this study, Maximum Normalized Cross-Correlation (MNCC, Akhouayri 2014) is compared.

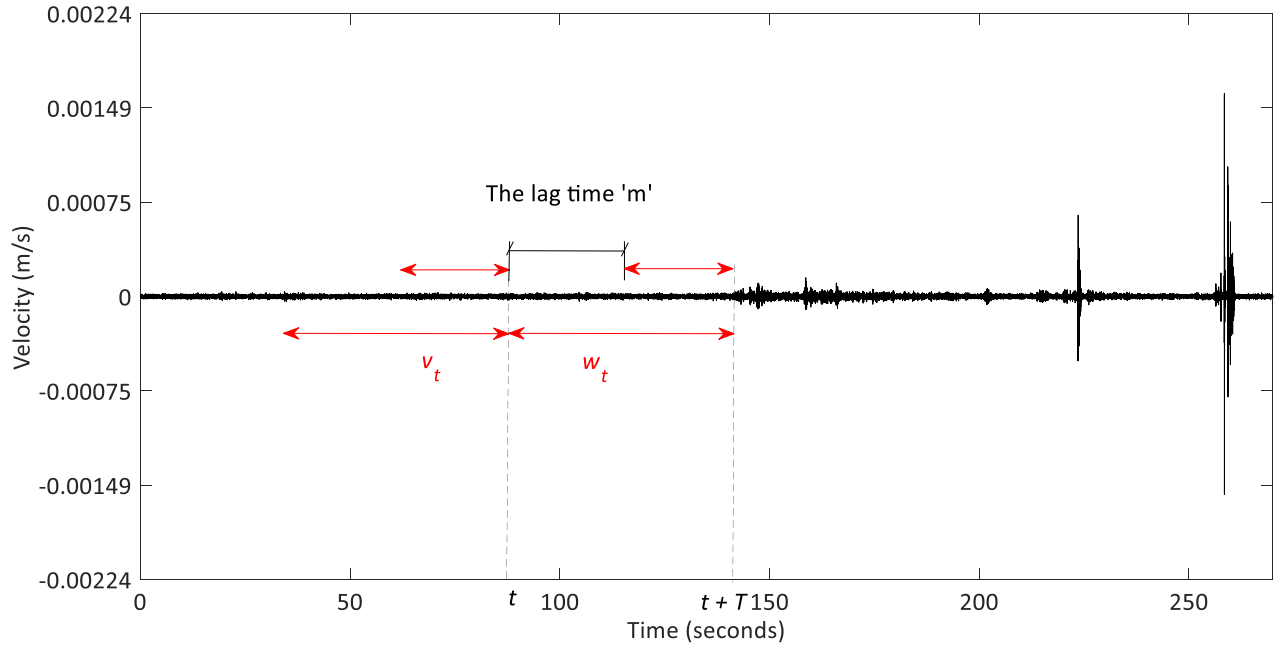


Figure 17. Position of two consecutive windows v_t and w_t at time t , and the windows upside are computed with lag time m .

In MNCC method, at each time t , two windows, w_t and v_t , of the same length T or (N samples) are selected; v_t is before the time t and w_t is after the time t (Figure 17):

$$v_t = [x(t - N\Delta t), x(t - (N - 1)\Delta t), \dots, x(t - \Delta t)], \quad (15)$$

$$w_t = [x(t), x(t + \Delta t), \dots, x(t + (N - 1)\Delta t)], \quad (16)$$

Then the function of MNCC ($\hat{\rho}_{max}(t)$) is computed as (Akhouayri, 2014):

$$\hat{\rho}_{max}(t) = \max(|\hat{\rho}_{wv}(t, m)|) = \frac{\max(|\hat{r}_{wv}^b(t, m)|)}{\sqrt{\hat{r}_{ww}^b(t, 0)\hat{r}_{vv}^b(t, 0)}} = \frac{\max\left(\left|\frac{1}{N}\sum_{n=0}^{N-1-|m|} w_t[n+m]v_t[n]\right|\right)}{\sqrt{\left(\frac{1}{N}\sum_{n=0}^{N-1} w_t[n]w_t[n]\right)\left(\frac{1}{N}\sum_{n=0}^{N-1} v_t[n]v_t[n]\right)}}, \quad (17)$$

At the end, latest computed MNCC value is compared with the previous ones to detect abrupt changes. Once a threshold δ is defined, if $\left|\hat{\rho}_{max}(t) - \frac{1}{n}\sum_{k=1}^n \hat{\rho}_{max}(t - k\theta)\right| < \delta$, then an event is 'declared', where n is the number of samples prior to t , and θ is the window sliding pitch, while $\frac{1}{n}\sum_{k=1}^n \hat{\rho}_{max}(t - k\theta)$ is the mean value of MNCC measured over n previous samples.

3.2.3 Methods comparison

For the detection methods comparison, a short signal trace (270 seconds) that included two strong events and three weak events (marked with green ellipses in Figure 20 and Figure 21) was analysed with both the STA/LTA and the MNCC methods. This trace was extracted from the seven-month monitoring data and was chosen for the analysis thanks to its clarity. We remember here that in Torgiovanetto, rockfalls bounce on the benches and every rebound is recorded by the seismic network as an impact (Gracchi et al. 2017; Feng et al. 2019).

With respect to the observation of the manually released rockfalls, the shortest length of one impact (the time over which the block contacts the slope surface) is 0.4 s, and the average length of one whole rockfall event is 14 s. Therefore, the lengths of the short-time window and long-time window in DESTRO were chosen equal to 0.4 s and 14 s, respectively. Figure 18 shows the seismic event detection result and computing parameters detected by the STA/LTA method. Figure 18a, in particular, is the original signal trace, and the red lines are the onset times of each event automatically detected by STA/LTA, while the dashed green ellipses are the manually detected events. Figure 18b shows two computing variables, i.e., the energy average values over a short-time window (STA) and long-time window (LTA). Figure 18c shows the two STA/LTA thresholds employed. The first one (*threshold1*) employed for event detection was fixed equal to 4, and the second (*threshold2*) used for checking the onset times of the events was set equal to 2. The difference of the two thresholds was used to pick the event onset time more precisely. In the automatic STA/LTA event detection example shown in Figure 18, four events were detected, and one weak event was missed (highlighted by the second green ellipse in Figure 18a). This happened because the two events are too close to each other (i.e., the interval time between them is less than 2800 samples, i.e., 14 s, set as the minimum interval time between two separate events; for more details on the parameters' settings and the detection flowchart in DEtection and SStorage of ROckfall Occurrence (DESTRO), see Section 5.1 and Figure 47). However, this does not mean that STA/LTA method failed to detect events. In fact, in the program DESTRO, there are many components integrated for event detection should one component fail, which are introduced and discussed in Section 5. In the STA/LTA method, the values of the thresholds and the lengths of two sliding windows are not permanent, and the fittest value should be modified depending on the monitoring site condition and the type of target events (Trnkoczy 1998).

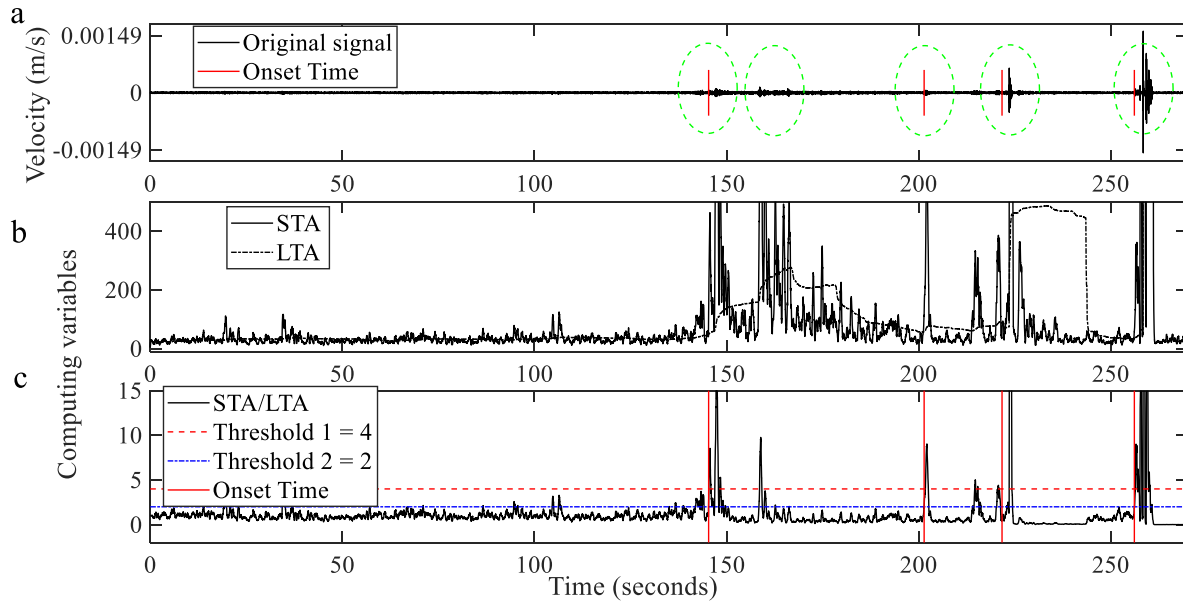


Figure 18. STA/LTA analysis results; a: original signal where the five events (circled in green) have been manually selected, and the solid red lines are the event onset times detected by STA/LTA; b: values of STA and LTA; c: thresholds used as criteria for target event detection.

For MNCC method estimation, Figure 19 illustrates the result of the MNCC method applied on the same original signal of the previous example. In Figure 19b, the black line is the value of the MNCC calculated with a moving window of 20 s and stepped in $\theta = 0.005$ s; the blue dashed line is the MNCC mean value; and the red dashed lines are the detection thresholds suggested by (Akhouayri 2014), which are equal to the mean of MNCC plus and minus the standard deviation (STD) of the MNCC mean value ($\text{mean} \pm \text{STD}$). The red solid lines are the event onset times detected by the MNCC using the value ($\text{mean} - \text{STD}$), according to the method suggested by Akhouayri 2014. As a result, there are eight events detected by the MNCC, but only two of them (the second and the sixth ones) have been detected correctly. Notably, some events are missed, and some other are identified even if they did not occur. In Figure 19b, the MNCC curve displays considerable variation, and it is easily disrupted by nearby events. For these reasons, it is suggested that MNCC is preferable for use in a quiet environment (or with filtered signals and high signal-to-noise ratio data) or for single event detection, and therefore, it is not a suitable method for DESTRO, which operates with raw signals and in complicated environments.

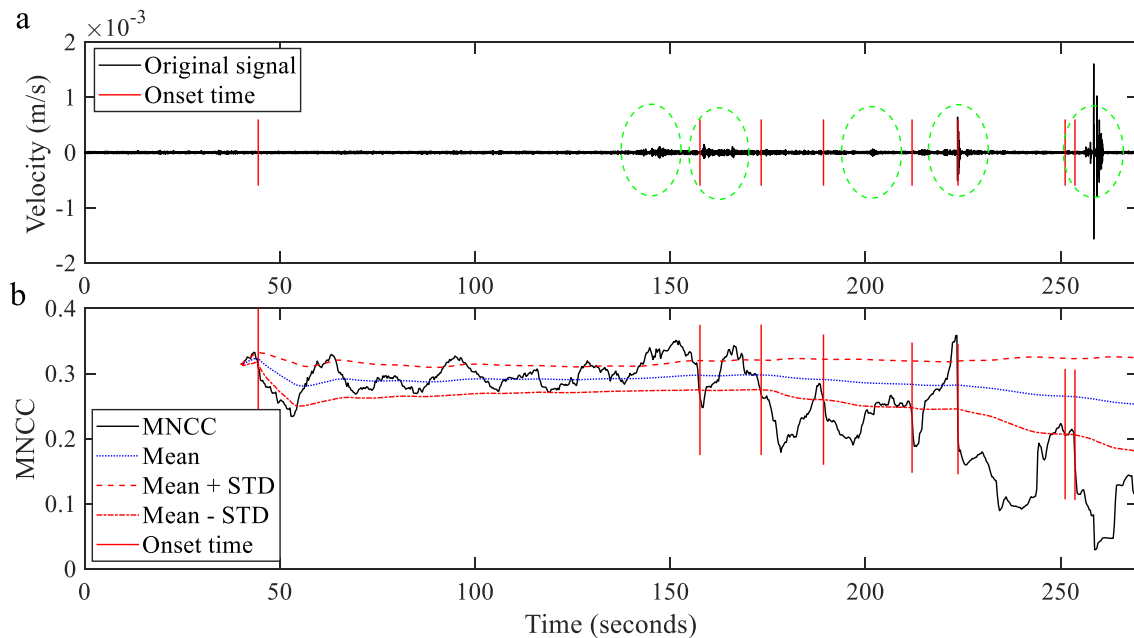


Figure 19. Cross-correlation detection (MNCC) result. a: original signal, where the five events (circled in green) have been manually selected, and the solid red lines are the event onset times detected by MNCC; b: analysis result where the thresholds used to detect the events are represented.

Finally, STA/LTA is chosen for the detection part of DESTRO in single component. Beside the detection thresholds (*threshold1* and *threshold2* defined previously), a minimum event duration (0.4 s, *MINevent* equal to the short-time window, *STw*) and a minimum interval time (14 s, *MINinterval* equal to the long-time window, *LTw*) between two consecutive events are assigned to separate events. The threshold *MINevent* is the minimum length of one short event triggered by *threshold1* and represents the minimum duration of one event defined in DESTRO. The threshold *MINinterval* is the minimum interval length supposed between the last triggered sample of the first event and the first triggered samples of the following event; *MINinterval* is used as a criterion to end one event. The detailed detection process flowchart is shown in Section 5.1.

3.3 Rockfall localization methods

3.3.1 Polarization-bearing

(1) Polarization localization theory

The instruments employed in this study is a kind of three-component sensor, *Tromino*, that recorded seismic wave in three directions, East-West direction (E), North-South direction (N), and vertical direction (Z), and in time domain with velocity dimension. To better evaluate the of localization methods, one of the rockfalls released during the tests, the N.39 was chosen thanks to its clear signals and video recordings. The seismic signals from rockfall N.39 that were recorded by four geophones are shown in Figure 20 (more detail information about this in situ artificial rockfall released test in Section 4), and the localization estimation was performed for the first impact onto the slope surface. The signal of the first impact is shown between the two vertical red dashed lines (in the following marked as rockfall N.39-impact #1).

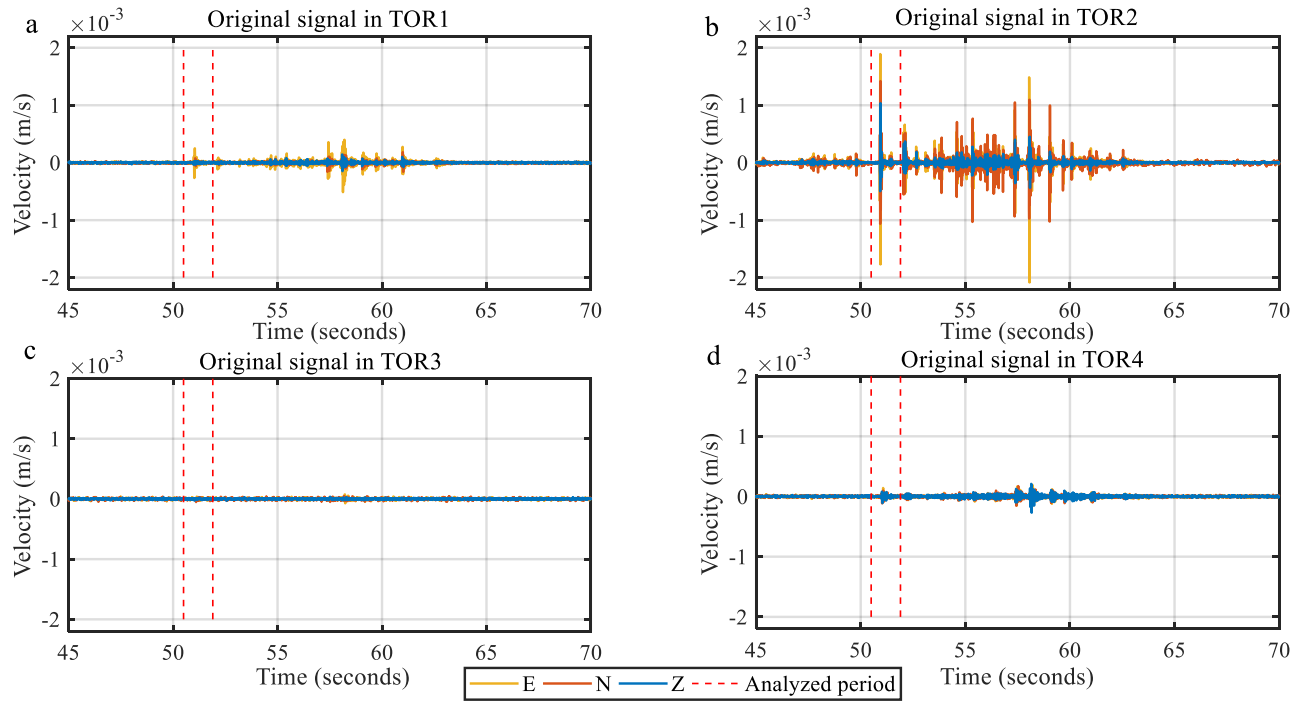


Figure 20. Original signals recorded in four seismic stations, and the short period of signal between two red dash lines is Rockfall N.39-impact #1.

For back-azimuth calculations and polarization processing, bandpass filters are employed to analyse the three-component seismograms. Moreover, short time windows are selected to analyse signals corresponding to single seismic events. The signal quality is better if the phase of the P-wave is considered. However, the length of the time window and the frequency bands of the P-wave are controlled by the event duration and the event type. The most appropriate frequency bands for data from rockfalls for polarization analyses are suggested in the following of this section. In this study, the bandwidth was set to 1 Hz, as illustrated schematically in Figure 21. The three components of the original signal from rockfall N.39-impact #1 and its related particle motions are shown in Figure 21a and Figure 21c, respectively. The filtered signal in the frequency band 26 – 27 Hz and the particle motion in the same band are plotted in Figure 21b and Figure 21d, respectively. The polarization is usually estimated in a short-time window to keep the signal stable and come from a single event-source. The frequency band width and length of time window are controlled by event type and event duration.

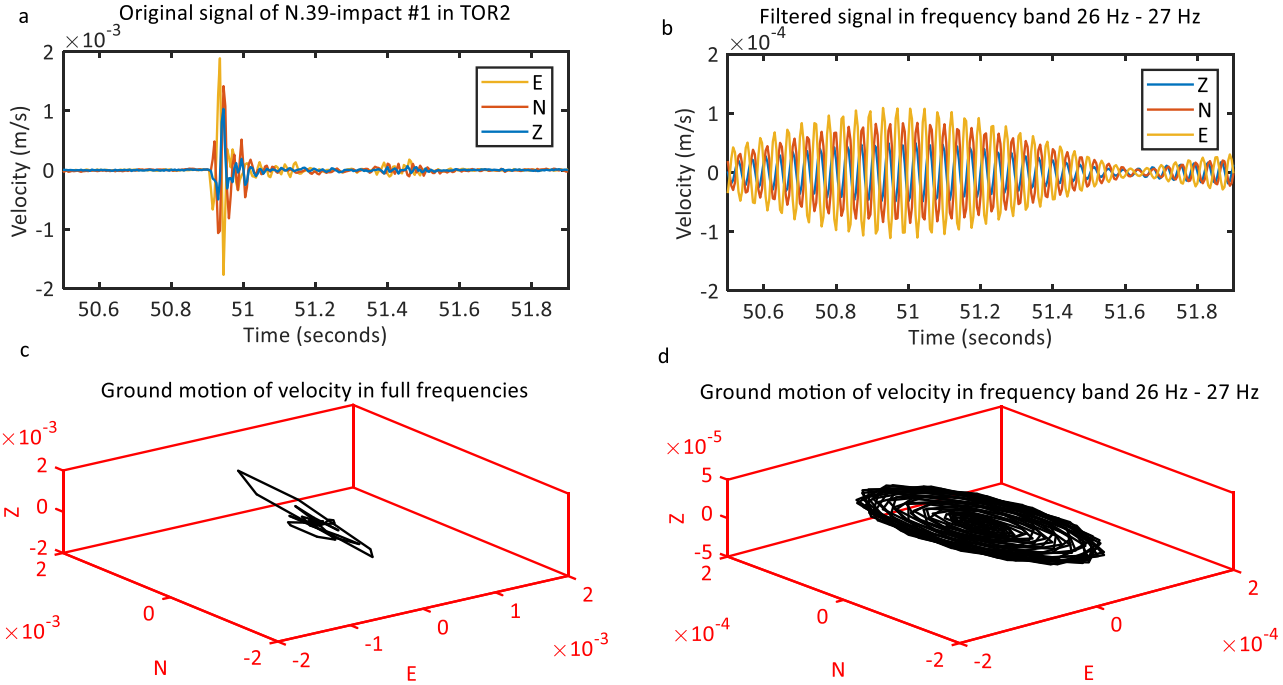


Figure 21. The original signal and the bandpass-filtered signal of rockfall N.39-impact #1 shown in panel a and panel b, respectively; their related particle motions are shown in panel c and panel d, respectively.

The seismic polarization methodology refers to the studies by Jurkevics (1988) and Vilajosana (2008), based on bandpass filtering. Supposing a signal trace $\mathbf{X} = [x_{ij}]$; $i = 1, 2, \dots, N$; $j = 1, 2, 3$ be the data matrix in one window, where x_{ij} is the i th sample of component j and N is the number of samples. The mean for each component of \mathbf{X} over this window is taken here to zero. The covariance matrix S_{jk} is evaluated as

$$S_{jk} = \frac{\mathbf{X}\mathbf{X}^T}{N} = \left[\frac{1}{N} \sum_i^N x_{ij}x_{ik} \right], \quad (18)$$

Where T denoted transpose. The cross-variance matrix is 3×3 , real and symmetric. Explicitly, the terms of \mathbf{S} are the auto- and cross-variances of the three components of motion:

$$\mathbf{S} = \begin{bmatrix} S_{zz} & S_{zn} & S_{ze} \\ S_{zn} & S_{nn} & S_{ne} \\ S_{ze} & S_{ne} & S_{ee} \end{bmatrix}, \quad (19)$$

Where S_{zn} denotes the cross-variance of the vertical and north components, etc.

The ground motion under the seismic monitoring station in each frequency band over the time window is an ellipsoid (Figure 21d). In linear algebra, the ellipsoid algebraic expression and its eigenvectors are:

$$\mathbf{X}^T \mathbf{A} \mathbf{X} = 1, \quad (20)$$

$$\mathbf{A} = (\mathbf{X}\mathbf{X}^T)^{-1}, \quad (21)$$

$$(\mathbf{A} - \lambda' \mathbf{I}) \mathbf{u}' = \mathbf{0}, \quad (22)$$

Where \mathbf{A} is coefficient matrix of the ellipsoid, \mathbf{I} is the 3×3 identity matrix and $\mathbf{0}$ is a column vector of zeros. and the lengths and orientations of ellipsoid's axis (a_1, a_2, a_3) are the square root of the inverse eigenvalues $(\lambda'_1, \lambda'_2, \lambda'_3)$ and the eigenvectors $(\mathbf{u}'_1, \mathbf{u}'_2, \mathbf{u}'_3)$ of coefficient matrix \mathbf{A} .

\mathbf{S} is the inverse of coefficient matrix for a quadratic from which is an ellipsoid (Equation 23 and 24). This ellipsoid, termed the polarization axes of the ellipsoid are found by solving the algebraic eigenproblem for \mathbf{S} . This involves finding the eigenvalues $(\lambda_1, \lambda_2, \lambda_3)$ and eigenvectors $(\mathbf{u}_1, \mathbf{u}_2, \mathbf{u}_3)$ which are nontrivial solutions to

$$(\mathbf{S} - \lambda \mathbf{I})\mathbf{u} = 0, \quad (23)$$

$$\mathbf{S} = \mathbf{A}^{-1}, \quad (24)$$

$$\lambda = \frac{1}{\lambda'}, \quad (25)$$

$$\mathbf{u} = \mathbf{u}', \quad (26)$$

$$a_j = \sqrt{\frac{1}{\lambda'_j}} = \sqrt{\lambda_j}, \quad (27)$$

The three principal axes of the polarization ellipsoid are given by $a_j \mathbf{u}_j$, $j = 1, 2, 3$ (Equation 26 and 27). The eigenproblem of a well-conditioned 3×3 symmetric matrix can be computed very quickly using standard numerical libraries in MATLAB (Equation 23). The eigenvalues are ordered such that $a_j \geq a_k$ for $j < k$ to find the longest principal axes.

Once the principal axes of the polarization ellipsoid are estimated, the particle motion in the data window is determined. The information describing the characteristics of ground motion is extracted using attributes computed from the principal axes. The back-azimuth of P-wave propagation is the orientation of event-source that can be estimated from the horizontal orientation, given by the eigenvector \mathbf{u}_1 correspond to the largest eigenvalue (Jurkevics 1988):

$$\text{Back azimuth} = \tan^{-1} \left(\frac{u_{21} \text{sign}(u_{11})}{u_{31} \text{sign}(u_{11})} \right), \quad (28)$$

Where $u_{j1}, j = 1, 2, 3$ are the three direction cosines of eigenvector \mathbf{u}_1 , and u_{21} and u_{31} is the Northern component and Eastern component of the dominant eigenvector \mathbf{u}_1 , respectively. The sign function is introduced to resolve the 180° ambiguity by taking the positive vertical component of \mathbf{u}_1 .

In the polarization processing, the individual covariance matrix \mathbf{S}^k for the k th frequency band is computed in the usual way (Equation 18), while to get a stable Back azimuth estimate result, a wide relevant frequency bands are applied, and the wide-band estimate obtained by:

$$\bar{\mathbf{S}} = \left(\sum_{k=1}^K \text{trace}(\mathbf{S}^k) \right) \sum_{k=1}^K \frac{\mathbf{S}^k}{\text{trace}(\mathbf{S}^k)}, \quad (29)$$

Where K is the number of bands to include, and the function $\text{trace}(\mathbf{S})$ is the sum of the diagonal values of the matrix \mathbf{S}^k .

Within seismic polarization processing, assuming that the back azimuths estimated in a horizontal plane are $\theta_1, \theta_2, \dots, \theta_s$, the event-source location is (x, y) , and the location from seismic station (s) is (x_s, y_s) , Therefore, at seismic station s , the analytical localization equation will be:

$$\tan(\theta_s) = \frac{y - y_s}{x - x_s}, \quad (30)$$

and its matrix expression will be:

$$[-\tan(\theta_s), 1] \begin{bmatrix} x \\ y \end{bmatrix} = y_s - x_s \tan(\theta_s), \quad (31)$$

In geometry, the event-source location can be easily determined by two seismic stations with their estimated back azimuths (Bishop et al. 2009), while in practically, to get a more precise result and to avoid errors or arbitrary decision made by only two stations, more than two stations are employed in seismic monitoring, as shown in Figure 22.

When more than two stations are employed in a monitoring network, the analytical localization equation can be presented as the overdetermined matrix shown in Equation 32:

$$\mathbf{M}\mathbf{x} = \mathbf{N}, \quad (32)$$

$$\text{Where } \mathbf{M} = \begin{bmatrix} -\tan(\theta_1) & 1 \\ -\tan(\theta_2) & 1 \\ \vdots & \vdots \\ -\tan(\theta_s) & 1 \end{bmatrix}, \quad \mathbf{N} = \begin{bmatrix} y_1 - x_1 \tan(\theta_1) \\ y_2 - x_2 \tan(\theta_2) \\ \vdots \\ y_s - x_s \tan(\theta_s) \end{bmatrix}, \quad \mathbf{x} = \begin{bmatrix} x & x & \dots & x \\ y & y & \dots & y \end{bmatrix}.$$

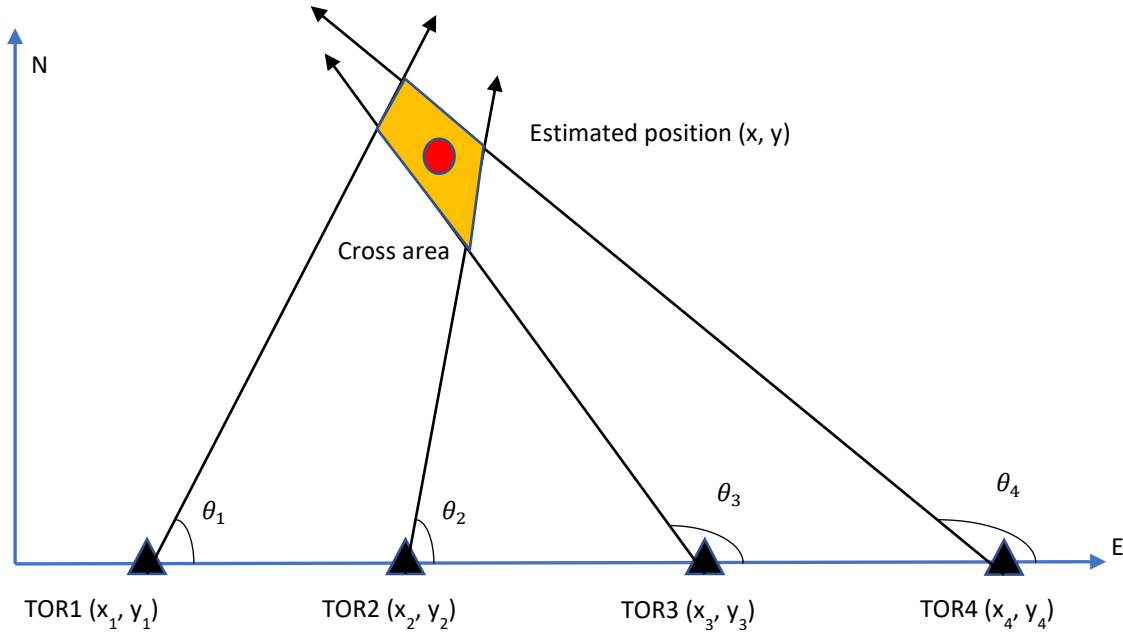


Figure 22. Localization optimizing with multiple stations.

Therefore, the optimal result for the event location will be the solution of the overdetermined matrix shown in Equation 33, calculated as follows:

$$\begin{bmatrix} \hat{x} \\ \hat{y} \end{bmatrix} = \text{argmin}((\mathbf{M}\mathbf{x} - \mathbf{N})^T (\mathbf{M}\mathbf{x} - \mathbf{N})), \quad (33)$$

where *argmin* is the function's minimum value of \mathbf{x} .

Furthermore, considering that signal intensity and quality are different among stations, a confidence weight is assigned to each station in the overdetermined matrix calculation. The confidence weight is calibrated based on the seismic energy of the analysed signal recorded at each station, i.e., higher signal energy indicates higher reliability for the calculated back azimuth and a higher confidence weight. Moreover, when the signal energy is

below the noise level, the confidence weight is set to 0, and the station is not considered in the estimation of back azimuths.

The confidence weights, defined as (w_1, w_2, \dots, w_s) with s as the number of stations, form a matrix:

$$\mathbf{W} = \begin{bmatrix} w_1 & \dots & 0 \\ \vdots & \ddots & \vdots \\ 0 & \dots & w_s \end{bmatrix}, \quad (34)$$

Finally, combining the overdetermined and confidence weight matrices, the improved event source location is:

$$\begin{bmatrix} \hat{x} \\ \hat{y} \end{bmatrix} = \operatorname{argmin}((\mathbf{M}\mathbf{x} - \mathbf{N})^T \mathbf{W}(\mathbf{M}\mathbf{x} - \mathbf{N})), \quad (35)$$

In addition, we usually obtain event locations on a horizontal plane, but when the altitude of a seismic event is required, it can be determined by projecting the horizontal coordinates onto a 3D topographic map to find the correct altitude value.

(2) Marker parameters for frequency bands choose

To localize rockfalls by means of the P-B method, we must know the detailed seismic wave mode of the rockfall signal and determine the appropriate frequency bands, for which the particle movement is in the direction of propagation (e.g., the P-wave). From the studies of Kao et al., (2012), the seismic characteristics of the landslide and mud/debris flow (LMDF) waveforms are significantly different from those of earthquakes. In fact, LMDF signals are sharp and are characterized by irregular P/S bursts related to the landslide history. After a careful examination of all LMDF waveforms that were recorded in Taiwan by a broadband array in a seismograph network, the authors suggested the P and S phases intermix as a robust feature to distinguish LMDF events (Kao et al., 2012). Therefore, three marker parameters, energy (E), rectilinearity (I), and a special permanent frequency (SPF), were analysed in this study to determine the appropriate frequency bands for P-waves for seismic polarization and back-azimuth calibration.

a) Energy (E)

To evaluate the usefulness of energy as marker parameter, the energy and back azimuths of each bandpass filtered signal from rockfall N.39-impact #1 were calculated, and the back azimuths were then compared with the in-situ measurements to determine the correct frequency bands and their relationships with energy.

The signal from rockfall N. 39-impact #1 was bandpass filtered into 96 frequency bands, each with a width of 1 Hz and ranging from 3 Hz to 99 Hz. The frequencies (0 Hz-3 Hz) and the frequency band (99 Hz – 100 Hz) were discarded since noise dominated and there were filter and recording errors (Feng et al., 2019). For each of the 96 frequency bands evaluated, the back azimuths and the FFTA (fast Fourier transform coefficient) were calculated. The FFTA values represent the energy of a signal in a given frequency band as defined by Feng et al., (2019). Figure 23 is a plot of the results. Moreover, the back azimuths measured in situ as illustrated in Gracchi et al., (2017) and referred to here as “real back azimuths” are also shown (dashed blue line) in Figure 23.

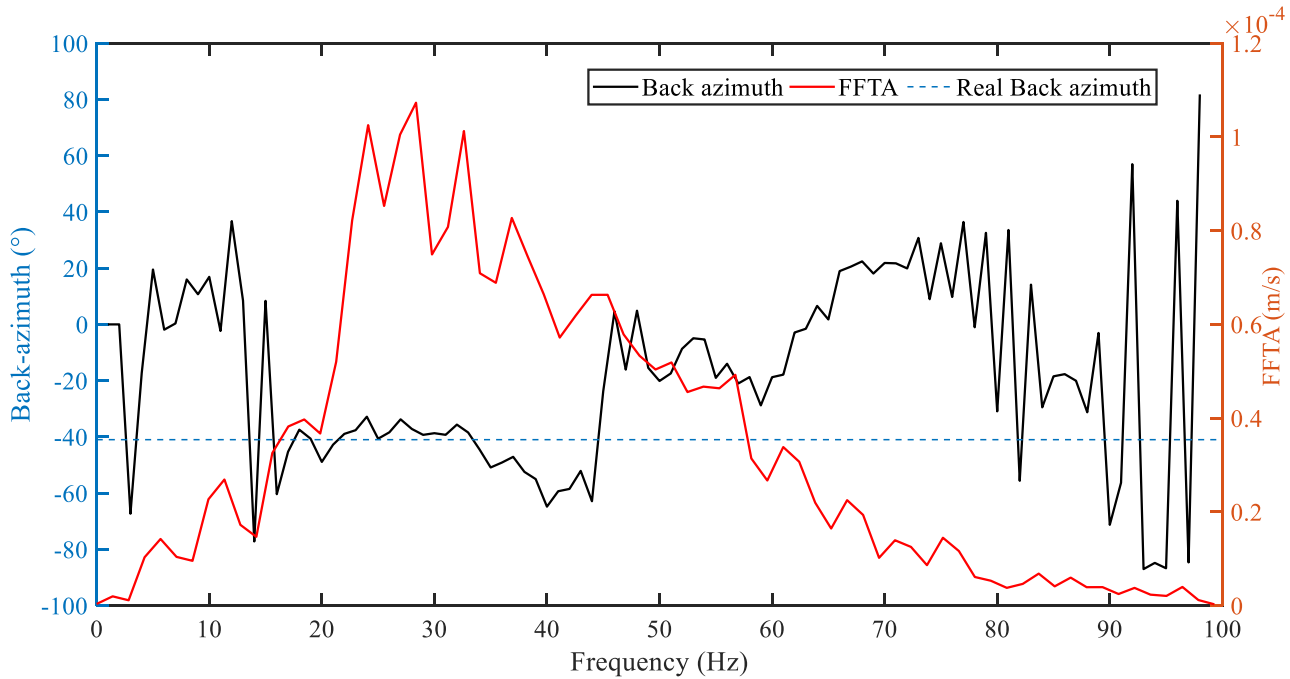


Figure 23 The correlation between back azimuths (black solid line) that were calculated in each frequency band (1 Hz width) and the FFTA values (i.e., representing energy; red solid line) from Impact #1 of N.39 recorded by TOR2 (the original signal is shown in Figure 21a).

The results show that the back azimuths calculated from the frequency bands from 15 Hz – 45 Hz are mainly close to the real back azimuth, and in parallel, the energies in the frequency bands from 20 Hz – 40 Hz have the most energy in the full-frequency bands. This rule is valid for all artificial rockfalls launched from the right side of the test slope. Therefore, we assumed that the frequency bands with the greatest energy from rockfalls would be suitable for the P-B method, as assessed by the studies of Kao (2012) and discussed at the beginning of this section. To provide the most stable estimates, the top 30 highest energy frequency bands (30E) were chosen, and seismic polarization was performed by normalizing and averaging the series of frequency bands. The theory forming the basis of this methodology can be found in the studies of Jurkevics (1988). Moreover, the confidence weights of rockfall N.39-impact #1 data are set to (0.20, 0.62, 0, and 0.18) for stations (TOR1, TOR2, TOR3, and TOR4), respectively. In particular, the confidence weight for TOR3 is 0, as the energy this at the station is lower than the noise level according to the confidence weights defined in Equation 34.

The results of P-B and T-B are shown in Figure 24. The green point in Figure 24b was localized by only one frequency band with the maximum energy, the cyan colour point was localized by the frequency bands of 30E, and the blue colour point was localized by T-B. From the results in this case, we found the localizations of three approaches are quite close to the rockfall in situ trajectory, and the marker parameter 30E provides results as good as T-B (that is introduced in the next section). Moreover, 30E is more precise and stable than when only one frequency band is applied.

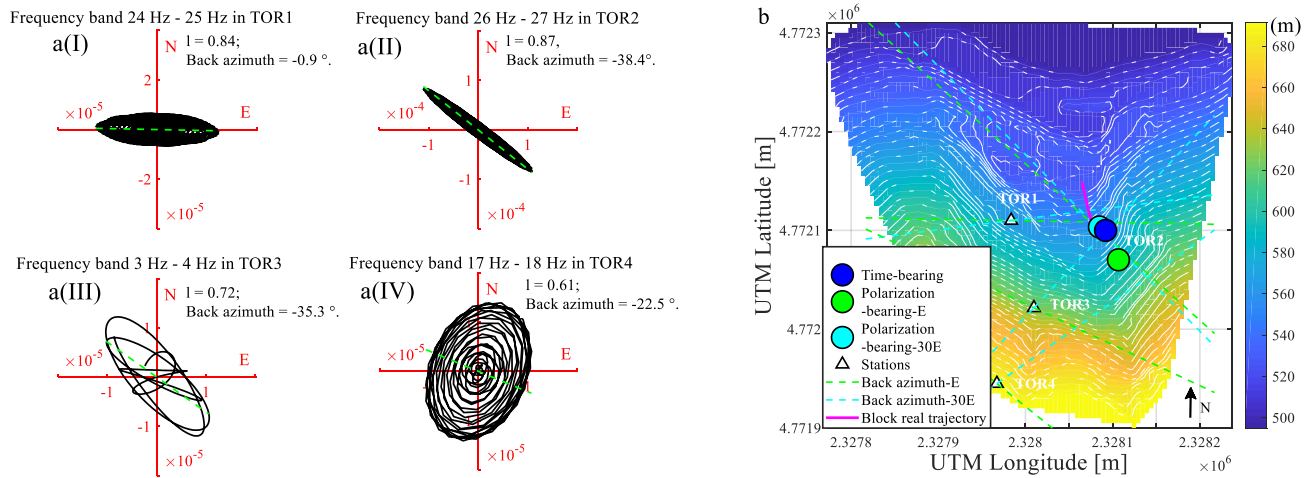


Figure 24. Picture (a): the particle motion and back-azimuth calculated in each station with energy decision, and the variance of R is the rectilinearity of particle motion; Picture (b): the localization decided by the parameter of maximum energy.

b) Rectilinearity (l)

Rectilinearity is a characteristic of particle motion that corresponds to the linearity of particle motion. Higher values mean that it is easier to obtain correct and precise ground motion directions. In contrast, planarity (p) indicates how the particle motion develops on a plane (Jurkevics, 1988).

The degree of rectilinearity is given by Equation 36:

$$l = 1 - \frac{a_2 + a_3}{2 \times a_1}, \quad (36)$$

and the degree of planarity is given by Equation 37:

$$p = 1 - \frac{2 \times a_3}{a_1 + a_2}, \quad (37)$$

Where the values of $a_1 \geq a_2 \geq a_3$ are the lengths of principle ellipsoid's axis of the covariance matrix of analyzing signal period. a) When a_1 is infinitely large compared to a_2 and a_3 ($a_1 \gg a_2 \geq a_3$), then $l \approx 1$, and $p \approx 1$, i.e.; the particle motion is linear. b) When a_1 and a_2 are equal and infinitely large compared to a_3 ($a_1 \geq a_2 \gg a_3$), then $l \approx 0.5$, and $p \approx 1$; i.e., the particle motion moves in a plane. c) Finally, when a_1 , a_2 , and a_3 are approximate equal, then $l \approx 0$ and $p \approx 0$; i.e., the particle motion moves in a sphere.

The rectilinearity and planarity values are calculated for the 96 bandpass-filtered bands and are plotted in Figure 25. Along with the calibrated back azimuths and the real back azimuths. We observe that the l and p trends do not show a significant correlation with the back azimuths. Moreover, repeating the P-B procedure to localize rockfall N.39-impact #1 by using the frequency band with the maximum rectilinearity value provides a localization result (Figure 26), from P-B- l that is not as precise as the results from either P-B-E or P-B-30E .

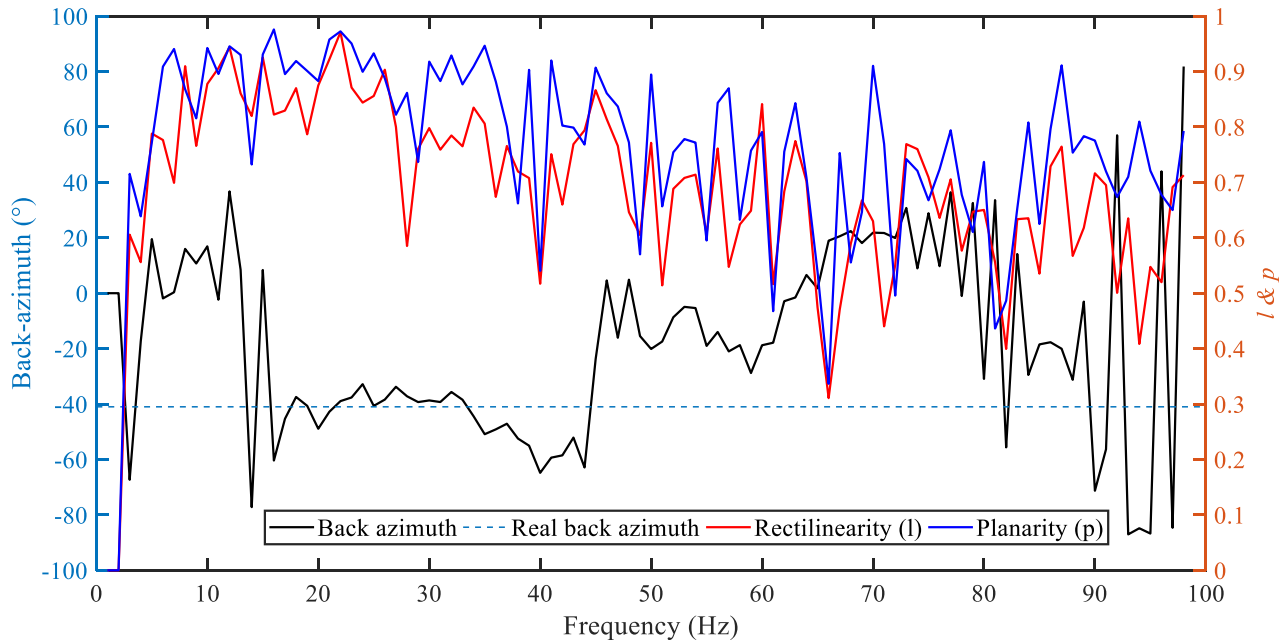


Figure 25. The correlations between the B-azimuths, and the rectilinearity and planarity values distributed in the frequency bands used for N.39-impact #1 in TOR2.

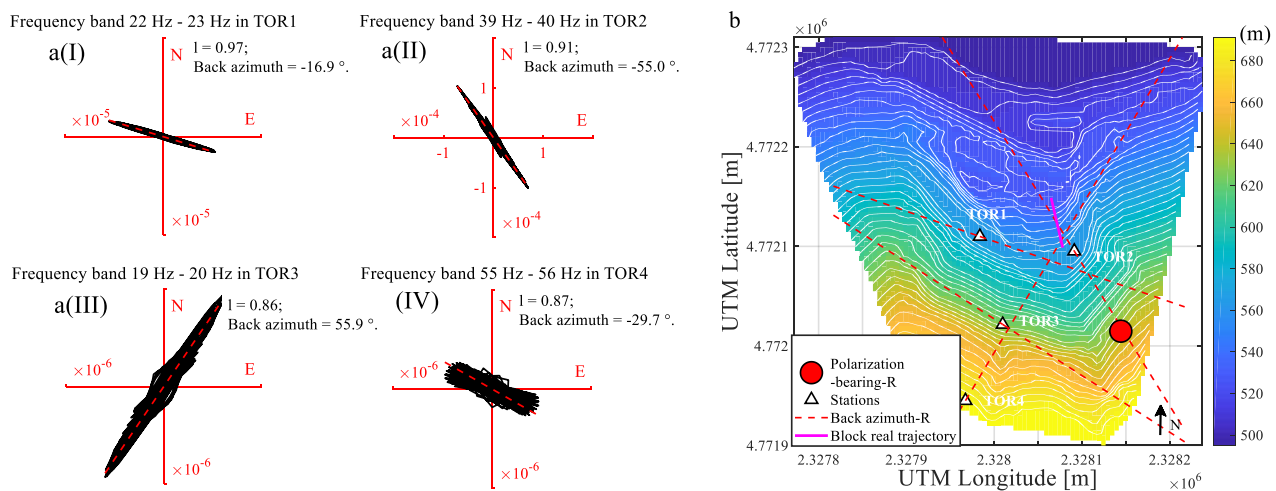


Figure 26. Panel (a): the particle motions and back azimuths calculated for each station with the rectilinearity decision; and Panel (b): the localizations obtained by means of the maximum rectilinearity procedure. The pink line indicates the real block trajectory measured in situ.

c) Special permanent frequency band for all stations (SPF)

Assuming that the frequency bands created by rockfall as measured by the four stations are consistent, we defined a special permanent frequency (SPF) band for all stations that refers to the maximum energy in the seismic station closest to the rockfall across the monitoring network. For artificial rockfall N.39, the nearest station is TOR2, and the most powerful frequency band is 26 Hz to 27 Hz; hence, the SPF band for impact #1 is from 26 Hz to 27 Hz. We find that the localization results of SPF are better than those obtained for P-B-I and are quite similar to the results obtained by using P-B-E but are not as good as those obtained by using P-B-30E.

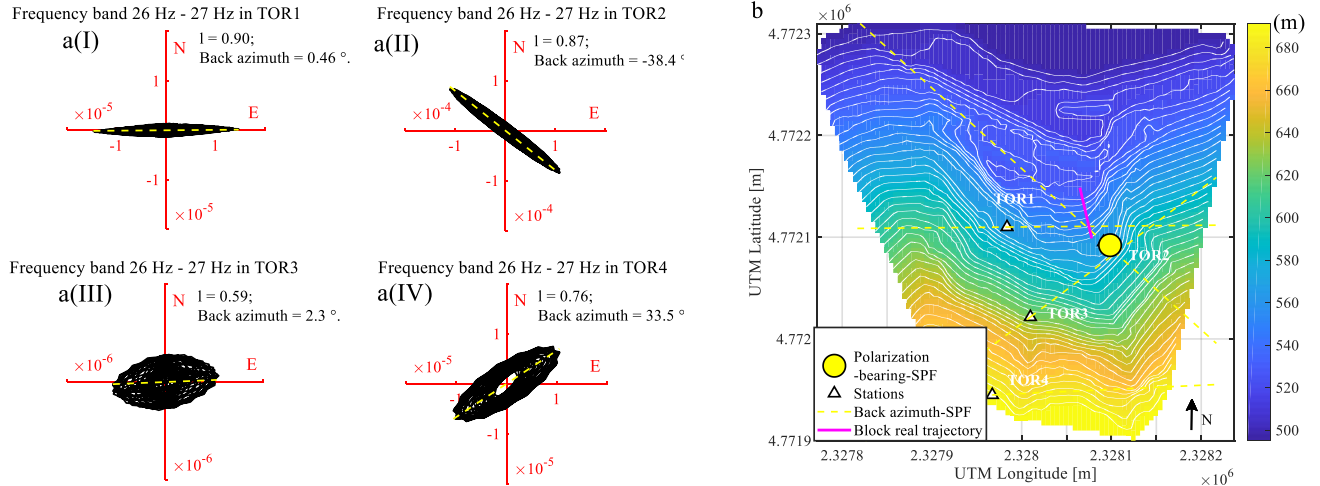


Figure 27. Panel (a): the particle motions and back azimuths calculated in each station using the permanent frequency band; Panel (b): the localization obtained by the SPF band procedure in the 26 Hz – 27 Hz band.

3.3.2 Time-bearing

The seismic wave arrival times were non-linearly inverted to locate the block impact point when utilizing T-B. The monitoring slope was divided into equal cells to obtain a regular grid in which each node is accurately georeferenced; the points were then searched by minimizing the misfit function derived from the differences between the measured and theoretical times calculated for each node of the gridded topographic surface. More information can be found in Moser et al. (1992) and Gracchi et al. (2017). The misfit function is calculated as follows:

$$\sum_{s=1}^{nsta} |[t_s - \bar{T}] - [\Delta_s^{theo} - \bar{\Delta}]|^2, \quad (38)$$

Where t_s is the arrival time recorded at station s ; \bar{T} is the average arrival time of t_1, t_2, \dots, t_s ; $nsta$ is the number of stations applied; Δ_s^{theo} is the theoretical travel time from the search point to station s in the grid map; and $\bar{\Delta}$ is the average travel time of $\Delta_1^{theo}, \Delta_2^{theo}, \dots, \Delta_s^{theo}$.

The representation of subsequent impacts localization over a single map allowed the possibility to retrack the trajectory fallen by the block.

To compare the performance of T-B and P-B in the following estimations, the arrival times of the rockfall N.39-impact #1 were manually picked for the four stations and are shown in Figure 28, as red dashed lines. They are 50.97 s, 50.91 s, 51.06 s and 50.98 s at geophones TOR1, TOR2, TOR3 and TOR4, respectively. The velocity adopted in T-B localization is 2000 m/s after several tests modifying from 1500 m/s to 5000 m/s with 500 m/s step, that are typical values for the Maiolica formation. Comparing the results with the videos, 2000 m/s was proved to be the most reliable velocity.

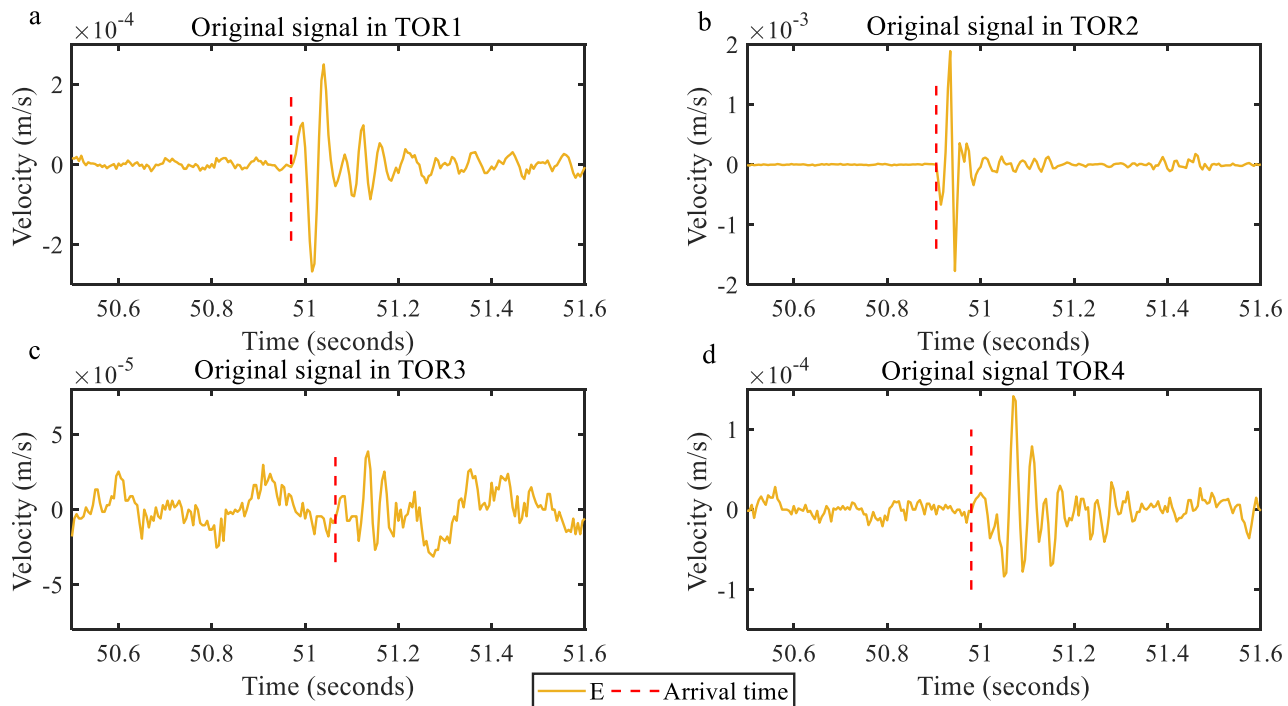


Figure 28. The arrival times of the rockfall N.39-impact #1 signal at four stations. The signals shown above are from the short period between the two red dashed lines in Figure 2.

3.3.3 Methods comparison

When comparing the estimations of the marker parameters, the P-B-SPF and P-B-E methods are quite similar, as both methods select the frequency bands on the basis of maximum energy. The P-B-SPF method does not consider the most powerful frequency bands recorded from the far stations, which probably induces differences from the near stations because the frequency content is not only influenced by the event source but also by wave propagation. The rectilinearity marker parameter denotes particle motion, and we do not find a significant relationship between rectilinearity and the real back azimuth. This finding probably means that rectilinearity is not very suitable for choosing frequency bands. Moreover, the results of marker parameter 30E, which considers the 30 highest power frequency bands, are as good as the results of the T-B method and avoids high accuracy onset time picks; therefore, it was suggested to apply P-B for rockfalls in the following rockfall trajectory reconstructions.

In the following, we discuss some applications of localizations performed by using the P-B-30E and T-B methods. In particular, we applied these methods to three typical artificially released rockfall trajectory reconstructions (N.39, N.40, and N.15), which were characterized by different sliding types and three or four impacts of each block that were clearly recorded by at least three seismic stations.

Artificial rockfall N.39 is a type of sliding rockfall in which the block slides along a gentle slope that is covered by fragmented rocks, and the seismic signal shows numerous and continuous spikes. The blue and cyan circles in Figure 29a are the positions estimated by the T-B and P-B-30E methods, respectively. The cyan circles in Figure 29b are the analysed impacts, and the grey areas indicate the analysed sections of the signal. In this case, only three impacts were clearly recorded by three seismic stations and were chosen for localization. From the results,

both T-B and P-B-30E are very precise: in particular, for impact #3, T-B is more precise than P-B-30E; thus, it is preferable to apply T-B, for which the arrival times are more distinct and can be precisely identified.

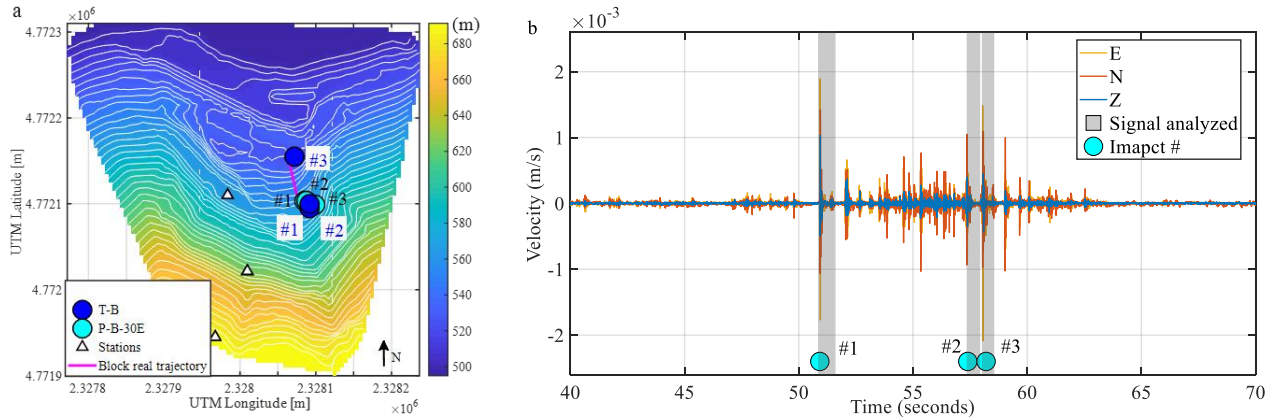


Figure 29. Rockfall N.39: a): impacts localized by T-B (in blue) and by P-B-30E (in cyan). The pink line indicates the real block trajectory as measured in situ; b): the original signal trace with the impacts highlighted. The traces are analysed via the polarization method.

Artificially released rockfall N.40 is also a sliding rockfall, but the sliding slope in this case was bare and smooth and was covered with a few fragmented rocks. Thus, the seismic signal shows only a few visible strong spikes. In this case, four impacts were selected for localization and are plotted in Figure 30. From the results, the localizations calculated by P-B-30E are very precise because all of the estimated positions are distributed along the real rockfall trajectory. In contrast to T-B, only impact #1 is precise, while the others are far from the real trajectory; the minimum error for impact #2 is 161 m, and the maximum error for impact #3 is 216 m.

The T-B accuracy difference between rockfalls N.39 and N.40 can be attributed to the difficulty in picking first-arrival times. As previously mentioned, the sampling frequency of the instrument employed was set to 200 Hz (e.g., one sample every 0.005 s), and the velocity suggested for T-B was 2,000 m/s. Therefore, the localization error caused by one sample difference is 10 m; moreover, the error for T-B will increase to 100 m when one wave length is missed at 20 Hz when picking the arrival time (i.e., in Figure 28, where the length of impact #1 determined from the furthest station, TOR3, is shorter than for the other stations).

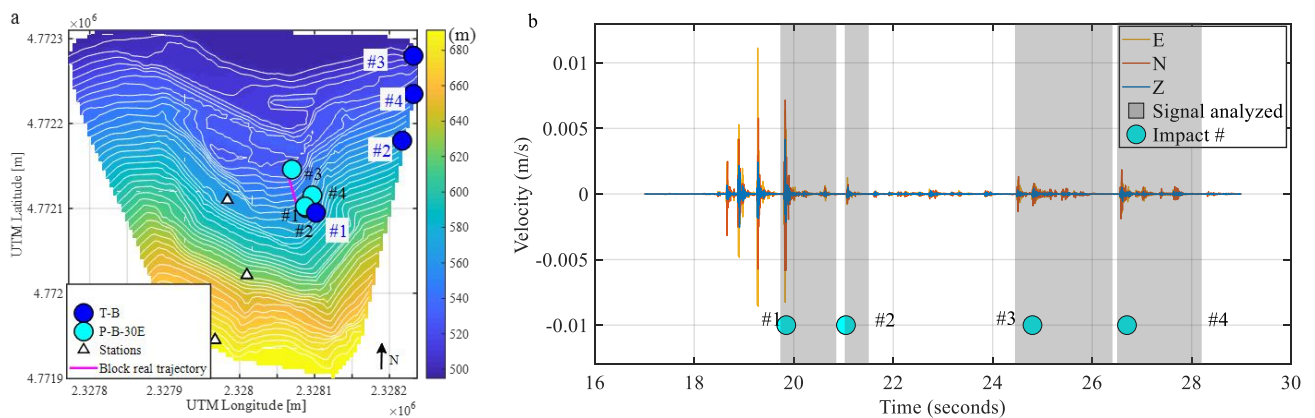


Figure 30. Rockfall N.40: a): impacts localized by T-B (in blue) and by P-B-30E (in cyan). The pink line indicates the real block trajectory as measured in situ; Panel (b): the original signal trace with the impacts highlighted. The traces are analysed with the polarization method.

c) Artificially released rockfall N.15 is a rebounding rockfall that took place on a steep slope and produced four clear impacts. Both T-B and P-B-30E successfully located four impacts on the topographic map, but the results are not good; in particular, refer to the results for P-B-30E, as shown in Figure 31. For the T-B method, the best localization result and the worst result were for impact #1 and impact #3, respectively, with localization errors of 34 m and 241 m, respectively. For the P-B-30E method, the location errors for impact #3 and impact #1 were 94 m and 184 m, respectively.

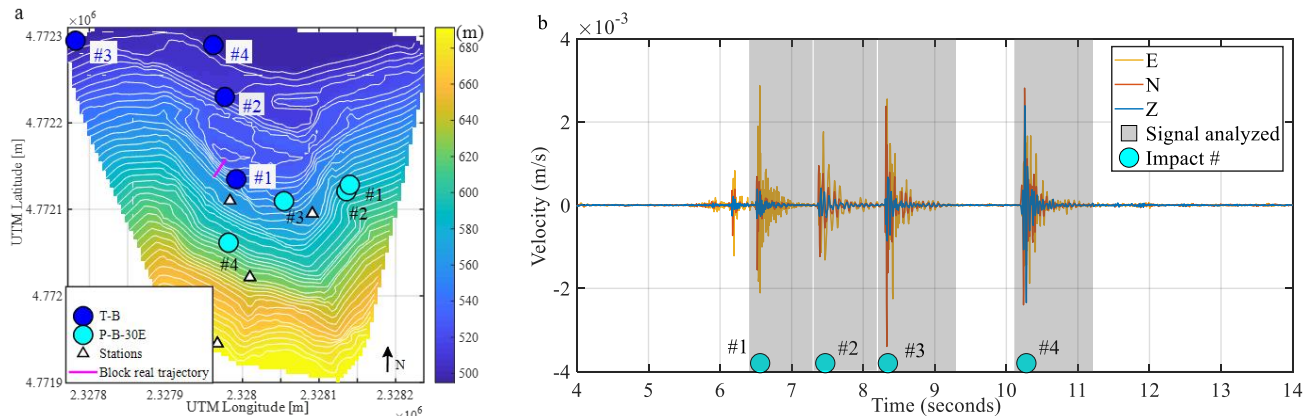


Figure 31. Rockfall N.15: a): impacts localized by T-B (in blue) and P-B-30E (in cyan). The pink line indicates the real block trajectory as measured in situ; Panel (b): the original signal trace with the impacts highlighted. The traces are analysed with the polarization method.

In the first and second cases, the localizations by P-B-30E are more stable and precise than those from T-B, given the difficulty of accurately picking arrival times by using T-B, while neither method performed very well for the third case. Moreover, when analysing the localizations estimated for all 90 released blocks in the in situ tests, we found that for all blocks released near station TOR1 (such as the third case, representing a rebounding rockfall on a steep slope with clear impacts), the P-B results are not as good as those for the blocks released near station TOR2 (as in the first and second cases), representing sliding rockfalls on gentle slopes. Unfortunately, the causes of this phenomenon are still not clear. The possible causes likely arose from the instrument installation issues, geomorphology, or some other factor and is still under study. In any case, when utilizing the worst localization results, the estimated locations with P-B-30E are still in the monitoring area and are not far from the real trajectory limits.

Furthermore, since there are still many drawbacks for this improved P-B method, additional in situ artificially released rockfall tests or a long-period monitoring case are necessary a) to evaluate the impact factors that caused the localization differences between the case of a sliding rockfall on a gentle slope and the case of a rebounding rockfall on a steep slope, b) to make analysis with more influence factors included and measured in situ, such as block falling velocity and energy, mechanical characteristics of ground material, and c) more geophones installed along falling trajectory are required to analyse the seismic attenuation and influence of geomorphology. The method presented will provide the possibility of automatically performing rockfall seismic localizations and continuous processing in an early warning system (EWS).

4. Seismic features analysis of rockfall

4.1 Artificial released rockfall test

The test area interested by the artificial rockfall test is located at the downhill portion of the quarry slope (light green area in Figure 32) and covers 15,960 m². The elevation of the slope test area ranges from 526 m to 683 m a.s.l. and its width is up to 300 m. The elevations of the blocks release locations range from 562 m to 565 m a.s.l. and the elevations of the arrival points range from 526 m to 529 m a.s.l. The dip direction of testing slope ranges from 335° to 35° (Figure 32).

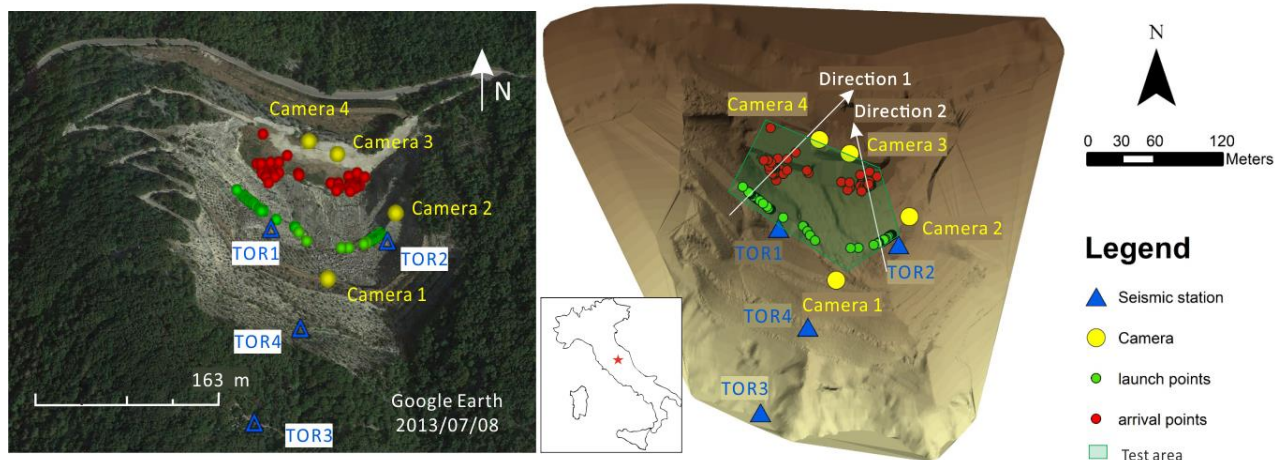


Figure 32. The outline of test site and instruments arrangement. Left: satellite photo (dated July 2013). Right: DEM of the study area. In both pictures the blue triangles indicate the positions of the tri-axial seismic velocimeters, the yellow dots of the photo cameras, while green and red dots locate the starting and ending position, respectively, of each released block. White arrows named direction 1 and direction 2 indicate the block fall directions, along steep slope and gentle slope, respectively.

The slope material consists mainly in micritic limestone belonging to the Maiolica Formation (Upper Jurassic-Lower Cretaceous) that widely outcrops in the area (Figure 33). The thickness of the formation is about 100 m and is composed by white or light grey well stratified micritic limestone layers, whose thickness ranges between 10 cm and 1 m, sometimes separated by thin clay interlayers (Intrieri et al. 2012; Lotti et al. 2018 and references within). The site is also partially covered by very heterometric debris (from pebble- to cobble-sized granular clasts, with scattered boulders, in a silty or coarse-grained sandy matrix) (Figure 33). The density of fractures and the quality of the rock mass are very variable across the area. Surveys revealed RQD values (Rock Quality Designation; Deere 1968) ranging from 20% to 90% (Graziani et al. 2009).

The dip direction and the dip of bedding planes may vary respectively from 350° to 5° and from 25° to 35°, which means that, in general, the layers dip in the same direction of the block release direction 2 (Figure 32) with a gentler angle. The dip of test direction 1 ranges from 45° to 90°, with a height difference of 38 m and steep slope; direction 2 is less steep (its dip ranges from 25° – 65°, while the height difference is 40 m) and much more debris is deposited on the talus of the slope. This also means that there are two main different kinematic modes of blocks falling down along these two directions, which are “block rebounding” (i.e., the movement mainly occurs through bouncing) and “block rolling” (whose main mechanism is rolling and sliding), generally occurring along

direction 1 and direction 2, respectively. Such modes result in different seismic features, as discussed in the next section.

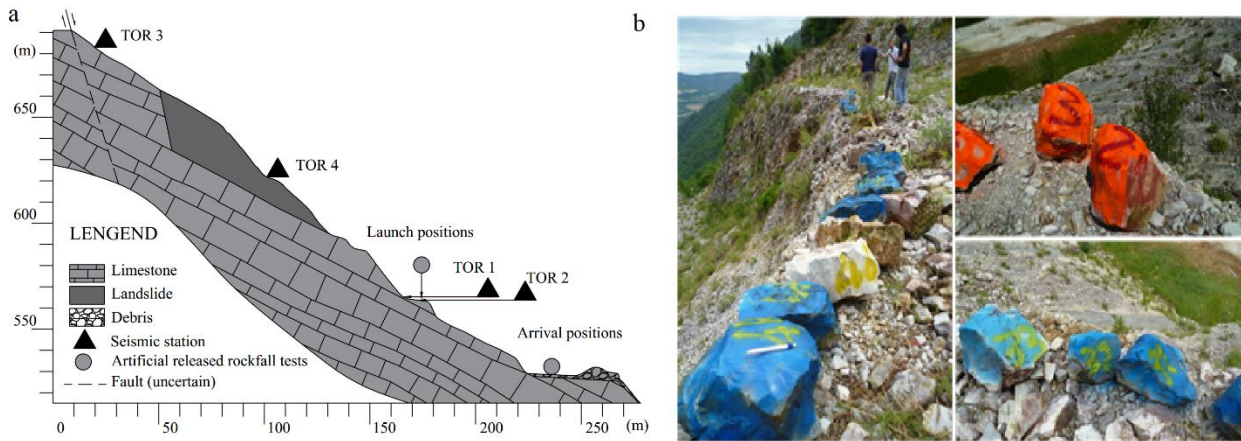


Figure 33. a) Geological profile map of the test site modified from Intrieri et al. (2012), and b) artificially released blocks painted in bright colors and numbered, used for the artificial rockfalls test (Gracchi et al. 2017).

The artificial rockfall tests were carried out in two days (June 25, 2013 and July 4, 2013). During the test, rockfalls were produced by pushing in total 90 blocks from different points of the slope (green points in Figure 32). All the blocks were collected from the quarry (the average intact rock unit weight is 26 kN/m^3 and the average uniaxial compressive strength is around 120 MPa). The size of thrown rock blocks, approximating their shape to a regular parallelepiped, ranged from a minimum of $21 \text{ cm} \times 20 \text{ cm} \times 19 \text{ cm}$ to a maximum of $105 \text{ cm} \times 58 \text{ cm} \times 39 \text{ cm}$ and all of them have been painted with bright colors (Figure 33b) to make them more recognizable in the videos. The dimensions of the blocks were chosen taking into account both the size of the blocks of past rockfalls found across the quarry, the availability of material and the maximum volume that a man can pick up and throw. The blocks were numbered to precisely relate them to their launch; launch and arrival coordinates were acquired through a GPS and integrated with geo-referenced Digital Terrain Model (DTM) in a GIS environment (Gracchi et al. 2017). Each releasing was also filmed by four high resolution cameras (two Canon EOS 600D, one Canon 660D and a Nikon D700, yellow circles Figure 32), with the aim of comparing the localization of the subsequent impacts recorded by the seismic stations with the effective trajectories travelled by the blocks.

4.2 Frequency content

4.2.1 Frequency with impacted material

In order to present the results of the analysis carried out on the whole dataset and discuss the relationship between the signal frequency and the impacted area materials, six representative rockfall events that include both kinematic modes (rebounding and rolling) were chosen. The positions of the 6 rockfalls are shown in Figure 34 and are named from N.1 to N.6. From N.1 to N.3, the rockfalls are rebounding blocks which fall down along the steeper slope of direction 1 near seismic station TOR1; from N.4 to N.6 are rolling blocks, which fall down on the gentler slope of direction 2. The volumes of the blocks respectively are 0.041 m³, 0.022 m³, 0.044 m³, 0.041 m³, 0.024 m³, 0.012 m³. In the test area the slope is constituted by the same limestone of the blocks; some areas are covered by debris, especially at the toe of benches.

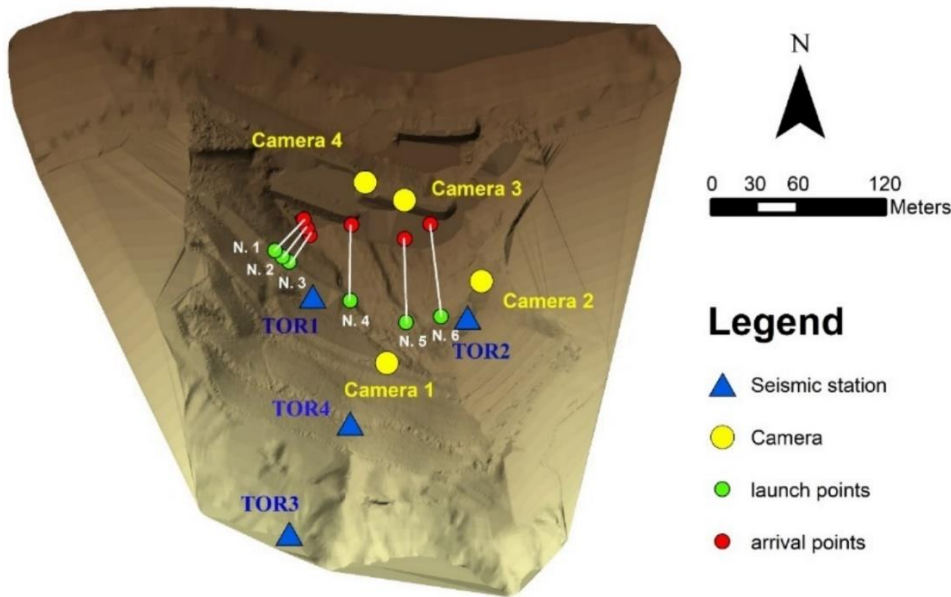


Figure 34. The distribution of six typical rockfalls selected for frequency content analysis.

To make use of the higher signal energy recorded, all the analyzed signals were chosen from station TOR1 or TOR2, E–W component, except for the signal N.6 which was analyzed using data from TOR2 N–S component. The frequency content of each impact was analyzed via the Fast Fourier Transform (FFT) and wavelet transform in MATLAB environment. First of all, the rockfalls from N.1 to N.3 are presented and discussed. The geological profiles along the trajectory of each rockfall from launch point to arrival point with the indication of the impacts positions, as reconstructed by the videos, are shown in Figure 35a. The original seismic signal traces generated by these rockfalls are shown in Figure 35b. Figure 35c is the time-frequency distribution of each rockfall obtained by wavelet transform that shows the frequency content of each impact (note that the frequency content of impact #2 is significantly lower than the other impacts). Finally, Figure 35d is the frequency content of each rockfall obtained by FFT.

Aided by the videos recorded by the four cameras the impacts are separated. As shown in Figure 35, the waveforms of the three rockfalls signal traces are well synchronized with the falling down process of the block, since each major peak corresponds to one impact. The main frequency contents (i.e., the frequencies with a high

FFTA value; refer to Section 3.1 for more information) of these three cases are very similar (Figure 35c & d), and all of them are focused on the range 10 Hz – 60 Hz and 80 Hz – 90 Hz.

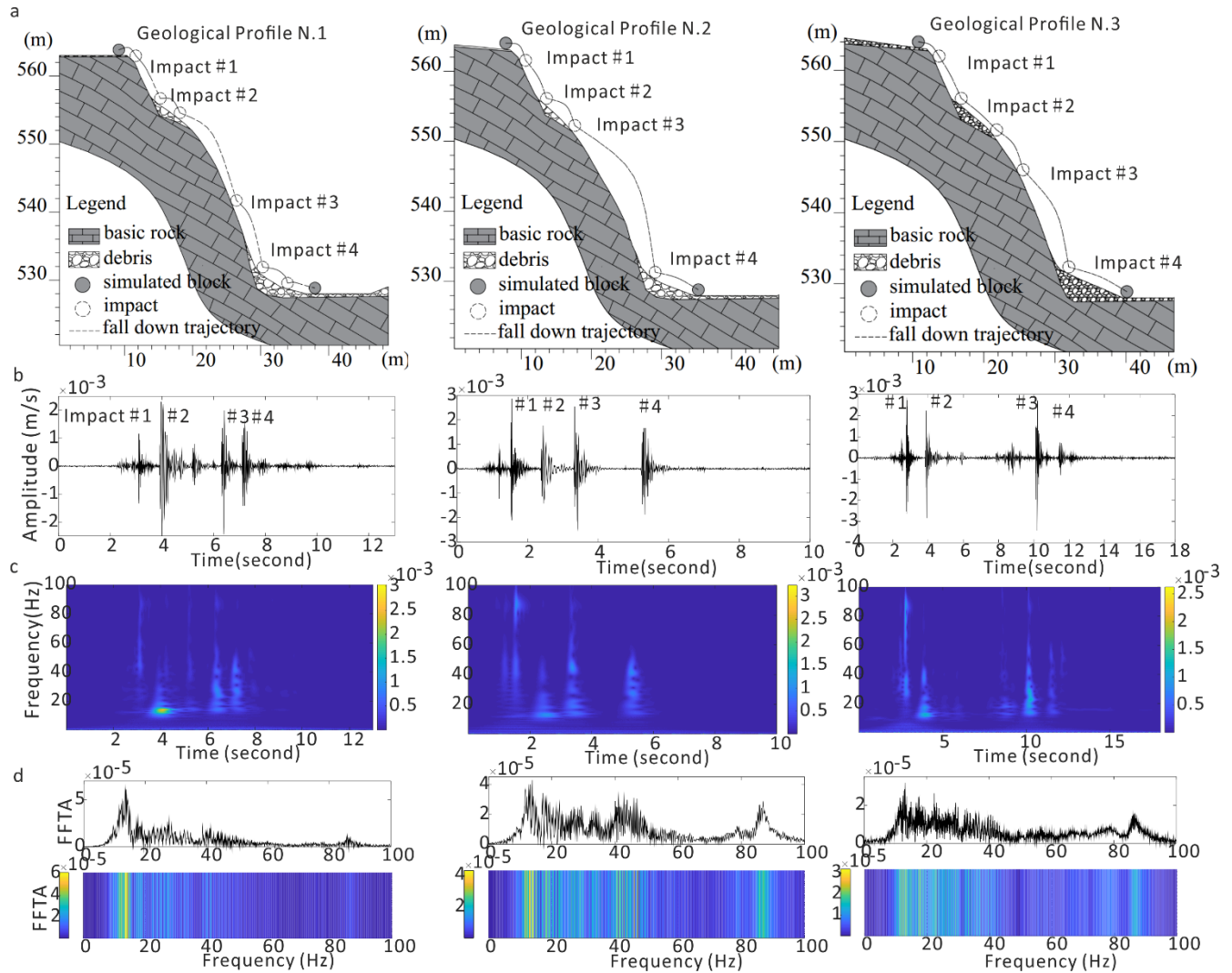


Figure 35. Results of the frequency content analysis of rockfalls N.1, N.2, N.3, respectively.

Secondly, the frequency content of the four main impacts of each rockfall (indicated in Figure 35a with Impact #1, #2, #3, and #4) are analyzed. Therefore, each seismic trace is cut that only include one short impact moment (in this case 0.4 second) (Figure 36). After this extraction, the length of each cut signal is unified (2 seconds, like condition 3) to improve the resolution of the FFT frequency analysis performed by MATLAB. At the end, the frequency content of each impact is obtained and plotted in Figure 36.

The result shows a good correlation between the signal frequency and the material of the impacted area, and from the picture, we can find: 1) the frequency content of Impact #1 (occurring on bedrock for all the three rockfalls) is wide (especially for rockfall N.1), ranging almost from 0 Hz to 100 Hz, with a focus between 80 Hz and 90 Hz; 2) the frequency content of Impact #2 (occurring on debris) is characterized by a narrow band and low frequencies, being concentrated between 10 Hz – 20 Hz; 3) the frequency content of Impact #3 (on bedrock) of the three rockfalls is, like Impact #1, very wide, ranging almost from 0 Hz to 100 Hz, with the main frequency

content focused on 10 Hz– 40 Hz and, secondarily, between 80 Hz and 90 Hz; 4) the frequency content of impact #4 (on debris) is focused on 10 Hz – 60 Hz.

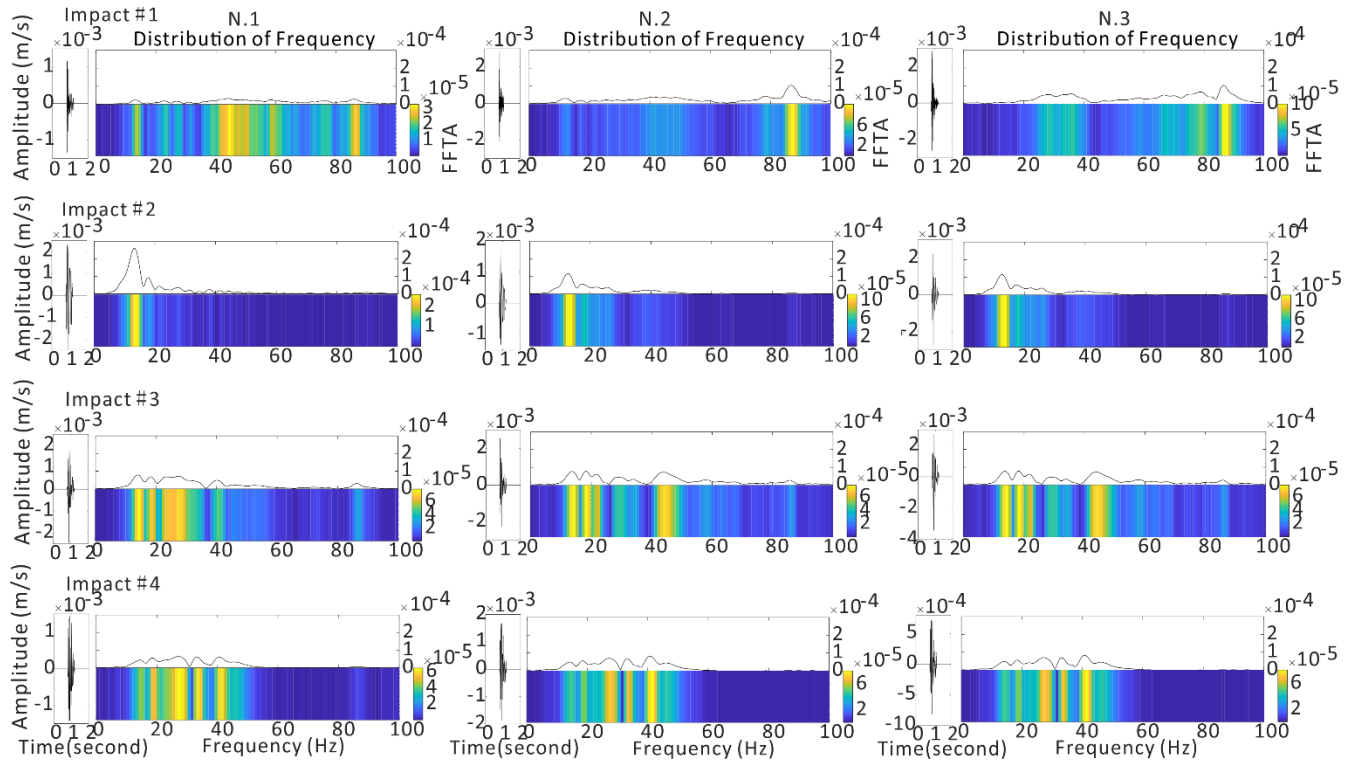


Figure 36. Frequency contents of the four impacts analyzed by FFT in a unified length 2 s.

In order to find the relationship between the frequency content and impacted material, the characteristics of the impacted material were analyzed. Results are summarized in Table 4. As shown in Figure 35a, most part of the slope along the rockfall trajectories of N.1, N.2, N.3, where Impact #1 and Impact #3 occurred, is constituted by the limestone bedrock with different weathering degrees. For Impact #1 and Impact #3, the signal trace created by an impact between two hard materials without fragmentations (Impact #1) shows frequencies content in the range of 10 Hz– 90 Hz, while the signal trace created by an impact between two hard materials with fragmentations (of both block or bedrock) or between a block and a broken up bedrock (Impact #3) usually shows lower frequency content (10 Hz – 60 Hz).

On the other hand, as visible in Figure 36, the high frequency content between 80 Hz and 90 Hz of Impact #3 is not as strong as for Impact #1, because of the distance between seismic station TOR1 and Impact #3 area is longer than that between TOR1 and Impact #1 and it is well known that the high frequency content is more easily attenuated with distance than the low frequencies content (Hibert et al. 2017a). Another possible reason is that the block was broken and fragmented at the moment of Impact #3, thus causing a change in the frequency content, and the Impact #1 is the nearest impact with monitoring station.

Debris deposits cover the toes of benches where Impact #2 and Impact #4 took place. The debris deposit on the second bench (Impact #2) is constituted by compacted soil, with a fine granulometry, less fractured and with less fragmented rocks dispersed, than those at the slope toe (Impact #4, Table 4). Therefore, the signal generated by Impact #2 has a frequency content of 10 Hz – 20 Hz. On the other hand, since the debris at the slope toe (Impact #4) is more heterometric and also comprehends finer sediments (gravel and sand sized), the impact on this kind

of material consists of many micro-impacts with different sized rock fragments, from pebble- to cobble-sized, and sand. As a result, the signal generated is more complex and produces a wider range of frequencies (10 Hz – 60 Hz) than Impact #2. The analysis of the results of the relationship between impacted material and frequency content shows that the value of frequency content is proportional to the stiffness of the impacted material in general (Table 4).

Table 4. Frequency content of different impact material of rockfall.

Impact material	Hard to hard (without fragmentation)	Hard to hard (with fragmentation)	Hard to fragmented rock (non-cemented)	Hard to soft
Typical picture				
Frequency content	10 – 90 Hz	10 – 60 Hz	10 – 60 Hz	10 – 20 Hz
Descriptions	Impact #1: both the impacting and impacted materials are hard rock, and the impact process does not cause fragmentation. Both parts are intact.	Impact #3: both the impacting and impacted materials are hard rock but the impact causes fragmentation.	Impact #4: the impacted area is consisting of different sized rock fragments and sand debris pile and softer than the block.	Impact #2: the impacted area is soft soil with few rock fragments scattered on the surface.

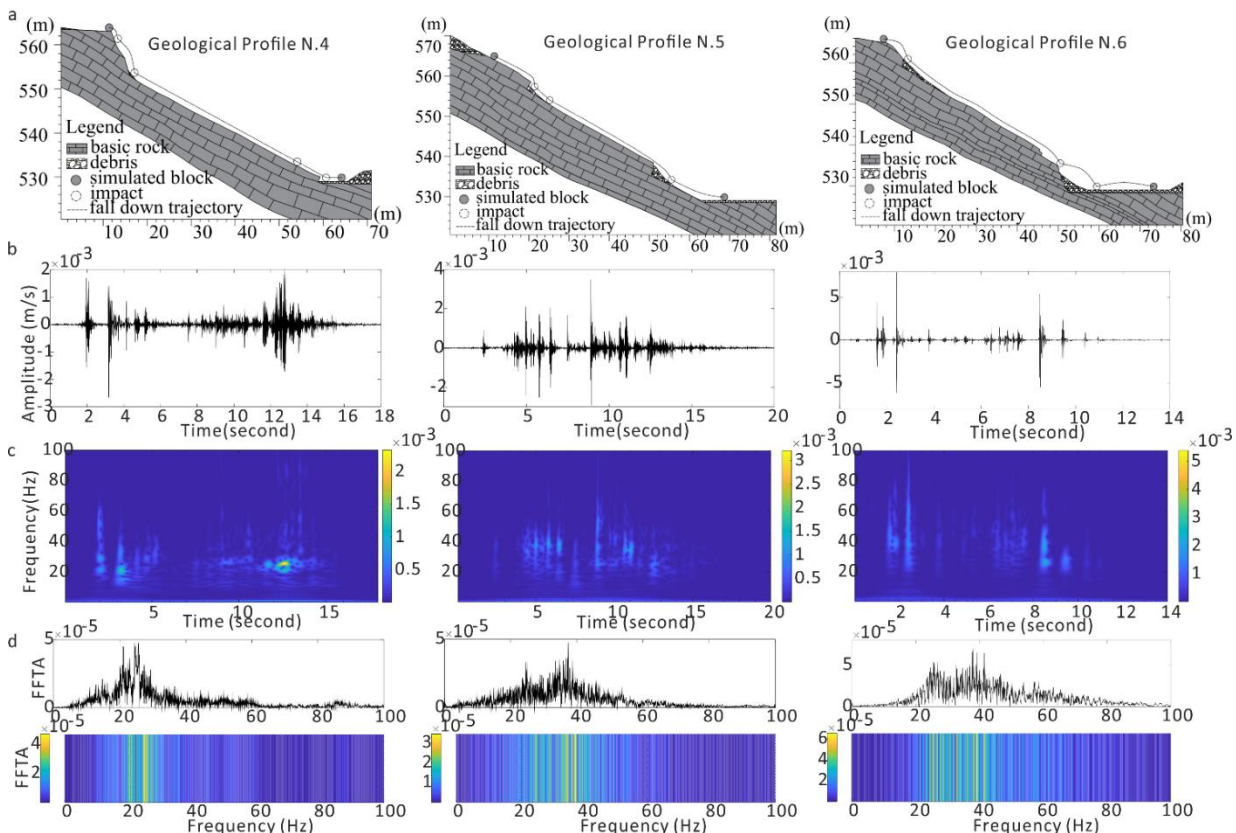


Figure 37. Results of the frequency content analysis of rockfalls N.4, N.5, N.6.

To evaluate the relationship between frequency content and rock falling trajectory, the same analysis was performed for rockfalls N.4, N.5, N.6 (rolling blocks) and the results are plotted in Figure 37. As in Figure 35, Figure 37a shows the geological profiles along the rockfall trajectories, with the reconstruction of the rockfalls paths, Figure 37b the original seismic signal generated by each rockfall, Figure 37c the time-frequency distribution of each rockfall obtained with wavelet transform, showing the frequency content of each impact, Figure 37d is the frequency content of each rockfall obtained with FFT. Also in these cases, the benches are covered by debris, and the frequency contents of impacts on the debris focused on 10 – 60 Hz. Figure 37b clearly shows that the signal created by rolling or sliding rocks is weaker than the rebounding impacts signal, and that the rolling seemingly consists of many micro-impacts. Therefore, the “rockfall rolling” frequency contents are also depending on the frequency content of each impact as in case of “rockfall rebounding” and rolling or sliding frequencies are concentrated between 10 Hz and 60 Hz, similarly to the Impact #4 in case of rebounding blocks.

4.2.2 Frequency with distance

In order to analyze the relation between the frequency and the impacted area distance, the rebounding rockfalls N.1, N.2, N.3 were chosen, since they include a complete frequency content from 10 Hz to 100 Hz (especially high frequencies from 20 Hz to 100 Hz). The distance between the launch point and the receiving seismic stations TOR1 (the nearest), TOR2, TOR3 (the farthest), TOR4 are shown in Table 5.

Seismic station TOR1 is the nearest station at all the three launch points, so the frequency contents are the widest and focused on 10 Hz – 60 Hz and 80 Hz – 90 Hz, and the FFTA values of TOR1 are the biggest in all the stations (Figure 38). The main frequencies of TOR2 and TOR4 stations focus on 10 Hz – 60 Hz, and the FFTA values are lower than TOR1. That is because of the attenuation of the highest frequency content (80 Hz – 90 Hz) and FFTA values with the increasing distance. In the farthest station TOR3, the main frequency contents are the lowest, focused on 0 Hz – 20 Hz and the frequency of the highest FFTA value are near 10 Hz. As expected, the high frequencies contents are easily attenuated in the propagation and the frequency content range is inversely proportional to distance, like in this case, where the frequency content between 80 Hz and 90 Hz is damped in only 100 m distance from TOR1 to TOR2. This phenomenon of high frequency content attenuation is significantly for rockfall event.

Table 5. The distance (m) between rockfall launch points and each seismic station

	TOR1	TOR2	TOR3	TOR4
N.1	41.0	141.6	196.9	130.9
N.2	34.5	135.3	192.4	125.0
N.3	28.9	129.7	188.8	120.0

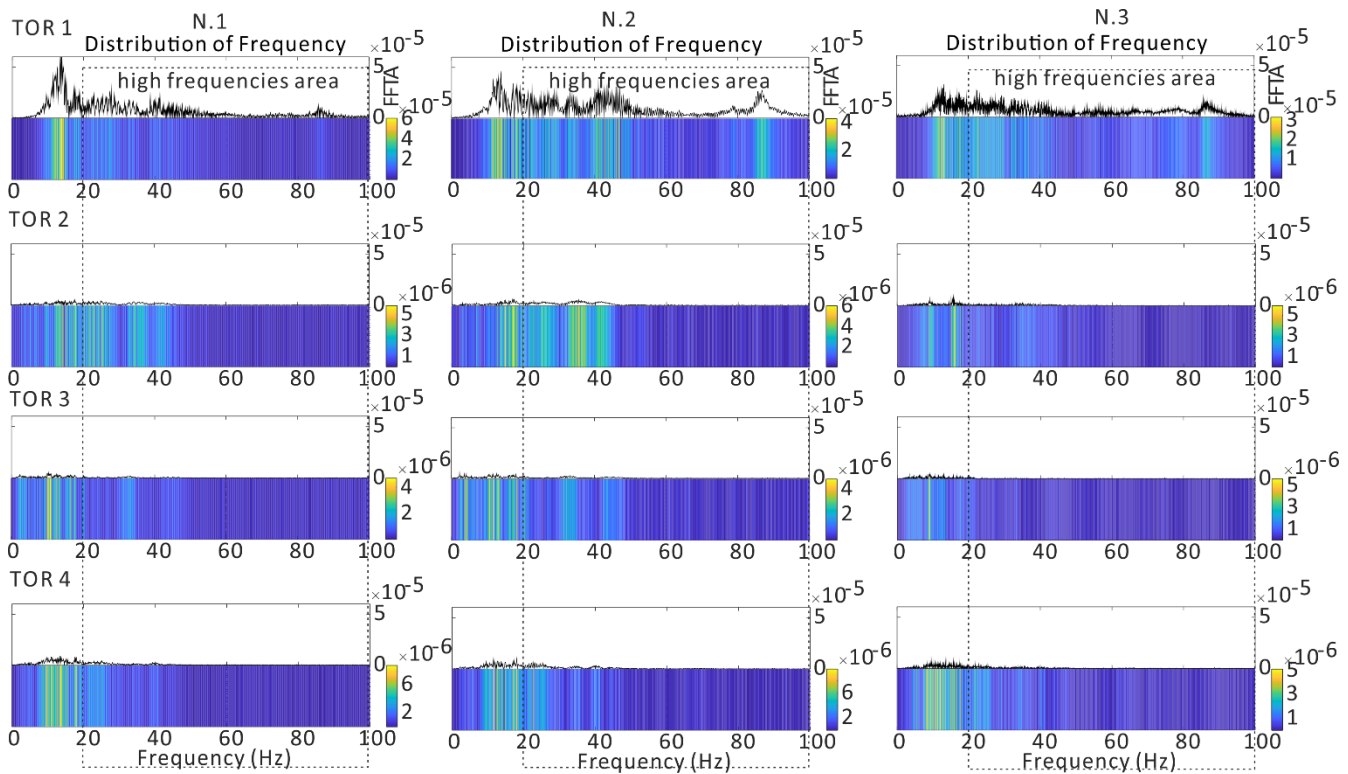


Figure 38. Frequency contents of signal traces of rockfalls N.1, N.2, and N.3 in four seismic stations, TOR1, TOR2, TOR3, and TOR4. The dashed square indicates the high frequencies area.

4.2.3 Maximum frequency

After the analysis of the relationships between frequency and impacted material and between frequency and distance, to improve the accuracy of rockfall event automatic detection and classification, the maximum frequency of rockfall signal traces should be analyzed. The maximum frequency is defined as the frequency with the biggest FFTA value, that means the signal of the maximum frequency generated by rockfall is the most powerful frequency band. The maximum frequency of each rockfall signal (1080 totally) from the four seismic stations has been calculated and the distribution of the main frequencies is plotted in Figure 39.

The results show that the maximum frequency of rockfall is focused on 3 – 5 Hz, 10 – 60 Hz and 80 – 90 Hz. The frequency content between 3 and 5 Hz of most signals are from the farthest seismic station TOR3 and can be neglected, due to the high attenuation, and we can find the difference from an example of one rockfall signals recorded by nearest station TOR2 and the farthest station TOR3, that is shown in Figure 40: the maximum frequency detected by the nearest seismic station TOR2 is 38 Hz, while the maximum frequency recorded by the farthest seismic station TOR3 is only 3 Hz, also characterized by a very low amplitude (at the limit of detectability). Beside the reason of long-distance attenuation that result in 3 – 5 Hz of maximum frequency, the natural frequency of geophone of 4.5 Hz is another possible problem, that could result a resonance of geophone.

Therefore, in further analysis and classification, the maximum frequency of rockfall could be set higher than 10 Hz, or even than 20 Hz to perform a safer recognition. The feature of maximum frequency indicates the frequency content of one event and represents the most powerful frequency band, so it is important for an event recognition and events classification.

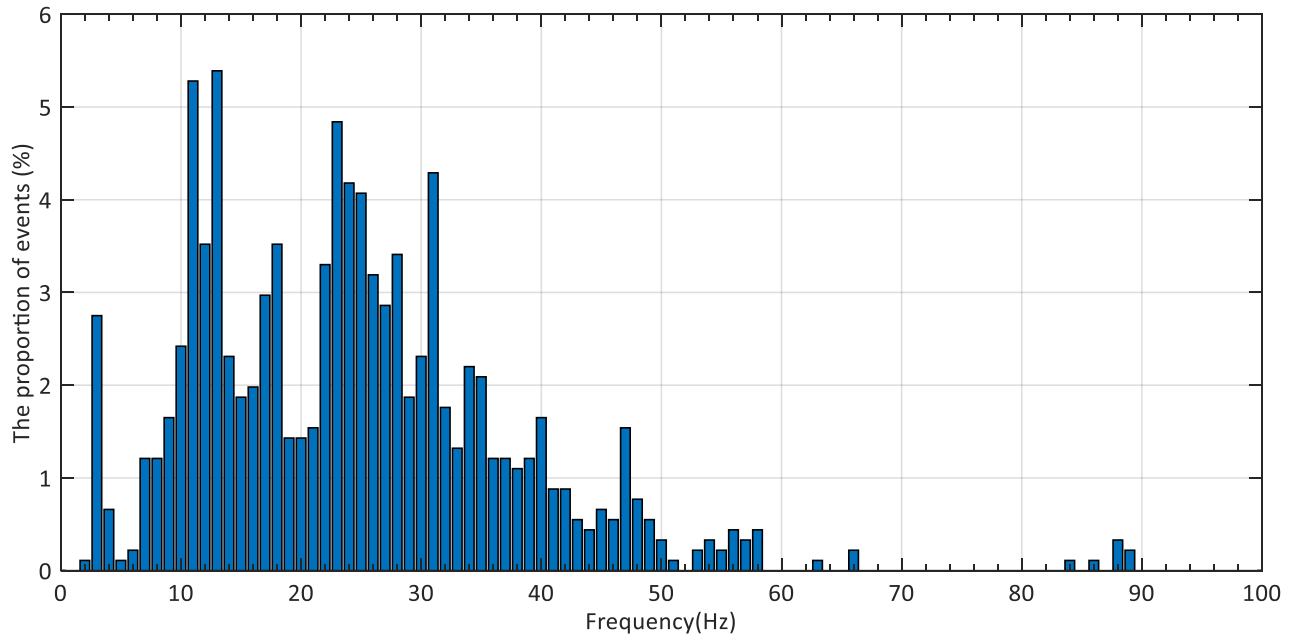


Figure 39. The distribution of maximum frequency of the 90 rockfalls produced during the test. The y-axis indicates the percentage of events, and x-axis the maximum frequency of signals.

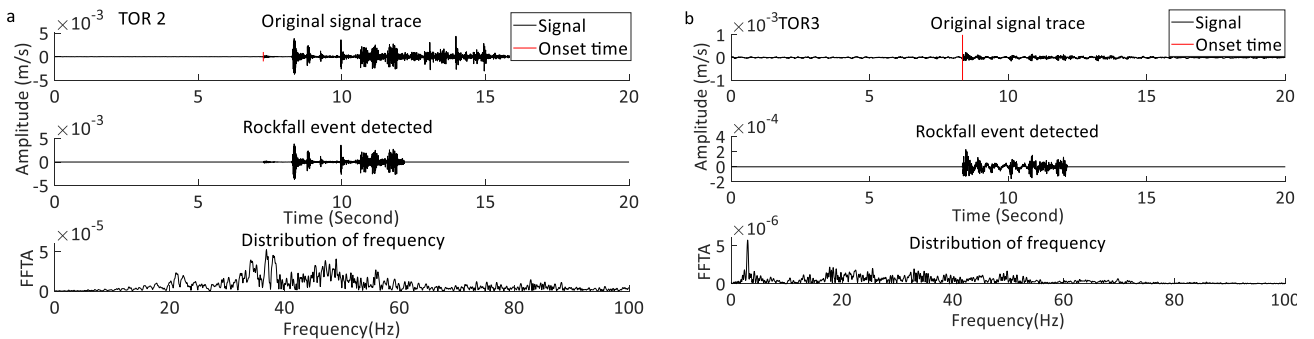


Figure 40. a) one signal trace and frequency content of one rockfall event recorded by the nearest seismic station TOR2, E – W component; b) the signal trace recorded by the farthest seismic station TOR3, E – W component.

4.3 Amplitude

4.3.1 Amplitude ratio

The amplitude of a signal trace (i.e., ground velocity) is defined to indicate the energy of the signal generated by the rockfall, and the maximum amplitude is the most powerful part of the whole signal. Considering that the higher frequencies are more easily attenuated in wave propagation, and that the signal generated by rockfall includes a large part of high frequencies, amplitude ratio was proposed as a key parameter to recognize rockfall event from noise or other events like earthquakes. The amplitude ratio (R_a) here defined in Equation 39 is the ratio between the maximum amplitude of one event signal recorded by two different seismic stations A_{m1} , A_{m2} , which always represent the station recording the higher and the lower amplitude, respectively (this is also discussed in section 5.2.4):

$$R_a = \frac{A_{m1}}{A_{m2}} \quad (39)$$

As discussed in section 4.2.2, a signal consisting of higher frequency content is more easily attenuated with distance increasing, and the affection generated by different geomechanical characteristics of the propagation path, so the amplitudes recorded by two far away stations would be very different, resulting in a high R_a . In this study, the signal received by the farthest seismic station TOR3 has a lower amplitude than that received by the nearest seismic station TOR1 or TOR2 (i.e., $A_{m1} \gg A_{m2}$), moreover, the value of R_a is also higher in the signal containing high frequencies compared with the signal mainly consisting in low frequencies (e.g., earthquake). For most earthquakes, due to the far epicenter, deep focus and the small size of rockfall monitoring network, there is no big difference between the signals recorded at different stations, therefore, R_a is typically lower than other seismic events. Consequently, we can find the feature of R_a is a good parameter to distinguish rockfalls from earthquakes.

During the seven-months continuous monitoring campaign, there were many earthquake events detected by our monitoring network, referred to the INGV earthquake catalog (<http://cnt.rm.ingv.it/>). Among these, twenty-three earthquakes clearly recorded are selected for discussion. The distances of the twenty-three earthquakes between the epicenters and Torgiovanetto range from 8 km to 78 km, and the average distance is 25 km, and the average hypocenter depth is about 10 km. The amplitude ratios of the whole artificial rockfall dataset (90 events) are calculated as well as the selected earthquakes. The difference between the two kinds of event and results are plotted in Figure 41. In this figure the positions of TOR1 and TOR2 are also shown in the x-axis (the dashed square below x-axis) and the earthquakes are grouped near TOR1 without the epicenter distance.

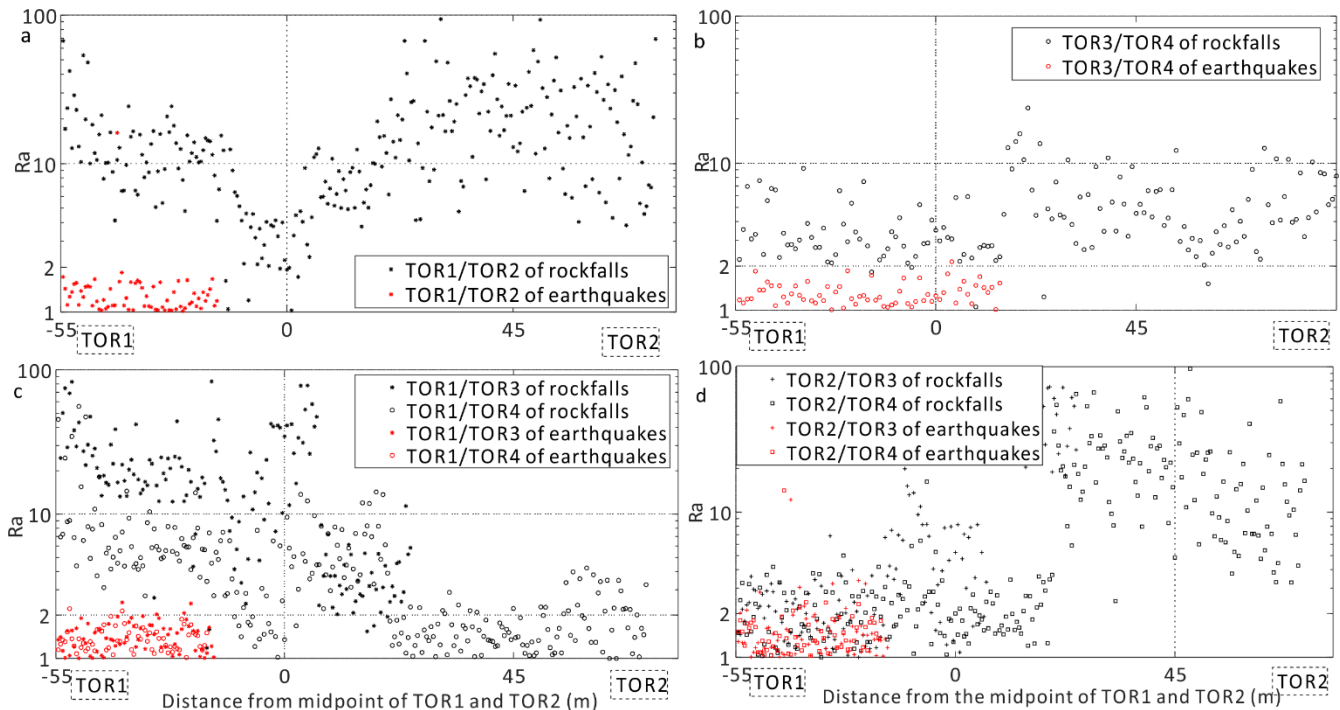


Figure 41. The amplitude ratios of artificial rockfalls and earthquakes between different seismic station. The black points are rockfalls, and the red points are earthquakes. The word “TOR1” and “TOR2” in dashed square below x-axis show the relative positions with rockfall launch positions (for example, the rockfall position of the sample on the left was located near TOR1).

In Figure 41a, the amplitude ratios of artificial rockfalls and earthquakes between TOR1/TOR2 (or TOR2/TOR1, because the launch position of artificial rockfalls were distributed along the line TOR1-TOR2) is shown. In this graph, the amplitude ratio near TOR2 is bigger than that of TOR1 for the launch positions near TOR2. The

amplitude ratio of 22 earthquakes are less than 2, and only for one earthquake is bigger than 2, while for almost all rockfall amplitude ratio is bigger than 2. In Figure 41b, valid for TOR4/TOR3, since both the position of TOR3 and TOR4 are far from the launch positions and the distances are never the same, almost all the R_a values of rockfall events are higher than 2, even for the rockfalls located between TOR1 and TOR2. In Figure 41c, the amplitude ratios of TOR1/TOR3 and TOR1/TOR4 of the rockfalls that are located near TOR1 are higher than 2 (i.e., higher than the ratio of earthquakes), but when the launch position of the rockfalls moves toward TOR2, the distances of the launch position from TOR1 and TOR4 are increasingly similar and the signal attenuation is more or less of the same degree, therefore, the values of R_a decreased until less than 2. The same behavior is visible in Figure 41d, where the ratios of TOR2/TOR3 and TOR2/TOR4 are represented.

From the results of R_a , the value R_a of rockfall is usually higher than 2 when the distance between the location of rockfall and two seismic stations, respectively, is not equal, while the R_a value of most earthquakes is often smaller than 2.

To evaluate the amplitude ratio variation in the whole dataset of 90 rockfalls and 23 selected earthquakes, the mean values and the standard deviation (STD) are computed. The results are shown in Table 6. The mean R_a of 23 earthquakes among all the seismic stations is very stable (i.e., low STD values) regardless of the distance from the hypocenters, with a value varying from 1.31 to 1.68. The rockfalls mean R_a as well as the STD are not stable, and all the mean values are bigger than 2 and higher than those of the earthquake.

Table 6. The amplitude ratio (R_a) mean value and standard deviation (STD) of rockfalls and earthquakes. For each couple of station their relative distance in meters is indicated.

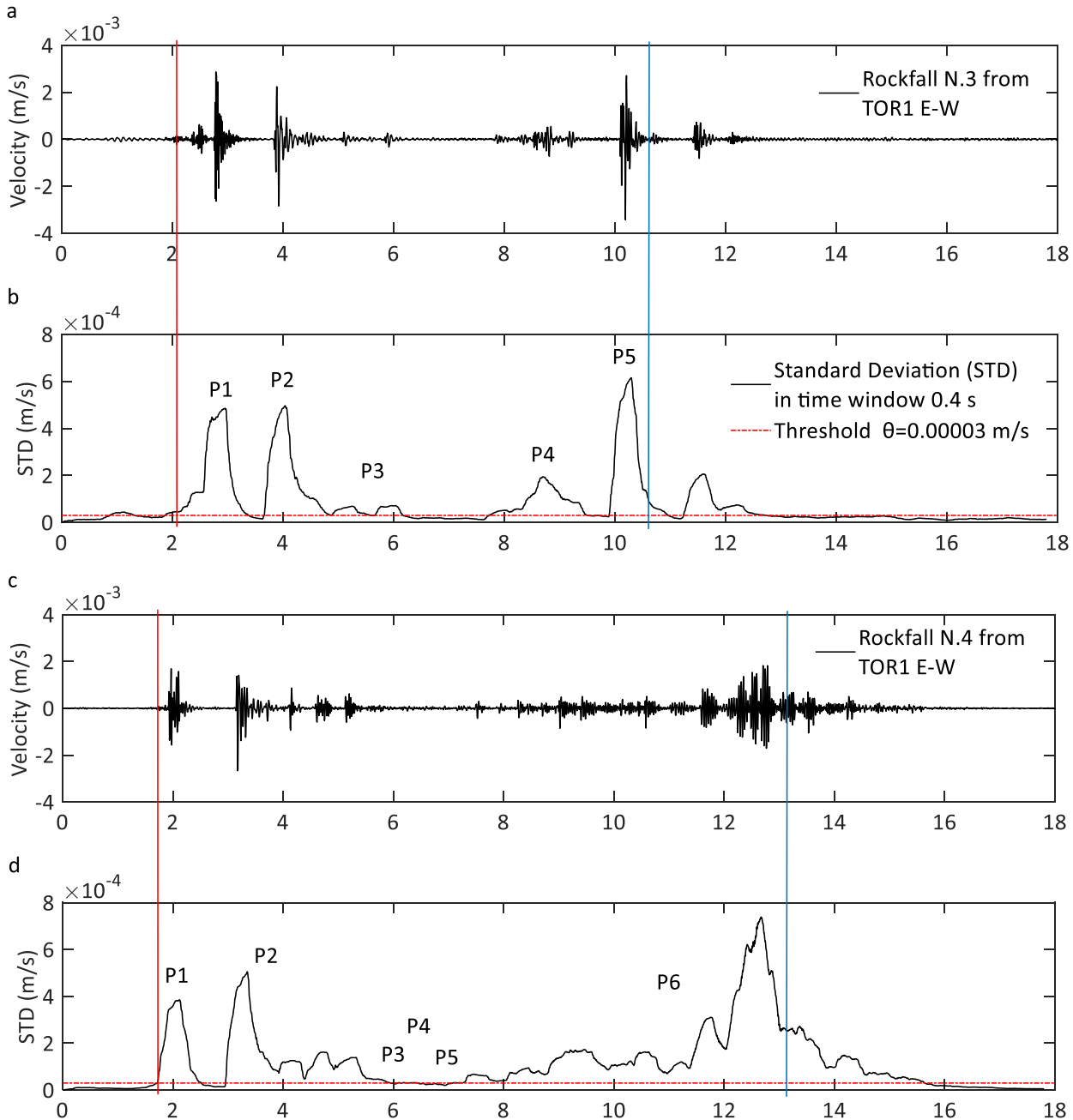
R_a	TOR1/TOR2 (109 m)	TOR1/TOR3 (166 m)	TOR1/TOR4 (92 m)	TOR2/TOR3 (195 m)	TOR2/TOR4 (110 m)	TOR4/TOR3 (88 m)
Rockfalls mean	16.49	20.31	5.14	22.16	10.740	6.50
Rockfalls STD	15.12	20.12	9.58	61.24	14.60	19.90
Earthquake mean value	1.50	1.44	1.38	1.68	1.64	1.31
Earthquake STD	1.80	0.34	0.26	1.39	1.60	0.24

4.3.2 Waveform-peaks

The falling down process of a rockfall generally consists of a series of impacts and a period of rolling. Each impact generates an abrupt peak in the seismic signal trace. Waveform-peaks is defined as the number of peaks in waveform of the analyzed trace. In other words, in this study, the waveform-peaks is calculated as the number of periods that the standard deviation (computed in a sliding window with a 0.4 s length, that was chosen correspond to the minimum duration of one microseismic event) overcomes a threshold ($\theta = 0.00003$ m/s). The threshold is set equal to the minimum amplitude of the artificial rockfall detected by one of the four seismic stations (i.e., the minimum sensitivity of STA/LTA method, with initial parameters setting). In this way, for further analysis (i.e., the analysis of the whole seven-month monitoring period), it is expected that all the detected rockfall events will have at least one waveform-peak with an impact energy higher than the minimum energy of rockfall in the test. It must be noted that the imposed threshold is strictly related to the test conditions, i.e., the released blocks dimensions, and is not able to detect small rockfall. The energy of impact, in fact, and therefore the amplitude of seismic signals, are strictly related with the falling block dimensions. Choosing to throw blocks with a volume range of 0.008 m³- 0.2 m³, we decided to neglect the effects of smaller and/or bigger blocks.

Nevertheless, the influence of ignoring the small blocks is negligible, since in seismic rockfall monitoring and rockfall hazard assessment, there is no interest in events able to mobilize only small volumes of rock.

Example of waveform-peaks calculation of rockfalls N.3, 4 and of an earthquake is plotted in Figure 42. In the artificial rockfall test, also in the events classified as “rolling block” category, all the peaks in signal trace are related to separated impacts, because a number of short free falls occurs during the movement, and eventually the signal trace consists of several discrete signals (Figure 35, Figure 37, Figure 42). This can be a great difference between rockfall and earthquake that shows just one peak (P1 in Figure 42f).



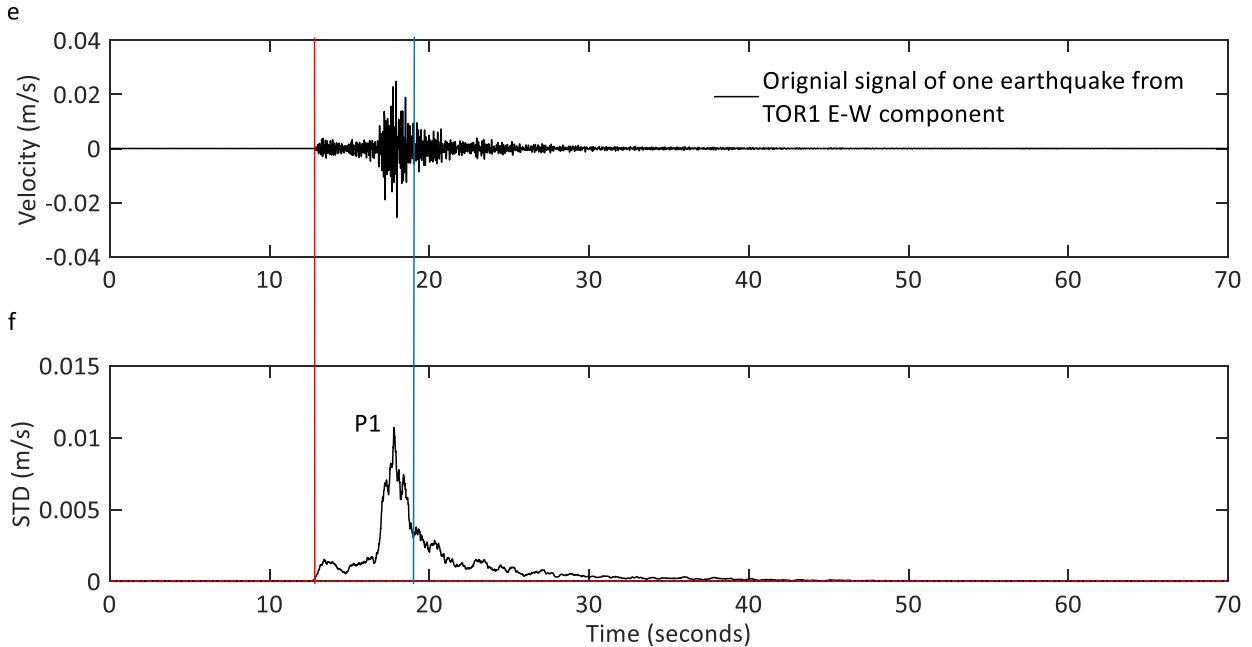


Figure 42. a) Rockfall N.3 original signal trace of TOR1 E-W component and b) its curve of amplitude standard deviation in sliding time window 0.4 s, where P1, P2, etc. are the peaks detected; c) Rockfall N.4: original signal trace of TOR1 E-W component and d) its curve of amplitude standard deviation in sliding time window 0.4 s, where P1, P2, etc. are the peaks detected, and P3, P4 and P5 are generated by small movements that not show significantly in signal trace; e) an earthquake original signal trace of TOR1 E-W component and f) its curve of amplitude standard deviation in sliding time window 0.4 s, where only one peak (P1) is detected. Vertical red and blue lines in all figures indicate the start and ending time, respectively, of the STA/LTA analysis (more detail information in section 3.2.1).

To determine the differences in waveform-peaks of rockfall and earthquakes, the number of waveform-peaks of each event (rebounding blocks, rolling blocks, earthquakes) are counted and plotted in Figure 43. The result suggests that: i) more than 87% of rockfall events include more than 2 peaks, while more than 66% earthquake events only one peak; ii) the 13% of rockfall events have only one peak and mostly come from a) seismic station TOR3 (because the signals so weak due to the distance that they are barely detected), or from b) the nearest seismic station (because the signals are so strong that the amplitudes of all samples are over the threshold). Note that, in case of rockfall, the number of peaks sensibly depends on the topography of the site. This means that, even though the falling blocks actually hit the ground more than once, sometimes the energy of the rockfall is too high or too small compared to the waveform-peaks detection threshold, so only one waveform-peak is detected.

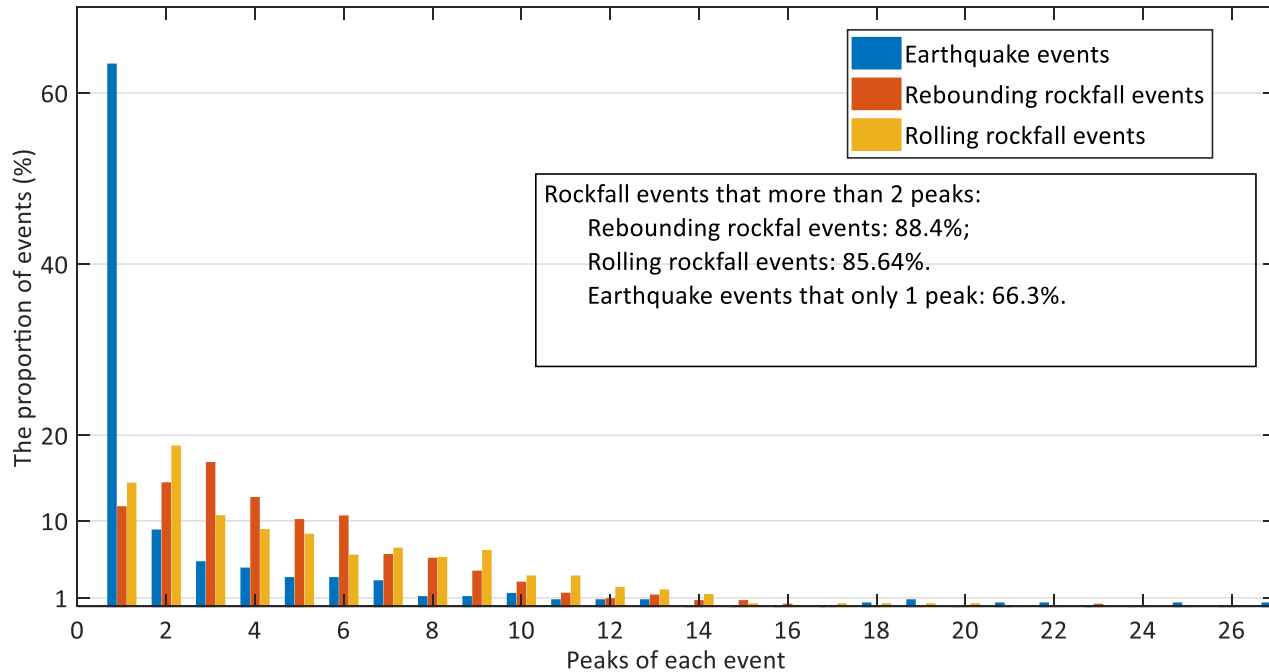


Figure 43. The percentage of events distributed in the number of waveform-peaks.

As a result, at Torgiovannetto test site most rockfalls produced two or (secondarily) three impacts, but from Figure 43 it is also possible to note that 13% of rockfall events include only one peak. For the waveform-peaks of earthquakes, some events included more than 18 peaks caused by the low energy, long duration of P waves period and post-earthquake phenomena.

Anyway, there is a significant difference of waveform between earthquake and rockfall, and the method used in this study to calculate waveform-peaks is very useful to detect such difference.

4.4 Duration

The duration of a rockfall event is another very important parameter to recognize and distinguish it from other events. In the Torgiovannetto test the duration of artificial rockfalls usually ranged from 6 s to 12 s. Like for the waveform-peaks, the duration also depends on the specific topographical conditions of the site (mainly the length and gradient of the slope), and the distance between seismic station and rockfall location. However, once calibrated precisely, this feature can be a good indicator to correctly interpret a seismic signal.

In this study, the duration of an event is defined as the time elapsed from the first sample triggered by the threshold $STA/LTA=2$ (for more information on the seismic event detection method, STA/LTA , see Allen 1982 and Trnkoczy 1998) to the last sample triggered by the threshold $STA/LTA=4$. The calculation method to define the rockfall N.3 duration is plotted in Figure 44. The triggered duration should be shorter than the real duration, since the principle of STA/LTA detection method.

We calculated the durations of the whole artificial rockfall dataset and plotted them vs the signal amplitude, all the points clustered per seismic station (Figure 45), because of the difference of energy of the signal recorded by each station.

Given the length of the short window of the STA/LTA set in this study is equal to 0.4 s (80 samples), considering the duration of a single impact, the minimum duration of rockfall event is 0.4 s, and the duration mean value is 4.1 s. More than 98% of the rockfall events lasts less than 12 s, and more than 91% at least 1 s.

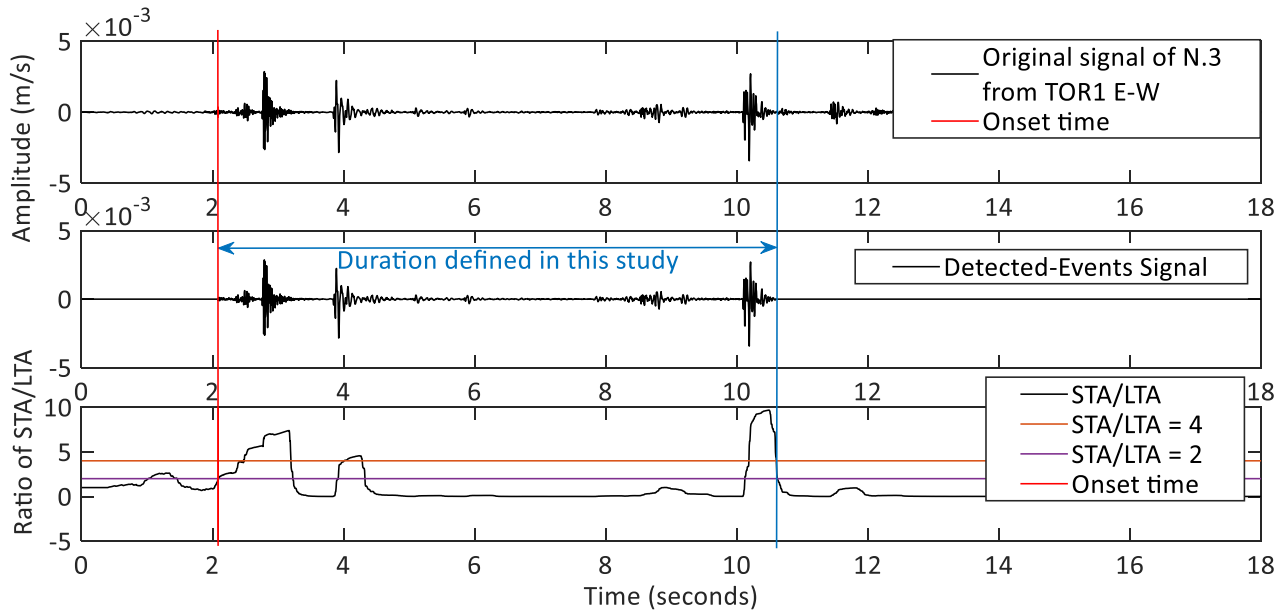


Figure 44. The duration of N.3 rockfall event. The time elapsed between the vertical red line and the vertical blue line is calculated from the first sample triggered by STA = 2 and the last sample triggered by STA = 4, respectively.

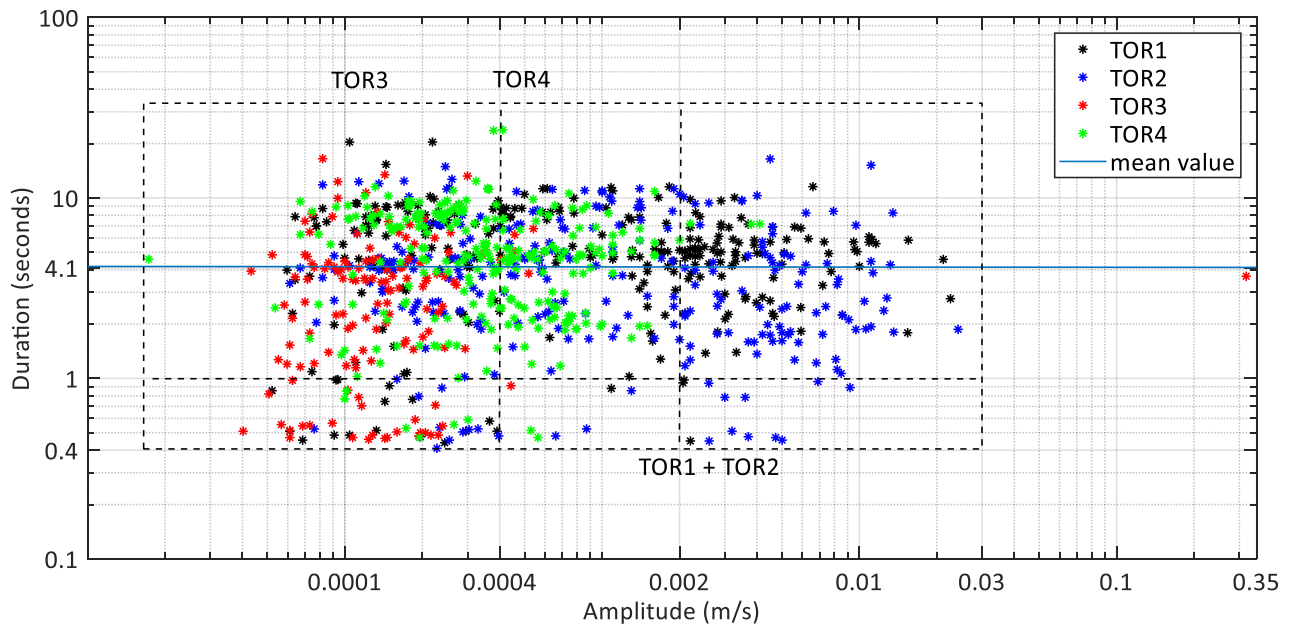


Figure 45. The distribution of duration vs signal amplitude (velocity) of each seismic station with different colors.

4.5 Conclusions

An artificial rockfall test was performed in the former quarry of Torgiovanetto by launching 90 limestone blocks down the slope, recording the related seismic signals and shooting the fall down. This study is the first step of a wider project that aims to calibrate an algorithm, useful in the seismic rockfall monitoring, for automatic rockfall

event detection and classification. The experiment produced interesting results to better understand the seismic features of rockfalls, in terms of frequency, amplitude, seismic waveform and duration of the signal.

Moreover, the results can also be usefully employed in rockfall trajectory and location studies and can be summarized as follows:

- a) the frequency content of rockfall impact has a strong relationship with the impacted materials (usually it is proportional to the stiffness);
- b) high frequency contents as well as the rockfall R_a are more easily attenuated in the propagation (almost in an inverse proportion to distance) and almost not detected if the distance between the event and the seismic station is more than 200 m (e.g., from TOR3 to the events near TOR2) for rockfall events, since the intrinsic limitations of the employed array;
- c) the frequency content of artificial rockfall is mostly focused on 10 Hz – 60 Hz and 80 Hz – 90 Hz;
- d) the rockfall R_a value is proportional to the distance source-receiver and higher than 2, while earthquake R_a is lower than 2;
- e) the earthquake and rockfall seismic waveforms look completely different (85% of rockfall events include more than 2 peaks, while more than 66% earthquake events have only one peak);
- f) the artificial single block duration ranged from 1 s to 12 s.

The obtained results show a qualitative relationship between seismic features (frequency content, amplitude, waveform, and duration) and local characteristics (geological material, geomorphology, topography). Nevertheless, there are many factors influencing the seismic wave propagation and attenuation, like formation lithology, rock integrity, and topography, that have to be taken into account to obtain a more quantitative relation. Therefore, the influence of elevation could not be neglected, as well as the relationship between frequency and impact materials could be studied adding data on the block's velocity, the lithological characteristic and the physical condition of the impact ground. Moreover, the site-dependent frequency attenuation could be studied by means of ad hoc in situ test.

In general, the R_a parameter and the waveform-peaks analysis are proven to be significant and useful to separate a rockfall event from an earthquake, even though the first parameter is strictly related to the implemented seismic monitoring array, while the second can fail when there are weak earthquakes, or the detected earthquake energy is comparable to that of a rockfall. Therefore, wider studies are needed.

Finally, also the event duration has been proven to be an important parameter to identify rockfall, even if it mostly depends on the local geomorphology and it is difficult to calculate the real length from seismic signal trace automatically. In this study, in fact, the duration of detected event was defined as the length of triggered samples by STA/LTA threshold, that is shorter than the real duration, since the last part of signal trace after the maximum energy sample was not triggered by STA/LTA length. A solution could be to integrate data from multiple seismic stations.

The detail artificial rockfall seismic studies would be helpful for the subsequent seismic event classification and possible early warning study.

5. DESTRO: joint detection and classification of rockfall in seismic monitoring

DESTRO (DEtection and STorage of ROckfall program) is specially designed for rockfall hazard monitoring but combined with earthquake detection. A Graphical User Interface (GUI) is designed in MATLAB 2017b (Figure 46) for joint seismic event detection, classification, and event spectrogram re-checking, and the DESTRO code package consists of fifteen main analysis functions ad hoc and four monitoring data format transform functions written by Peng (2018). Moreover, the event-types, onset-time, and all the parameters of key and complementary features are provided as output.

Mainly, the parameters that can be set are divided into five phases: i) choosing input monitoring data (in this case, the name of the input data file consists of year, month, day, monitoring period, station, and component, e.g., 2035.07.08-18.00.01.TOR2.SHETG.SAC), four monitoring periods (00, 06, 12, 18) per day are set to separate the daily data in four time windows that limit the file size in this case); ii) initializing all parameters and choosing a frequency filter if necessary (in case of some instrument problems or permanent environmental noise); iii) choosing the seismic stations and components you want to include in analysis; iv) choosing the event-types of interest: the user can choose to output multiple event-types (from ET_i to ET_j) or even only one single event-type ($ET_i = ET_j$); and v) rechecking the event spectrogram with event-type (ET) and serial-number of that event ($NUMevent$) in output file.

In this section, the design algorithm and theories of DESTRO are introduced, that’s about seismic event detection, seismic features definition and classifiers designing in seismic event classification.

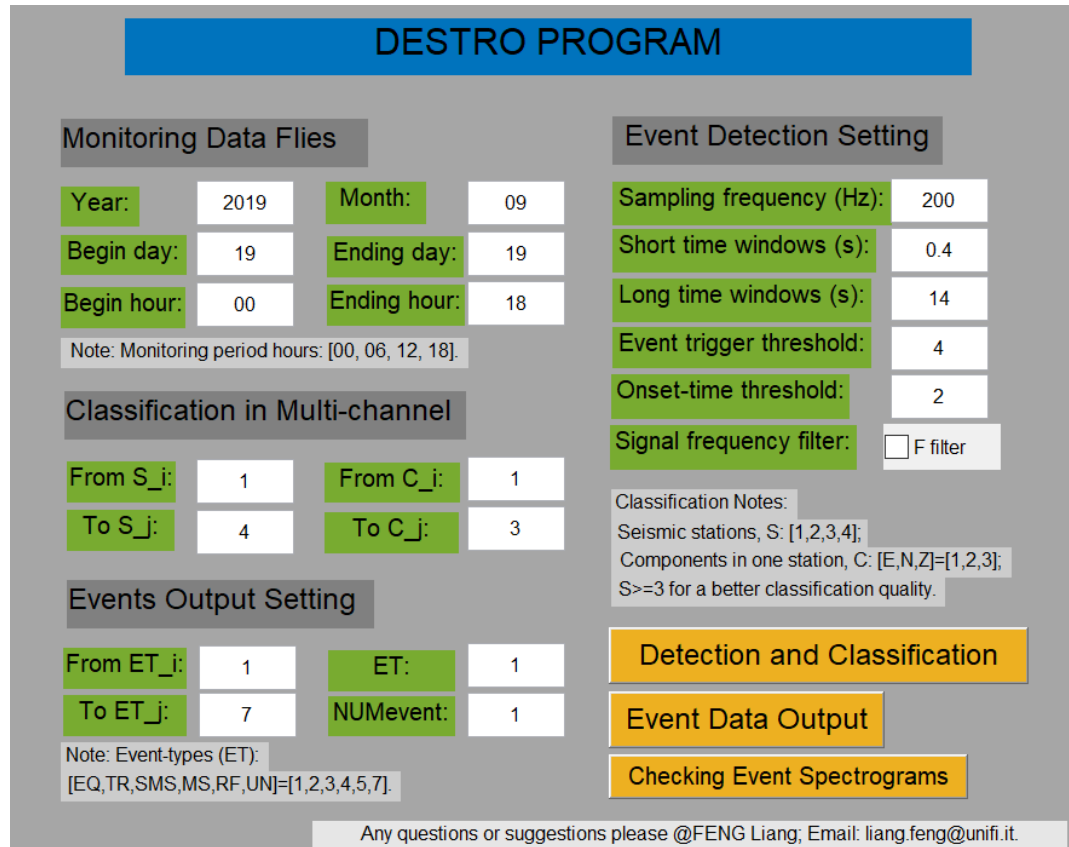


Figure 46. GUI of DESTRO based on MATLAB 2017b.

5.1 Seismic event detection flowchart

As discussed in section 3.2, the STA/LTA is chosen for the detection part of DESTRO. Beside the detection thresholds (*Threshold1* and *Threshold2* defined previously), there are six key initial parameters defined in DESTRO, that are shown in Table 7. They are: ① *STw*, and *LTw* are the length of short-time and long-time windows, respectively, that influenced by local ambient noise, detecting events and seismic monitoring experiences. ② *MINevent* is the minimum length of one seismic event impact with samples consecutively triggered. ③ *MINinterval* is the minimum interval length between the first triggered sample of one event and the last triggered sample of the previous event. *MINinterval* is a criterion that decide the ending of one event and separate two continuous event. In this study, supposed $STw = MINevent$, $LTw = MINinterval$. ④ *Threshold1* and *Threshold2* are the thresholds (STA/LTA) that for event detection and onset time detection, respectively.

Table 7. Input initial parameters for seismic detection in this case.

parameters	values
<i>MINevent</i>	80
<i>MINinterval</i>	2800
<i>STw</i>	<i>MINevent</i>
<i>LTw</i>	<i>MINinterval</i>
<i>Threshold1</i>	4
<i>Threshold2</i>	2

In detection processing, after initialized all the parameters, the program creates two sliding windows in short-time and long-time, and computes the average energy in two windows, STA_t , LTA_t , respectively, and then calculates the ratio between STA_t and LTA_t , i.e. R_t . The windows sliding step by one sample, t , and you can also increase it to speed up calculation. The program recording the accumulated number of triggered samples and de-triggered samples since the first triggered sample, respectively, and named *Slength* and *INTlength*. Event “declared” according to criteria: (1) $Slength > MINevent$ and ending when (2) $INTlength > MINinterval$. When $Slength < MINevent$, the “signal period” triggered declares as noise and clear logging, all parameters initialized and starting a new detection; otherwise, declares one event happened and computes the onset time and maximum amplitude, and save the event signal trace for seismic feature extraction and subsequent classification processing. The flowchart of detection part of DESTRO is shown in Figure 47.

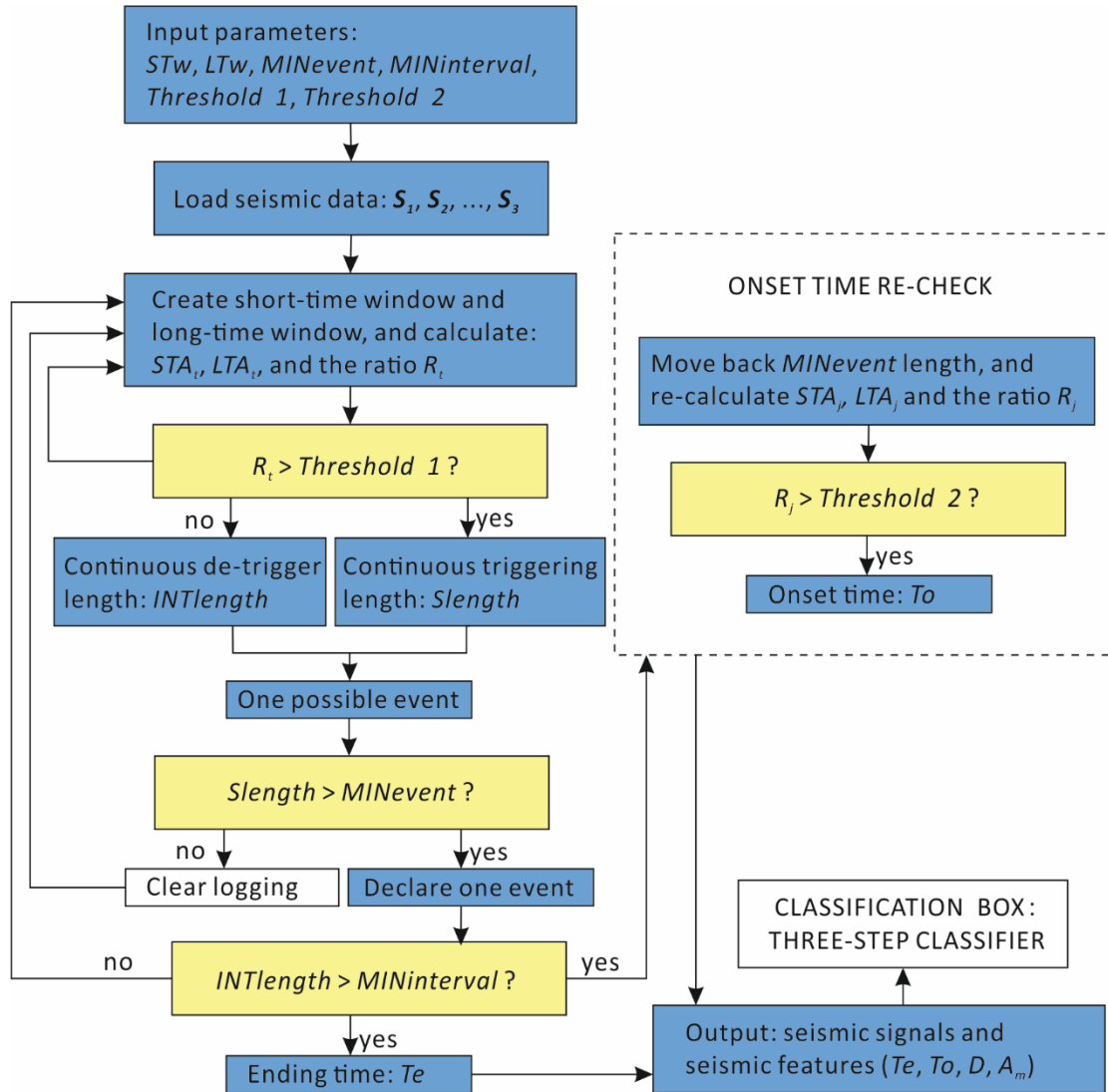


Figure 47. DESTRO detection flow chart.

5.2 Seismic features definition

5.2.1 Definition of the types of seismic events

To obtain a good quality classification of seismic events, the choice of seismic features is critical, and at the same time, it is important to keep their number as low as possible (Benitez et al. 2007; Provost et al. 2017; Vallejos et al. 2013). It is possible, in fact, that more than two parameters describe the same feature but with different weights; that could lead to a different result, and therefore, conflict and confusion could occur between features. In this study, nine seismic features are defined related to event power (maximum amplitude A_m , average energy E_a , and energy variation R_{ea}), spectrogram (maximum frequency F_m and frequency spectrum variation R_{fv}), waveform (number of peaks N_p), duration (D), and seismic network geometry (amplitude ratio R_a and frequency ratio R_f).

In DESTRO, based on the characteristics of the frequency and amplitude, five seismic event types are defined: earthquake (EQ), tremor (TR), rockfall (RF), multi-spike event (MS), and subordinate MS (SMS) events, where the only difference between MS and SMS is in the maximum frequency (F_m), set as higher than 60 Hz and lower than

60 Hz, respectively. This difference is related to the material and the distance between the event source and receiver.

The typical original signal traces and spectrograms of the five event types and those for the artificial rockfall are shown in Figure 48. EQ (Figure 48a) is identified as an easily detectable regional earthquake, and the TR event (Figure 48b) is a remote earthquake or tectonic activity characterized by a long duration, low amplitude and low frequency due to the long distance of and energy attenuation during propagation. MS (Figure 48c-d) and RF (Figure 48e-f) are supposed as rock cracking or small block falls and rockfalls, respectively, since the high frequency, short duration and multiple spikes as many rock impacts. For the purpose of rockfall classification, the discrimination between RF and MS is based on the maximum amplitude (A_m) because their spectral attributes and waveform attributes look very similar. Unfortunately, this hypothesis has not been validated with eyes witness until now (Arosio et al. 2009; Lenti et al. 2012; Lu et al. 2012, 2013).

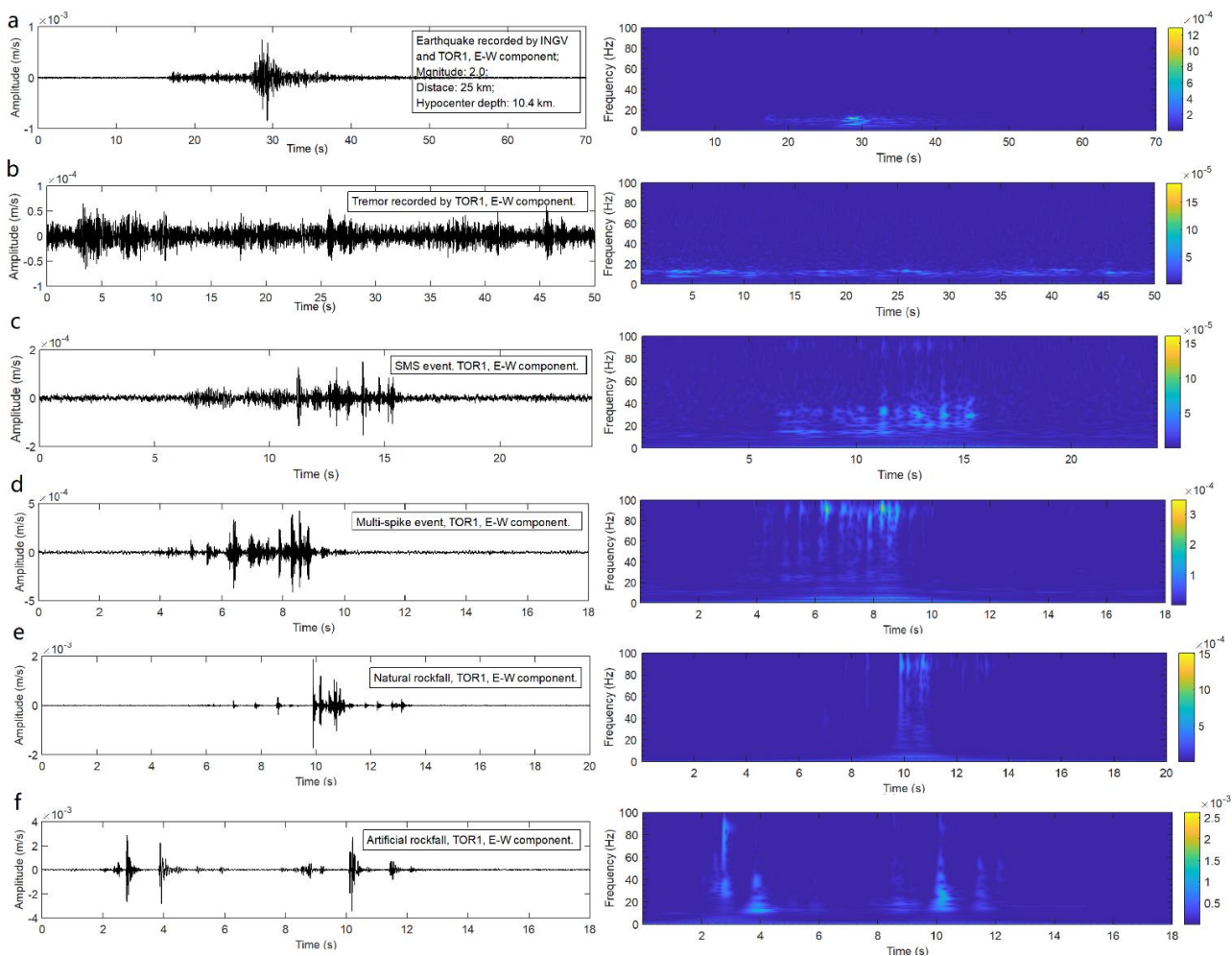


Figure 48. Original signal traces and time-frequency wavelet transform of the five event-types.

To analyse the seismic features and feature weights, a seismic event-type training database is built. All the events in the database are manually picked from the east-west component of the traces recorded by station TOR1 (see Figure 12 and Lotti et al. (2018) or Feng et al. (2019) for its location within the quarry area) during a seismic monitoring window of 12 days, including the two days of the artificially released rockfall test. The database

contains 174 EQ events; 239 TR events; 90 artificially released rockfalls (ARF); 75 natural rockfalls (NRF) manually selected based on the waveform, amplitude, duration, etc.; and 1424 MS events (including SMS).

5.2.2 Spectral attributes

1) Maximum frequency (F_m)

Frequency is one of the most important parameters of seismic signals that indicates the physical characteristics of event source. The maximum frequency (F_m) is defined as the frequency value of the Fast Fourier Transform coefficient (FFTA) with the highest value in the spectrogram (Daubechies 1992). It means that the signal with F_m frequency band is the most powerful in the whole trace generated by the event.

To analyse the characteristics of the all events F_m , the F_m percentage values of all the events in the database are analysed and plotted (Figure 49). In this figure, each colour represents an event-type, and the dashed line rectangles represent the low frequency event range, [3 Hz -16 Hz], and high frequency event range, [20 Hz -100 Hz]. In Figure 49a, the F_m of all events in training dataset are presented in their real values, and the F_m of all the events are also shown in four frequency ranges: less than 3 Hz, from 3 Hz to 16 Hz, from 16 Hz to 20 Hz, and more than 20 Hz, that plotted in Figure 49b.

The results, as expected, show that different events are clearly separated by F_m . Significantly, EQ and TR are distributed in the low-frequency part, while the MS and RF are distributed in the high-frequency part (Pazzi et al. 2017a). Therefore, the seismic events detected could be separated into two groups: high frequency events (RF and MS, with 20 – 100 Hz) and low frequency events (EQ and TR, with 3 – 16 Hz). As shown in Figure 49: EQ and TR events are clearly defined by this parameter and all of them are distributed in low frequency area, and more than 90% of the RF and MS events are distributed in the high frequency area, while there are still some RF and MS events characterized by low frequencies. According to this phenomenon, an explanation could be suggested:

(a) for RF events, the frequency content of rockfall is mostly related to the impact material and seismic wave propagate attenuation. Usually, high frequency content is generated by hard rock impaction, and low frequency content is generated by soft rock impaction. This is one reason why some ARF show a low F_m . On the other hand, for long-distance propagate attenuation, high frequency content is more easily attenuated through propagation, special for high frequency event rockfall. Moreover, this drawback also is a barrier that limits the monitoring scale of seismic networks (Manconi et al. 2016). (b) for MS events, together with the reasons at point (a), another reason could be found: some MS events are surrounded by TR events, since the features of long duration and low F_m of TR, the mixed MS event could be easily incorrect classified as TR events by DESTRO.

Given the limitations of F_m , in DESTRO, more seismic features are introduced, and the frequency range [16 Hz – 20 Hz] is isolated and treated as a fuzzy range to avoid bias made by F_m .

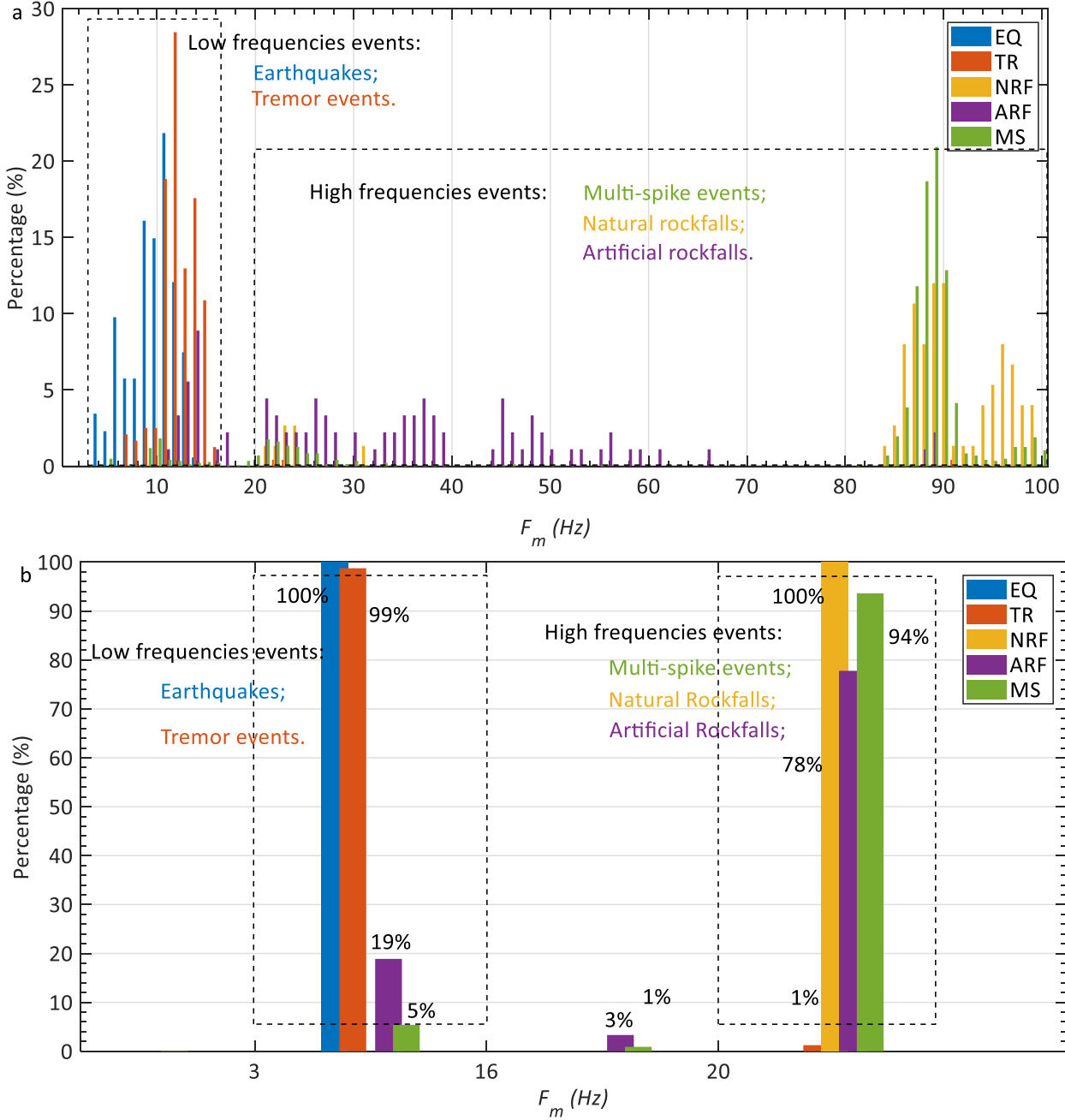


Figure 49. The percentages of maximum frequency (F_m) of all the type events in the training database. See section 5.2.3 to understand how we separate NRF and MS.

2) Frequency spectrum variation (R_{fv})

To avoid the shortcomings brings by F_m , the frequency spectrum variation (R_{fv}) is introduced that analyses the energy distributed in the high-frequency range [20 – 100 Hz] and low-frequency range [3 – 16 Hz] and calculates the ratio of the energies in the two ranges. It is defined as in Equation 40:

$$R_{fv} = \frac{\sum_{i=20}^{i=100} FFTA_i^2}{\sum_{j=3}^{j=16} FFTA_j^2}, \quad (40)$$

The R_{fv} of five typical event-types (original signals are shown in Figure 48) are analyzed by fast Fourier transform and the value of R_{fv} of each event are calculated and plotted in Figure 50. As shown, the picture a and b are EQ and TR events respectively, and both the value of R_{fv} of these two events are less than 0.5, meanwhile, the values of SMS, MS NRF and ARF in picture c, d, e and f, are more than 1. Obviously, R_{fv} could be an efficient parameter for high frequency and low frequency events separation. The R_{fv} of all events in the database are calculated and plotted in Figure 51. In Figure 51a, where R_{fv} is plotted versus A_m , each different event-type is significantly separated from others. The R_{fv} values of more than 94% RF and 99% MS, respectively, are bigger than 1, while the 100% and 97% R_{fv} values of low frequency events EQ and TR, respectively, are smaller than 0.5 (Figure 51b), as shown in Figure 50. Besides, there is also a small percentage of events with R_{fv} values in the range 0.5-1, that could not be classified only by R_{fv} as in F_m , that required a combination with other features. Anyway, the feature R_{fv} is significantly clear and visible in classification, and that could be an efficient and key parameter for seismic event classification with combine F_m in spectral attributes.

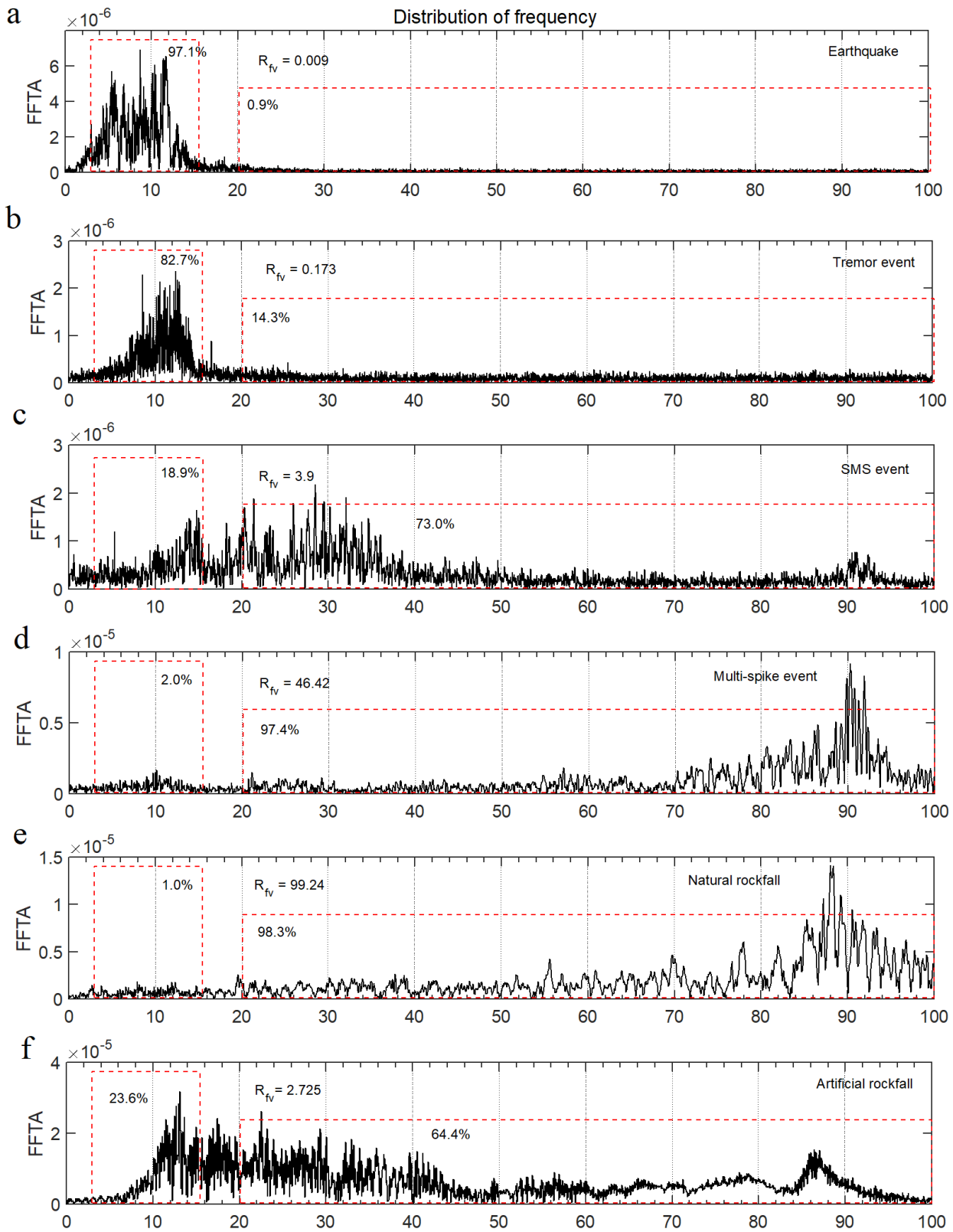


Figure 50. Frequency spectrum of six events, and frequency spectrum variation (R_{fv}). The original signals of six events were shown in Figure 50; a, b, c, d, e, f represent EQ, TR, SMS, MS, NRF, and ARF events, respectively. The value in each rectangle is the percentage of the energy of that frequency range.

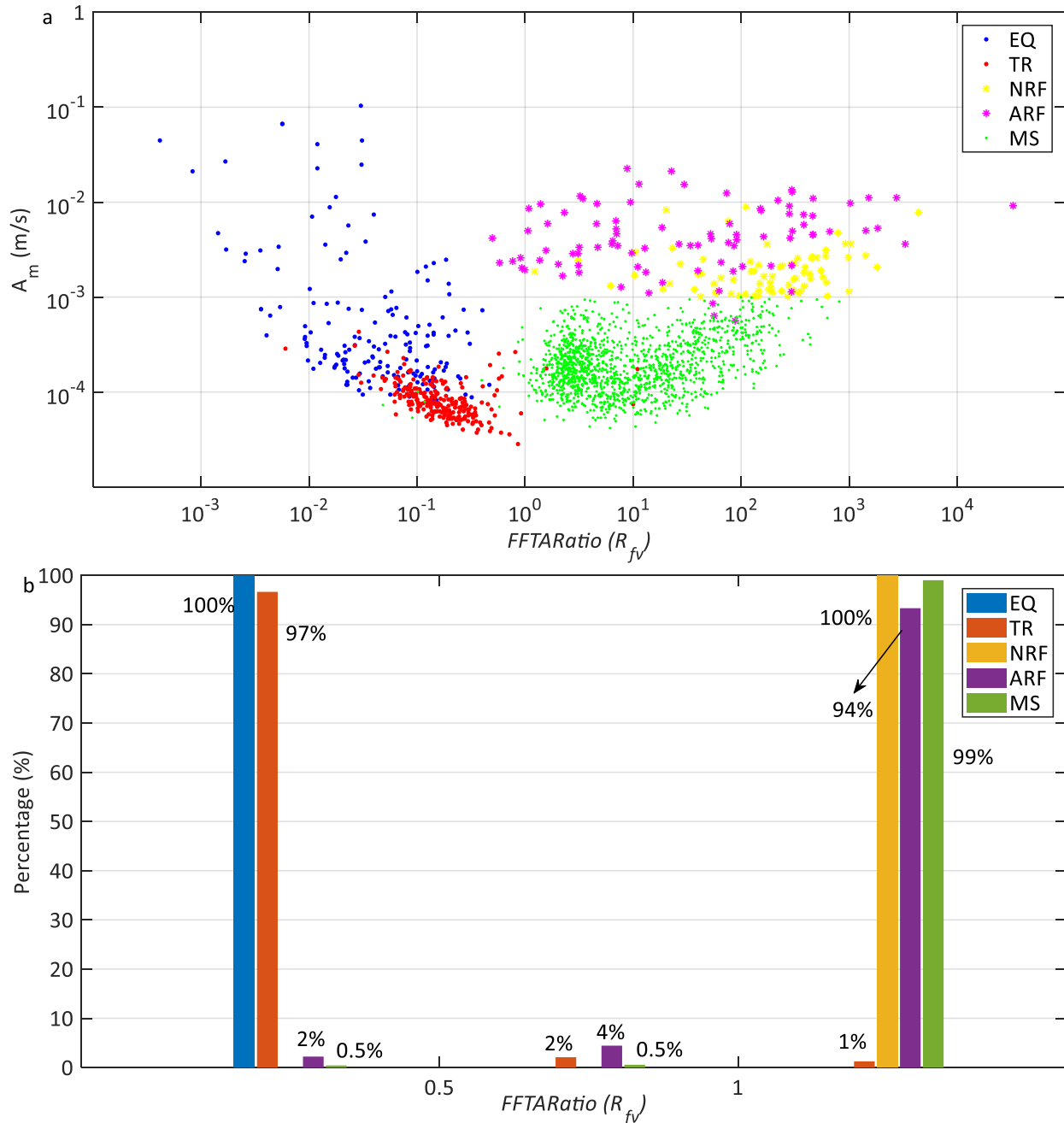


Figure 51. The distribution of FFTA ratio (R_{fv}) of all the events in the training database correspond with maximum amplitude (A_m); a) values of R_{fv} , where each event-type is represented in a different colour; b) percentage of R_{fv} of each event-type, the results of which are clustered in three ranges, less than 0.5, from 0.5 to 1, and more than 1.

5.2.3 Event-power attributes

In section 5.2.2, the seismic event-types are classified into high frequency events (RF and MS) and low frequency events (EQ and TR); however, it is still difficult to separate between RF and MS and between EQ and TR by the spectrogram, since there exist overlap ranges of frequencies.

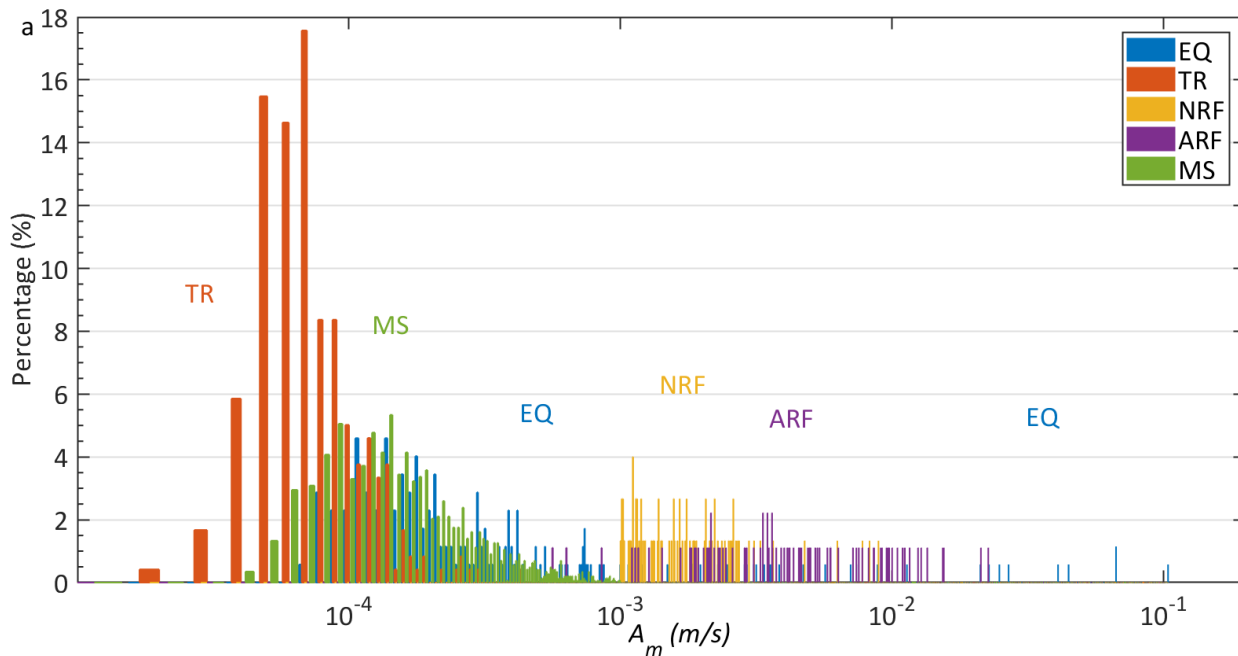
Event-power attributes are directly connected with the event source energy and potential destructibility, even though they are influenced by distance and propagation in the geological environment. In this section, we will

analyse three representative seismic features of event-power attributes, i.e., maximum amplitude (A_m) in signal trace, average energy (E_a) in event duration, and energy variation (R_{ea}) between average energy and maximum amplitude, to distinguish between RF and MS and between TR and EQ, respectively.

1) Maximum amplitude (A_m)

Maximum amplitude (A_m) is the maximum signal value in a time series and represents the most powerful moment in the whole event duration. To evaluate the differences of A_m in each event-type, the percentages of A_m of all events in database with a spacing of 1×10^{-5} m/s are calculated and plotted in Figure 52. Based on this, the A_m value of 97% ARF events is more than 1×10^{-3} m/s. It means that the energy of one seismic event of MS, recorded by the nearest seismic station, with A_m more than 1×10^{-3} m/s could be considered as powerful as a rockfall.

The higher the A_m of one event, the more powerful of the event and the more damaging it will be, therefore, from the consideration of local safety, in this study, the threshold of A_m equal to 1×10^{-3} m/s is set to classify MS and rockfall (RF) robustly, and the separation of the NRF and MS events in Figure 48 is according to this A_m threshold. While for the EQ and TR events' classification, only A_m is not sufficient, so the values of A_m are divided into four ranges, $(-\infty, 1 \times 10^{-4})$, $[1 \times 10^{-4}, 2 \times 10^{-4})$, $[2 \times 10^{-4}, 1 \times 10^{-3})$, $[1 \times 10^{-3}, +\infty)$ to be used with another complementary feature, such as duration, energy and waveform-peaks, as discussed in the next sections.



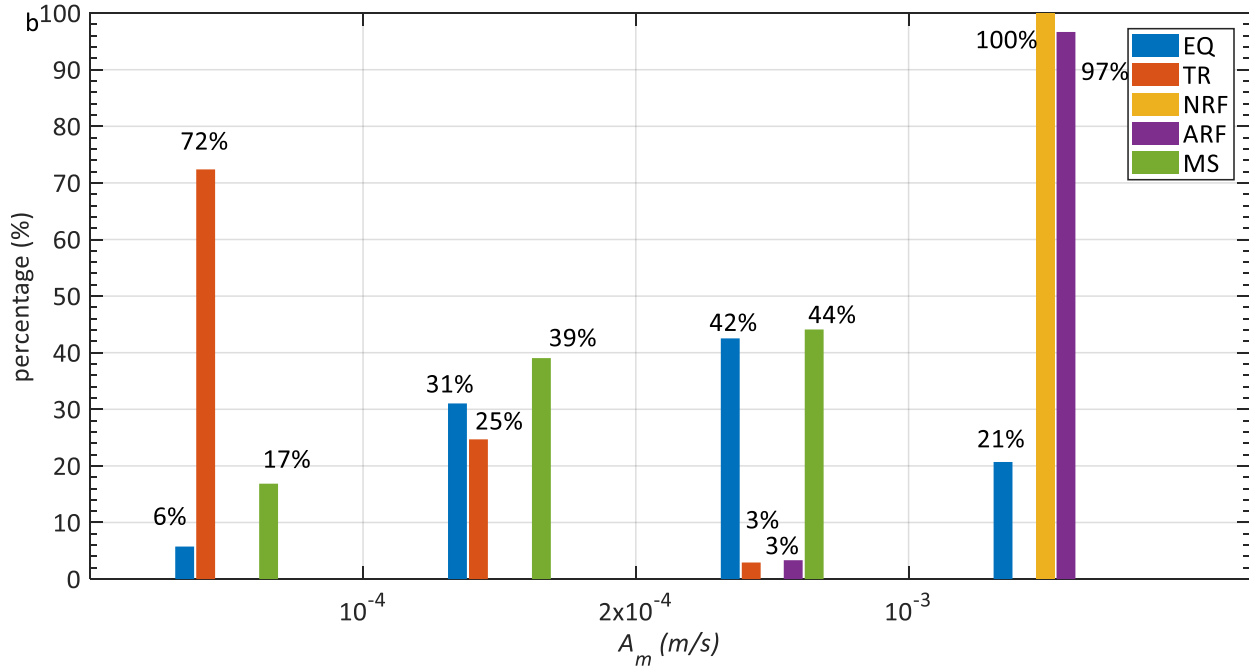


Figure 52. The percentage of maximum amplitude (A_m) of five event-types; a) percentage of all events of database distributed in A_m with the spacing of 1×10^{-5} m/s; b) percentage of five event-types clustered in spatial A_m ranges, $(-\infty, 1 \times 10^{-4})$, $[1 \times 10^{-4}, 2 \times 10^{-4})$, $[2 \times 10^{-4}, 1 \times 10^{-3})$, $[1 \times 10^{-3}, +\infty)$.

2) Average energy (E_a)

Seismic energy (E) is a relevant feature used to separate EQ events from TR events, and in this study, it is calculated at each station and is defined as the integral of the squared seismic amplitude (A_m). It is important to note that given this definition, the employed energy is a relative quantity and not an absolute quantity because it is calculated at each station. Thus, factors such as attenuation effects and geometrical spreading are not included, and the chance of introducing processing errors is reduced (Dammeier et al., 2011). To decrease the duration effect in the energy calculation, a feature of the energy density (E_a) reflecting the energy density distributed over the entire event duration is proposed. The equations for E and E_a are shown in Equations 41 and 42:

$$E = \sum_{i=1}^N A_i^2, \quad (41)$$

$$E_a = \frac{E}{D}, \quad (42)$$

where N is the number of samples in a single event detected, D is the duration of one event, and A_i is the velocity (signal amplitude) of sample i .

The E_a for all events in database are calculated and plotted in Figure 53a, which shows that E_a is proportional to A_m . Most RF and many MS (E_a indeed does not work very well with this event-type) are concentrated above the black line, while EQ and TR are concentrated below it. It is because of the difference of R_{ea} (energy variation, a feature described next section).

Given the linear correlation between E_a and A_m on the basis of the results three A_m ranges are chosen and then calculated the percentage of EQ and TR in each A_m ranges (Figure 53b). This allowed to separate EQ and TR events on the basis of the E_a value. In fact, in the range of A_m less than 10^{-4} m/s, 10% of EQ events have an E_a value higher

than $10^{-9} \text{ m}^2/\text{s}^3$ but without TR events, and 34% TR that E_a value less than $10^{-10} \text{ m}^2/\text{s}^3$ without EQ. As well as in the range of A_m from 10^{-4} m/s to $2 \times 10^{-4} \text{ m/s}$, 24% of EQ has E_a value higher than $2 \times 10^{-9} \text{ m}^2/\text{s}^3$ and without TR events, and 2% TR has E_a value lower than $2 \times 10^{-10} \text{ m}^2/\text{s}^3$ without EQ, while in the medium range of E_a , both the percentage of EQ and TR events is very high.

Consequently, respect to the safest way to classify EQ and TR events and complement with A_m , the highest and lowest E_a ranges are chosen as a complement feature for classification, but the thresholds of E_a are defined differently in each A_m ranges (more discussions about the thresholds and the weights attribute to different parameters are presented in section 5.3.1).

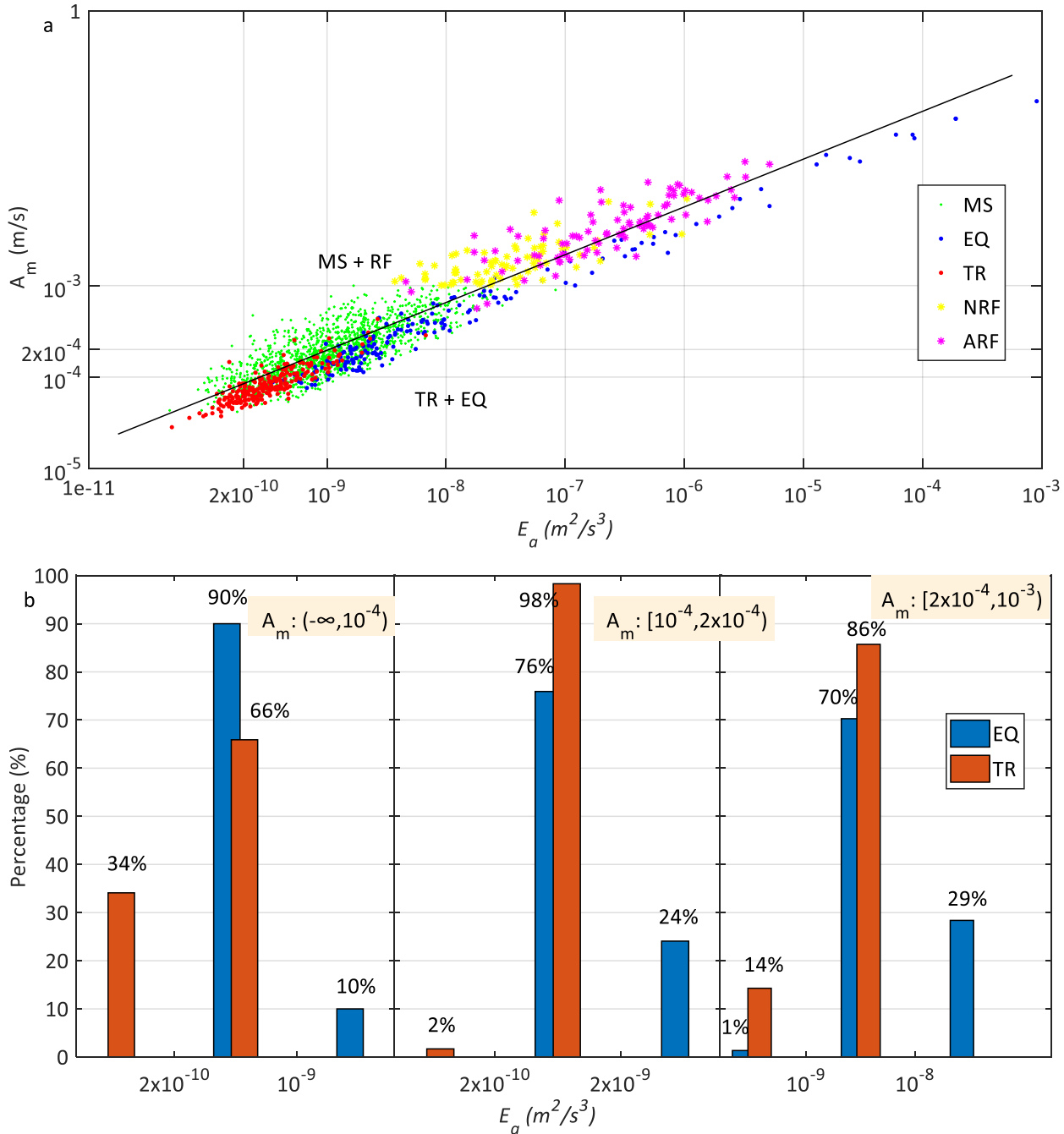


Figure 53. a) linear correlation between E_a and A_m ; b) E_a of EQ and TR events distributed in three A_m ranges.

3) Energy variation (R_{ea})

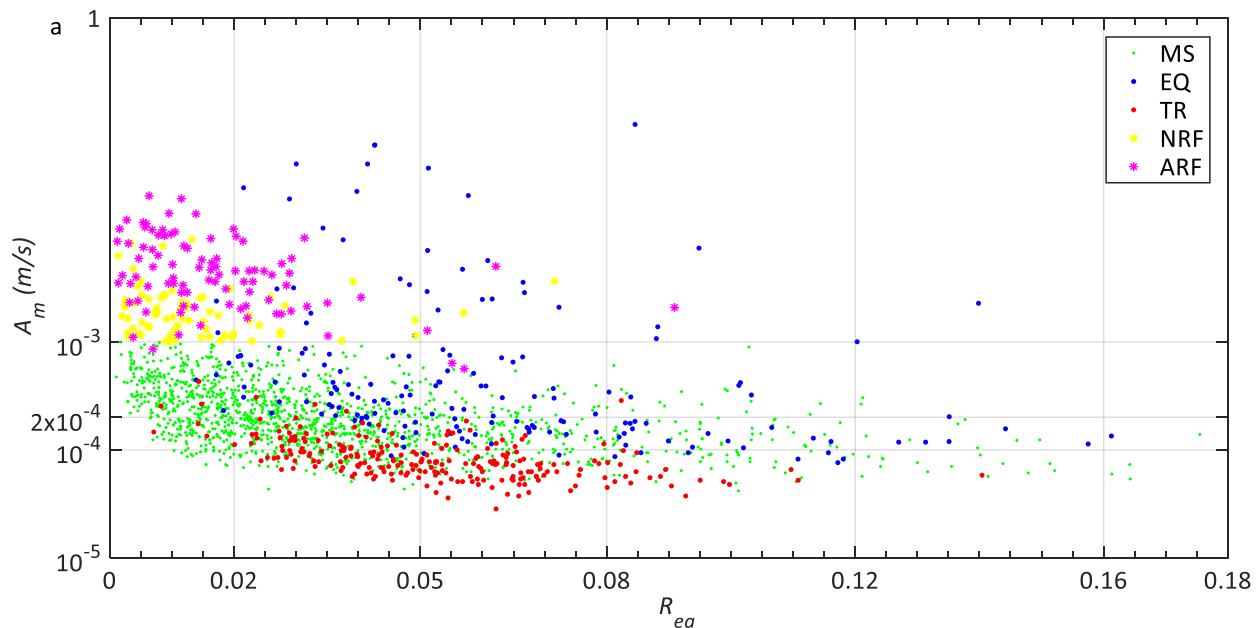
We defined the energy variation (R_{ea}) as the value of E_a divided by the square of A_m (Equation 43) to represent the degree of energy variated and distributed in the event whole duration.

$$R_{ea} = \frac{E_a}{A_m^2}, \quad (43)$$

According to the observations of the rockfall simulation test and the generated signal traces, in RF and MS events, a large portion of the seismic energy is usually concentrated at the impact or cracking moment, and the energy of EQ and TR events is mostly distributed and varies over the entire event duration (could be observed from the waveform in Figure 48). This phenomenon is especially clear for RF events. Therefore, energy variation (R_{ea}) could be efficiently used to distinguish RF events from EQ events.

Learned from Figure 53a, the E_a of EQ and TR are generally higher than those of RF and MS, respectively, so the R_{ea} of EQ and TR could higher than RF and MS (Figure 54a). This is because the signal traces of RF and MS are composed of many individual impacts and interval rests, and the energy is more scattered and distributed than EQ or TR. This phenomenon is especially clear for RF events (Figure 48), while for MS the signal of mass cracking or noise are more complex and partially overlapping, sometimes there is no interval rest between two spikes, that’s different from RF. Therefore, R_{ea} could be an efficient feature used RF and EQ classification, while MS and EQ will be classified by another attributes (spectrogram and network station) discussed in the following section.

In terms of this relationship, the R_{ea} value of all the events and the percentage of EQ and RF (including NRF and ARF) in the ranges less than 0.05 and more than 0.05 are calculated and plotted in Figure 54b to classify EQ and RF. The threshold of R_{ea} is chosen equal to 0.05 (Figure 54b), as only 3% and 6% of NRF and ARF events respectively have a R_{ea} value higher than 0.05, while 50% EQ events have a R_{ea} value higher than 0.05. Therefore, this threshold could recognize rockfall efficiently, while that’s not a valid threshold for earthquakes



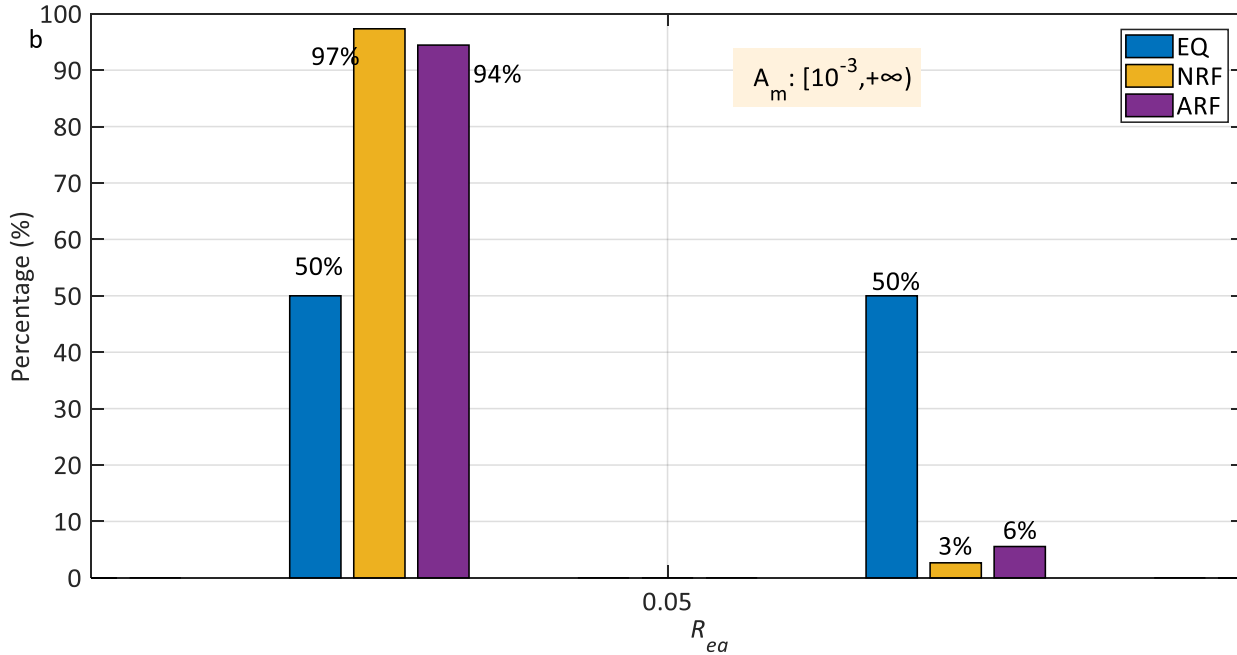


Figure 54. a) Energy variation (R_{ea}) plotted against maximum amplitude (A_m); b) the percentages of EQ and RF events with A_m more than 10^{-3} m/s distributed in the <0.05 and >0.05 ranges.

5.2.4 Network geometry attributes (R_a and R_f)

Amplitude ratio (R_a), as defined in Equation 44, is the ratio of A_m between two different seismic stations TOR_i , TOR_j , in which $A_{mi} \geq A_{mj}$:

$$R_a = \frac{A_{mi}}{A_{mj}}, \quad (44)$$

Consequently, as defined in Equation 45 frequency ratio (R_f) is the ratio of F_m between two different seismic stations TOR_i , TOR_j , in which $F_{mi} \geq F_{mj}$:

$$R_f = \frac{F_{mi}}{F_{mj}}, \quad (45)$$

R_a and R_f are very important features and newly proposed in DESTRO to classify remote and local events. For some seismic events that occurred far from the seismic network, in fact, the event A_m and F_m at different stations are similar, and so their R_a , R_f values are usually near 1, since the part of the energy within high frequencies had already been attenuated. On the other hand, for seismic events that occurred near the seismic network or inside it (such as a local rockfall or crack breaking), the R_a and R_f are usually very high, as the respective distances between stations and sources are proportionally different.

The values of R_a and R_f of all events in database between two seismic were calculated and the percentage of each event-type is plotted in Figure 55. The following observations can be made: (1) for more than 96% of EQ and 86% of TR, R_f is lower than 2.5, while for more than 67% of RF and 81% of MS events, R_f is higher than 2.5. However, several ARF and NRF events have a R_f value lower than 1.2. This happens when the signals generated by the rockfall are equal distance from both stations (and so the attenuation is similar) and/or the frequency content is low due to the nature of the impacted material. (2) For more than 98% of EQ and 96% of TR, R_a is lower than 2.5, while for almost all RF and 88% of MS events, R_a is higher than 2.5. Significantly, since these two features are

able to clearly separate RF from EQ events, they have been given high weights for the classification in weight manual modification.

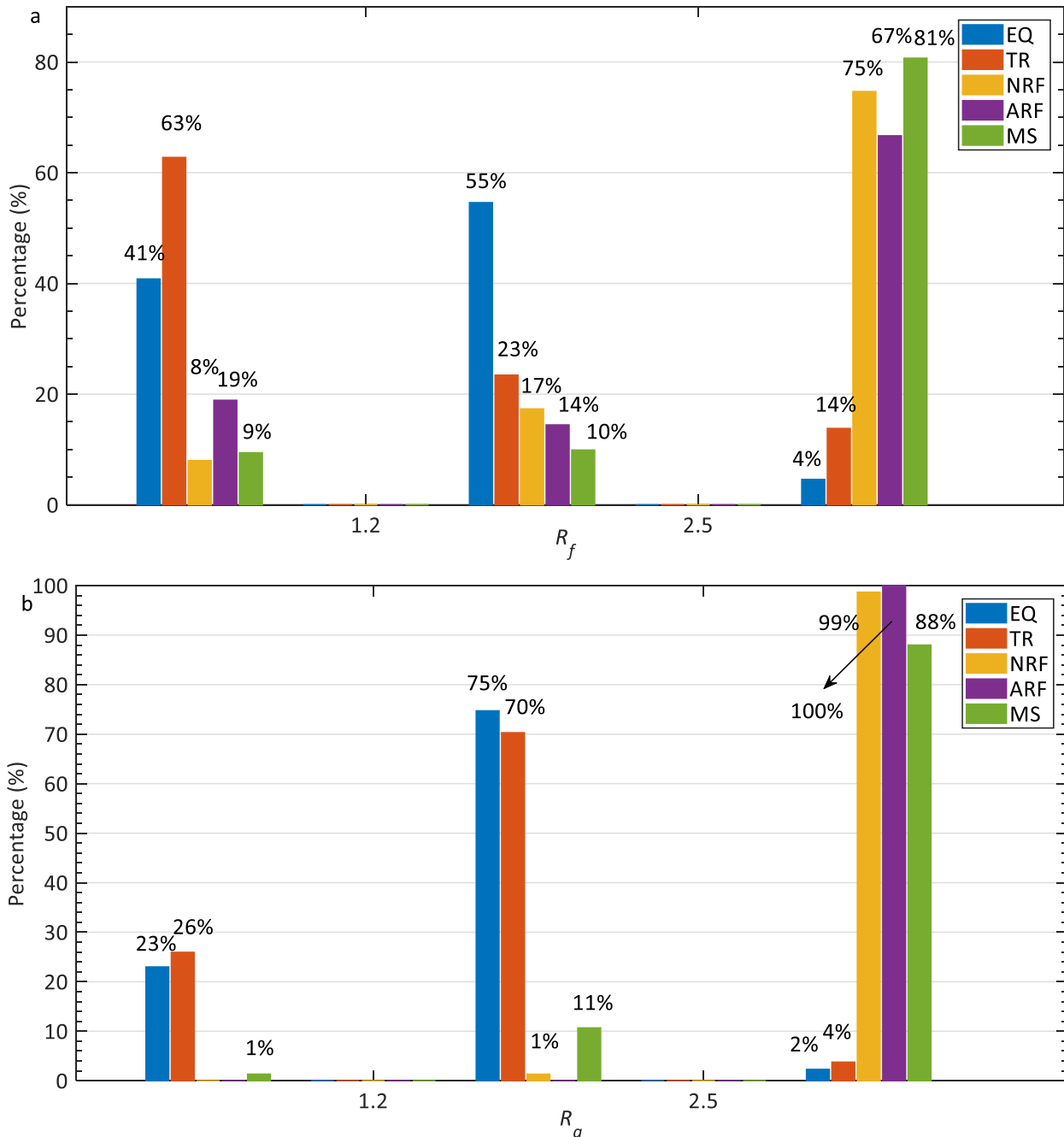


Figure 55. The percentage of five event-types distributed according to: a) maximum frequency ratio (R_f); b) maximum amplitude ratio (R_a).

5.2.5 Waveform-peaks (N_p)

The waveform-peaks (N_p) has been defined as the number of periods (peaks) exceeding a threshold calculated on the basis of the amplitude standard deviation (computed in a 0.4 s-long sliding window). Even though N_p is significantly influenced by many factors, such as geomorphology, energy of the event, and the threshold chosen

for their detection, it clearly discriminates between EQ (that typically have a single peak) and RF (which have as many peaks as the rebounds of the rock on the ground). For TR and MS events, the amplitude of the signals is too small to detect waveform peaks with the same threshold used for EQ and RF, so it is only used in EQ and RF classification.

The number of waveform-peaks for all the EQ and RF events in the database has been calculated and plotted in Figure 56. More than 60% EQ events include only one peak, while only 20% NRF and 27% ARF include one peak. The rockfalls causing only one peak are probably those that slid along the slope or those that rebounded, but their amplitude did not exceed the amplitude threshold.

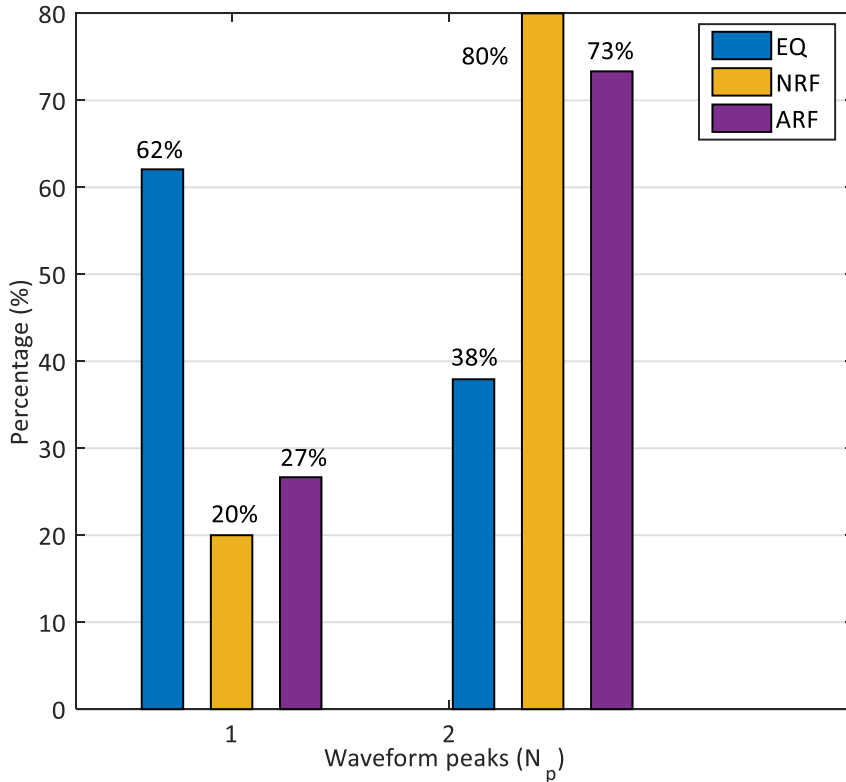


Figure 56. The percentage of EQ and RF events distributed according to the waveform-peaks.

5.2.6 Duration (D)

Duration is another very important complementary feature for seismic events classification, even though it dramatically depends on specific topographical conditions, event source location, and the attenuation in propagation. The durations of all the events in the training database have been calculated and plotted in Figure 57a. The duration of MS, TR, and NRF ranges very widely, from 1 s to 30 s, especially for MS, for which the longest duration reached 95 s, and the shortest duration only 0.46 s. Therefore, this seismic feature can hardly be used for RF and MS classification, while it can be used to distinguish EQ from TR. The events duration has been analyzed according to three A_m ranges: less than 10^{-4} m/s, from 10^{-4} m/s to 2×10^{-4} m/s, from 2×10^{-4} m/s to 10^{-3} m/s, and more than 10^{-3} m/s. The percentages of all the event-types grouped in these three A_m ranges is shown plotted in Figure 57b. The following observations can be made: (1) the duration of TR events is generally longer than EQ, especially in the A_m range less than 10^{-4} m/s, so it confirms our definition of TR; (2) usually, the durations of all the TR events are more than 7 s, while, the durations of all the EQ events are less than 17 s.

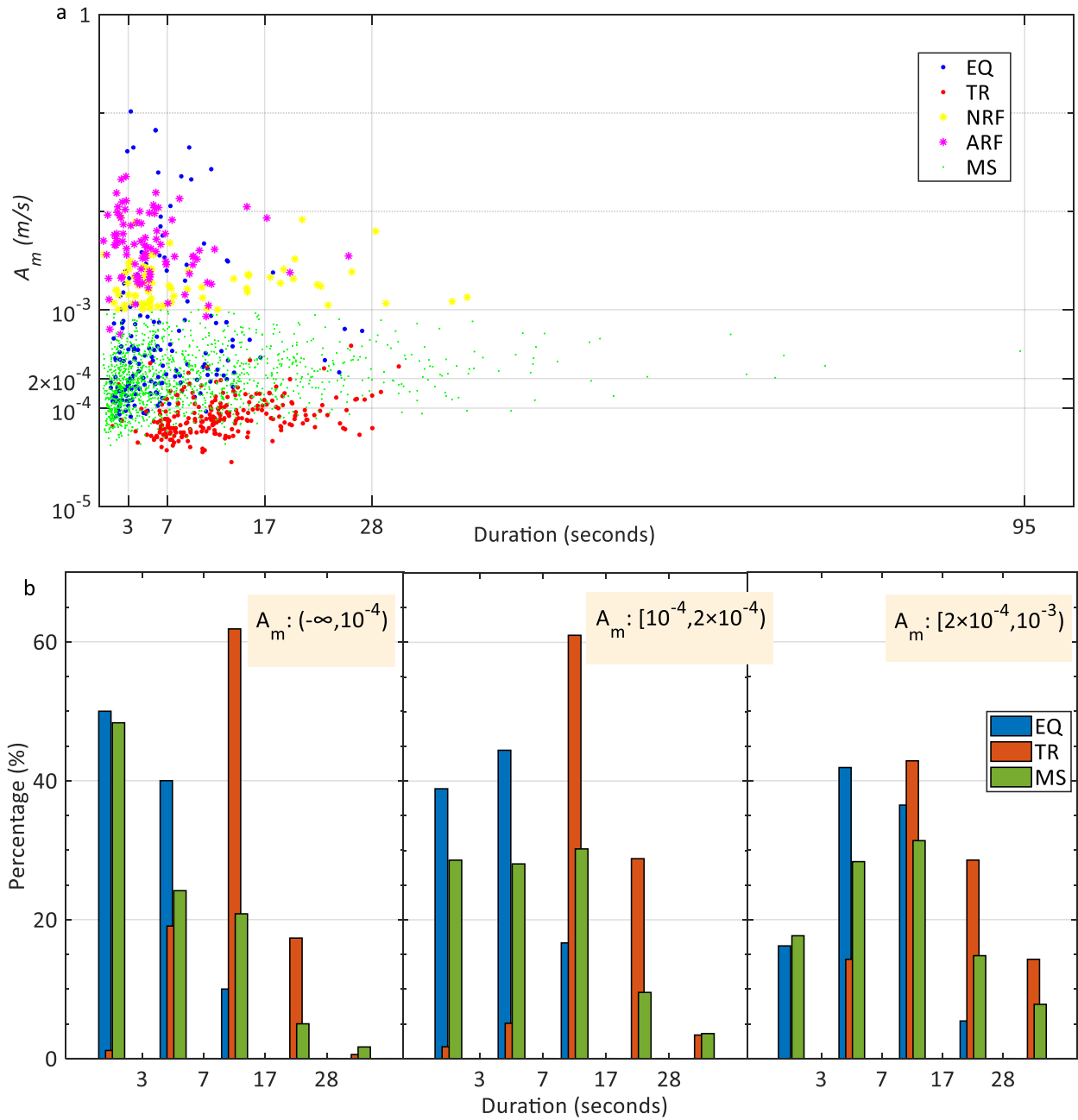


Figure 57. The duration distribution of events from the database; a: the durations of all events distribution vs A_m ; b: the percentage of EQ, TR, and MS events distributed at three different A_m ranges.

5.3 Classifier design

In this thesis, the seismic features and multi-classifier are both applied in seismic event classification. To classify events based on their seismic signals, as discussed in Section 5.2, five key features (F_m , R_{fv} , A_m , R_f , and R_a) that play a determinant role and four complementary features (E_a , D , R_{ea} , and N_p) were defined to support the classification and make it more precise. The complementary features are introduced to better classify events under different amplitude ranges.

Three different classifiers are designed in the three-step classifier. The first classifier (classifier S) is designed as a single component classifier. The second classifier (classifier C) is designed as a multicomponent classifier, i.e., at one seismic station, multi-component event integration and re-classification are performed, based on the results of classifier S of the three components. The third classifier (classifier M) performs site-event integration and event-type reclassification considering the results of classifier C for the entire monitoring network.

The full classification flowchart is shown in Figure 58. In this study, as shown in Figure 1, the monitoring network is comprised of four seismic stations, and each station has three components, E–W, N–S, and vertical Z–Z components. Additionally, in addition to the five event types, namely, EQ, TR, SMS, MS, and RF defined above, another event type, unknown events (UNs), is defined. UNs consist of MS events with $F_m < 3$ Hz or $A_m > 1$ m/s and EQ or TR events recognized by only a single component. In DESTRO classification, the event detection and classifier S has been performed for all the components, and all the onset-times, ending-times, and e_i (event-type classified in Classifier S, for more detail see their definition in the following) will be recorded for follow-up classifier C and classifier M.

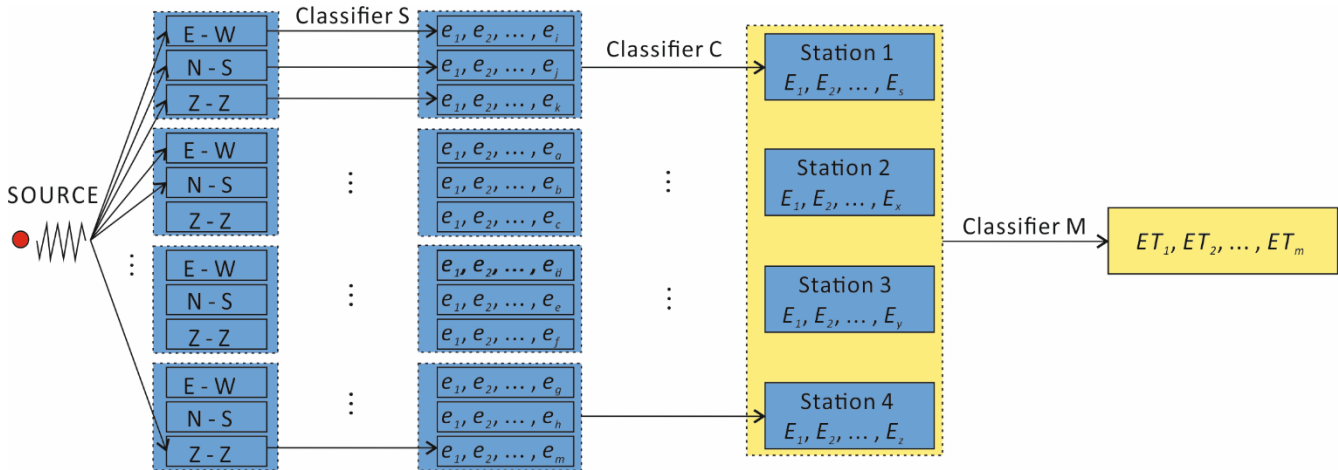


Figure 58. Seismic event classification flowchart in DESTRO. In the picture, e_i , E_i , and ET_i are the event-types as classified by classifier S, classifier C and classifier M, respectively (for their definitions, see sections 5.3.1, 5.3.2, and 5.3.3).

5.3.1 Classifier design in a single component (classifier S)

To perform a single component classification, first of all, each feature (key and complementary) is differently weighted. The initial weight is represented by the event-type occurrence rate in the database, and it is then modified with a manual calibration to address the bias of the database, since some event types could be over- or under-represented. In fact, there are many biases in a finite training database if the weight of each feature is only dependent on the training database, since the number of training samples of each event-type is not truly equal to the actual event-type occurrence rate. For example, in the amplitude range $A_m > 0.001$ m/s, there are not

as many EQ events in the database as rockfall events, since in nature there are few earthquakes with amplitudes higher than 0.001 m/s that were recorded by this monitoring network. Therefore, the initial EQ weight is calculated as 0.18—compare to that of RF (equal to 0.82)—as consequently, in classification processing, most of the EQ events with A_m larger than 0.001 m/s would be wrongly classified as RF. Therefore, in DESTRO, as a key feature, EQ and RF are not classified only by A_m , and the initial weights computed from the training database are modified.

An example of how the initial weight of EQ (W_{EQfm1}) is computed in the first range of F_m (0 – 3 Hz) is shown in Equation 46:

$$W_{EQfm1} = \frac{P_{EQfm1}}{P_{EQfm1} + P_{TRfm1} + P_{MSfm1} + P_{RFfm1}}, \quad (46)$$

where P_{EQfm1} is the percentage of EQ events in the first range of F_m , and similarly, P_{TRfm1} , P_{MSfm1} , and P_{RFfm1} are the percentages of TR, MS, and RF events in the same frequency range, respectively.

Similarly, the initial weights of other event-types and for different amplitude ranges are calculated similar to Equation 46. The initial and final weights of the five key features are shown in Table 8. In the range 3 Hz – 16 Hz of the key feature F_m , because of the bias number of event samples chosen in the training database, the initial weights of MS and RF were not equal in frequency. But they are modified to be equal, since there is no bias between MS and RF in the event-type definition according to F_m . In contrast, the initial weights of all the event-types are in F_m range 16 Hz – 20 Hz and are levelled out since the events in that range are difficult to classify and required more features to make a decision. The event-types SMS and MS could be separated only by F_m with the modified weights. For the key feature R_{fv} , the initial weights of all the event-types have large variability, therefore, all of them are modified since the huge difference cannot be compensated by other features in the later classification processing.

Table 8. The initial and modified weight of five key features of each event-type in different feature ranges.

Key features	Ranges	The initial weight of each event-type				The modified weight of each event-type			
		EQ	TR	MS	RF	EQ	TR	MS	RF
F_m	0 – 3 Hz	1	0	0	0	0.2	0.2	0.4	0.2
	3 Hz – 16 Hz	0.47	0.47	0.04	0.02	0.6	0.6	0.4	0.4
	16 Hz – 20 Hz	0	0	0.4	0.6	1	1	1	1
	20 Hz – 60 Hz	0	0.01	0.48	0.51	0.1	0.2	0.8(SMS)	0.8
	0.01					0.1	0.9(MS)	0.9	
R_{fv}	0 – 0.5	0.50	0.49	0.005	0.003	0.8	0.8	0.2	0.2
	0.5 – 1	0	0.31	0.62	0.07	0.33	0.33	0.67	0.67
	1 – +∞	0	0.005	0.49	0.50	0.2	0.2	0.8	0.8
A_m	-∞ – 1×10^{-4} m/s	0.06	0.76	0.18	0	0.4	0.7	0.4	0
	1×10^{-4} m/s – 2×10^{-4} m/s	0.33	0.26	0.41	0	1	1	1	0
	2×10^{-4} m/s – 1×10^{-3} m/s	0.46	0.03	0.49	0.02	0.8	0.2	0.8	0
	1×10^{-3} m/s – +∞	0.18	0	0	0.82	1	0	0	1
R_f	1 – 1.2	0.32	0.49	0.11	0.07	0.7	0.7	0.3	0.3
	1.2 – 2.5	0.53	0.22	0.15	0.1	0.6	0.6	0.4	0.4
	2.5 – +∞	0.02	0.08	0.42	0.48	0.3	0.3	0.7	0.7
R_a	1 – 1.2	0.46	0.52	0	0.02	0.8	0.8	0.2	0.2
	1.2 – 2.5	0.48	0.45	0.52	0.45	0.6	0.6	0.4	0.4
	2.5 – +∞	0.01	0.02	0.51	0.46	0.2	0.2	0.8	0.8

The weights of the complementary features' changes also depend on the amplitude of the signal. The complementary features E_a and D are used to discriminate between EQ and TR, and the features R_{ea} and N_p are used to discriminate between EQ and those RF with F_m lower than 20 Hz. The initial weights of the complementary features have been calculated with the same method used for the key features. The initial and modified weights of complementary features are shown in supplemental information Table 9 and Table 10, respectively.

The last step is merging all the different features weights analysed by DESTRO and get a final value that represents an event-type. Each feature is therefore extracted with a weight matrix (\mathbf{W}) containing the modified weights (W) of all the event-types and representing the event-type occurrence rate. Next, all the weight matrixes from the nine features are multiplied, and the final product matrix (\mathbf{V}) represents the final occurrence rate of each event-type (see Equations 47 and 48).

$$\mathbf{W}_{fm} = [W'_{eqfm}, W'_{trfm}, W'_{smsfm}, W'_{msfm}, W'_{rffm}, W'_{unfm}], \quad (47)$$

$$\mathbf{V} = \mathbf{W}_{fm} \cdot \mathbf{W}_{rfv} \cdot \mathbf{W}_{am} \cdot \mathbf{W}_{rf} \cdot \mathbf{W}_{ra} \cdot \mathbf{W}_{ea} \cdot \mathbf{W}_d \cdot \mathbf{W}_{rea} \cdot \mathbf{W}_{np} = [V_{eq}, V_{tr}, V_{sms}, V_{ms}, V_{rf}, V_{un}], \quad (48)$$

where W'_{eqfm} , W'_{trfm} , W'_{smsfm} , W'_{msfm} , W'_{rffm} , W'_{unfm} are the modified weights of EQ, TR, SMS, MS, RF, and unknow event (UN), respectively; the variables of \mathbf{W}_{fm} , \mathbf{W}_{rfv} , \mathbf{W}_{am} , \mathbf{W}_{rf} , \mathbf{W}_{ra} , \mathbf{W}_{ea} , \mathbf{W}_d , \mathbf{W}_{rea} , \mathbf{W}_{np} are the weight matrixes of seismic features F_m , R_{fv} , A_m , R_f , R_a , E_a , D , R_{ea} , N_p , respectively.

In addition, each event-type is assigned an ID number, i.e., events EQ, TR, SMS, MS, RF and UN were represented by 1, 2, 3, 4, 5, and 7, respectively, and the maximum element in a final matrix \mathbf{V} representing the event-type (e_i) classified in classifier S .

Table 9. The initial weight of each event-type calculated for the complementary features.

Complementary features	Ranges	A_m			
		$-\infty - 1 \times 10^{-4}$	$1 \times 10^{-4} - 2 \times 10^{-4}$	$2 \times 10^{-4} - 1 \times 10^{-3}$	$1 \times 10^{-3} - +\infty$
		(EQ, TR, MS, RF)	(EQ, TR, MS, RF)	(EQ, TR, MS, RF)	(EQ, TR, MS, RF)
E_a	$0 - 2 \times 10^{-10}$	(0, 1, 0, 0)	(0, 1, 0, 0)	(0.07, 0.93, 0, 0)	(1, 1, 1, 1)
	$2 \times 10^{-10} - 1 \times 10^{-9}$	(0.58, 0.42, 0, 0)	(0.43, 0.57, 0, 0)	(0.07, 0.93, 0, 0)	(1, 1, 1, 1)
	$1 \times 10^{-9} - 2 \times 10^{-9}$	(1, 0, 0, 0)	(0.43, 0.57, 0, 0)	(0.07, 0.93, 0, 0)	(1, 1, 1, 1)
	$1 \times 10^{-9} - 1 \times 10^{-8}$	(1, 0, 0, 0)	(1, 0, 0, 0)	(0.45, 0.55, 0, 0)	(1, 1, 1, 1)
	$1 \times 10^{-8} - +\infty$	(1, 0, 0, 0)	(1, 0, 0, 0)	(1, 0, 0, 0)	(1, 1, 1, 1)
D	0 s – 3 s	(0.5, 0.01, 0.49, 0)	(0.56, 0.03, 0.41, 0)	(0.47, 0, 0.53, 0)	(1, 1, 1, 1)
	3 s – 7 s	(0.48, 0.23, 0.29, 0)	(0.57, 0.06, 0.36, 0)	(0.5, 0.17, 0.33, 0)	(1, 1, 1, 1)
	7 s – 17 s	(0.11, 0.67, 0.23, 0)	(0.16, 0.56, 0.28, 0)	(0.33, 0.39, 0.28, 0)	(1, 1, 1, 1)
	17 s – 28 s	(0, 0.77, 0.23, 0)	(0, 0.74, 0.26, 0)	(0.1, 0.59, 0.31, 0)	(1, 1, 1, 1)
	28 s – $+\infty$	(0, 0.33, 0.67, 0)	(0, 0.43, 0.57, 0)	(0, 0.64, 0.36, 0)	(1, 1, 1, 1)
R_{ea}	0 – 0.5	(1, 1, 1, 1)	(1, 1, 1, 1)	(1, 1, 1, 1)	(0.34, 0, 0, 0.65)
	0.5 – $+\infty$	(1, 1, 1, 1)	(1, 1, 1, 1)	(1, 1, 1, 1)	(0.92, 0, 0, 0.08)
N_p	1	(1, 1, 1, 1)	(1, 1, 1, 1)	(1, 1, 1, 1)	(0.73, 0, 0, 0.27)
	1 – $+\infty$	(1, 1, 1, 1)	(1, 1, 1, 1)	(1, 1, 1, 1)	(0.33, 0, 0, 0.67)

Table 10. The modified weight of each event-type calculated for the complementary features.

Complementary features	Ranges	A_m			
		$-\infty - 1 \times 10^{-4}$ (EQ, TR, MS, RF)	$1 \times 10^{-4} - 2 \times 10^{-4}$ (EQ, TR, MS, RF)	$2 \times 10^{-4} - 1 \times 10^{-3}$ (EQ, TR, MS, RF)	$1 \times 10^{-3} - +\infty$ (EQ, TR, MS, RF)
E_a	$0 - 2 \times 10^{-10}$	(0.3, 0.7, 0.5, 0.5)	(0.2, 0.8, 0.5, 0.5)	(0.3, 0.7, 0.5, 0.5)	(1, 1, 1, 1)
	$2 \times 10^{-10} - 1 \times 10^{-9}$	(1, 1, 1, 1)	(1, 1, 1, 1)	(0.3, 0.7, 0.5, 0.5)	(1, 1, 1, 1)
	$1 \times 10^{-9} - 2 \times 10^{-9}$	(0.8, 0.2, 0.5, 0.5)	(1, 1, 1, 1)	(0.3, 0.7, 0.5, 0.5)	(1, 1, 1, 1)
	$1 \times 10^{-9} - 1 \times 10^{-8}$	(0.8, 0.2, 0.5, 0.5)	(0.8, 0.2, 0.5, 0.5)	(1, 1, 1, 1)	(1, 1, 1, 1)
	$1 \times 10^{-8} - +\infty$	(0.8, 0.2, 0.5, 0.5)	(0.8, 0.2, 0.5, 0.5)	(0.7, 0.3, 0.5, 0.5)	(1, 1, 1, 1)
D	$0 - 0.9$ s	(0.1, 0.9, 0.9, 0.9)	(0.1, 0.9, 0.9, 0.9)	(0.1, 0.9, 0.9, 0.9)	(1, 1, 1, 1)
	0.9 s – 3 s	(0.7, 0.1, 0.4, 0.4)	(0.7, 0.3, 0.7, 0.7)	(0.9, 0.1, 0.9, 0.9)	(1, 1, 1, 1)
	3 s – 7 s	(0.7, 0.1, 0.4, 0.4)	(0.7, 0.3, 0.7, 0.7)	(0.5, 0.1, 0.5, 0.5)	(1, 1, 1, 1)
	7 s – 17 s	(0.1, 0.6, 0.6, 0.6)	(1, 1, 1, 1)	(1, 1, 1, 1)	(1, 1, 1, 1)
	17 s – 28 s	(0.1, 0.9, 0.9, 0.9)	(0.1, 0.9, 0.9, 0.9)	(1, 1, 1, 1)	(1, 1, 1, 1)
	28 s – $+\infty$	(0.1, 0.9, 0.9, 0.9)	(0.1, 0.9, 0.9, 0.9)	(0.3, 0.7, 0.7, 0.7)	(1, 1, 1, 1)
R_{ea}	$0 - 0.5$	(1, 1, 1, 1)	(1, 1, 1, 1)	(1, 1, 1, 1)	(0.4, 0, 0, 0.6)
	$0.5 - +\infty$	(1, 1, 1, 1)	(1, 1, 1, 1)	(1, 1, 1, 1)	(0.7, 0, 0, 0.3)
N_p	1	(1, 1, 1, 1)	(1, 1, 1, 1)	(1, 1, 1, 1)	(0.7, 0, 0, 0.3)
	$1 - +\infty$	(1, 1, 1, 1)	(1, 1, 1, 1)	(1, 1, 1, 1)	(0.4, 0, 0, 0.6)

5.3.2 Classification in multi-component (classifier C)

Classifier C is designed to decide the station event-types (E_1, E_2, \dots, E_s) by integrating component by component the event-types identified in the three components of one station. The processing flowchart of Classifier C is shown in Figure 59. The main processing can be divided into three phases. First, all the event parameters such as the onset-time (To), ending time (Te), and event-type (e_i) classified by classifier S and the component that detected the event are identified.

Second, all the events from the three components with the respective features are integrated into one event series and sorted in the time domain, and a judgement for event integration and the re-classification of specific integrated events is performed. The events integration judgment according to: a) the difference in the onset time ($\Delta t = To_{i+1} - To_i$) between two continuous events (i and $i+1$) and b) the time order among $To_i, To_{i+1}, Te_i,$ and Te_{i+1} . If the Δt of two events is lower than a threshold δ (set equal to 7 s in this study; half of $MINinterval$ in detection) or the onset time of event i (To_i) is lower (i.e., earlier) than the end time of the previous event (Te_{i-1}), two events will therefore be regarded as one event from the same source, and the smallest To_i , the largest Te_i , and maximum A_m will be saved. Otherwise, the two events will be saved as two different events from different sources, and all the $e_i, To_i, Te_i,$ and A_m values will be recorded.

Usually, two continuous events considered one event are detected from two different components, but sometimes they are from the same component. In such cases, the reclassification of integrated events is performed under the following criteria: a) if both event types are $e \leq 2$ (the ID number assigned for the event type is for an EQ or TR) or at least one of them is $e = 1$ (i.e., EQ), then the event type will be set to EQ (i.e., $e = 1$); b) if both event types are $e \neq 7$ (i.e., both are not unknown events), the final event type will be set as the larger ID number ($\max(e_i)$); otherwise, if one event type is $e \neq 7$ and the other event-type $e = 7$, the event type will be considered the same as that for $e \neq 7$.

The final step of classifier C is the definition of single station-event-type (E_i) taking into account the number of components (c equal to 1, 2 or 3, the components that detected the same event) and the e_i in each component (e_{i1}, e_{i2}, e_{i3}). This classification is carried out according to the following criteria: a) EQ and TR events should be detected by more than 1 component; otherwise, the event will be classified as a UN event (i.e., $E_i = 7$); b) if an event is detected by three components ($c = 3$), two of which denote EQs and another classified as a TR, the event will be classified as an EQ; c) for high-frequency events (SMS, MS, and RF events) detected by only one component, the e_i value will be divided by 10 to denote possible weak cracking or noise; d) for events with $e_i \neq 7$, if more than two components are detected with the same e_i value, the event type is kept; and e) for events with $e_i \geq 3$, if the components have different e_i values, that with the largest value (i.e., $E_i = \max(e_i \neq 7)$, $RF > MS > SMS$) is kept.

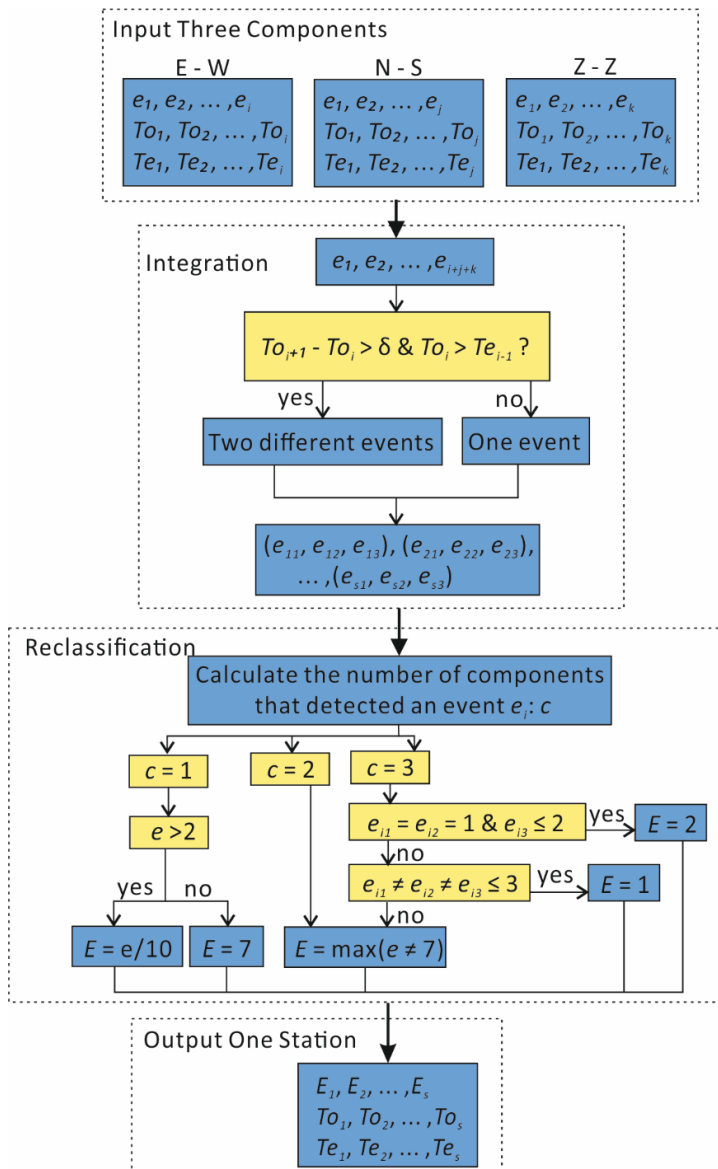


Figure 59. The flowchart of classifier C. To_i is the onset time of event i ; Te_i is the ending time of event i ; e_{i1}, e_{i2}, e_{i3} are the event types classified for the E-W, N-S and Z-Z components, respectively; and E is the event type for one station.

5.3.3 Classification in multi-station (classifier M)

Classifier M is designed to integrate all the events from all the seismic stations in the monitoring network. In addition to the event-types (EQ, TR, SMS, MS, RF, and UN, that defined as primary categories), classifier M introduces a secondary specification to characterize their influence scale (classified as regional event, slope-scale event, local event, very local event, and point event; see Table 11) by multiplying the event-type ID number with a power of 10 (from 10^3 to 10^{-1}). The events are therefore classified as a site-event series (ET_1, ET_2, \dots, ET_m) based on both the event type and scale.

In detail: i) regional event (R), multiplied by 10^3 : the event (e.g., earthquake, large rockfall or landslide) influences all the research area, detected by all the seismic stations (four in our case study), and classified as the same event-type by classifier C; ii) slope-scale event (S), multiplied by 10^2 : the event influences only the studied slope (e.g., small landslide, rockfall) and is therefore not detected by all the stations (in our case study, it was detected by three stations) and classified as the same event-type; iii) local event (L), multiplied by 10^1 : the event influences just a portion of the slope (e.g., small rockfall) and is detected by half of the seismic stations (two in our case study) and classified as the same event-type; iv) very local event (vL), multiplied by 10^0 : the event influences a very small part of the slope and is only detected by one station (e.g., small rockfall, strong rock crack or noise); v) point event (P), multiplied by 10^{-1} : the event is very local and weak (e.g., weak rock crack and noise) and is detected by only one component.

In classifier M, the processing is divided into three phases (the flowchart is shown in Figure 60): data preparation, event integration, and event-type re-classification. The first and second parts are the same as those for classifier C, in the third part, the number of stations (s equal to 1, 2, 3 or 4) that detected the event are counted, and the secondary specification is obtained.

The event-type re-classification follows these criteria: a) EQ and TR events should be detected by more than one station; otherwise, an event is classified as a UN event; b) when one event is detected by four stations, three of which denote EQs and one station denotes a TR, SMS or MS ($E \leq 4$), the event will be reclassified as an EQ; c) for all the events with $E_i \geq 3$ detected by more than two stations, we only keep the station with the highest value (i.e., $ET = \max(E \neq 7)$); and, d) a point event ($E_i < 1$) will be reclassified as a very local event (vL) when classified as P event by more than two stations.

Table 11. The identification numbers (ID numbers) of the event categories (event type and scale). Note that signals primarily classified as EQs or TRs but detected by only one component or one station are instead classified as UN.

Event-types		Scales				
		Regional (R)	Slope-scale (S)	Local (L)	Very Local (vL)	Point (P)
EQ	1	1000	100	10	7 (UN)	7 (UN)
TR	2	2000	200	20	7 (UN)	7 (UN)
SMS	3	3000	300	30	3	0.3
MS	4	4000	400	40	4	0.4
RF	5	5000	500	50	5	0.5
UN	7	7000	700	70	7	7

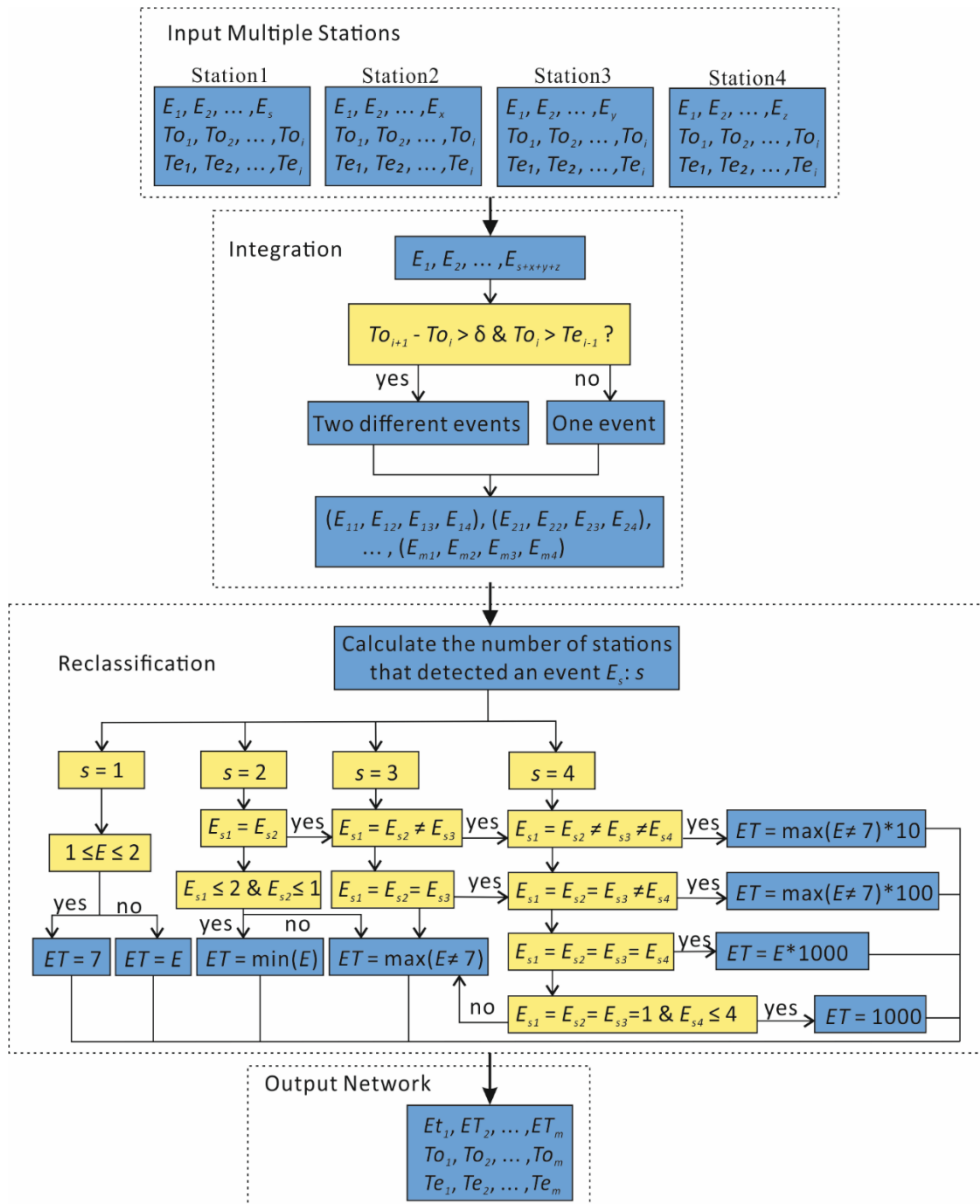


Figure 60. The flowchart of classifier M. (E_{12}, E_{12}, E_{13} , and E_{14}) are the event types classified for seismic stations TOR1, TOR2, TOR3, and TOR4, respectively, and ET is the final event type for the seismic monitoring network.

5.4 DESTRO performances

5.4.1 DESTRO detection accuracy

In DESTRO detection, the STA/LTA method is chosen, and two STA/LTA thresholds are set to improve the onset time detection accuracy. Moreover, two parameters, the minimum event duration ($MINevent$) and minimum interval duration ($MINinterval$), are proposed to separate seismic events. To evaluate the detection accuracy, a test signal of 55 minutes that recorded 30 different events was chosen among the entire seven-month monitoring dataset. The DESTRO code managed to automatically detect all 30 events.

Figure 61a is the original signal; in Figure 61b the detected events are isolated from the background noise and marked each one with a different color; Figure 61c is the detecting criterion of STA/LTA and the two thresholds are also represented ($threshold1$ used for events detection, $threshold2$ for onset time picking).

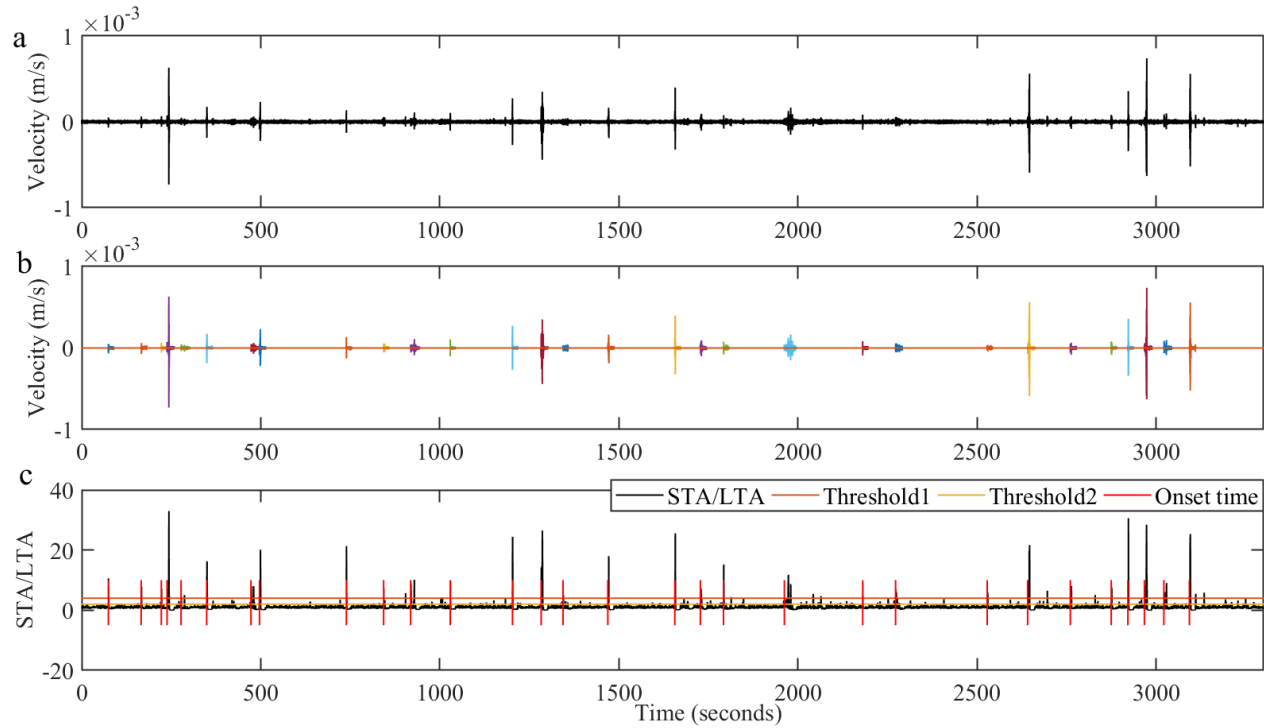


Figure 61. a) Original testing signal, b) detected events colored with different color, and c) detecting criteria and the onset times automatically detected by DESTRO.

The onset times detected by DESTRO (t_D) and the onset times manually picked (t_m) are plotted in Figure 12, together with all the errors between t_D and t_m (calculated as $t_D - t_m$). It can be noted that 1) only one error is larger than one second and most of the errors are close to zero; 2) all of the errors are larger than 0, which means the onset time picking method, STA/LTA, has a lag from itself due to the chosen sliding window; and 3) computing the average error of onset-time, it is 0.2178 s, which would be treated as median lag. The results also show there were no missing or fake events.

Table 12. The onset times picked manually and by DESTRO, and the associated errors.

Events Number	Onset times manually (s)	Onset times DESTRO (s)	Errors (s)	Events Number	Onset times manually (s)	Onset times DESTRO (s)	Errors (s)
1	374.4	374.52	0.12	16	1956.13	1956.16	0.03
2	466.71	466.75	0.04	17	2027.96	2028.025	0.065
3	522.825	522.86	0.035	18	2091.85	2092.01	0.16
4	538.25	538.345	0.095	19	2261.65	2261.95	0.3
5	577.23	577.87	0.64	20	2480.48	2480.505	0.025
6	649.01	649.05	0.04	21	2572.54	2572.64	0.1
7	772.8	773.205	0.405	22	2828.15	2828.3	0.15
8	796.38	796.685	0.305	23	2941.05	2941.565	0.515
9	1039.03	1039.11	0.08	24	3060.16	3060.23	0.07
10	1143.05	1143.185	0.135	25	3174.31	3174.355	0.045
11	1218.95	1219.015	0.065	26	3221.02	3222.235	1.215
12	1328.78	1329.145	0.365	27	3267.33	3267.445	0.115
13	1502.925	1502.96	0.035	28	3322.25	3322.28	0.03
14	1582.93	1582.945	0.015	29	3392.7	3392.795	0.095
15	1769	1769.44	0.44	30	3409.33	3410.145	0.815

5.4.2 DESTRO classification accuracy

1) Test with the training database

To evaluate the classification accuracy, a test is performed on a monitoring dataset of 12 days, from 7th to 18th December 2012, that includes all the events in training database. In totally, 471 EQ events, 194 TR events, 2819 SMS events, 3683 MS events and 318 RF events were classified by DESTRO. The classification results in the test monitoring period are compared with manual classified events in database, and results are plotted in Figure 62.

The following observation can be done: a) 96% EQ and 100% RF events in training database are correctly classified by DESTRO; b) there are still 4% EQ (i.e., six EQ events) that are not classified correctly by DESTRO, i.e. three EQ events were classified in TR category, one EQ as SMS, and two EQ as RF; c) 99.5% SMS and MS events were classified successfully, and only the 0.5% of MS events (i.e., seven MS events) were classified incorrectly, i.e. four events classified as EQ, two events classified as UN, and one event classified as TR; d) many TR events were incorrectly classified as UN, SMS and MS categories.

In summary, from the accuracy evaluation results, almost 100% of the event categories of RF, SMS, and MS were successfully classified and separated from the all-around noise. With respect to the strict classification criteria of EQs and TRs, some EQ and TR events were incorrectly classified as UN, and some EQs were classified as TRs when the energy of an EQ was too low to be detected by more than two stations. For these reasons, there are still two EQ events classified as RFs: i) in one case, the EQ event merged with too many other high-frequency events, which contributed to a high R_{fv} value, and ii) for the other EQ events, the maximum frequency is higher than the F_m threshold (20 Hz) used in the classification of EQs.

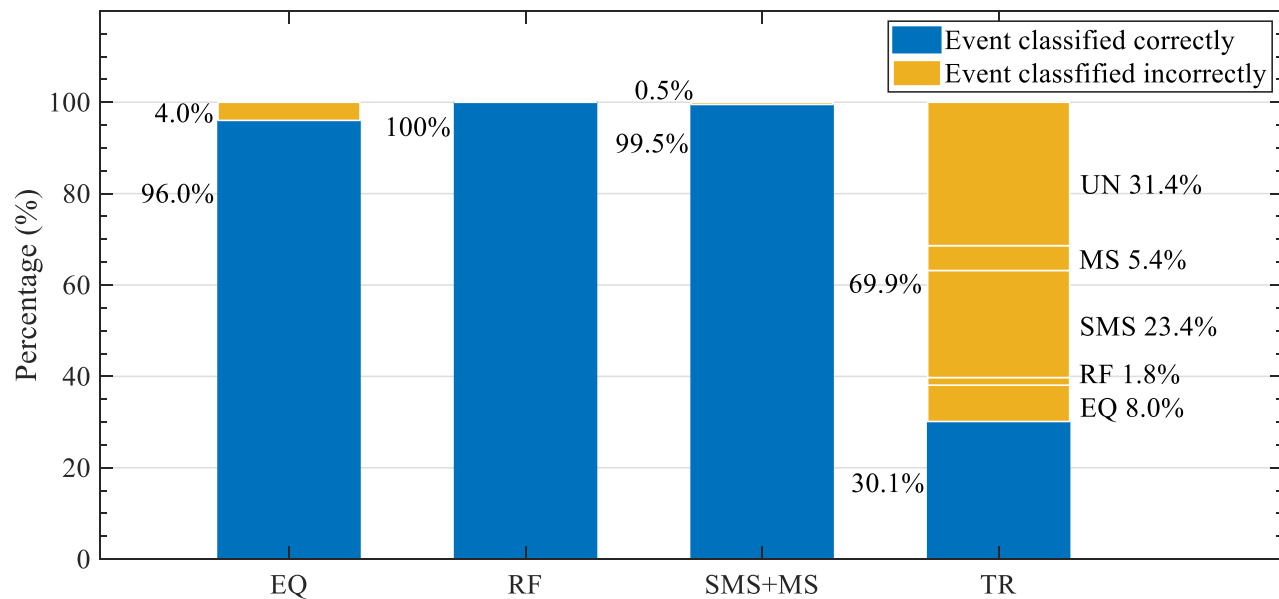


Figure 62. The classification results by DESTRO in the 12 days monitoring dataset.

2) Earthquake detection accuracy

To evaluate the DESTRO classification performance of EQs, a longer monitoring dataset of 25 days (7th–31st of December 2012) recorded at Torgiovannetto from the training database is selected. All the EQ and TR events detected by DESTRO (984 EQ and 370 TR) are compared with the events in the INGV earthquake database (573 earthquakes that occurred in the same period within a radius of less than 300 km). The result of this comparison

is shown in Figure 63. Almost 58.8% of the earthquakes recorded by INGV are also clearly recognized by DESTRO, simply from an onset time comparison, but 41.2% of the earthquakes were not confirmed in DESTRO.

To determine why 41.2% of the earthquakes are unconfirmed in DESTRO, the magnitudes and epicentre distances are analysed. The distance vs. magnitude results are shown in Figure 64, where the dots are tested earthquakes. In particular, blue dots are the earthquakes confirmed as EQs by DESTRO, and the red dots are earthquakes only recorded by INGV. The histogram shows the percentages of confirmed and unconfirmed earthquakes in two distance ranges: less than 100 km and from 100 km to 300 km. The earthquake distances recorded by INGV ranged from 4.4 km to 292 km, and the magnitudes ranged from 0.4 to 3.2. From the results, almost 64.9% of the earthquakes with epicentre distances less than 100 km are confirmed by DESTRO, and in the distance range of 100 km – 300 km, only 21.3% are confirmed. This result is because the earthquakes that occurred nearby are more easily confirmed with a small onset time delay and attenuation than earthquakes that occurred farther away with strong attenuation that are difficult to detect with DESTRO or cannot be simply confirmed with onset times because of large onset time delays. Moreover, high earthquake magnitudes are easier to detect by DESTRO than low magnitudes, which is validated in Figure 64.

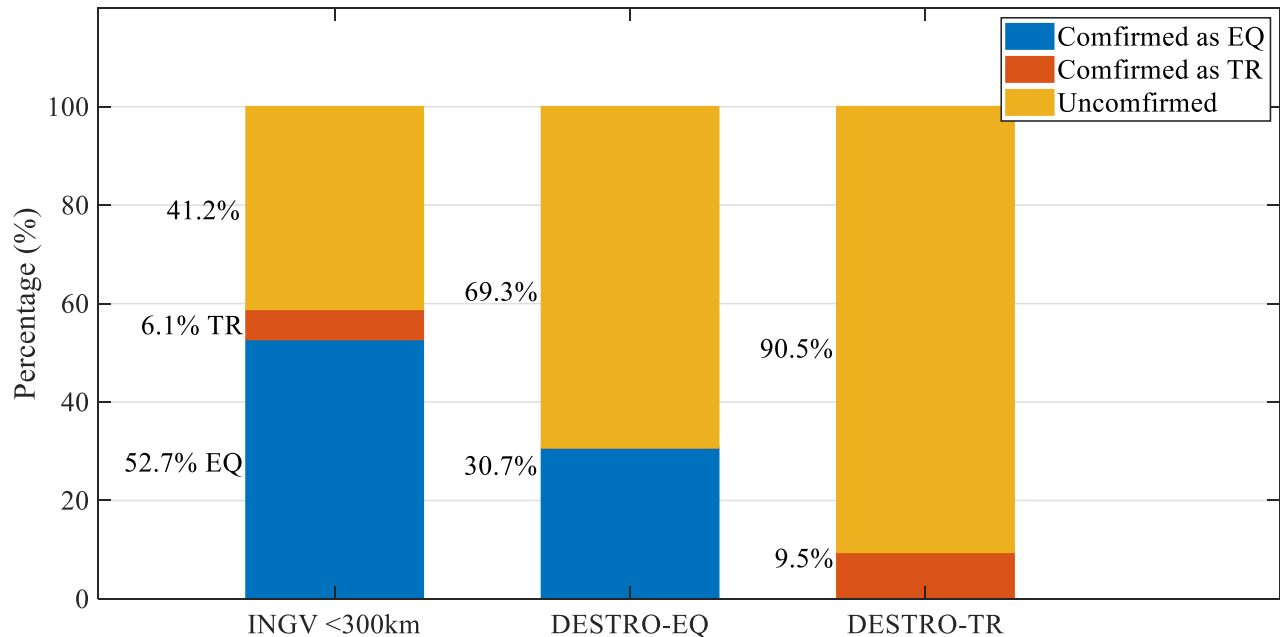


Figure 63. The detection result of EQ and TR in DESTRO and compared with INGV earthquake database from 7th – 31st December 2012, simply from onset-time.

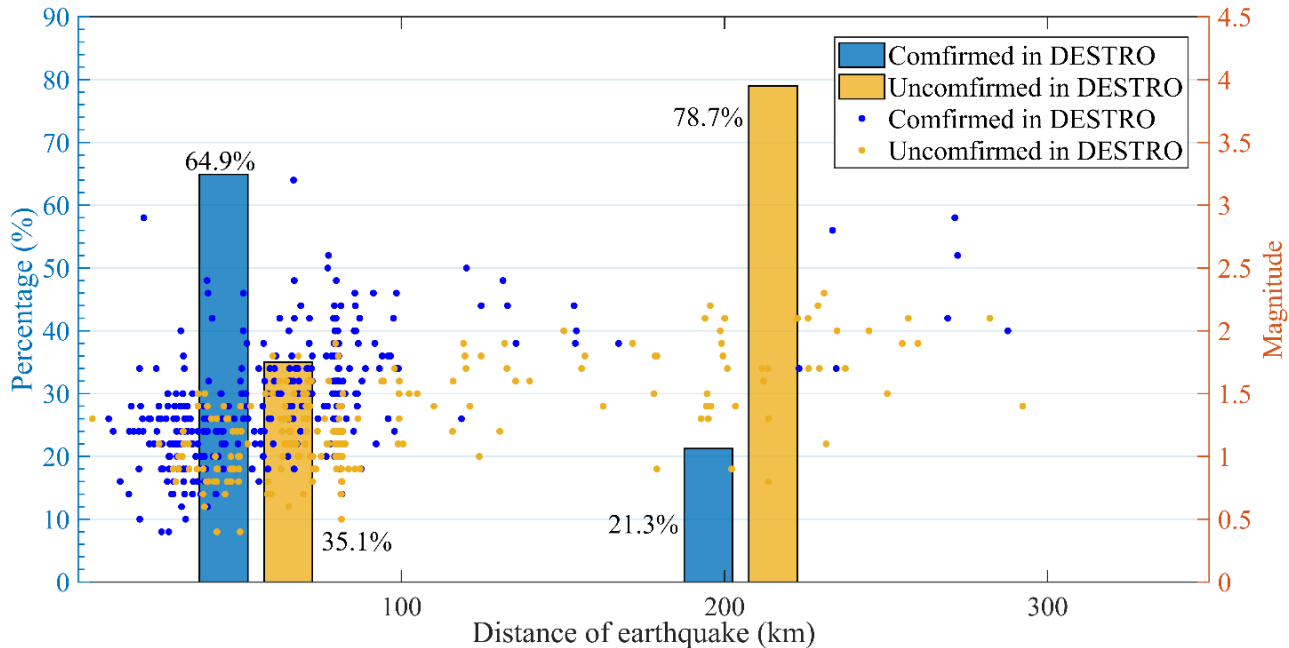


Figure 64. The distances and magnitudes of earthquakes recorded in the INGV earthquake database that less than 300 km, from 7th – 31st December 2012.

In summary, the reasons why 41.2% of earthquakes were not confirmed in DESTRO are as follows: a) the onset time delay makes it difficult to track earthquakes from INGV to DESTRO since some earthquake epicentres were distant from the stations and signal were influenced by high attenuation; b) a low-magnitude earthquake is not a single event but usually occurs with a series of post-shocks, so there will be some differences in post-shock recordings between the seismic network and INGV; c) the intrinsic drawbacks of this monitoring network (the stations are located at a distance of 200 m) is the small network scale, compared with the scale of the national earthquake monitoring network, so some earthquakes could be merged into one tremor event; and d) classification errors can occur in DESTRO. For example, i) some earthquakes could be classified as TR events since the definitions of TRs and EQs are similar (differences related to duration and energy attributes); ii) some earthquakes could be classified as UN events, since EQ and TR events should be detected by more than two stations; otherwise, an event will be classified as UN with the DESTRO definition and iii) some earthquakes may be classified as SMS, MS or RF events when EQ events merge with SMS, MS, or RF events since high-frequency events are prioritized and kept in DESTRO.

3) Artificial rockfall detection accuracy

To evaluate the capability of DESTRO in rockfall detection, a continuous monitoring period of four hours and forty minutes that covers the artificial released rockfall test (Feng et al. 2019) is analysed, the result is shown in Figure 65. A total of 109 RFs were detected. Of the 90 artificial rockfalls (ARFs), 88 ARFs were classified correctly by DESTRO, and 2 ARFs were classified as SMS events (because their amplitudes were less than the 0.001 m/s threshold defined). There were also 21 additional RF events detected by DESTRO. The signals of 19 extra RF and the rockfall simulation test videos were manually rechecked, and most of the additional RFs came from anthropic noise, such as removing testing blocks and other falling debris induced by walking or removal. In general, DESTRO performed well in rockfall detection and classification.

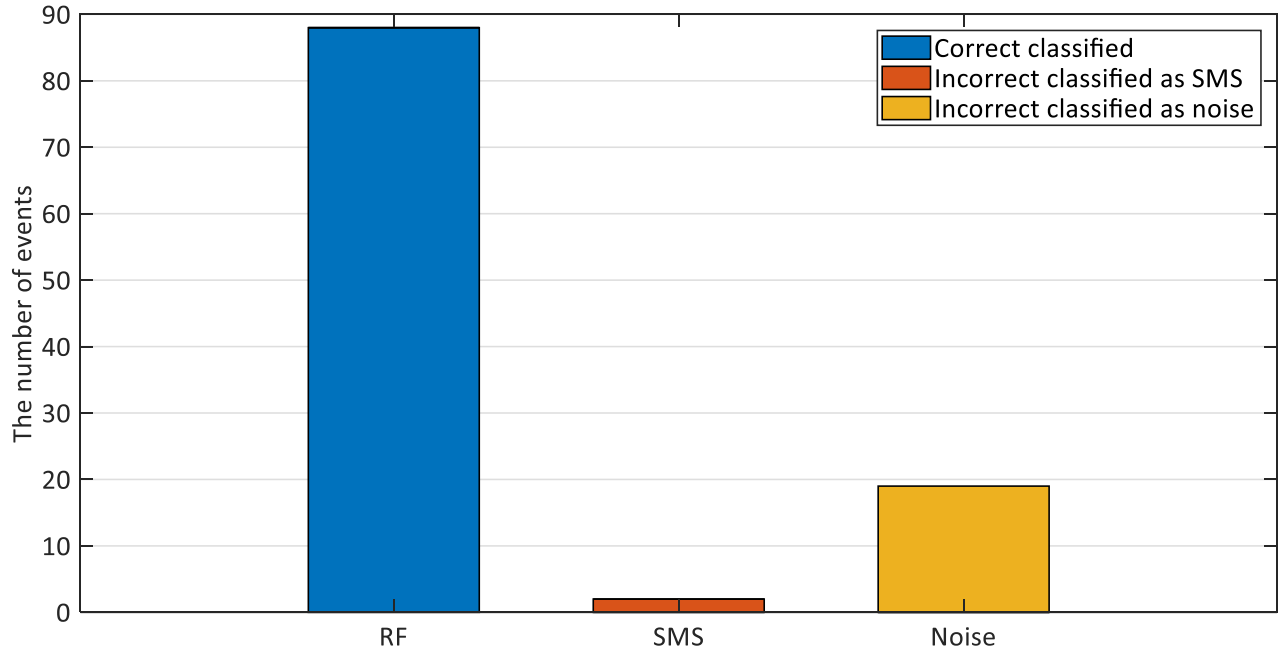


Figure 65. The classification result of RF by DESTRO in artificial released rockfall test.

5.5 Conclusions and discussions

In DESTRO design, we compared the differences and performances of the STA/LTA method and cross-correlation method, and the most traditional and widely used STA/LTA method was chosen in the DESTRO code because of a) the processing stability with raw monitoring data, b) the flexible parameters. In a signal trace for detection evaluation test, 30 events included are fully detected, and average onset time error is 0.22 seconds. That shows good performances in event detection and onset time picking. Nevertheless, the method STA/LTA also presents some difficulty in separating different events and defining the ends of two nearly coincidental events, even though two extra parameters were defined, *MINevent* and *MINinterval*.

Five key features (F_m , R_{fv} , A_m , R_f , and R_a) and four complementary features (E_a , D , R_{ea} , and N_p) are defined to classify events. Taking into account the spectral attributes, seismic events could be classified into high-frequency and low-frequency events, while with event-power attributes, the events could be classified into powerful events (EQ and RF) and weak events (TR and MS). The network geometry attributes classify events into local (MS and RF) and remote (EQ and TR) events. Finally, the waveform-peaks and durations allow to more precisely distinguish and classify event-types as EQ and RF and EQ and TR, respectively. Most of these features are extracted from signal traces precisely and applied very well, except the waveform-peaks and durations. In fact, it is difficult to pick an event’s ending time, even though the lengths of triggered samples are replaced by the true durations. Moreover, in this study, the waveform-peaks are introduced to describe waveform, but this still does not solve very well the computation of the waveform-peaks due to the amplitude threshold chosen and the strong variation of amplitudes of different events.

In general, the five key features performed very well, but the four complementary features should be improved to find a more relevant relationship with amplitude. To classify the events by integrating all the signal trace features from multiple components and multiple stations, three-step classifier (classifier S, classifier C, and

classifier M) are designed and performed in coordination. Classifier S integrates the seismic feature matrixes over time and classified each component as initial event-types. Then, classifier C integrates all the events detected in three components of one station and classifies them into primary event-types. Finally, classifier M, by introducing a secondary event type to define the event influence scale, integrates all the events detected by the monitoring network.

In addition to using DESTRO in detection and classifier design, more studies should be performed on the following topics: a) six event types (EQ, TR, SMS, MS, RF and UN) are defined in DESTRO, but only EQ and RF are confirmed with the INGV database and an artificial rockfall test, respectively, and MS and SMS, representing rock cracking or tiny block falls, were not confirmed in the laboratory or with field testing (Senfaute et al., 2009; Lu et al., 2012, 2013 and Coviello, et al., 2015); b) the weights of features for classifier S were modified from the distribution of seismic features in the training database, and the training database is not sufficiently relevant and has some bias; therefore, a more relevant and larger database or more cases should be used in the future. DESTRO is especially applied in rock slope seismic monitoring combines with earthquake monitoring. This approach is useful for rock mass dynamic monitoring, not only for the surface but also the subsurface, even in slope instability forecasting and risk evaluation in the future when MSs are checked in the laboratory and field tests. Moreover, because DESTRO can separate the event types of earthquakes and rockfalls, the method would also be useful in defining the relationship between rockfalls or microcracking and earthquakes or meteorological events in earthquake prone areas.

6. Slope susceptible area mapping and risk early warning studies

The general framework proposed in this study is based on the observation that the occurrence of rockfall and small landslides increases with time prior to a larger failure (Huggel et al., 2005; Rosser et al., 2007; Szwedzicki, 2003). Moreover, since Suwa (1991) and Suwa et al. (1991) suggest that the magnitude of the ultimate failure is proportional to the level of precursory behavior, this introduces a dependence on the scale of the precursory events (Rosser et al., 2007). This phenomenon has been validated also for volcanic eruptions (that obey to the same pre-collapse behaviors as landslides, as demonstrated by Voight, 1988) by the long-period observation of Hibert (2017b) that continuously monitored Piton de la Fournaise volcano using seismic and video cameras, analyzed the temporal evolution of the daily number of rockfalls from 2007 to 2011, and found that the most active period, in terms of both the number of rockfalls occurring and the volumes of material displaced, was the one immediately preceding the collapse of the Dolomieu crater. For this reason, instead of using the frequency of rockfall events as a proxy for predicting a larger failure, the accumulated energy recorded by a seismic network when the rock hits the ground (and which is a function of the volume) is employed in this thesis.

6.1 Risk early warning methodology

Consistently with Voight (1988), who extended the application of the Fukuzono (1985) method to a set of different variables, among which seismic quantities, the inverse number of this parameter is used in a modified version of the classic Fukuzono-Voight model. In this case, the accumulated energy A_e (i.e. the total measured energy relative to all the rockfall impacts measured in m^2/s^2 in a certain time window; see the next section for a quantitative definition) is used. The inverse of the accumulated energy ($1/A_e$) is then plotted as a line against time. The time when the extrapolated line tends to zero, corresponds with the forecasted time of failure. Fukuzono and Voight use the derivative of the parameter of choice (i.e. velocity in case the parameter is accumulated displacement). Here the accumulated energy is used instead of the energy rate because the increase in accumulated energy can be so steep (increasing by up to four orders of magnitude) that the linear regression can be easily obtained without calculating the derivative, which only introduces more noise.

Since increases in A_e giving birth to possible linear fitting of the $1/A_e$ curve are frequent, the inverse line method is only implemented whenever the increase of A_e (or ΔA_e) in a reference time window (in this case 1 hour) exceeds a certain empirical threshold.

As long as ΔA_e is still over the threshold the warning is maintained, indicating that the energy in the system calculated in the reference time window is still high.

The whole framework is illustrated in Figure 66 and described in detail in the next section. To perform this framework, the first step is transforming seismic data recorded by the instruments into a data format that can be processed in MATLAB, in order to detect and classify the different seismic events by a rockfall detection and classification model, and to extract all the seismic signals and features of the rockfalls, such as onset time, duration etc.; then, A_e and ΔA_e are calculated and, if ΔA_e exceeds the threshold, $1/A_e$ is calculated, a time of failure is automatically extrapolated and a warning time declared. In parallel, as soon as the time of failure is computed, all the rockfalls detected in the last one hour before the triggering of the first alarm time are localized in a topographical map to find the susceptible area from where the events probably originated.

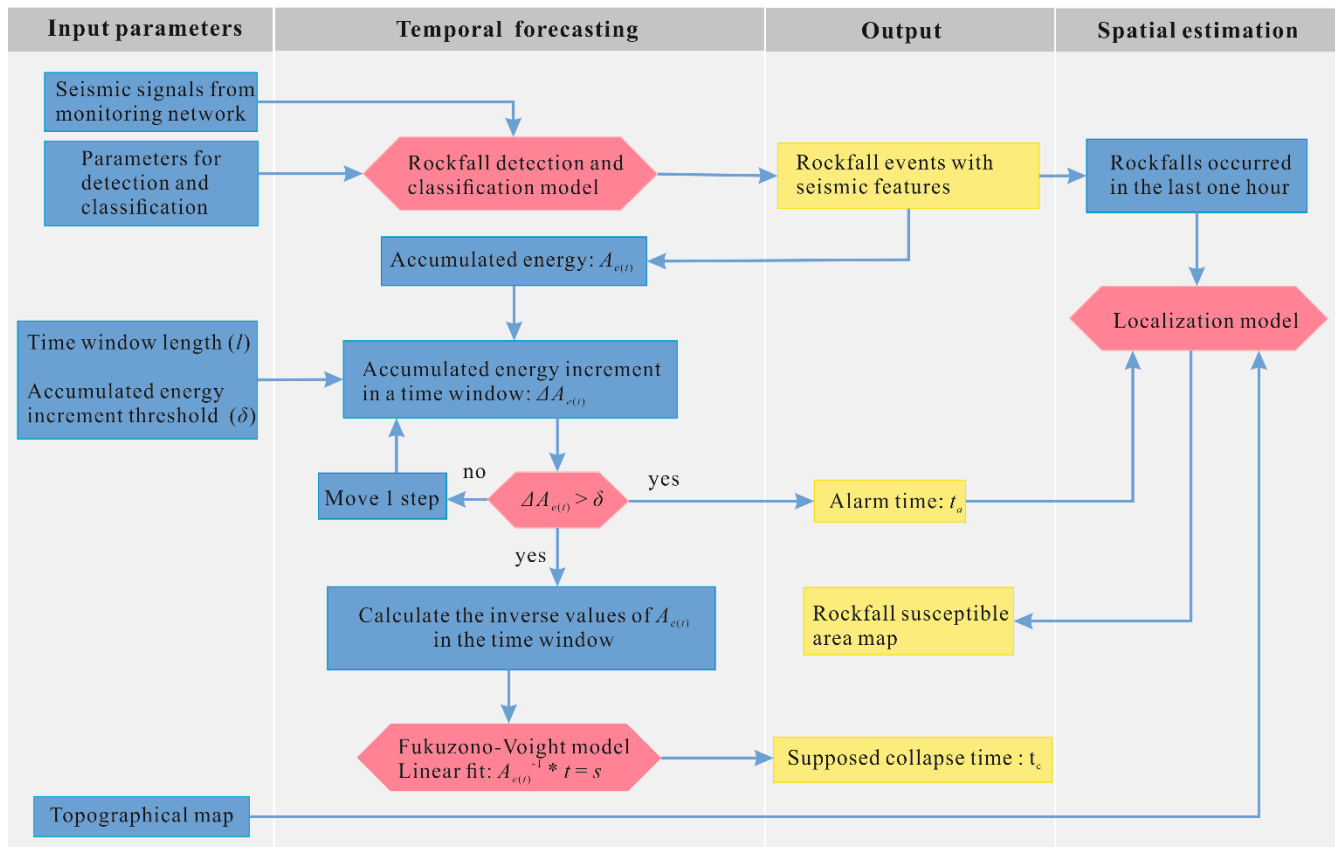


Figure 66. The framework of rockfall spatiotemporal early warning.

From Figure 67-Figure 70, the examples of rockfall secondary event type: RF-P, RF-vL, RF-L, RF-S, are presented. Each figure shows the rockfall original signal traces that were recorded in three components: from east-west, north-south and up-down within one station. The red lines in each figure are the onset time and ending time picked by an ad hoc program, DESTRO, for rockfall detection and classification using seismic monitoring.

When all seismic events occurred in that monitoring period are detected and classified, we extract their seismic features, such as onset times, durations and seismic signal traces, etc. to make polarization and localization in the study area, and do slope susceptible area mapping and early warning. Significantly, in seismic event polarization and localization, more seismic stations are employed, more precisely of results would be obtained.

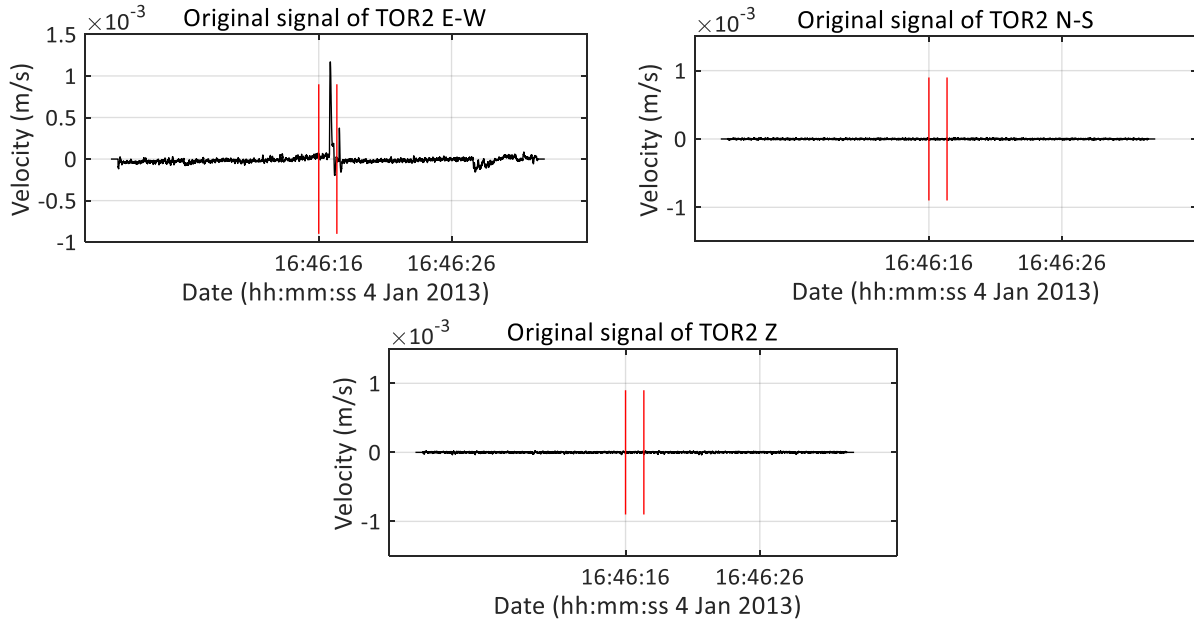


Figure 67. The original signals of RF-P event in TOR2, the event that classified correctly only by one component TOR2 E-W (ID number: RF = 0.5), and the other components are undetected. (red lines are automatic detected onset time and ending time, respectively)

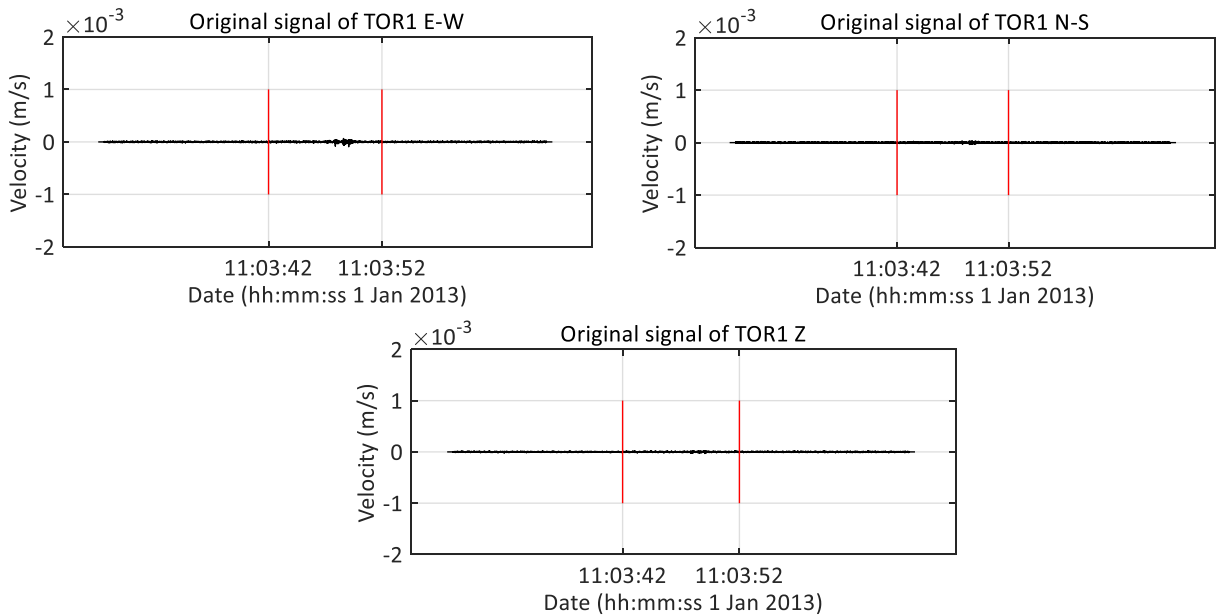


Figure 68(1). The original signal of RF-vL event in TOR1, the event was classified correctly by three components in one station, TOR4, (ID number: RF = 5), and the event was classified as SMS event-type in TOR1 and TOR2, since the low amplitude. (red lines are automatic detected onset time and ending time, respectively)

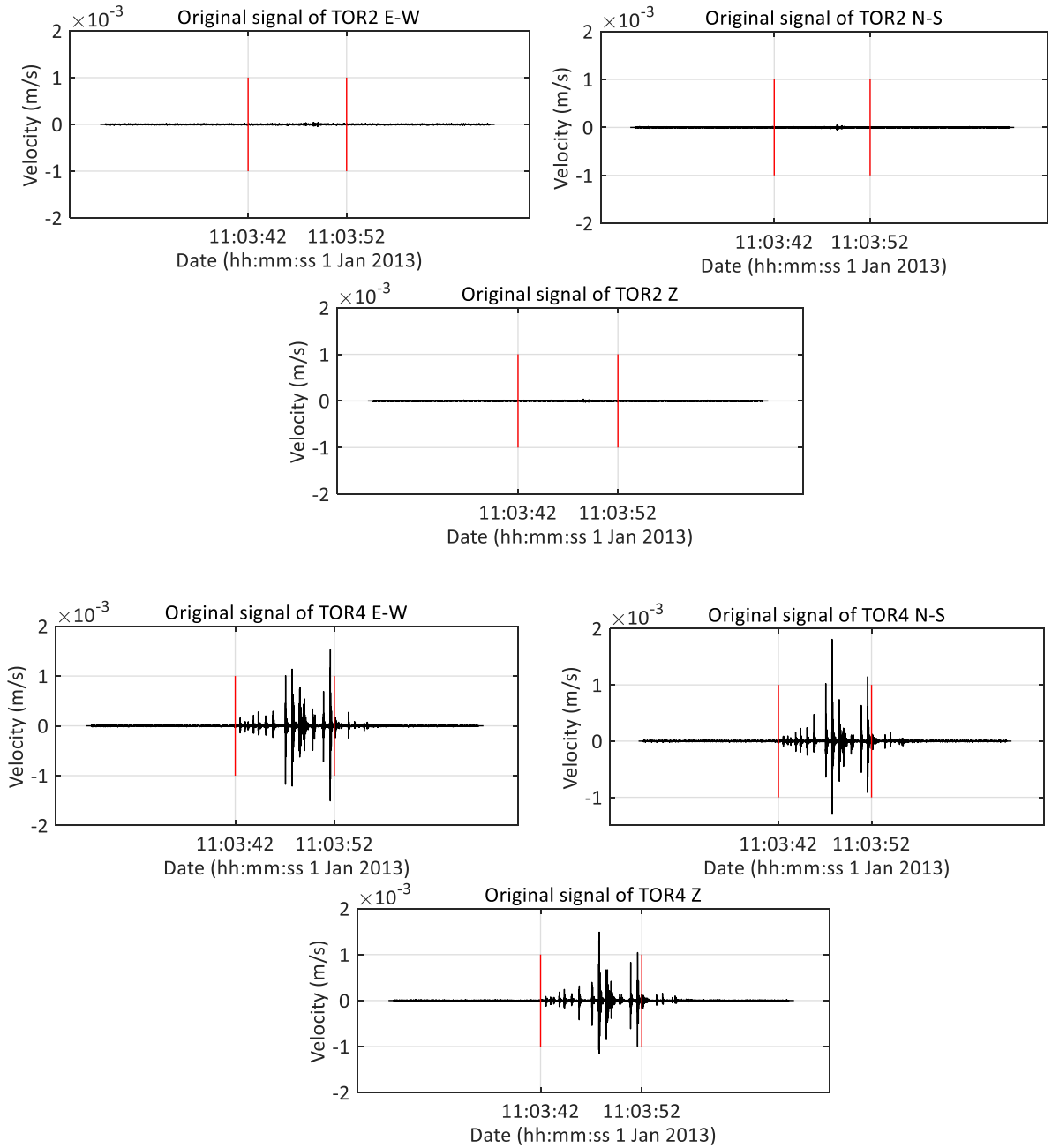


Figure 67(2). The original signals of RF-vL event in TOR2 and TOR4, the event was classified correctly by three components in one station, TOR4, (ID number: RF = 5), and the event was classified as SMS event-type in TOR1 and TOR2, since the low amplitude. (red lines are automatic detected onset time and ending time, respectively)

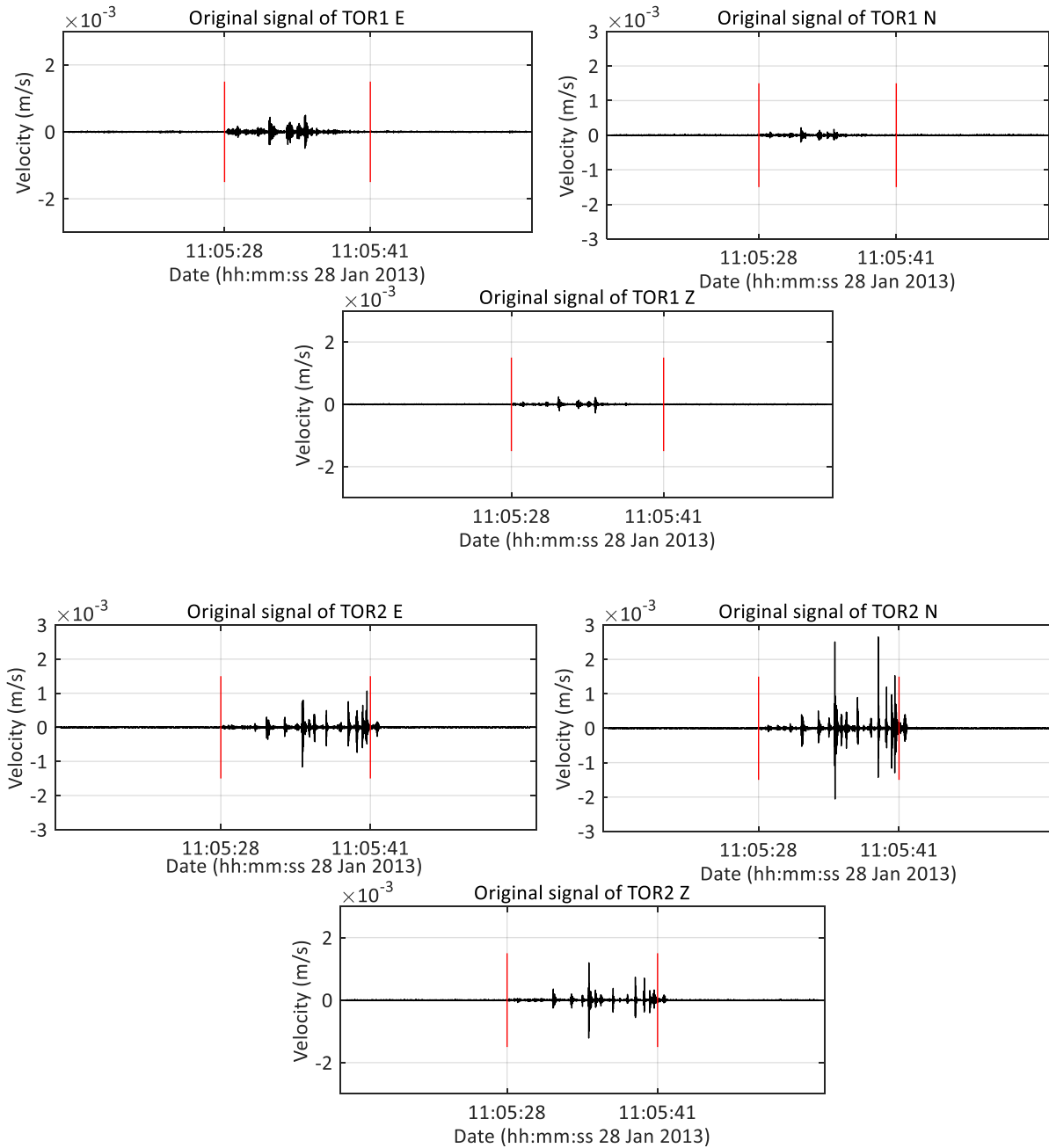


Figure 69(1). The original signals of RF-L event in TOR1 and TOR2, the event was classified correctly by two stations, TOR2, TOR4, (ID number: RF = 50), and the event detected in TOR1 and TOR3 were classified as SMS event-type and EQ event-type, respectively, since the low amplitude and frequency. (red lines are automatic detected onset time and ending time, respectively)

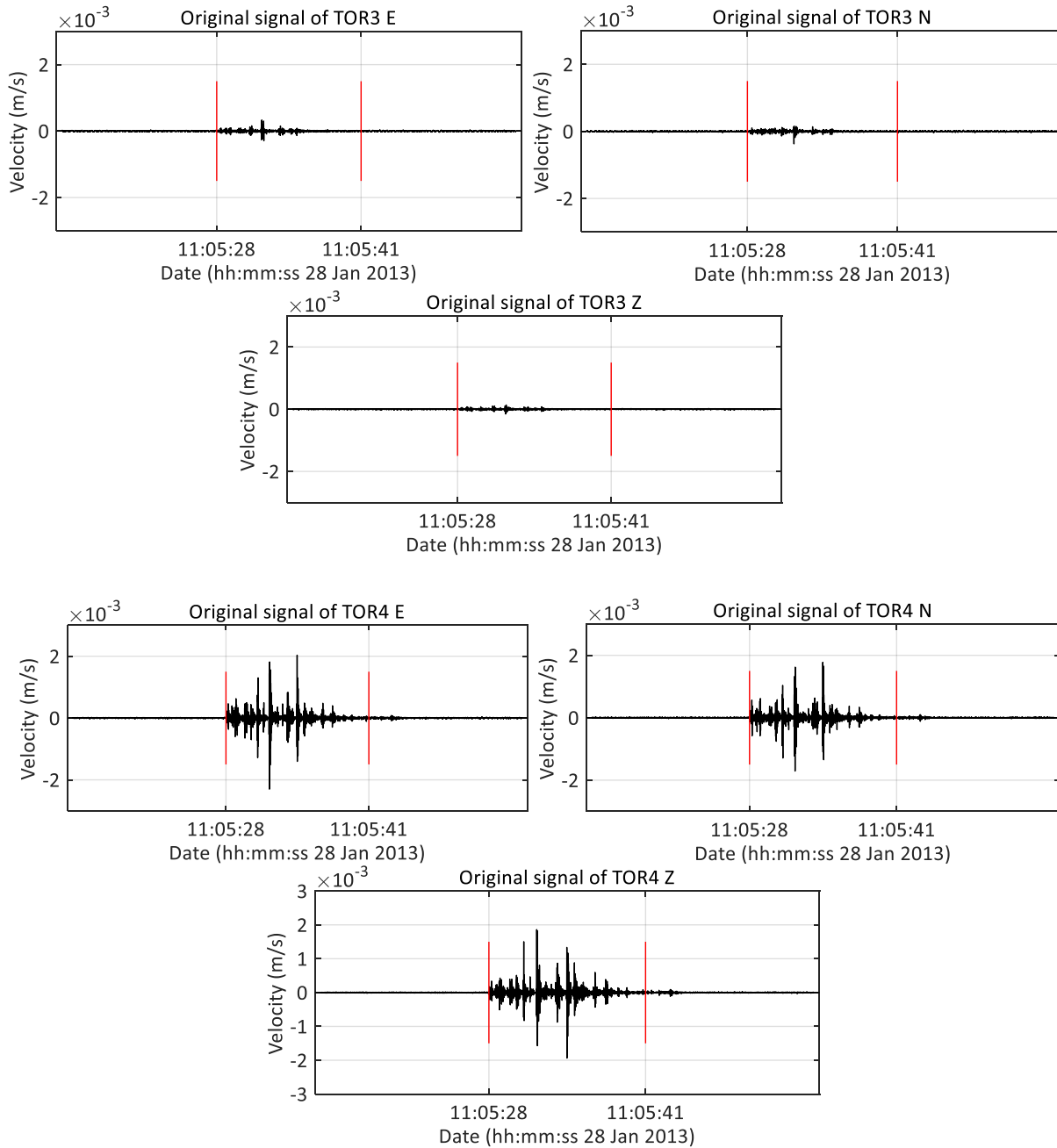


Figure 68(2). The original signals of RF-L event in TOR3 and TOR4, the event was classified correctly by two stations, TOR2, TOR4, (ID number: RF = 50), and the event detected in TOR1 and TOR3 were classified as SMS event-type and EQ event-type, respectively, since the low amplitude and frequency. (red lines are automatic detected onset time and ending time, respectively)

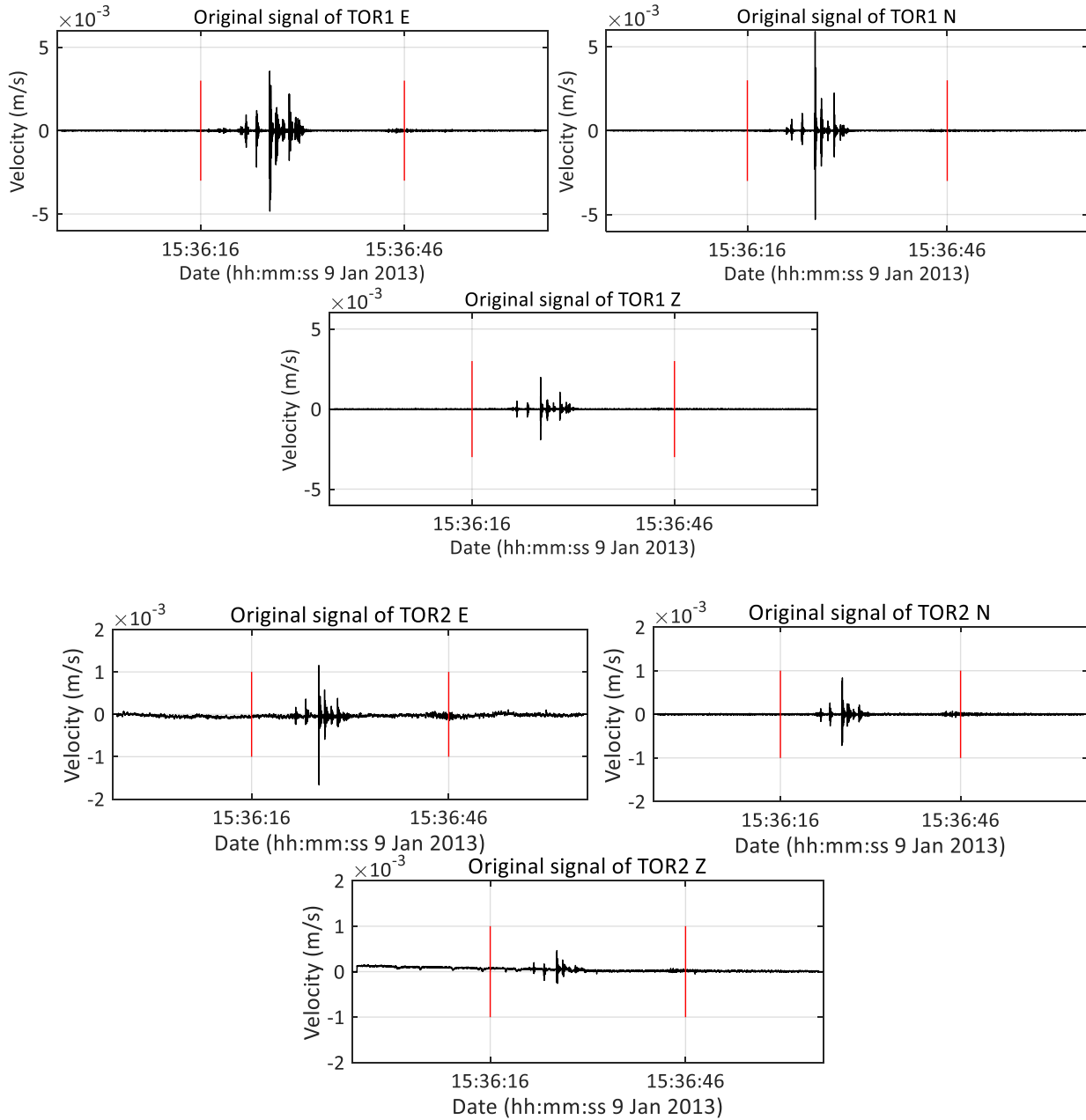


Figure 70(1). The original signals of RF-S event in TOR1 and TOR2, the event was classified correctly by three stations, TOR1, TOR2, TOR4, (ID number: RF = 500), and the event was classified as SMS event-type in TOR3, since the low amplitude. (red lines are automatic detected onset time and ending time, respectively)

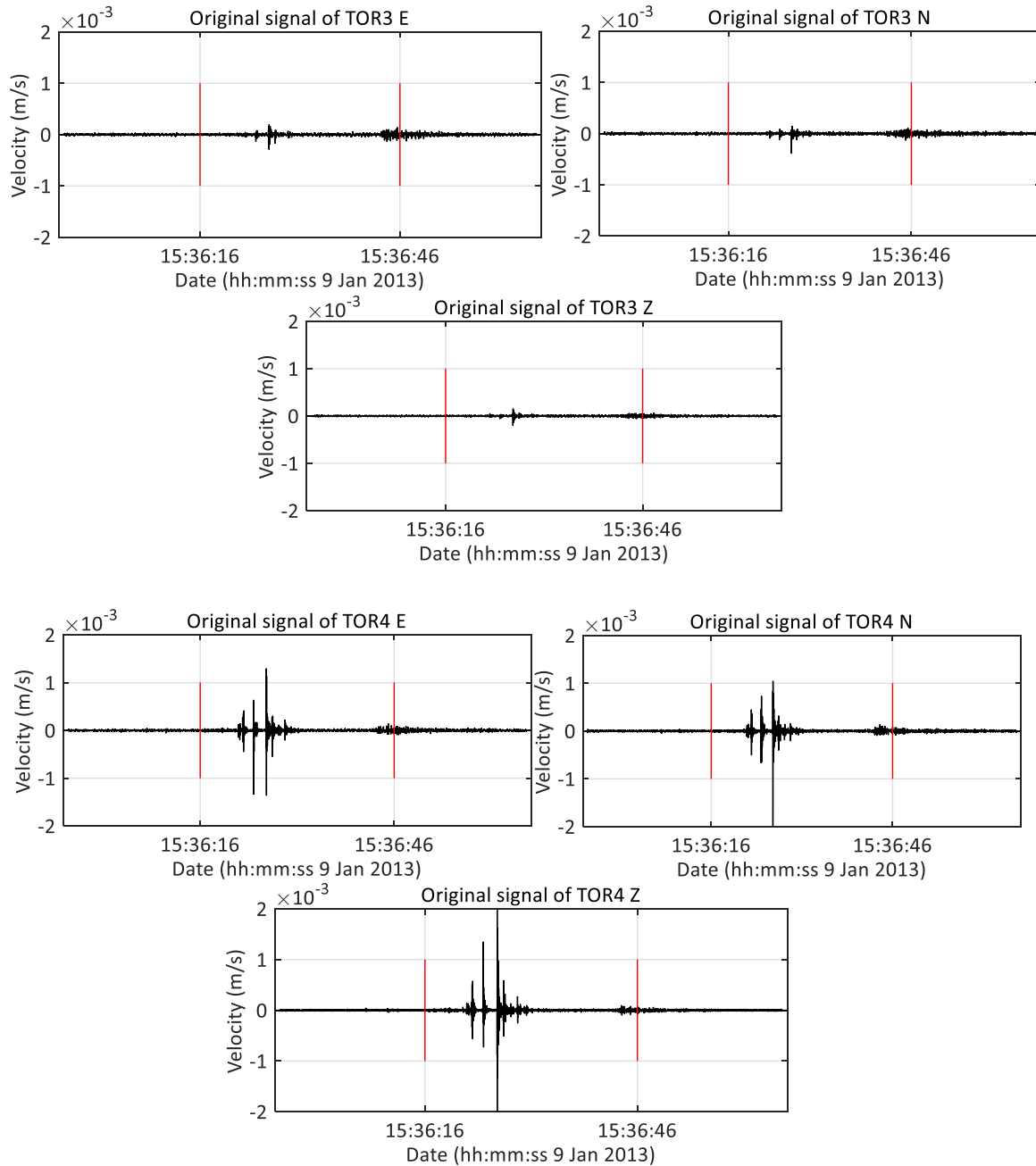


Figure 69(2). The original signals of RF-S event in TOR3 and TOR4, the event was classified correctly by three stations, TOR1, TOR2, TOR4, (ID number: RF = 500), and the event was classified as SMS event-type in TOR3, since the low amplitude. (red lines are automatic detected onset time and ending time, respectively)

6.1.1 Temporal forecasting

Let us assume that a rockfall event series (R_1, R_2, \dots, R_t) is detected in the time-period $(t_0 - t)$. Instead of the real event source energy, a parameter represented by the sum of the relative seismic energy (E_{net}) , measured in m^2/s^2 , recorded through the seismic network, is adopted in this study, to overcome the calculation errors of the environmental influence and the effects due to energy loss through propagation attenuation, rock fragmentation and heat generation (Amitrano et al. 2005; Dammeier et al. 2011). Therefore, the sum of their seismic energy is

E_1, E_2, \dots, E_k , respectively. Assuming one rockfall’s seismic signal time-series recorded in component c and station s is: $X_{sc1}, X_{sc2}, \dots, X_{scn}$.

There are four three-component geophones employed in this case, so the sum of the seismic energy of one rockfall (E_{net}) and the accumulated energy of all the rockfalls ($A_{e(t)}$) from time t_0 to t , respectively, are:

$$E_{net} = \sum_{s=1}^{s=4} \sum_{c=1}^{c=3} \sum_{i=1}^{i=N} x_{sci}^2 \quad (49)$$

$$A_{e(t)} = \sum_{k=1}^{k=M(t)} E_k \quad (50)$$

Where i, j, k , and s are the number of seismic samples, components, seismic stations, and rockfalls, respectively.

In order to trigger the calculation of the time of failure, a sliding time window is created, and the accumulated energy increment ($\Delta A_{e(t)}$) in that sliding window at time t is calculated as discussed before. This parameter represents a threshold below which the forecasting methods are not implemented because they would probably trigger false alarms. Here the length of the sliding window is set as 1 hour (the yellow in Figure 71). and stepped in 1 minute. The accumulated energy increment at time t is calculated as in Equation 51.

$$\Delta A_{e(t)} = \sum_{k=t-1h}^{k=t} A_{e(k)} \quad (51)$$

The time when $\Delta A_{e(t)}$ exceeds a certain threshold in a certain time (here called ‘alarm time’, t_a) is shown as red circles in Figure 71.

The fundamental law of failure material of Fukuzono-Voight model is presented in Equation (52) (Fukuzono 1985; Voight 1988). As demonstrated by Voight, the seismic quantities (Ω) (such as the square root of cumulative energy release) is an observable quantity suitable for early warning. Similarly, this model was also applied in the studies of Amitrano et al. (2005). Therefore, in this case, the accumulated energy (A_e) of rockfalls, is adopted. Generally, this observable quantity should represent Ω and the forecasting method of Fukuzono should use the inverse of $\dot{\Omega}$ against time (for example, if Ω is the displacement, the forecasting is made through the inverse velocity). In this case, since A_e is already characterized by very abrupt accelerations, extrapolating the $1/A_e$ line until it intercepts the time axis gives approximately the same results as using the inverse of the rate of A_e , only the rate of A_e generates a much noisier time series (Figure 71).

$$\dot{\Omega}^{-\alpha} \cdot \ddot{\Omega} - A = 0 \quad (52)$$

In practice, once the first t_a is declared, a linear fitting processing is initialized using $A_{e(t)}^{-1}$ (as Equation 53) from time $t_a - 1h$ to t_a in a sliding window (the yellow window in Figure 71) to obtain the slope (s) of the linear fitting line. Finally, the early warning function is Equation 54 with the y-axis coordinate of the first alarm time ($\frac{1}{A_{e(t_a)+0.99}}$), and the supposed collapse time (t_c) is calibrated as Equation 55. The only function of the addition of 0.99 to the equation is a useful artifice to show the results (e.g. Figure 71) more clearly since A_e of rockfalls measured in m^2/s^2 is typically a very small number (in the order of $10^{-2} - 10^{-5}$), and the addition of 0.99 keeps the results close to 1. The early warning sketch is shown in Figure 71.

$$(s) = \text{linear fit} \left(\frac{1}{A_{e(t-1h)}}, \frac{1}{A_{e(t-1h+1)}}, \dots, \frac{1}{A_{e(t)}} \right) \quad (53)$$

$$s(t_c - t_a) + \frac{1}{A_e(t_a)+0.99} = 0 \quad (54)$$

$$t_c = t_a - \frac{1}{s(A_e(t_a)+0.99)} \quad (55)$$

where the lead time will be $t_c - t_a$, and if we define t_{c2} as the last forecasted time of collapse calculated at the last alarm time t_{a2} , the warning period will be $t_{c2} - t_a$. The linear fit is performed with the *polyfit* function in MATLAB.

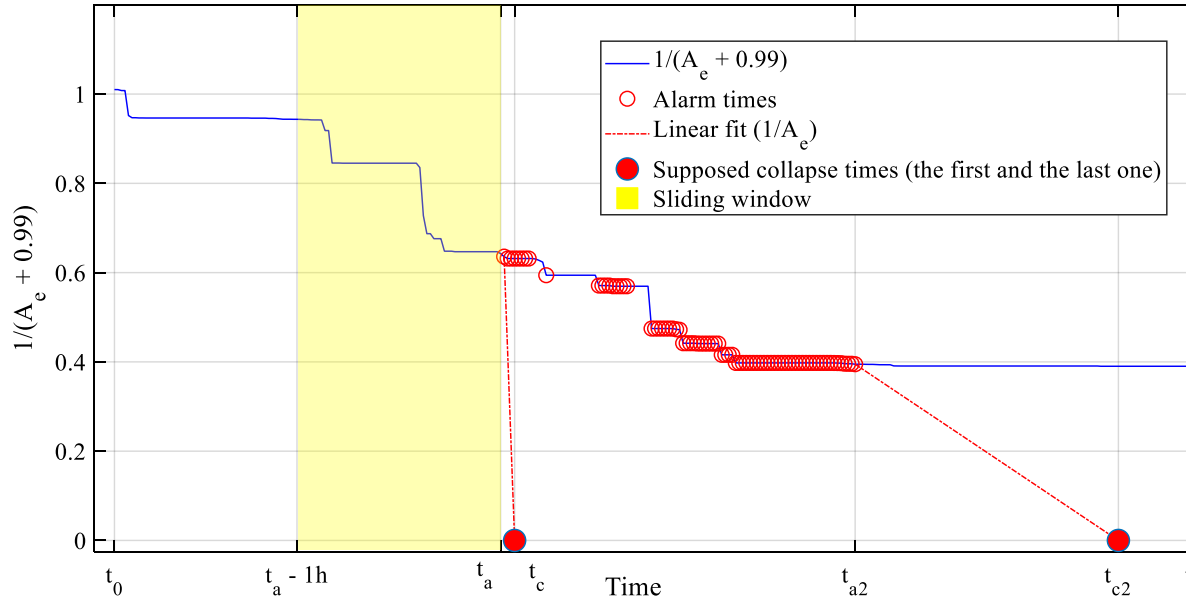


Figure 71. A sketch for collapsing time forecasting with experimental data. The blue dashed line in the sliding window is the inverse value of accumulated energy ($1/A_e$) for linear fitting, and the red dashed line is the collapsing prediction line.

6.1.2 Spatial estimation

As soon as the alarm time and forecasted collapse times are calculated, all the rockfall events that occurred in the last one hour can be localized in a topographic map and the susceptible area can be found consequently.

In this case, the method of seismic polarization (polarization bearing, P-B method) was adopted for rockfall localization. The method uses the polarization from a three-component sensor to calculate the source back azimuth through finding the correct P wave band from event signal, which is commonly used in earthquake localization (Flinn, 1965; Jurkevics, 1988). Vilajosana et al. (2008) and Guinau et al. (2019) extended the technique to rockfall localization.

Starting from this point, we optimized the P-B method with an overdetermined matrix computing in geophone network and proposed a confidence weight for each sensor according to the received signal quality and the reliability of back-azimuths calculated. We also compared three marker parameters for proper frequency bands selection in seismic polarization: energy, rectilinearity and special permanent frequency band, and finally suggest the first 30 powerful frequency bands to perform the P-B localization (P-B-30E). One example of P-B-30E localization of an artificial rockfall from an in-situ test consisting in manually released rockfall is shown in Figure 72. In this case, four impacts were picked and automatically localized in a topographic map as plotted in Figure 72 (b). All the estimated positions are almost distributed along the real rockfall trajectory; the maximum error is impact #4 with 48.2 m, and the minimum error is impact #1 with 10.2 m.

Moreover, the early warning framework can also be complemented with alternative or complementary localization methods, such as arrival times and grip search methods.

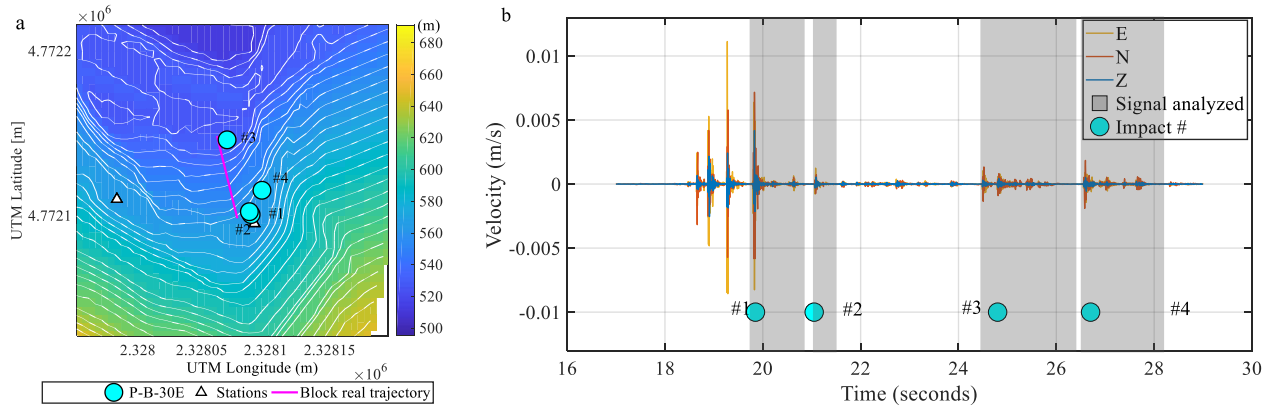


Figure 72. (a) An artificial rockfall moving trajectory localized with the P-B-30E method. The pink line indicates the real block trajectory measured in situ. The cyan spots a represent each block impact position localized with the stations (black triangles); (b) the original signal trace of the same artificial rockfall with highlighted in grey the impacts and the traces analyzed with the polarization method.

6.2 Susceptible area mapping

For slope stability evaluation and susceptibility area mapping, data from a significant monitoring time period (1st – 31st January 2013), are chosen from the seven-month monitoring period. All the data are examined with an ad-hoc program to detect and classify all the seismic events that occurred in that monitoring period (Feng et al. 2019b). The events have been grouped in the following classes: earthquake (EQ), rockfall (RF), tectonic tremor (TR); other events (like rock micro-cracking) and noise are also detected and classified but are not considered in our analysis. In this one-month period, 1322 EQ, 585 TR, and 428 RF were detected. It should be pointed out that among RF events also very small-scale failures (i.e. small rolling stones) are included. In detail, considering the scales of event classified for RF, there are 416 very local events (vL), 8 local events (L), and 4 slope scale events (S). The detection and classification results are plotted in Figure 73.

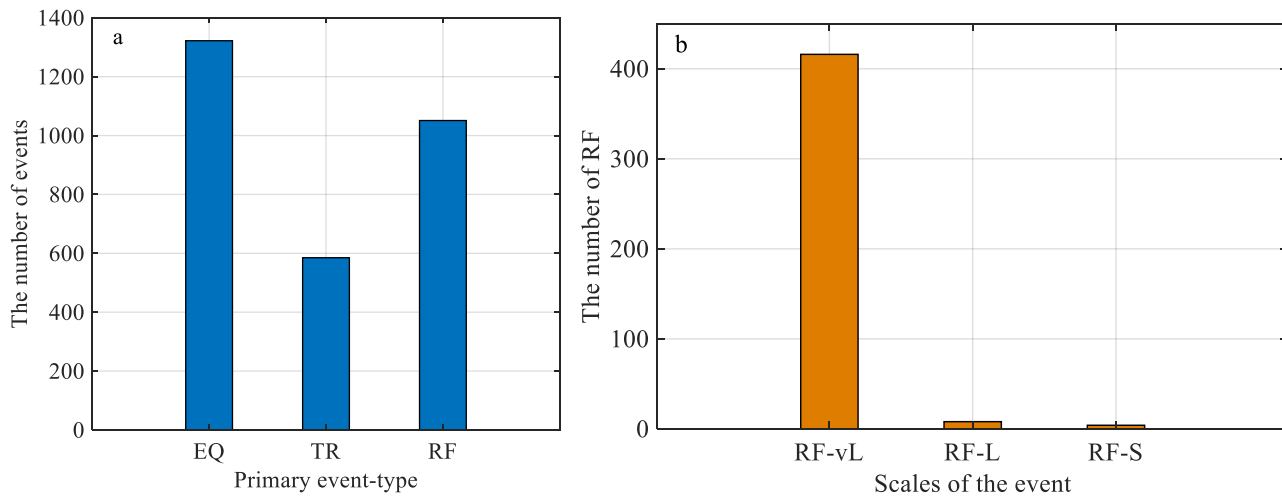


Figure 73. panel a: all the seismic events detection and classification results relative to the time period 1st – 31st January 2013; panel b: distribution of RF in scales.

To better understand the slope stability evolution and seismic events occurrence frequency, the distribution of detected seismic events (e.g. earthquakes and rockfalls) and their parameter A_e are plotted in Figure 74 and Figure 75, respectively. In Figure 74, each event is represented with a point whose diameter is proportional to its seismic spectral maximum amplitude; a maximum dimension was set corresponding to a fixed threshold. The different scales of RF are marked with different colors. In Figure 75, the daily precipitation and accumulated precipitation in this month are also shown with A_e .

From the results of Figure 74 and Figure 75, the curves of the accumulated number and A_e of RF display a step-shaped behavior, with the steps indicating the sudden occurrence of many RF in a short time. Usually, a series of vL events happened before L and S events. Moreover, we find from Figure 7 that the maximum precipitation and its maximum increment happened 13 hours before the maximum increasing of rockfall events, and there is no clear correlation between earthquake and the occurrence of rockfall events or other micro-seismic events in this study. This suggests that, in this case, the main triggering factors are probably from environmental conditions, such as rainfall.

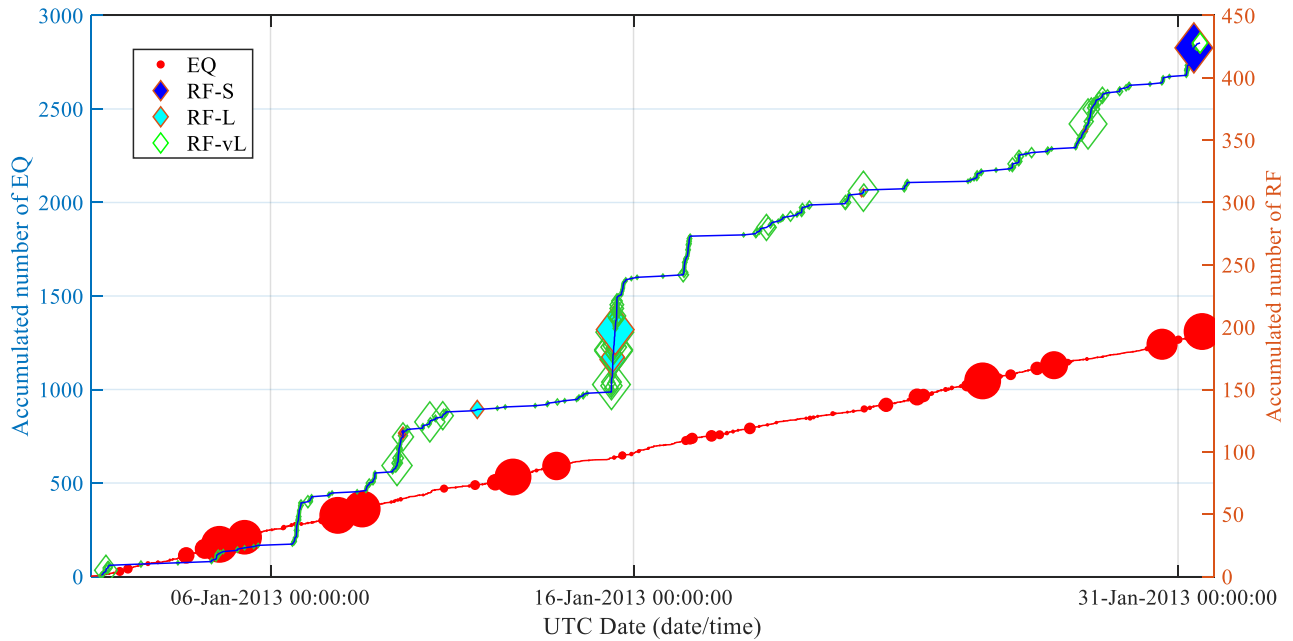


Figure 74. The accumulated number of events detected in the 1st – 31st January 2013 time period. The size of the points is proportional to the recorded seismic energy.

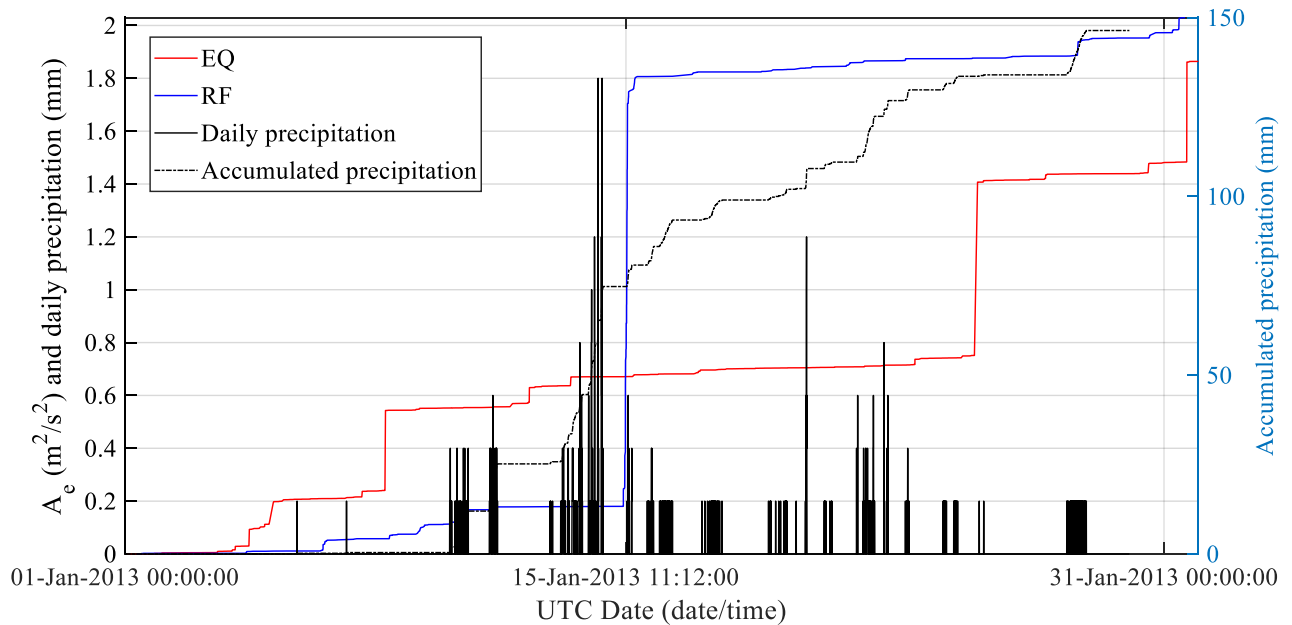


Figure 75. The evolution of E_t of seismic events EQ, MS and RF from 1st to 31st January 2013, and correlation with precipitation.

To set a warning relative to rockfall events, the inverse value of A_e vs time can be calculated in the most active three days of rockfall, between 14th – 16th January 2013. In the presented case, the input parameter of the empirical threshold of ΔA_e in the one-hour sliding window is set to $0.5 \text{ m}^2/\text{s}^2$, and all the time points (stepped in 1 minute) that exceeded $0.5 \text{ m}^2/\text{s}^2$ are marked as t_a (the red circles in Figure 77). The rockfall occurrence frequency of these three days is plotted in Figure 76.

In these three days, 101 RF events were recorded, including five RF-L events (named from I to V in Table 13). Figure 76 clearly shows the increasing rockfall occurrence in a short time period and displays the event IV as the longest and most powerful. The event has been highlighted in a dashed square in both Figure 76 and Figure 77. As visible from the seismic signal of RF-L-IV (Figure 78), plenty of smaller RF are detected before the largest block fall, and many were later induced and were recorded after the large block fall. The rockfall activities occurred in the monitoring area are clearly reconstructed in a seismic record. The relative basic seismic features are shown in Table 13, where the values in Table 13 are the maximum among all the stations.

Furthermore, in this case, the first alarm point and predicted time of collapse are at 11:12 and 11:15 15th January 2013, respectively; and the last alarm time and predicted time of collapse are 12:52 and 14:07 15th January 2013, respectively. Within this warning time frame, two large events (IV and V) occurred at 11:54 and 12:06 respectively, that is 42 and 54 minutes after the first t_a .

Table 13. Basic seismic features of RF-L events occurred in 14th -16th Jan 2013.

Date	Time	Secondary event type	Maximum amplitude (m/s)	Maximum frequency (Hz)	Seismic energy (E) (m^2/s^2)	Duration (s)	Location
2013-01-15	10:20:32	RF-L-I	0.017	88.7	0.027	106.1	Near TOR2
2013-01-15	10:22:35	RF-L-II	0.012	89.0	0.013	11.8	Near TOR2
2013-01-15	10:22:59	RF-L-III	0.014	87.6	0.081	107.6	Near TOR2
2013-01-15	11:54:40	RF-L-IV	0.042	99.9	0.351	336.7	Near TOR4
2013-01-15	12:06:32	RF-L-V	0.002	66.8	0.003	38.9	Near TOR4

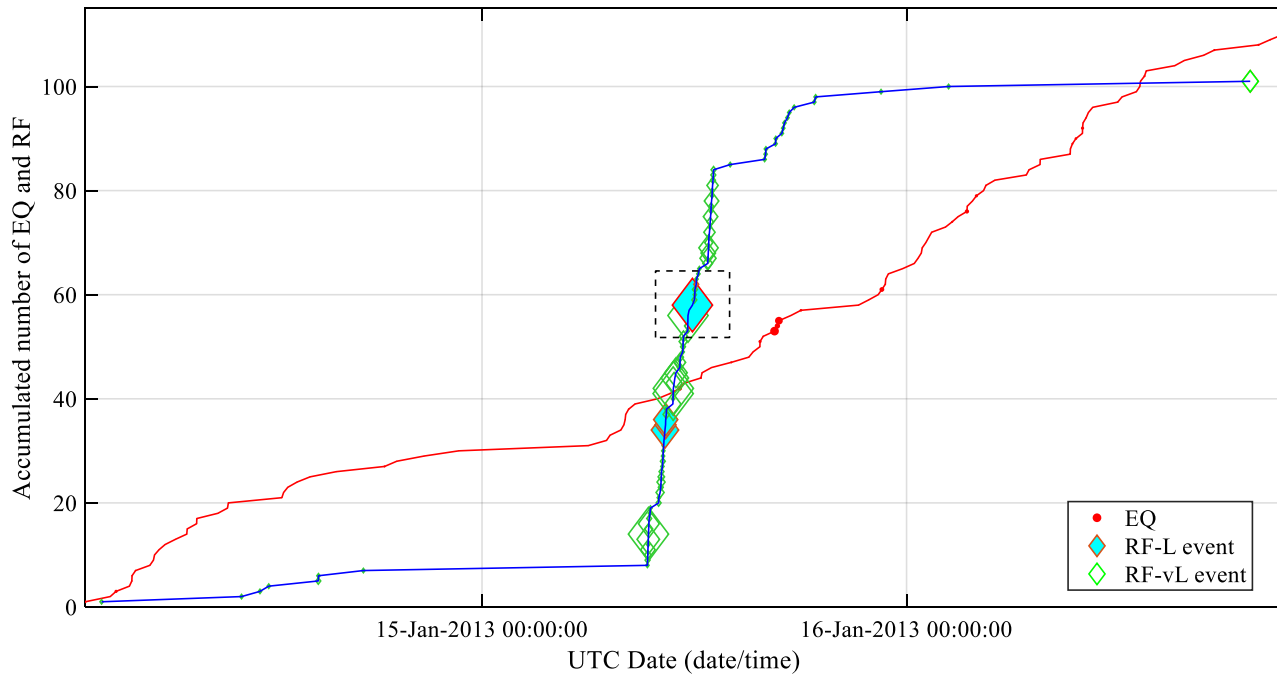


Figure 76. Rockfall and earthquake occurrence frequency in three days, from 14th to 16th January 2013.

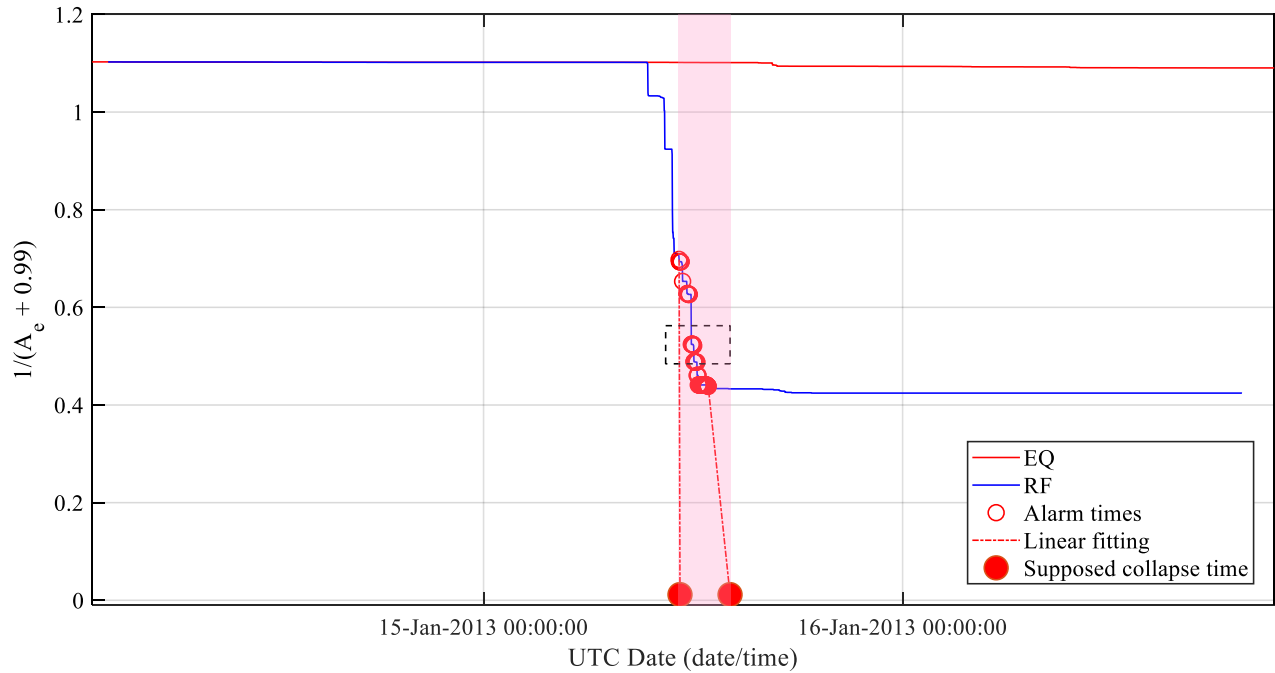


Figure 77. Rockfall early warning from 14th to 16th January 2013; the red point on x-axis is the predicted time of collapse time, and the pink window is the warning time period declared from 14th – 16th January 2013.

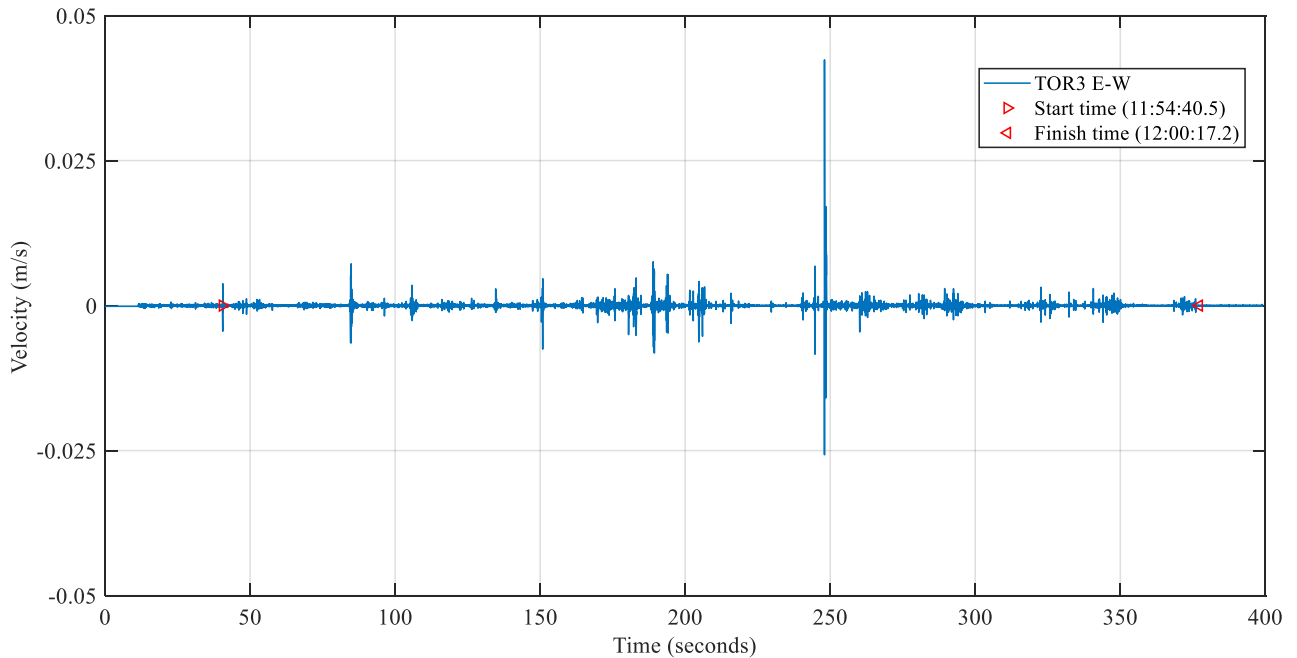


Figure 78. Seismic signal of the largest rockfall (IV) occurred from 14th to 16th January 2013, that highlighted in dash square in Figure 76 and Figure 77.

As soon as the first t_a was declared, all the rockfall events detected in one hour (from $t_a - 1h$ to t_a) before the triggering of the first t_a have been localized with the improved P-B method. Moreover, in the presented case, all the rockfalls occurred in three days (5 RF-L and 100 RF-vL events) are localized in a topographic map to clearly show the susceptible area (the red ellipse Figure 79a)

As visible from the field surveys and the 3D LiDAR scan (Figure 79b), this area is in fact marked by the presence of a debris talus that confirms the susceptibility to rockfalls of this portion of the former quarry (see the red ellipse in Figure 79b). Once the area has been delimited, the early warning system can also be complemented with other countermeasures that would benefit from this spatial information and for example forbid access to the area (especially for active open-pit mines), turn on traffic lights or close endangered streets, automatically activate or intensify monitoring in that area.

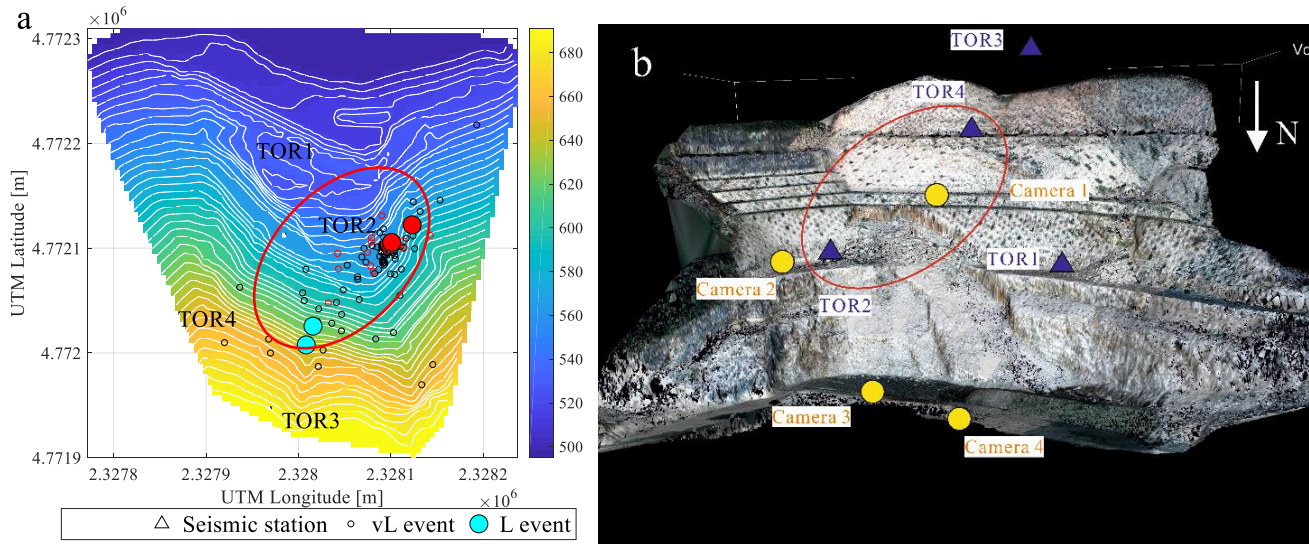


Figure 79. (a) localization result of the rockfalls detected in the time period 14th – 16th January 2013; the red points are the rockfalls occurred one hour before the triggering of the first alarm time (18 RF-vL and 3 RF-L), all concentrated in the red ellipse with the color bar indicating the altitude of the topographical map in meters; b) DEM of Torgiovannetto quarry with resolution of 0.25 m ; the blue triangles represent the seismic stations.

As the methodology applied in time-period 14th – 16th January 2013, the long-period monitoring data from 1st January to 30th June 2013 are analyzed. The inverse value of A_e has been calculated and the evolution of $1/(A_e + 0.99)$ has been analyzed in Figure 80 -Figure 82. A total of six warnings have been identified in these six months, the largest event being the one occurred in January and previously analyzed. However, there is an issue that should be pointed out when performing a long-term (at least a few months) real-time forecasting; in fact, since A_e is a cumulated value, its value is constantly increasing. When A_e is sufficiently high, variations of $1/A_e$ become very small and difficult to notice. Therefore, it is recommended that the value of A_e is reset to zero periodically (e.g. weekly, depending on the state of activity of the slope).

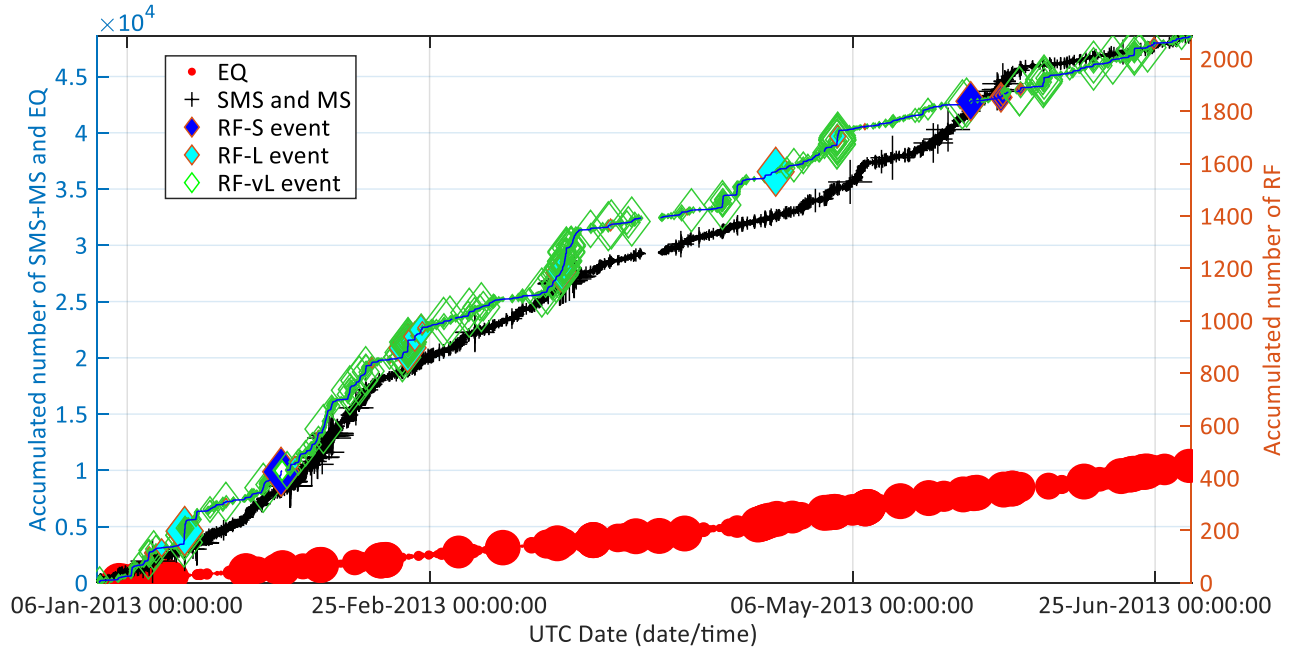


Figure 80. The accumulated number of events detected in the 1st January– 30th June 2013 time period. The size of the points is proportional to the recorded seismic energy.

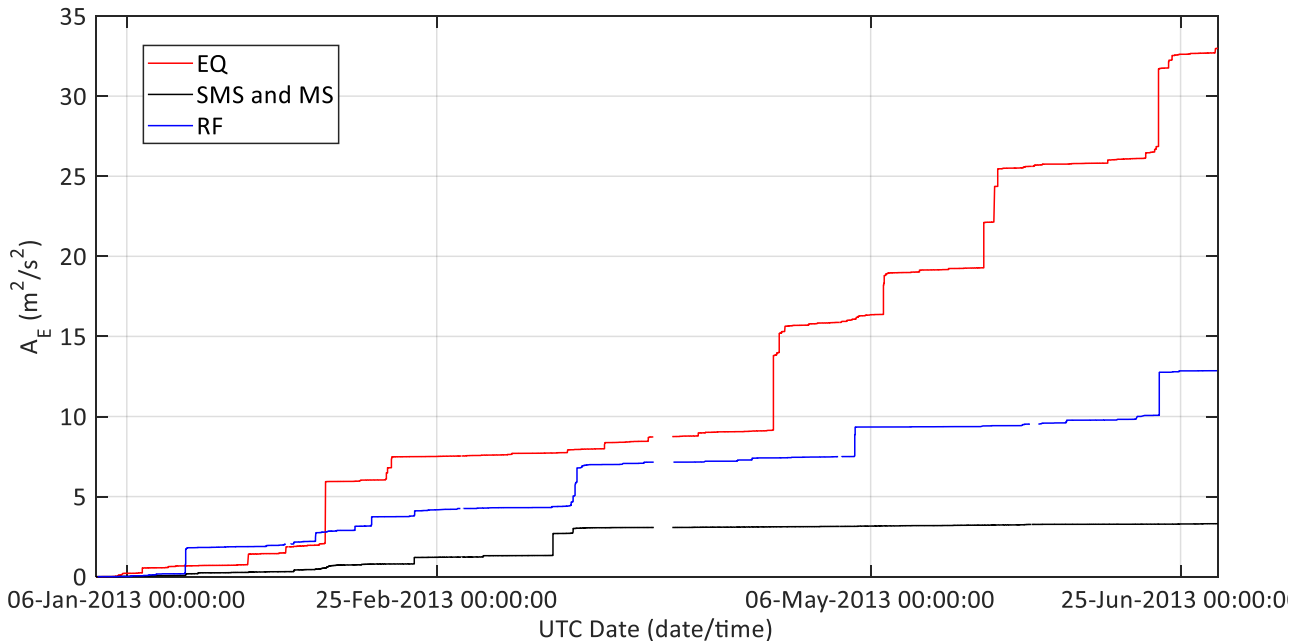


Figure 81. The evolution of E_t of seismic events EQ, MS and RF from 1st January – 30th June 2013.

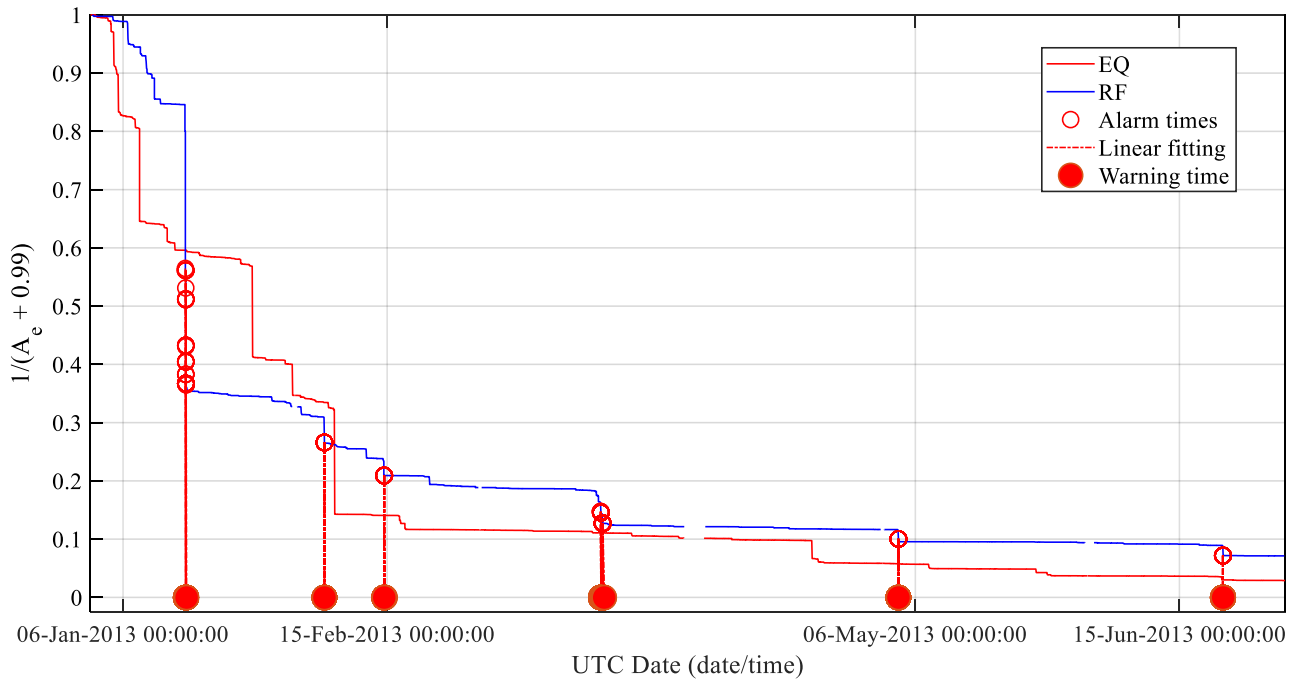


Figure 82. Application of the rockfall forecasting methodology to the 1st January – 30th June 2013 dataset of Torgiovannetto quarry. The monitoring data between 1st and 4th of April are missing due to battery depletion and change.

6.3 Discussions

In this study, a framework for rockfall spatial and temporal early warning using micro-seismic monitoring network was proposed. According to Fukuzono-Voight failure model, an observable quantity of accumulated energy (A_e) of rockfall is adopted for rockfall early warning. Whenever, over a sliding time window, the threshold ΔA_e is exceeded, an alarm time is declared. As confirmed by several studies in literature, an increased amount of rockfalls occurring in a short time period takes place before a larger rockfall and/or collapse. This is represented as an abrupt step in a rockfall occurrence frequency curve against time, which is taken into account as a significant foretell sign of an imminent event. As soon as the first alarm time and consequent time of failure forecast are declared, all the rockfalls occurred in the previous one hour are localized in a topographic map to simultaneously show the rockfall susceptible area.

The monitoring performed by micro-seismic networks is not only specific for slope surface phenomena, but also for subsurface movement or cracking, which can significantly complement the drawbacks of image-based techniques such as satellite or ground-based InSAR. The relative low-cost of geophones applied in this framework make it possible to perform rockfall early warning, for example in mountainous area where transportation lines are at risk.

In the future, the research on this methodology will involve the following issues:

1) for collapsing time prediction, the problem of inverse function, $1/A_e$, as A_e increasing, the $1/A_e$ difference coming smaller, makes barriers for the seismic event evolution visual and collapsing time prediction in the long-term monitoring case, so in this study, a temporary solution has made, it's suggested to update A_e as zero per one-month;

2) in this study, the threshold of ΔA_e ($0.5 \text{ m}^2/\text{s}^2$ in sliding window of one-hour) was used for slope warning alarm point declaration; of course, that is not a universal value for all monitoring cases, and more micro-seismic monitoring cases are required to study the possible variation of this parameter; moreover, the event source energy can also be used for collapse time prediction with more in situ tests performed;

3) The properties of MS detected in this study are still not clear enough. Previously, MS was supposed as rock cracking and its evolution should be correlated with rockfall, but there is no significant correlation between MS events and rockfalls in analysis (the black line and blue line in figures in this section). Possibly, they represent small fragments moving. In the future, more micro-seismic monitoring cases will be performed, and combined with other image-based monitoring techniques, drone or TLS, to validate the seismic event MS and analyze the correlation between seismic events evolution; moreover, thanks to the earthquake detection ability of DESTRO, the methodology proposed will be applied in the correlation research between earthquake and rockfall, and rock cracking evolution in seismic areas.

7. Conclusions and outlook

The goal of the PhD was to develop the knowledge concerning seismic event detection, classification, and the analysis of seismic event series evolution, applied to the micro-seismic monitoring of rockfall. Rockfall hazard is characterized by high frequency occurrence, great destructive damage and virtually no time for evacuation to people and infrastructures, given the lack of noticeable forerunners (such as displacement) and complex mechanism.

It is widely accepted that some unnoticed event (such as crack breaking, small rock fragments falling down) occurring before rockfall could be good indicators of the slope stability evolution, with the seismic noise emitted by those events that can be detected by micro-seismic monitoring. On the other hand, in the monitoring data processing, much staff must still be learnt about how to detect the precursor events and separate it from environment noise, localize the source to find the slope susceptible area and perform risk early warning.

In this context, the critical processing seismic data are derived from seven-month field monitoring case and one artificial released rockfall in situ test in Torgivannetto (Assisi, central Italy), combined with the review of a large number of seismic monitoring cases from literature. Accordingly, the research includes the collection and analysis of field monitoring data and writing of an ad hoc program based on MATLAB. One of the obvious outcomes of this research is that we proposed a complete set of data processing in rockfall seismic monitoring, from data collection, seismic event detection, classification, localization, and risk early warning method. Moreover, the seismic event classification is not only based on the physical mechanism characteristics but also considers the event influence size (or event power). We also done an improvement in localization method with compared the methods of first-arrival times and seismic polarization.

A large part of the thesis is focused on the rockfall seismic feature studies and seismic event classification (Section 4 and Section 5), and the rockfall seismic feature study is the base of classification. In this study, nine seismic features are proposed for rockfall identification, moreover, several seismic features are innovating defined: network geometric attributes (section 5.2.4) including frequency ratio and amplitude ratio play critical roles and performed well in this study. Three classifiers for detection and classification have been designed, respectively for single seismic component, three-component station and monitoring network (section 5.3). As a result, the classification program DESTRO could detect rockfall correctly with the accuracy of 80.7% in the artificial released rockfall test even within considerable man-induced noise. Earthquake have been correctly detected and classified with accuracy of 79.2% with earthquake epicentre distances less than 100 km.

Another important part of this study is presented in section 3.3, where we analysed the methods for seismic event localization, and compared the advantage and disadvantage between two localization methods: time-bearing (onset time first-arrival method) and polarization-bearing (seismic polarization). Concerning the polarization-bearing method, a mark parameter of energy (30E, represented in section 3.3.3) is newly suggested for frequency bands choosing, to improve the accuracy of seismic event localization.

Finally, the last part of the thesis in Section 6 is dedicated to the risk early warning corresponding to the seismic event recognized from the historical monitoring data, and the accumulated seismic energy of received signals has been proposed as a parameter to perform early warning and determine 'alarm points'. Once an 'alarm point' is declared, the supposed risk time would be predicted according to the parameter evolution in the past one hour. In general, this kind of data-review approaches are a research field of potential interest, and share

similarities to how described by Voight (1988) and Fukuzono (1985) with different parameters. They give an opportunity to look for new parameters or variables to be deemed as indicators of impending failure conditions.

Ultimately, micro-seismic monitoring applied in geohazard is a very complex topic and still developing. In landslide seismic monitoring, vast amounts of important information on the characteristics of seismic source could be interpreted from three-axis seismogram (e.g., the event-type, energy, duration, location and event developing process) that not only occurred on surface but also in the subsurface (Deparis et al. 2007; Vilajosana et al. 2008; Helmstetter and Garambois 2010; Hibert et al. 2011 & Coviello et al. 2019). It is useful to find out the dangerous part of a slope, or shear surface and evaluate the stability by seismic monitoring, when all event-types (e.g. crack breaking, rockfall) information has to be interpreted from continuous broadband seismograms. More study cases and long period monitoring are required in the future. In the part of detection and classification, still some issues remain to be addressed and investigated, such as the validation of seismic signal samples of micro-crack breaking noise or the time delay of detection. Also, for polarization and the method for risk early warning, more cases and a longer period of monitoring required are in the future. Any monitoring program and early warning system is effective only if thoroughly calibrated and contextualized in the frame of the on-site slope characteristics and deformation behaviour.

References

- Akhouayri, E. S., Agliz, D., & Atmani, A. (2014). Automatic detection and picking of P-wave arrival in locally stationary noise using cross-correlation. *Digital Signal Processing*, 26, 87-100. DOI: <https://doi.org/10.1016/j.dsp.2013.12.009>
- Akhouayri, E. S., Agliz, D., Zonta, D., & Atmani, A. (2015). A fuzzy expert system for automatic seismic signal classification. *Expert Systems with Applications*, 42(3), 1013-1027. DOI: <https://doi.org/10.1016/j.eswa.2014.08.023>
- Akram, J., & Eaton, D. W. (2016). Refinement of arrival-time picks using a cross-correlation based workflow. *Journal of Applied Geophysics*, 135, 55-66. DOI: <https://doi.org/10.1016/j.jappgeo.2016.09.024>
- Allen, R. V. (1978). Automatic earthquake recognition and timing from single traces. *Bulletin of the Seismological Society of America*, 68(5), 1521-1532.
- Allen R (1982) Automatic phase pickers: their present use and future prospects. *Bulletin of the Seismological Society of America* 72(6): S225-S242
- Allmann BP, Shearer PM, Hauksson E (2008). Spectral discrimination between quarry blasts and earthquakes in Southern California. *Bulletin of the Seismological Society of America* 98(4): 2073-2079. <https://doi.org/10.1785/0120070215>
- Almendros, J., Ibáñez, J.M., Alguacil, G. and Del Pezzo, E., 1999. Array analysis using circular-wave-front geometry: an application to locate the nearby seismo-volcanic source. *Geophysical Journal International*, 136(1), pp.159-170. DOI: <https://doi.org/10.1046/j.1365-246X.1999.00699.x>
- Alta Scuola (2005a) – Studio del fenomeno franoso interessante la cava di Torgiovannetto di Assisi (PG) - Relazione di prima fase.
- Alta Scuola (2005b) – Studio del fenomeno franoso interessante la cava di Torgiovannetto di Assisi (PG) - Relazione di seconda fase.
- Alta Scuola (2006a) – Studio del fenomeno franoso in essere in località Torgiovannetto di Assisi (PG) ed individuazione degli interventi volti alla riduzione del rischio idrogeologico – Relazione finale. Committente: Comunità Montana del Subasio.
- Alta Scuola (2006b) – Studio del fenomeno franoso in essere in località Torgiovannetto di Assisi (PG) ed individuazione degli interventi volti alla riduzione del rischio idrogeologico – Integrazione alla relazione finale.
- Amitrano D, Grasso JR, Senfaute G (2005) Seismic precursory patterns before a cliff collapse and critical point phenomena. *Geophysical Research Letters* 32(8): L08314. <https://doi.org/10.1029/2004GL022270>
- Antolini F, Barla M, Gigli G, et al. (2016) Combined finite–discrete numerical modeling of runout of the Torgiovannetto di Assisi rockslide in central Italy. *International Journal of Geomechanics* 16(6): 04016019. [https://doi.org/10.1061/\(ASCE\)GM.1943-5622.0000646](https://doi.org/10.1061/(ASCE)GM.1943-5622.0000646)

- Antolini F, Barla M, Gigli G, et al. (2016) Combined finite–discrete numerical modeling of runout of the Torgiovanetto di Assisi rockslide in central Italy. *International Journal of Geomechanics* 16(6): 04016019. DOI: [https://doi.org/10.1061/\(ASCE\)GM.1943-5622.0000646](https://doi.org/10.1061/(ASCE)GM.1943-5622.0000646)
- Arosio, D., Longoni, L., Papini, M., Scaioni, M., Zanzi, L., & Alba, M. (2009). Towards rockfall forecasting through observing deformations and listening to microseismic emissions. *Natural Hazards and Earth System Sciences*, 9(4), 1119-1131. DOI: <https://doi.org/10.5194/nhess-9-1119-2009>
- Arosio, D., Longoni, L., Papini, M., Boccolari, M., & Zanzi, L. (2018). Analysis of microseismic signals collected on an unstable rock face in the Italian Prealps. *Geophysical Journal International*, 213(1), 475-488. DOI: <https://doi.org/10.1093/gji/ggy010>
- Atkinson PM, Massari R (1998) Generalised linear modelling of susceptibility to landsliding in the Central Apennines, Italy. *Computer & Geosciences* 24: 373-385. [https://doi.org/10.1016/S0098-3004\(97\)00117-9](https://doi.org/10.1016/S0098-3004(97)00117-9)
- Bagheri, V., Uromeihy, A., & Aghda, S. F. (2019). Predicting the probability of rockfalls occurrence caused by the earthquake of Changureh-Avaj in 2002 using LR, MLP, and RBF methods. *Bulletin of Engineering Geology and the Environment*, 78(5), 3119-3141. DOI: <https://doi.org/10.1007/s10064-018-1323-5>
- Bai, X., Jian, J., He, S., & Liu, W. (2019). Dynamic process of the massive Xinmo landslide, Sichuan (China), from joint seismic signal and morphodynamic analysis. *Bulletin of Engineering Geology and the Environment*, 78(5), 3269-3279. DOI: <https://doi.org/10.1007/s10064-018-1360-0>
- Balducci M., Regni R., Buttiglia S., Piccioni R., Venanti L.D., Casagli N. and Gigli G. (2011). Design and built of a ground reinforced embankment for the protection of a provincial road (Assisi, Italy) against rockslide. Proc. XXIV Conv. Naz. Geotecnica, AGI, Napoli, 22th-24th June 2011.
- Barchi M., DeFeyter A., Magnani B., Minelli G., Pialli G. and Sotera B. (1998b) – The structural style of the Umbria-Marche fold and thrust belt. *Memorie della Società Geologica Italiana*, 52, pp. 557-578.
- Bataille, K., & Chiu, J. M. (1991). Polarization analysis of high-frequency, three-component seismic data. *Bulletin of the Seismological Society of America*, 81(2), 622-642.
- Beccar-Varela MP, Gonzalez-Huizar H, Mariani MC, et al. (2016) Use of wavelets techniques to discriminate between explosions and natural earthquakes. *Physica A: Statistical Mechanics and its Applications* 457: 42-51. <https://doi.org/10.1016/j.physa.2016.03.077>
- Bendat, J.S. and Piersol, A.G., 2000. *Random data analysis and measurement procedures*.
- Benítez MC, Ramírez J, Segura JC, et al. (2007) Continuous HMM-based seismic-event classification at Deception Island, Antarctica. *IEEE Transactions on Geoscience and Remote Sensing* 45(1): 138-146. <https://doi.org/10.1109/TGRS.2006.882264>
- Beyreuther, M., & Wassermann, J. (2008a). Continuous earthquake detection and classification using discrete Hidden Markov Models. *Geophysical Journal International*, 175(3), 1055-1066. DOI: 10.1111/j.1365-246X.2008.03921.x
- Beyreuther, M., Carniel, R., & Wassermann, J. (2008b). Continuous hidden Markov models: application to automatic earthquake detection and classification at Las Cañadas caldera, Tenerife. *Journal of Volcanology and Geothermal Research*, 176(4), 513-518. DOI: 10.1016/j.jvolgeores.2008.04.021

- Beyreuther, M., & Wassermann, J. (2011). Hidden semi-Markov model based earthquake classification system using weighted finite-state transducers. *Nonlinear Processes in Geophysics*, 18(1), 81-89. DOI: <https://doi.org/10.5194/npg-18-81-2011>
- Beyreuther, M., Hammer, C., Wassermann, J., Ohrnberger, M., & Megies, T. (2012). Constructing a Hidden Markov Model based earthquake detector: application to induced seismicity. *Geophysical Journal International*, 189(1), 602-610. DOI: <https://doi.org/10.1111/j.1365-246X.2012.05361.xs>
- Bhatti, S. M., Khan, M. S., Wuth, J., Huenupan, F., Curilem, M., Franco, L., & Yoma, N. B. (2016). Automatic detection of volcano-seismic events by modeling state and event duration in hidden Markov models. *Journal of Volcanology and Geothermal Research*, 324, 134-143. DOI: <http://dx.doi.org/10.1016/j.jvolgeores.2016.05.015>
- Bicego, M., Acosta-Muñoz, C., & Orozco-Alzate, M. (2012). Classification of seismic volcanic signals using hidden-Markov-model-based generative embeddings. *IEEE Transactions on Geoscience and Remote Sensing*, 51(6), 3400-3409. DOI: 10.1109/TGRS.2012.2220370
- Bishop, A. N., Anderson, B. D., Fidan, B., Pathirana, P. N., & Mao, G. (2009). Bearing-only localization using geometrically constrained optimization. *IEEE Transactions on Aerospace and Electronic Systems*, 45(1), 308-320. DOI: 10.1109/TAES.2009.4805281
- Blikra, L.H., 2012. The Åknes rockslide. In: Clague, Norway.J.J., Stead, D. (Eds.), *Landslides: Types, Mechanisms and Modeling*. Cambridge University Press, pp. 323–335.
- Boccaletti M., Elter P. and Guazzone G. (1971) – Plate tectonic models for the development of the western Alps and Northern Apennines. *Nature*, 234, pp. 108-111.
- Boore, D. M., & Thompson, E. M. (2014). Path durations for use in the stochastic-method simulation of ground motions. *Bulletin of the Seismological Society of America*, 104(5), 2541-2552. DOI: 10.1785/0120140058
- Burtin A, Bollinger L, Cattin R, et al. (2009) Spatiotemporal sequence of Himalayan debris flow from analysis of high-frequency seismic noise. *Journal of Geophysical Research Earth Surface* 114(F4): F04009. DOI: <https://doi.org/10.1029/2008JF001198>
- Burtin A, Hovius N, Milodowski DT, et al. (2013) Continuous catchment-scale monitoring of geomorphic processes with a 2-D seismological array. *Journal of Geophysical Research Earth Surface* 118(3): 1956-1974. DOI: <https://doi.org/10.1002/jgrf.20137>
- Burtin A, Hovius N, McArdell BW, et al. (2014) Seismic constraints on dynamic links between geomorphic processes and routing of sediment in a steep mountain catchment. *Earth Surface Dynamics* 2(1): 21-33. DOI: <https://doi.org/10.5194/esurf-2-21-2014>
- Burtin A, Hovius N, Turowski JM (2016) Seismic monitoring of torrential and fluvial processes. *Earth Surface Dynamics* 4(2): 285-307. DOI: <https://doi.org/10.5194/esurf-4-285-2016>
- Carlà, T., Farina, P., Intrieri, E., Botsialas, K., & Casagli, N. (2017). On the monitoring and early-warning of brittle slope failures in hard rock masses: Examples from an open-pit mine. *Engineering geology*, 228, 71-81.
- Carniel, R., Jolly, A. D., & Barbui, L. (2013). Analysis of phreatic events at Ruapehu volcano, New Zealand using a new SOM approach. *Journal of Volcanology and Geothermal Research*, 254, 69-79. DOI: <http://dx.doi.org/10.1016/j.jvolgeores.2012.12.026>

Casagli N., Gigli G., Lombardi L. and Nocentini M. (2006a) – Valutazione delle distanze di propagazione relative ai fenomeni franosi presenti sul fronte della cava di Torgiovannetto (PG) – rapporto 1.0. Studio commissionato dal Dipartimento della Protezione Civile.

Casagli N., Gigli G., Lombardi L. and Nocentini M. (2006b) – Valutazione delle distanze di propagazione relative ai fenomeni franosi presenti sul fronte della cava di Torgiovannetto (PG) – rapporto 2.0. Studio commissionato dal Dipartimento della Protezione Civile.

Casagli N., Gigli G., Lombardi L., Nocentini M. and Vannocci P. (2007a) – Indagini geofisiche e geotecniche e modellazione dinamica della frana di Torgiovannetto (Pg) – Rapporto 1.0. Convenzione fra il Dipartimento di Scienze della Terra dell'Università di Firenze e la Provincia di Perugia.

Casagli N., Gigli G., Lombardi L., Nocentini M., Mattiangeli L. and Vannocci P. (2007b) - Indagini geofisiche e geotecniche e modellazione dinamica della frana di Torgiovannetto (Pg) – Rapporto 2.0. Convenzione fra il Dipartimento di Scienze della Terra dell'Università di Firenze e la Provincia di Perugia.

Chouet, B. A., & Matoza, R. S. (2013). A multi-decadal view of seismic methods for detecting precursors of magma movement and eruption. *Journal of Volcanology and Geothermal Research*, 252, 108-175. DOI: <http://dx.doi.org/10.1016/j.jvolgeores.2012.11.013>

Colombero, C., Comina, C., Vinciguerra, S., & Benson, P. M. (2018). Microseismicity of an unstable rock mass: From field monitoring to laboratory testing. *Journal of Geophysical Research: Solid Earth*, 123(2), 1673-1693. DOI: <https://doi.org/10.1002/2017JB014612>

Coviello, V., Chiarle, M., Arattano, M., Pogliotti, P. and di Cella, U.M., 2015. Monitoring rock wall temperatures and microseismic activity for slope stability investigation at JA Carrel hut, Matterhorn. In *Engineering Geology for Society and Territory-Volume 1* (pp. 305-309). Springer, Cham. DOI: https://doi.org/10.1007/978-3-319-09300-0_57

Coviello, V., Arattano, M., Comiti, F., Macconi, P., & Marchi, L. (2019). Seismic characterization of debris flows: insights into energy radiation and implications for warning. *Journal of Geophysical Research: Earth Surface*. DOI: 10.1029/2018JF004683

Curilem, G., Vergara, J., Fuentealba, G., Acuña, G., & Chacón, M. (2009). Classification of seismic signals at Villarrica volcano (Chile) using neural networks and genetic algorithms. *Journal of volcanology and geothermal research*, 180(1), 1-8. DOI: <https://doi.org/10.1016/j.jvolgeores.2008.12.002>

Curilem, M., Vergara, J., San Martin, C., Fuentealba, G., Cardona, C., Huenupan, F., ... & Yoma, N. B. (2014). Pattern recognition applied to seismic signals of the Llaima volcano (Chile): An analysis of the events' features. *Journal of Volcanology and Geothermal Research*, 282, 134-147. DOI: <http://dx.doi.org/10.1016/j.jvolgeores.2014.06.004>

Dammeier, F., Moore, J. R., Haslinger, F., & Loew, S. (2011). Characterization of alpine rockslides using statistical analysis of seismic signals. *Journal of Geophysical Research: Earth Surface*, 116(F4). DOI: 10.1029/2011JF002037

Dammeier, F., Moore, J. R., Hammer, C., Haslinger, F., & Loew, S. (2016). Automatic detection of alpine rockslides in continuous seismic data using hidden Markov models. *Journal of Geophysical Research: Earth Surface*, 121(2), 351-371. DOI: 10.1002/2015JF003647

Daubechies I (1992) Ten lectures on wavelets. Society for Industrial and Applied Mathematics. p 357.

- Deere, D. U. (1968). Geological consideration. Rock mechanics in engineering practice.
- Del Gaudio, V., Luo, Y., Wang, Y., & Wasowski, J. (2018). Using ambient noise to characterise seismic slope response: The case of Qiaozhuang peri-urban hillslopes (Sichuan, China). *Engineering geology*, 246, 374-390. DOI: <https://doi.org/10.1016/j.enggeo.2018.10.008>
- Deparis, J., Jongmans, D., Cotton, F., Baillet, L., Thouvenot, F., & Hantz, D. (2008). Analysis of rock-fall and rock-fall avalanche seismograms in the French Alps. *Bulletin of the Seismological Society of America*, 98(4), 1781-1796. DOI: <https://doi.org/10.1785/0120070082>
- Diersen, S., Lee, E. J., Spears, D., Chen, P., & Wang, L. (2011). Classification of seismic windows using artificial neural networks. *Procedia computer science*, 4, 1572-1581. DOI: 10.1016/j.procs.2011.04.170
- Dietze, M., Mohadjer, S., Turowski, J. M., Ehlers, T. A., & Hovius, N. (2017a). Seismic monitoring of small alpine rockfalls—validity, precision and limitations. *Earth Surface Dynamics*, 5(4), 653-668. DOI: <https://doi.org/10.5194/esurf-5-653-2017>
- Dietze, M., Turowski, J. M., Cook, K. L., & Hovius, N. (2017b). Spatiotemporal patterns, triggers and anatomies of seismically detected rockfalls. *Earth Surface Dynamics*, 5(4). DOI: <https://doi.org/10.5194/esurf-5-757-2017>
- Fan, X., Xu, Q., Scaringi, G., Dai, L., Li, W., Dong, X., Zhu, X., Pei, X., Dai, K. and Havenith, H.B., 2017. Failure mechanism and kinematics of the deadly June 24th 2017 Xinmo landslide, Maoxian, Sichuan, China. *Landslides*, 14(6), pp.2129-2146. DOI: <https://doi.org/10.1007/s10346-017-0907-7>
- Fan, X., Scaringi, G., Xu, Q., Zhan, W., Dai, L., Li, Y., ... & Huang, R. (2018). Coseismic landslides triggered by the 8th August 2017 M s 7.0 Jiuzhaigou earthquake (Sichuan, China): factors controlling their spatial distribution and implications for the seismogenic blind fault identification. *Landslides*, 15(5), 967-983. DOI: <https://doi.org/10.1007/s10346-018-0960-x>
- Farin M, Mangeney A, Toussaint R, et al. (2015) Characterization of rockfalls from seismic signal: Insights from laboratory experiments. *Journal of Geophysical Research Solid Earth* 120(10): 7102-7137. <https://doi.org/10.1002/2015JB012331>
- Farin, M., Mangeney, A., De Rosny, J., Toussaint, R., Sainte-Marie, J., & Shapiro, N. M. (2016). Experimental validation of theoretical methods to estimate the energy radiated by elastic waves during an impact. *Journal of Sound and Vibration*, 362, 176-202. DOI: <http://dx.doi.org/10.1016/j.jsv.2015.10.003>
- Farin, M., Mangeney, A., De Rosny, J., Toussaint, R., & Trinh, P. T. (2018). Link between the dynamics of granular flows and the generated seismic signal: insights from laboratory experiments. *Journal of Geophysical Research: Earth Surface*, 123(6), 1407-1429. DOI: 10.1029/2017JF004296
- Feng, Z. (2011), The seismic signatures of the 2009 Shiaolin landslide in Taiwan, *Nat. Hazards Earth Syst. Sci.*, 11, 1559– 1569, doi:10.5194/nhess-11-1559-2011.
- Feng, L., Pazzi, V., Intrieri, E., Gracchi, T., & Gigli, G. (2019). Rockfall seismic features analysis based on in situ tests: frequency, amplitude, and duration. *Journal of Mountain Science*, 16(5), 955-970. *Journal of Mountain Science*: DOI: <https://doi.org/10.1007/s11629-018-5286-6>
- Fiorucci, M., Iannucci, R., Lenti, L., Martino, S., Paciello, A., Prestininzi, A., & Rivellino, S. (2015, November). Seismic monitoring of the gravity-induced deformation involving the Peschiera Spring Slope (Italy) for the

management of a main infrastructure. In 6th international conference on earthquake geotechnical engineering, Christchurch, New Zealand (pp. 1-4).

Flinn, E.A., 1965. Signal analysis using rectilinearity and direction of particle motion. *Proceedings of the IEEE*, 53(12), pp.1874-1876.

Fuchs, F., Lenhardt, W., Bokelmann, G., & AlpArray Working Group. (2018). Seismic detection of rockslides at regional scale: examples from the Eastern Alps and feasibility of kurtosis-based event location. *Earth Surface Dynamics*, 6(4), 955-970. DOI: <https://doi.org/10.5194/esurf-6-955-2018>

Fukuzono, T., 1985. A new method for predicting the failure time of a slope failure. *Proceedings of the 4th International Conference and Field Workshop on Landslides, Tokyo (Japan)*, pp. 145–150.

Gibbons, S. J., Sørensen, M. B., Harris, D. B., & Ringdal, F. (2007). The detection and location of low magnitude earthquakes in northern Norway using multi-channel waveform correlation at regional distances. *Physics of the Earth and Planetary Interiors*, 160(3-4), 285-309. DOI: 10.1016/j.pepi.2006.11.008

Gibbons, S. J., Ringdal, F., & Kværna, T. (2012). Ratio-to-moving-average seismograms: a strategy for improving correlation detector performance. *Geophysical Journal International*, 190(1), 511-521. DOI: <https://doi.org/10.1111/j.1365-246X.2012.05492.x>

Gigli G, Morelli S, Fornera S, et al. (2014a) Terrestrial laser scanner and geomechanical surveys for the rapid evaluation of rock fall susceptibility scenarios. *Landslides* 11(1): 1-14. <https://doi.org/10.1007/s10346-012-0374-0>

Gigli G, Intrieri E, Lombardi L, et al. (2014b) Event scenario analysis for the design of rockslide countermeasures. *Journal of Mountain Science* 6: 1521-1530. <https://doi.org/10.1007/s11629-014-3164-4>

Glasgow, M. E., Schmandt, B., & Hansen, S. M. (2018). Upper crustal low-frequency seismicity at Mount St. Helens detected with a dense geophone array. *Journal of Volcanology and Geothermal Research*, 358, 329-341. DOI: <https://doi:10.1016/j.jvolgeores.2018.06.006>

Goldstein, P., Dodge, D., Firpo, M., Minner, L., Lee, W. H. K., Kanamori, H., ... & Kisslinger, C. (2003). SAC2000: Signal processing and analysis tools for seismologists and engineers. *The IASPEI International Handbook of Earthquake and Engineering Seismology*, 81, 1613-1620.

Goldstein, P, & Snoke, A (2005). SAC availability for the IRIS Community, *Electronic Newsletter, Incorporated Institutions for Seismology, Data Management Center*.

Graziani A, Marsella M, Rotonda T, et al. (2009). Study of a rock slide in a limestone formation with clay interbeds. *Proceeding International Conference on Rock Joints and Jointed Rock Masses, Tucson, Arizona, USA 7th-8th January 2009*.

Gracchi, T., Lotti, A., Saccorotti, G., Lombardi, L., Nocentini, M., Mugnai, F., ... & Fiaschi, A. (2017). A method for locating rockfall impacts using signals recorded by a microseismic network. *Geoenvironmental Disasters*, 4(1), 26. DOI: <https://doi.org/10.1186/s40677-017-0091-z>

Grigoli, F., Cesca, S., Vassallo, M., & Dahm, T. (2013). Automated seismic event location by travel-time stacking: An application to mining induced seismicity. *Seismological Research Letters*, 84(4), 666-677. DOI: 10.1785/0220120191

- Guéguen, P., Cornou, C., Garambois, S., & Banton, J. (2007). On the limitation of the H/V spectral ratio using seismic noise as an exploration tool: application to the Grenoble valley (France), a small apex ratio basin. *Pure and applied geophysics*, 164(1), 115-134. DOI: <https://doi.org/10.1007/s00024-006-0151-x>
- Guinau, M., Tapia, M., Pérez-Guillén, C., Suriñach, E., Roig, P., Khazaradze, G., ... & Echeverria, A. (2019). Remote sensing and seismic data integration for the characterization of a rock slide and an artificially triggered rock fall. *Engineering Geology*, 257, 105-113. DOI: <https://doi.org/10.1016/j.enggeo.2019.04.010>
- Gutiérrez, L., Ramírez, J., Benítez, C., Ibañez, J., Almendros, J., & García-Yeguas, A. (2006, July). HMM-based classification of seismic events recorded at Stromboli and Etna volcanoes. In 2006 IEEE International Symposium on Geoscience and Remote Sensing (pp. 2765-2768). IEEE. DOI: 10.1109/IGARSS.2006.711
- Hafez, A. G., Khan, T. A., & Kohda, T. (2009). Earthquake onset detection using spectro-ratio on multi-threshold time–frequency sub-band. *Digital Signal Processing*, 19(1), 118-126. DOI: <https://doi.org/10.1016/j.dsp.2008.08.003>
- Hafez, A.G., Khan, M.T.A. and Kohda, T., 2010. Clear P-wave arrival of weak events and automatic onset determination using wavelet filter banks. *Digital Signal Processing*, 20(3), pp.715-723. DOI: <https://doi.org/10.1016/j.dsp.2009.10.002>
- Hafez, A. G., Rabie, M., & Kohda, T. (2013). Detection of precursory signals in front of impulsive P-waves. *Digital Signal Processing*, 23(3), 1032-1039. DOI: <https://doi.org/10.1016/j.dsp.2012.12.018>
- Hammer, C., Fäh, D., & Ohrnberger, M. (2017). Automatic detection of wet-snow avalanche seismic signals. *Natural hazards*, 86(2), 601-618. DOI: 10.1007/s11069-016-2707-0
- Heck, M., Hammer, C., Herwijnen, A. V., Schweizer, J., & Fäh, D. (2018). Automatic detection of snow avalanches in continuous seismic data using hidden Markov models. *Natural Hazards and Earth System Sciences*, 18(1), 383-396. DOI: <https://doi.org/10.3929/ethz-b-000239019>
- Helmstetter, A., & Garambois, S. (2010). Seismic monitoring of Séchilienne rockslide (French Alps): Analysis of seismic signals and their correlation with rainfalls. *Journal of Geophysical Research: Earth Surface*, 115(F3). DOI: 10.1029/2009JF001532
- Hibert C, Mangeney A, Grandjean G, et al. (2011) Slope instabilities in Dolomieu crater, Réunion Island: From seismic signals to rockfall characteristics. *Journal of Geophysical Research Earth Surface* 116(F4): F04032. <https://doi.org/10.1029/2011JF002038>
- Hibert, C., Mangeney, A., Grandjean, G., Baillard, C., Rivet, D., Shapiro, N. M., ... & Crawford, W. (2014a). Automated identification, location, and volume estimation of rockfalls at Piton de la Fournaise volcano. *Journal of Geophysical Research: Earth Surface*, 119(5), 1082-1105. DOI: 10.1002/2013JF002970
- Hibert, C., Ekström, G., & Stark, C. P. (2014b). Dynamics of the Bingham Canyon Mine landslides from seismic signal analysis. *Geophysical research letters*, 41(13), 4535-4541. DOI: 10.1002/2013JF002970
- Hibert C, Malet JP, Bourrier F, et al. (2017a) Single-block rockfall dynamics inferred from seismic signal analysis. *Earth Surface Dynamics* 5(2): 283-292. <https://doi.org/10.5194/esurf-5-283-2017>

- Hibert C, Mangeney A, Grandjean G, et al. (2017b) Spatio-temporal evolution of rockfall activity from 2007 to 2011 at the Piton de la Fournaise volcano inferred from seismic data. *Journal of Volcanology and Geothermal Research* 333-334: 36-52. <https://doi.org/10.1016/j.jvolgeores.2017.01.007>
- Hibert C, Provost F, Malet JP, et al. (2017c) Automatic identification of rockfalls and volcano-tectonic earthquakes at the Piton de la Fournaise volcano using a Random Forest algorithm. *Journal of Volcanology and Geothermal Research* 340: 130-142. <https://doi.org/10.1016/j.jvolgeores.2017.04.015>
- Huggel, C., Zraggen-Oswald, S., Haeberli, W., Kääh, A., Polkvoj, A., Galushkin, I., & Evans, S. G. (2005). The 2002 rock/ice avalanche at Kolka/Karmadon, Russian Caucasus: assessment of extraordinary avalanche formation and mobility, and application of QuickBird satellite imagery. *Natural Hazards and Earth System Science*, 5(2), 173-187.
- Hungr, O., Leroueil, S., & Picarelli, L., (2014). The Varnes classification of landslide types, an update. *Landslides*, 11(2), 167-194. doi: 10.1007/s10346-013-0436-y
- Intrieri E, Gigli G, Mugnai F, et al. (2012) Design and implementation of a landslide early warning system. *Engineering Geology* 147-148: 124-136. <https://doi.org/10.1016/j.enggeo.2012.07.017>
- Intrieri, E., Carlà, T., & Gigli, G. (2019). Forecasting the time of failure of landslides at slope-scale: A literature review. *Earth-science reviews*. DOI: <https://doi.org/10.1016/j.earscirev.2019.03.019>
- Iovine, G., Petrucci, O., Rizzo, V., Tansi, C., 2006. The March 7th 2005 Cavallerizzo (Cerzeto) landslide in Calabria - Southern Italy. In: *Proceedings of the 10th IAEG Congress, Nottingham, Great Britain*. Geological Society of London, pp. 12 (paper n. 785)
- IRPI (2006). Caratteristiche litologiche, strutturali e geomorfologiche del Versante nel quale ricade l'area della ex-cava in prossimità di Casa Torgiovanetto, comune di Assisi. Unpublished report. In Italian.
- Jibson R.W. and Keefer D.K., (1993) - Analysis of the seismic origin of landslides: Examples from the New Madrid seismic zone, *Geol. Soc. Am. Bull.*, 105, pp. 521–536.
- Jolly, A. D., Thompson, G., & Norton, G. E. (2002). Locating pyroclastic flows on Soufriere Hills Volcano, Montserrat, West Indies, using amplitude signals from high dynamic range instruments. *Journal of Volcanology and Geothermal Research*, 118(3-4), 299-317. DOI: [https://doi.org/10.1016/S0377-0273\(02\)00299-8](https://doi.org/10.1016/S0377-0273(02)00299-8)
- Joswig M (1995) Automated classification of local earthquake data in the BUG small array. *Geophysical Journal International* 120(2): 262-286. <https://doi.org/10.1111/j.1365-246X.1995.tb01818.x>
- Jurkevics, A. (1988). Polarization analysis of three-component array data. *Bulletin of the seismological society of America*, 78(5), 1725-1743.
- Kao, H., & Shan, S. J. (2004). The source-scanning algorithm: Mapping the distribution of seismic sources in time and space. *Geophysical Journal International*, 157(2), 589-594. DOI: <https://doi.org/10.1111/j.1365-246X.2004.02276.x>
- Kao, H., Kan, C. W., Chen, R. Y., Chang, C. H., Rosenberger, A., Shin, T. C., ... & Liang, W. T. (2012). Locating, monitoring, and characterizing typhoon-induced landslides with real-time seismic signals. *Landslides*, 9(4), 557-563. DOI: <https://doi.org/10.1007/s10346-012-0322-z>

- Khazai B. and Sitar N. (2004) - Evaluation of Factors Controlling Earthquake- Induced Landslides Caused by Chi-Chi Earthquake and Comparison with the Northridge and Loma Prieta Events, *Eng. Geol.*, 71, pp. 79–95.
- Kim SG, Park YC, Kim WY (1998) Discrimination of small earthquakes and artificial explosions in the Korean Peninsula using Pg/Lg ratios. *Geophysical Journal International* 134(1): 267-276. <https://doi.org/10.1046/j.1365-246x.1998.00575.x>
- Kleinbrod, U., Burjánek, J., & Fäh, D. (2019). Ambient vibration classification of unstable rock slopes: A systematic approach. *Engineering geology*, 249, 198-217. DOI: <https://doi.org/10.1016/j.enggeo.2018.12.012>
- Kortström, J., Uski, M., & Tiira, T. (2016). Automatic classification of seismic events within a regional seismograph network. *Computers & Geosciences*, 87, 22-30. DOI: <https://doi.org/10.1016/j.cageo.2015.11.006>
- Kristensen, L., Rivolta, C., Dehls, J., & Blikra, L. H. (2013). GB-InSAR measurement at the Åknes rockslide, Norway. In *Proc. International Conference Vajont*.
- Küperkoch, L., Meier, T., Lee, J., Friederich, W., & EGELADOS Working Group. (2010). Automated determination of P-phase arrival times at regional and local distances using higher order statistics. *Geophysical Journal International*, 181(2), 1159-1170. DOI: <https://doi.org/10.1111/j.1365-246X.2010.04570.x>
- Küperkoch, L., Meier, T., Brüstle, A., Lee, J., & Friederich, W. (2012). Automated determination of S-phase arrival times using autoregressive prediction: application to local and regional distances. *Geophysical Journal International*, 188(2), 687-702. DOI: 10.1111/j.1365-246X.2011.05292.x
- Laasri EHA, Akhouayri ES, Agliz D, et al. (2015) A fuzzy expert system for automatic seismic signal classification. *Expert Systems with Applications* 42(3): 1013-1027. <https://doi.org/10.1016/j.eswa.2014.08.023>
- Lacroix P, Helmstetter A (2011) Location of seismic signals associated with microearthquakes and rockfalls on the Séchilienne landslide, French Alps. *Bulletin of the Seismological Society of America* 101(1): 341-353. <https://doi.org/10.1785/0120100110>
- Lacroix P, Grasso JR, Roulle J, et al. (2012) Monitoring of snow avalanches using a seismic array: Location, speed estimation, and relationships to meteorological variables. *Journal of Geophysical Research: Earth Surface* 117: F01034. <https://doi.org/10.1029/2011JF002106>
- Langer, H., Falsaperla, S., & Thompson, G. (2003). Application of artificial neural networks for the classification of the seismic transients at Soufriere Hills volcano, Montserrat. *Geophysical research letters*, 30(21). DOI: <https://doi.org/10.1029/2003GL018082>
- Langer H, Falsaperla S, Powell T, et al. (2006) Automatic classification and a-posteriori analysis of seismic event identification at Soufriere Hills volcano, Montserrat. *Journal of Volcanology and Geothermal Research* 153(1-2): 1-10. <https://doi.org/10.1016/j.jvolgeores.2005.08.012>
- Lara-Cueva RA, Benítez DS, Carrera EV, et al. (2016) Feature selection of seismic waveforms for long period event detection at Cotopaxi Volcano. *Journal of Volcanology and Geothermal* 316: 34-49. <https://doi.org/10.1016/j.jvolgeores.2016.02.022>
- La Rocca, M., Galluzzo, D., Saccorotti, G., Tinti, S., Cimini, G. B., and Del Pezzo, E. (2004), Seismic signals associated with landslides and with a tsunami at Stromboli volcano, Italy, *Bull. Seismol. Soc. Am.*, 94(5), 1850–1867, doi:10.1785/012003238.

Lenti, L., Martino, S., Paciello, A., Prestininzi, A., & Rivellino, S. (2012). Microseismicity within a karstified rock mass due to cracks and collapses as a tool for risk management. *Natural Hazards*, 64(1), 359-379. DOI: <https://doi.org/10.1007/s11069-012-0245-y>

Levy C, Mangeney A, Bonilla F, et al. (2015) Friction weakening in granular flows deduced from seismic records at the Soufrière Hills Volcano, Montserrat. *Journal of Geophysical Research Solid Earth* 120(11): 7536-7557. <https://doi.org/10.1002/2015JB012151>

Lin, C. H., Jan, J. C., Pu, H. C., Tu, Y., Chen, C. C., & Wu, Y. M. (2015). Landslide seismic magnitude. *Earth and Planetary Science Letters*, 429, 122-127. DOI: <http://dx.doi.org/10.1016/j.epsl.2015.07.068>

Lin, C. H., Kumagai, H., Ando, M., and Shin, T. C. (2010), Detection of landslides and submarine slumps using broadband seismic networks, *Geophys. Res. Lett.*, 37, L22309, DOI: 10.1029/2010GL044685.

Li, L., & Lan, H. (2015). Probabilistic modeling of rockfall trajectories: a review. *Bulletin of Engineering Geology and the Environment*, 74(4), 1163-1176. DOI: 10.1007/s10064-015-0718-9

Lomax A. and A. Michelini (2009), Mw_{pd}: A Duration-Amplitude Procedure for Rapid Determination of Earthquake Magnitude and Tsunamigenic Potential from P Waveforms, *Geophys. J. Int.*,176, 200-214, doi:10.1111/j.1365-246X.2008.03974.x

Lombardi, L., Nocentini, M., Frodella, W., Nolesini, T., Bardi, F., Intrieri, E., Carlà, T., Solari, L., Dotta, G., Ferrigno, F., Casagli, N., 2017. The Calatabiano landslide (Southern Italy): preliminary GB-InSAR monitoring data and remote 3D mapping. *Landslides* 14 (2), 685–696.

Lotti, A., Saccorotti, G., Fiaschi, A., Matassoni, L., Gigli, G., Pazzi, V., Casagli, N., (2015). Seismic monitoring of rockslide: the Torgiovanetto quarry (Central Apennines, Italy). In: G. Lollino et al. (eds), *Engineering Geology for Society and Territory – Vol.2*, Springer International Publishing, Switzerland. pp 1537-1540. doi: 10.1007/978-3-319-09057-3_272.

Lotti, A., Pazzi, V., Saccorotti, G., Fiaschi, A., Matassoni, L., Gigli, G., (2018). HVSR Analysis of Rockslide Seismic Signals to Assess the Subsoil Conditions and the Site Seismic Response. *International Journal of Geophysics*. Article ID 9383189. doi: <https://doi.org/10.1155/2018/9383189>

Lu, C.P., Dou, L.M., Liu, B., Xie, Y.S. and Liu, H.S., (2012). Microseismic low-frequency precursor effect of bursting failure of coal and rock. *Journal of Applied Geophysics*, 79, pp.55-63. DOI: <https://doi.org/10.1016/j.jappgeo.2011.12.013>

Lu, C. P., Dou, L. M., Zhang, N., Xue, J. H., Wang, X. N., Liu, H., & Zhang, J. W. (2013). Microseismic frequency-spectrum evolutionary rule of rockburst triggered by roof fall. *International Journal of Rock Mechanics and Mining Sciences*, 64, 6-16. DOI: <https://doi.org/10.1016/j.ijrmms.2013.08.022>

Li, L. Q., Ju, N. P., Zhang, S., Deng, X. X., & Sheng, D. (2019). Seismic wave propagation characteristic and its effects on the failure of steep jointed anti-dip rock slope. *Landslides*, 16(1), 105-123. DOI: <https://doi.org/10.1007/s10346-018-1071-4>

Ma, N., Wang, G., Kamai, T., Doi, I., & Chigira, M. (2019). Amplification of seismic response of a large deep-seated landslide in Tokushima, Japan. *Engineering Geology*, 249, 218-234. DOI: <https://doi.org/10.1016/j.enggeo.2019.01.002>

- Macciotta, R., Hendry, M., Cruden, D. M., Blais-Stevens, A., & Edwards, T. (2017). Quantifying rock fall probabilities and their temporal distribution associated with weather seasonality. *Landslides*, 14(6), 2025-2039. DOI: <https://doi.org/10.1007/s10346-017-0834-7>
- Magotra, N., Ahmed, N., & Chael, E. (1987). Seismic event detection and source location using single-station (three-component) data. *Bulletin of the Seismological Society of America*, 77(3), 958-971.
- Manconi, A., Picozzi, M., Coviello, V., De Santis, F., & Elia, L. (2016). Real-time detection, location, and characterization of rockslides using broadband regional seismic networks. *Geophysical Research Letters*, 43(13), 6960-6967. DOI: <https://doi.org/10.1002/2016GL069572>
- Manconi, A., Coviello, V., Galletti, M., & Seifert, R. (2018). Monitoring rockfalls with the Raspberry Shake. *Earth Surface Dynamics*, 6(4), 1219-1227. DOI: <https://doi.org/10.5194/esurf-6-1219-2018>
- Matsuoka, N. (2019). A multi-method monitoring of timing, magnitude and origin of rockfall activity in the Japanese Alps. *Geomorphology*, 336, 65-76. DOI: <https://doi.org/10.1016/j.geomorph.2019.03.023>
- McCarroll D, Shakesby RA, Matthews JA (1998) Spatial and temporal patterns of late Holocene rockfall activity on a Norwegian talus slope: a lichenometric and simulation-modeling approach. *Arctic and Alpine Research* 30(1): 51-60. <https://doi.org/10.1080/00040851.1998.12002875>
- Mendecki, A. J., Lynch, R. A., & Malovichko, D. A. (2010, November). Routine micro-seismic monitoring in mines. In *Australian Earthquake Engineering Soc., Annual Conference Perth, Australia* (pp. 1-33).
- Moran, S. C., Matoza, R. S., Garcés, M. A., Hedlin, M. A. H., Bowers, D., Scott, W. E., ... & Vallance, J. W. (2008). Seismic and acoustic recordings of an unusually large rockfall at Mount St. Helens, Washington. *Geophysical research letters*, 35(19). DOI: 10.1029/2008GL035176
- Moser, T. J., Van Eck, T., & Nolet, G. (1992). Hypocenter determination in strongly heterogeneous earth models using the shortest path method. *Journal of Geophysical Research: Solid Earth*, 97(B5), 6563-6572.
- Myers, S.C., Johannesson, G. and Hanley, W., 2007. A Bayesian hierarchical method for multiple-event seismic location. *Geophysical Journal International*, 171(3), pp.1049-1063. DOI: 10.1111/j.1365-246X.2007.03555.x
- Mykkeltveit, S., & Bungum, H. (1984). Processing of regional seismic events using data from small-aperture arrays. *Bulletin of the Seismological Society of America*, 74(6), 2313-2333.
- Norris, R. D. (1994). Seismicity of rockfalls and avalanches at three Cascade Range volcanoes: Implications for seismic detection of hazardous mass movements. *Bulletin of the Seismological Society of America*, 84(6), 1925-1939.
- Ohnaka, M., & Mogi, K. (1982). Frequency characteristics of acoustic emission in rocks under uniaxial compression and its relation to the fracturing process to failure. *Journal of geophysical research: Solid Earth*, 87(B5), 3873-3884. DOI: <https://doi.org/10.1029/JB087iB05p03873>
- Panagiotakis, C., Kokinou, E., & Vallianatos, F. (2008). Automatic P-Phase Picking Based on Local-Maxima Distribution. *IEEE Transactions on Geoscience and Remote Sensing*, 46(8), 2280-2287. DOI: 10.1109/TGRS.2008.917272

Pazzi, V., Lotti, A., Chiara, P., Lombardi, L., Nocentini, M., & Casagli, N. (2017a). Monitoring of the vibration induced on the Arno masonry embankment wall by the conservation works after the May 25, 2016 riverbank landslide. *Geoenvironmental Disasters*, 4(1), 6. doi: 10.1186/s40677-017-0072-2.

Pazzi, V., Tanteri, L., Bicchieri, G., D'Ambrosio, M., Caselli, A., & Fanti, R. (2017b). H/V measurements as an effective tool for the reliable detection of landslide slip surfaces: case studies of Castagnola (La Spezia, Italy) and Roccalbegna (Grosseto, Italy). *Physics and Chemistry of the Earth, Parts A/B/C*, 98, 136-153. DOI: <https://doi.org/10.1016/j.pce.2016.10.014>

Peng, Z., (2018). <http://geophysics.eas.gatech.edu/classes/SAC/>. Last access: December 2018.

Picotti, S., Francese, R., Giorgi, M., Pettenati, F., & Carcione, J. M. (2017). Estimation of glacier thicknesses and basal properties using the horizontal-to-vertical component spectral ratio (HVSr) technique from passive seismic data. *Journal of Glaciology*, 63(238), 229-248. DOI: <https://doi.org/10.1017/jog.2016.135>

Ponziani F., Berni N., Pandolfo C., Stelluti M. and Brocca L. (2010) – An integrated approach for the real-time monitoring of a high risk landslide by a regional civil protection office, EGU Leonardo Topical Conference Series on the hydrological cycle 2010, Luxembourg, 10-12 November 2010.

Provost, F., Hibert, C., & Malet, J. P. (2017). Automatic classification of endogenous landslide seismicity using the Random Forest supervised classifier. *Geophysical Research Letters*, 44(1), 113-120. DOI: <https://doi.org/10.1002/2016GL070709>.

Rabiner, L. R. (1989). A tutorial on hidden Markov models and selected applications in speech recognition. *Proceedings of the IEEE*, 77(2), 257-286. DOI: 10.1109/5.18626

Raspini, F., Bianchini, S., Ciampalini, A., Del Soldato, M., Solari, L., Novali, F., Del Conte, S., Rucci, A., Ferretti, A., Casagli, N. (2018). Continuous, semi-automatic monitoring of ground deformation using Sentinel-1 satellites. *Scientific reports*, 8(1), 7253.

Rodi, W., & Toksoz, M. N. (2000). Grid-search techniques for seismic event location. MASSACHUSETTS INST OF TECH CAMBRIDGE EARTH RESOURCES LAB.

Rodriguez, I. V., & Sacchi, M. D. (2011a). Development of a Guided User Interface for Microseismicity Analysis. In *Recovery CSPG CSEG CWLS Convention*, Calgary, Canada.

Rodriguez, I. V. (2011b). Automatic time-picking of microseismic data combining STA/LTA and the stationary discrete wavelet transform. In *CSPG CSEG CWLS Convention, convention abstracts*.

Rodriguez, I. V., Sacchi, M., & Gu, Y. J. (2012a). Simultaneous recovery of origin time, hypocentre location and seismic moment tensor using sparse representation theory. *Geophysical Journal International*, 188(3), 1188-1202. DOI: <https://doi.org/10.1007/s00024-006-0151-x>

Rodriguez, I. V., Sacchi, M., & Gu, Y. J. (2012b). A compressive sensing framework for seismic source parameter estimation. *Geophysical Journal International*, 191(3), 1226-1236. DOI: <https://doi.org/10.1111/j.1365-246X.2012.05659.x>

Romeo, G. (1994). Seismic signals detection and classification using artificial neural networks. *Annals of Geophysics*, 37(3). DOI: <https://doi.org/10.4401/ag-4211>

- Romeo, S., Di Matteo, L., Melelli, L., Cencetti, C., Dragoni, W., & Fredduzzi, A. (2017). Seismic-induced rockfalls and landslide dam following the October 30, 2016 earthquake in Central Italy. *Landslides*, 14(4), 1457-1465. DOI: <https://doi.org/10.1007/s10346-017-0841-8>
- Rosi, A., Segoni, S., Catani, F., & Casagli, N. (2012). Statistical and environmental analyses for the definition of a regional rainfall threshold system for landslide triggering in Tuscany (Italy). *Journal of Geographical Sciences*, 22(4), 617-629.
- Rosser, N., Lim, M., Petley, D., Dunning, S., & Allison, R. (2007). Patterns of precursory rockfall prior to slope failure. *Journal of geophysical research: earth surface*, 112(F4).
- Roux, P. F., Marsan, D., Métaixian, J. P., O'Brien, G., & Moreau, L. (2008). Microseismic activity within a serac zone in an alpine glacier (Glacier d'Argentiere, Mont Blanc, France). *Journal of Glaciology*, 54(184), 157-168. DOI: <https://doi.org/10.3189/002214308784409053>
- Samson, J.C. and Olson, J.V., 1980. Some comments on the descriptions of the polarization states of waves. *Geophysical Journal International*, 61(1), pp.115-129.
- Sasaki, S. (1998). Characteristics of microseismic events induced during hydraulic fracturing experiments at the Hijiori hot dry rock geothermal energy site, Yamagata, Japan. *Tectonophysics*, 289(1-3), 171-188. DOI: [https://doi.org/10.1016/S0040-1951\(97\)00314-4](https://doi.org/10.1016/S0040-1951(97)00314-4)
- Satriano, C., Elia, L., Martino, C., Lancieri, M., Zollo, A., & Iannaccone, G. (2011). PRESTo, the earthquake early warning system for southern Italy: Concepts, capabilities and future perspectives. *Soil Dynamics and Earthquake Engineering*, 31(2), 137-153. DOI: <https://doi.org/10.1016/j.soildyn.2010.06.008>
- Scarpetta, S., Giudicepietro, F., Ezin, E. C., Petrosino, S., Del Pezzo, E., Martini, M., & Marinaro, M. (2005). Automatic classification of seismic signals at Mt. Vesuvius volcano, Italy, using neural networks. *Bulletin of the Seismological Society of America*, 95(1), 185-196. DOI: <https://doi.org/10.1785/0120030075>
- Schimmel, A., Hübl, J., McArdell, B., & Walter, F. (2018). Automatic identification of alpine mass movements by a combination of seismic and infrasound sensors. *Sensors*, 18(5), 1658. DOI: <https://doi.org/10.3390/s18051658>
- Schöpa, A., Chao, W. A., Lipovsky, B. P., Hovius, N., White, R. S., Green, R. G., & Turowski, J. M. (2018). Dynamics of the Askja caldera July 2014 landslide, Iceland, from seismic signal analysis: precursor, motion and aftermath. *Earth Surface Dynamics*, 6(2), 467-485. DOI: <https://doi.org/10.5194/esurf-6-467-2018>
- Segoni, S., Lagomarsino, D., Fanti, R., Moretti, S., & Casagli, N. (2015). Integration of rainfall thresholds and susceptibility maps in the Emilia Romagna (Italy) regional-scale landslide warning system. *Landslides*, 12(4), 773-785.
- Segoni, S., Piciullo, L., & Gariano, S. L. (2018). A review of the recent literature on rainfall thresholds for landslide occurrence. *Landslides*, 15(8), 1483-1501.
- Senfaute G, Duperret A, Lawrence JA (2009) Micro-seismic precursory cracks prior to rock-fall on coastal chalk cliffs: a case study at Mesnil-Val, Normandie, NW France. *Natural Hazards and Earth System Sciences* 9(5): 1625-1641. <https://doi.org/10.5194/nhess-9-1625-2009>

- Song, F., Kuleli, H. S., Toksöz, M. N., Ay, E., & Zhang, H. (2010). An improved method for hydrofracture-induced microseismic event detection and phase picking. *Geophysics*, 75(6), A47-A52. DOI: <https://doi.org/10.1190/1.3484716>
- Soto, R., Huenupan, F., Meza, P., Curilem, M., & Franco, L. (2018). Spectro-temporal features applied to the automatic classification of volcanic seismic events. *Journal of Volcanology and Geothermal Research*, 358, 194-206. DOI: <https://doi.org/10.1016/j.jvolgeores.2018.04.025>
- Suriñach, E., Vilajosana, I., Khazaradze, G., Biescas, B., Furdada, G., & Vilaplana, J. M. (2005). Seismic detection and characterization of landslides and other mass movements. *Natural Hazards and Earth System Science*, 5(6), 791-798.
- Suwa, H. (1991), Visual observed failure of a rock slope in Japan, *Landslide News*, 5, 8–9.
- Suwa, H., M. N. Hirano, and K. Okunishi (1991), Rock failure process of cutting slope in Shimanto geologic belt in Kyushu, Japan, *Ann. Disaster Prev. Res. Inst.*, 31(B-1), 139–152.
- Szwedzicki, T., 2003. Rock mass behaviour prior to failure. *Int. J. Rock Mech. Min. Sci.* 40 (4), 573–584.
- Tang, C. A., & Kaiser, P. K. (1998). Numerical simulation of cumulative damage and seismic energy release during brittle rock failure—part I: fundamentals. *International Journal of Rock Mechanics and Mining Sciences*, 35(2), 113-121. DOI: [https://doi.org/10.1016/S0148-9062\(97\)00009-0](https://doi.org/10.1016/S0148-9062(97)00009-0)
- Tonnellier, A., Helmstetter, A., Malet, J. P., Schmittbuhl, J., Corsini, A., & Joswig, M. (2013). Seismic monitoring of soft-rock landslides: the Super-Sauze and Valoria case studies. *Geophysical Journal International*, 193(3), 1515-1536. DOI: [10.1093/gji/ggt039](https://doi.org/10.1093/gji/ggt039)
- Trnkoczy A (1998) Understanding and setting STA/LTA trigger algorithm parameters for the K2. *Application Note 41*: 1-30.
- Vallejos, J. A., & McKinnon, S. D. (2013). Logistic regression and neural network classification of seismic records. *International Journal of Rock Mechanics and Mining Sciences*, 62, 86-95. DOI: <https://doi.org/10.1016/j.ijrmms.2013.04.005>
- Van Herwijnen, A., Heck, M., & Schweizer, J. (2016). Forecasting snow avalanches using avalanche activity data obtained through seismic monitoring. *Cold Regions Science and Technology*, 132, 68-80. DOI: <http://dx.doi.org/10.1016/j.coldregions.2016.09.014>
- Vilajosana, I., Surinach, E., Khazaradze, G., & Gauer, P. (2007). Snow avalanche energy estimation from seismic signal analysis. *Cold Regions Science and Technology*, 50(1-3), 72-85. DOI: [10.1016/j.coldregions.2007.03.007](https://doi.org/10.1016/j.coldregions.2007.03.007)
- Vilajosana, I., Surinach, E., Khazaradze, G., & Gauer, P. (2007). Snow avalanche energy estimation from seismic signal analysis. *Cold Regions Science and Technology*, 50(1-3), 72-85. DOI: [10.1016/j.coldregions.2007.03.007](https://doi.org/10.1016/j.coldregions.2007.03.007)
- Vilajosana, I., Surinach, E., Abellán, A., Khazaradze, G., Garcia, D., & Llosa, J. (2008). Rockfall induced seismic signals: case study in Montserrat, Catalonia. *Natural Hazards and Earth System Sciences*, 8(4), 805-812. DOI: <https://doi.org/10.5194/nhess-8-805-2008>
- Voight B., 1988. A method for prediction of volcanic eruption. *Nature* 332, 125–130.

Volkwein, A., Schellenberg, K., Labiouse, V., Agliardi, F., Berger, F., Bourrier, F., ... & Jaboyedoff, M. (2011). Rockfall characterisation and structural protection-a review. *Natural Hazards and Earth System Sciences*, 11, p-2617. DOI:

Walter M, Arnhardt C, Joswig M (2012a) Seismic monitoring of rockfalls, slide quakes, and fissure development at the Super-Sauze mudslide, French Alps. *Engineering Geology* 128: 12-22. <https://doi.org/10.1016/j.enggeo.2011.11.002>

Walter M, Joswig M (2012b) Seismic monitoring of precursory fracture signals from a destructive rockfall in the Vorarlberg Alps, Austria. *Natural Hazards and Earth System Sciences* 12(11): 3545-3555. <https://doi.org/10.5194/nhess-12-3545-2012>

Weber, S., Faillettaz, J., Meyer, M., Beutel, J., & Vieli, A. (2018). Acoustic and microseismic characterization in steep bedrock permafrost on Matterhorn (CH). *Journal of Geophysical Research: Earth Surface*, 123(6), 1363-1385. DOI: <https://doi.org/10.1029/2018JF004615>

Wilson R.C. and Keefer D.K. (1983) - Dynamic analysis of a slope failure from the 6 August 1979 Coyote Lake, California, earthquake, *Bull. Seism. Soc. Am.*, 73, pp. 863–877.C

Wu, S., Wang, Y., Zhan, Y., & Chang, X. (2016). Automatic microseismic event detection by band-limited phase-only correlation. *Physics of the Earth and Planetary Interiors*, 261, 3-16. DOI: <http://dx.doi.org/10.1016/j.pepi.2016.09.005>

Wyss, C. R., Rickenmann, D., Fritschi, B., Turowski, J. M., Weitbrecht, V., & Boes, R. M. (2016). Laboratory flume experiments with the S wiss plate geophone bed load monitoring system: 1. Impulse counts and particle size identification. *Water Resources Research*, 52(10), 7744-7759. DOI: <https://doi.org/10.1002/2015WR018555>

Wyss, C. R., Rickenmann, D., Fritschi, B., Turowski, J. M., Weitbrecht, V., Travaglini, E., ... & Boes, R. M. (2016). Laboratory flume experiments with the S wiss plate geophone bed load monitoring system: 2. Application to field sites with direct bed load samples. *Water Resources Research*, 52(10), 7760-7778. DOI: <https://doi.org/10.1002/2016WR019283>

Xu, N., Tang, C. A., Li, H., & Wu, S. (2011). Optimal design of micro-seismic monitoring array and seismic source location estimation for rock slope. *Open Civil Engineering Journal*, 5(1), 36-45. DOI: 10.2174/1874149501105010036

Yamada, M., Kumagai, H., Matsushi, Y., & Matsuzawa, T. (2013). Dynamic landslide processes revealed by broadband seismic records. *Geophysical Research Letters*, 40(12), 2998-3002. DOI: <https://doi.org/10.1002/grl.50437>

Yamada, M., Mori, J., & Matsushi, Y. (2016). Possible stick-slip behavior before the Rausu landslide inferred from repeating seismic events. *Geophysical Research Letters*, 43(17), 9038-9044. DOI: <https://doi.org/10.1002/2016GL069288>

Zhang, Z., & He, S. (2019). Analysis of broadband seismic recordings of landslide using empirical Green's function. *Geophysical Research Letters*, 46(9), 4628-4635. DOI: 10.1029/2018GL081448

Zobin, V. M., Reyes, G. A., & Bretón, M. (2016). Volcanic tremor at Volcán de Colima, México recorded during May 2002 and its interactions with the seismic signals produced by low-energy explosive activity and rockfalls.

Journal of Volcanology and Geothermal Research, 317, 1-14. DOI:
<http://dx.doi.org/10.1016/j.jvolgeores.2016.02.029>

Zobin, V. M. (2018). Development of the 10–11 July 2015 two-stage sequence of multiple emplacements of pyroclastic density currents at Volcán de Colima, México: Insight from associated seismic signals. *Journal of Volcanology and Geothermal Research*, 351, 29-40. DOI: <https://doi.org/10.1016/j.jvolgeores.2017.12.012>